Agriculture and its role in the global carbon cycle

Thesis by

Liyin He

In Partial Fulfillment of the Requirements

for the degree of

Doctor of Philosophy

CALIFORNIA INSTITUTE OF TECHNOLOGY

Pasadena, California

2023

(Defended June 9, 2022)

Liyin He

ORCID: 0000-0003-4427-1438

To mom and dad

ACKNOWLEDGEMENTS

While the memory of my first day arriving at Caltech is still fresh, my PhD journey at this lush campus has come to an end. The past five years and eight months in Pasadena are the most memorable times in my life. I appreciate the scientific training that I received here, and also the many individuals that I met, who have encouraged and supported me along the way towards the completion of my PhD. Here I would like to take time to express my gratitude towards these people.

First of all, I would like to thank my advisor Prof. Christian Frankenberg for his endless support and input into every piece of my progress during my delving into science. You impressed me with a wide range of knowledge, sharp scientific insight, and positive attitude toward life. This thesis would never have been possible without your unconditional support. You spent a lot of time discussing with me every aspect of research, ranging from background knowledge to data processing, as well as scientific writing and communication. You also encouraged me to explore whatever scientific questions I was interested in to push the boundaries of knowledge. Christian, you are not only my mentor, but also my role model in life. I am determined to keep growing and wish that I can be like you one day.

I would like to express my sincere appreciation to the thesis committee: Prof. Paul Wennberg, Prof. Yuk Yung and Dr. David Schimel. Paul provided a lot of scientific guidance and support for my thesis. The opportunity to discuss atmospheric chemistry with you was very rewarding. You also gave me useful suggestions and encouragement that helped me as an international graduate student. Yuk, I appreciate the opportunity to work with you on one of my first-year projects. You taught me about how to think about and discover novel scientific questions. I am also grateful for your generosity for inviting me to the New Year group dinner in 2017, which made me feel at home. David, I am thankful that you joined my thesis committee. My research has benefited a lot from your feedback and advice. Your enthusiasm and optimism regarding my research have meant so much to me.

I have received a great amount of support from fellow members in Frankenberg's lab. I would like to thank Dr. Yi Yin, Dr. Troy Magney, Dr. Philipp Köhler, Dr. Ying Sun, Dr.

Yujie Wang, Dr. Debsunder Dutta, Dr. Russell Doughty, Dr. Yitong Yao and Dr. Vincent Humphrey for joyful discussions and collaborations. I also would like to thank Siraput Jongaramrungruang, Rui Cheng, Newton Nguyen, Ke Liu, Rupesh Jeyaram, Polina Khapikova and Costa Christopoulos for the friendship and good moments we shared. It was my pleasure to work with all of you.

Many colleagues from Caltech, JPL and UIUC also contributed significantly to my research. I especially thank Dr. Junjie Liu, Dr. Yuan Wang, Dr. Brendan Bryne, Dr. Stan Sander, Dr. Zhao-cheng Zeng, and Prof. Kaiyu Guan for all the help you have given me. Thanks to Junjie for helping me expand my knowledge in atmospheric CO_2 inversion systems. Yuan motivated me to conduct interdisciplinary research on air pollution and ecology. Brendan helped to understand atmospheric chemical transport modeling. I learned from Stan on measuring atmospheric composition by spectroscopy. Zhao taught me about the CLARS instrument and methane retrieval. I also benefited a lot from Kaiyu's expertise on the applications of remote sensing in precision agriculture.

My thanks also go to our staff in GPS, especially Nora Oshima, Julie Lee and Leilani Rivera-Dotson for their behind-the-scenes support on administration issues. Chinese friends at Caltech also supported me in adjusting to living here, with an incomplete list of Jiani Yang, Dien Wu, Yacong Zhou, Kangchen Bai, Xiaolin Mao, Junlong Kou, Haoyu Li, Hao Liu, Linghui Wang, Yue Lu, Weiyi Tang, Yalu Chen, Jin Sima, Hao Zhou, Zhe Jia and many others. Without you, my life in Pasadena would have been much less colorful.

My appreciation extends beyond the Caltech community. I would like to thank my undergraduate advisor Prof. Changqing Ke and Prof. Wenfeng Zhan in Nanjing University, who led me to the door of satellite remote sensing and helped me to find my passion to study global climate change using this novel technique. I would like to thank Zhuying (Zoey) Xu and Chunxiu Yan for encouraging me to apply to a PhD program abroad. I will never forget the glorious time that we prepared for the TOEFL and GRE tests together. Thank you, Jue Wang and Pingjie Zhu for chatting with me on a daily basis and for being the best listeners for decades to share my ups and downs. I would also like to thank Lin Meng, Zhaoxin Ban, Shuli Chen, Shuyue Li, Genghong Wu, Xinchen Lu, Siyu Wang and Xian Wang for weekly catch-ups on research and life discussions.

Last, but most importantly, I would like to express my deep gratitude to my parents, Juhua Peng and Zhigen He, who have been supportive towards all of the choices I made. I appreciate your effort and love in bringing me up to be a better individual. Mom, I am indebted to the sacrifices you made to give me better education resources since my childhood. Dad, thank you for working so hard all these years to support our family. You both brought me into the world and showed me the world. I would never have come this far with your love, trust, and support, and look forward to many tomorrows.

ABSTRACT

Crops not only feed the world's human population and livestock but also impact the global carbon cycle. The intensification of agriculture has allowed much greater crop yields by hybridization, irrigation, and fertilization in the five most recent decades. However, the increased frequency and severity of extreme weathers (e.g., heat wave, drought, flood) caused by global warming have led to large yield and economic losses. Thus, the monitoring of crop growth in a changing climate is of paramount importance to improve food security and alleviate poverty. It is via photosynthesis that crops use the energy of sunlight to reduce carbon dioxide (CO_2) into carbohydrates. An accurate quantification of plant photosynthesis is a key step towards estimating crop yield and understanding the carbon exchange between the biosphere and atmosphere. Satellite remote sensing has emerged as one promising solution for measuring photosynthesis from regional to global scales. In the thesis, first, we show the potential of solar-induced chlorophyll (SIF) signals emitted by the chlorophyll a of plants to track photosynthesis. Compared to traditional reflectance-based vegetation indices (VIs), SIF can better capture photosynthetic down-regulation under drought and heat stresses due to its physiological linkages with photosynthetic processes. Second, we demonstrate that SIF can be used to estimate crop yield. At field sites, we find a high correlation between SIF and crop photosynthesis measurements. Scaling up this relationship to the large scale, we show that crop yield estimates using satellite-derived SIF agree well with the United States Department of Agriculture (USDA) reported annual crop yield. Third, we examine how crops respond to climate change and air quality in China. We develop a crop yield prediction model, based on a large volume of historical crop data, as well as climate and pollution records. Our finding demonstrates the co-benefit of the recent air pollution control policy from an agriculture and food perspective. However, such a benefit will be significantly offset or even outweighed by continuing global warming. Fourth, we focus on how different ecosystems, especially intensified agriculture, has reshaped the seasonality of atmospheric CO_2.

Our satellite-derived global terrestrial carbon fluxes capture the observed CO_2 seasonal cycle amplitude (SCA) trends at surface sites very well. We further find that CO_2 SCA trends at mid latitude sites around the Midwest United States are mainly impacted by intensified agriculture, whereas high latitude sites are mainly driven by increasingly productive natural ecosystems. The approaches, findings and datasets developed through the thesis will contribute to agro-ecosystems management in the face of climate change and contribute to equitable solutions to climate challenges.

PUBLISHED CONTENT AND CONTRIBUTIONS

He, L., Byrne, B., Yin, Y., Liu, J. and Frankenberg, C., 2022. Remote-Sensing Derived Trends in Gross Primary Production Explain Increases in the CO2 Seasonal Cycle Amplitude. *Global Biogeochemical Cycles*, *36*(9), p.e2021GB007220. DOI: https://doi.org/10.1029/2021GB007220

H.L. participated in project conceptualization, literature collection, data analysis, and manuscript writing. All co-authors contributed to the writing of the paper.

He, L., Wei, J., Wang, Y., Shang, Q., Liu, J., Yin, Y., Frankenberg, C., Jiang, J.H., Li, Z. and Yung, Y.L., 2022. Marked impacts of pollution mitigation on crop yields in China. *Earth's Future*, *10*(11), p.e2022EF002936. DOI: https://doi.org/10.1029/2022EF002936

H.L. participated in project conceptualization, literature collection, experimental setups, data analysis, and manuscript writing. All co-authors contributed to the writing of the paper.

He, L., Magney, T., Dutta, D., Yin, Y., Köhler, P., Grossmann, K., Stutz, J., Dold, C., Hatfield, J., Guan, K. and Peng, B., 2020. From the ground to space: Using solar-induced chlorophyll fluorescence to estimate crop productivity. *Geophysical Research Letters*, *47*(7), p.e2020GL087474. DOI: https://doi.org/10.1029/2020GL087474

H.L. participated in project conceptualization, literature collection, data analysis, and manuscript writing. All co-authors contributed to the writing of the paper.

He, L., Wood, J.D., Sun, Y., Magney, T., Dutta, D., Köhler, P., Zhang, Y., Yin, Y. and Frankenberg, C., 2020. Tracking seasonal and interannual variability in photosynthetic downregulation in response to water stress at a temperate deciduous forest. *Journal of Geophysical Research: Biogeosciences*, *125*(8), p.e2018JG005002. DOI: https://doi.org/10.1029/2018JG005002

H.L. participated in project conceptualization, literature collection, data analysis, and manuscript writing. All co-authors contributed to the writing of the paper.

TABLE OF CONTENTS

LIST OF ILLUSTRATIONS AND/OR TABLES

Chapter 1

INTRODUCTION

1.1 Background

Nearly 24% of the Earth's land surface is covered by croplands (Cassman et al., 2005). Croplands not only provide sustenance for the world's human population and livestock, but also have a major impact on local climate and the global carbon cycle. The green revolution, which is associated with agricultural intensification, has greatly increased food grains per planted area by hybridization, irrigation, and fertilization beginning in the mid-20th century. However, the increased frequency and severity of extreme weathers (e.g., heat wave, drought, flood) caused by global warming have led to large yield and economic losses. With climate change, agricultural regions will likely experience more heat and water stresses, which leads to great threats to future global food security. Therefore, timely and accurate monitoring of crops and understanding crop yield responses to the changing climate is of paramount importance to meet the burgeoning food demand and achieve "zero hunger", one on the top 17 Sustainable Development Goals (SDGs) of the 2030 Agenda for Sustainable Development.

Crop productivity is reliant upon its ability to convert light energy into sugar via photosynthesis. Therefore, a reliable measure of gross primary production (GPP) is a key step toward crop monitoring. Previous studies relied on field experiment to study crop yield responses to surrounding environmental factors, which mainly focus on four main crops grown in developed countries, including maize, rice, wheat, and soybeans, which cover almost 50% of global farmland. However, crops grown in developing countries are significantly overlooked, e.g., sorghum and millets, and are major contributors to nutrient intake in the global south such as in African countries. A similar issue exists for using crop models to estimate crop yield. The model performance largely depends on parameterization of soil types

and biochemical parameters, which leads to large uncertainties in upscaling these conditions from local to regional and global scales.

Earth-observing satellites have provided an unprecedented view of the land surface. With recent advances in satellite sensors, spatially and temporally continuous surface features can be derived from remotely sensed observations, which can be used to quantify crop photosynthesis and estimate crop yield. Traditionally, vegetation indices (VIs) have been designed to assess whether the target being observed contains live green vegetation. One commonly used vegetation index, the normalized difference vegetation index (NDVI), quantifies vegetation by measuring the surface spectral reflectance differences between near-infrared (NIR) and red light. Live vegetation usually reflects strongly at NIR and absorbs at red bands, resulting in a high NDVI value. NDVI can thus be used to differentiate vegetated from non-vegetated areas, as well as monitor vegetation growth. To reduce atmospheric and soil background impacts, the Enhanced Vegetation Index (EVI) was later proposed with the additional information of spectral reflectance at green and blue bands. In agriculture, NDVI and EVI has been an indispensable part of precision farming that inform farmers of crop health and yield.

Previous studies have found that these spectral reflectance-based VIs usually capture changes in canopy structures but are usually insensitive to heat and water stresses, which hinders accurate tracking of vegetation health and growth. Solar-induced chlorophyll fluorescence (SIF), a by-product of photosynthesis, is a reemitted near-infrared light within the range of 650 to 850nm from chlorophyll-a molecules. Since it emanates during the light-reactions, i.e. the initial steps in photosynthesis, it has the potential to offer physiologically based photosynthesis estimates. Recent global satellite products of SIF from the Greenhouse Gases Observing Satellite (GOSAT) (Frankenberg et al., 2011; Guanter et al., 2012; Joiner et al., 2011), Global Ozone Monitoring Experiment-2 (GOME-2) (Joiner et al., 2013; Köhler et al., 2015), SCanning Imaging Absorption spectroMeter for

Atmospheric CHartographY (SCIAMACHY) (Köhler et al., 2015), Orbiting Carbon Observatory-2 (OCO-2) (Frankenberg et al., 2014; Sun et al., 2017, 2018), Chinese global carbon dioxide monitoring satellite (TanSat) (Liu et al., 2018), and TROPOspheric Monitoring Instrument (TROPOMI) (Guanter et al., 2015; Köhler et al., 2018) have shown promise to estimate regional to global scale photosynthesis from space (Li, Xiao & He, 2018; MacBean et al., 2018; Song et al., 2018; Sun et al., 2015, 2017; Zhang et al., 2016). However, it is still less well known to what extent SIF can track GPP changes under varying water and heat stresses. A holistic analysis with the combination of field measurements, satellite observations and photosynthesis models would serve as an important step to answer this question.

Some efforts have been made to explore the potential of satellite SIF in estimating crop yields. Guanter et al. (2014) find that the highest SIF values observed by the Global Ozone Monitoring Experiment-2 (GOME-2) satellite are located in the Corn Belt in the United States (US) Midwest. Furthermore, it was shown that SIF captures the photosynthetic activity over highly productive croplands, while VIs, such as NDVI and EVI, show saturation effects over these dense canopies. Thus, SIF has its own unique advantage to track crop photosynthesis over VIs. Guan et al. (2016) used GOME-2 SIF to constrain photosynthetic electron transport rate (ETR) to derive crop yield, which has shown a significant improvement in county-level crop yield estimates in the US. However, a single GOME-2 footprint (80 km × 40 km) thus covers several counties, making it challenging to compare SIF with the benchmark of USDA county-level annual crop statistics. Therefore, high spatially and temporally resolved remote sensing SIF datasets are encouraged to achieve robust SIF measurements to improve the estimate and understanding of crop yields at every piece of farmland on Earth.

More frequent extreme weather events influenced by climate change has led to larger interannual variations of crop yield. Globally, climate variability accounts for roughly a third (~32–39%) of the observed yield variability (Ray et al., 2015),

which is the primary driver of food system instability (IPCC, 2019). Assessing the effects of climate change on yield variability is critical to understanding the impact of climate change on food security (FAO, 2019). Crop yields are strongly influenced by both regional climate and air quality (Wang et al., 2020). Many previous studies have focused on climate factors, such as temperature and precipitation, on crop yield. For example, temperature increase usually leads to crop respiration enhancement, which leads to a global yield loss in recent decades (Lobell et al., 2011; Zhao et al., 2017). Precipitation exerts impacts on crop yield by altering soil and air moisture (Kimm et al., 2020) but in a non-monotonic manner (Li et al., 2019; Rosenzweig et al., 2002). Meanwhile, atmospheric pollutants such as anthropogenic aerosols and near-surface ozone exert detectable impacts on regional crop yields by changing physical, biochemical, and physiological processes during plant growth (Ainsworth, 2017; Chameides et al., 1999). However, limited understanding has been established on how crop yields respond to air quality, particularly in rapidly developing countries, where high levels of aerosol and ozone pollution are always collocated with croplands. A better understanding of how air pollution and climate change compete or work together on crop yield can then help to assess future crop yield and develop adaptation strategies.

The intensified agriculture may also contribute to reshape the seasonality of atmospheric CO_2. An increase in the seasonal cycle amplitude (SCA) of atmospheric CO_2 since the 1960s has been observed in the Northern Hemisphere (NH). However, dominant drivers of the amplified CO_2 seasonality are still debated. Current earth system models generally underestimate the CO_2 SCA increase and disagree on the underlying mechanisms of such an increase (Bastos et al., 2019; Graven et al., 2013; Piao et al., 2018; Thomas et al., 2016; Zhao et al., 2016). This suggests that some key biophysical or biochemical processes are missing or underrepresented in these models. Satellite remote sensing has the potential to track spatial and temporal changes in global ecosystem carbon fluxes. These flux estimates can then be coupled with an atmospheric transport model to explain

relative contributions from different ecosystems to explain the observed CO_2 SCA trends.

1.2 Scientific questions

In this thesis, we aim to answer the following scientific questions with the integration of in-situ measurements, satellite remote sensing, machine learning and earth system models:

(i) How well can SIF track GPP changes especially under different environmental conditions? Does SIF have better performance than traditional VIs to track seasonal and interannual variations of GPP?

(ii) How well can SIF be used to estimate crop yield? What are relationships between SIF and GPP (or crop yield) for different crop species?

(iii) How does crop yield respond to climate and air quality? How will crop yield change under future climate and pollution scenarios?

1.3 Thesis outline

The thesis is composed of four chapters. The first chapter demonstrates the potential of solar-induced chlorophyll (SIF) signals emitted by chlorophyll-a of green plants to track photosynthesis. I compared satellite-derived SIF with traditional reflectance-based vegetation indices and show that SIF can better capture photosynthetic down-regulation under drought and heat stresses due to its physiological linkages with plant photosynthetic processes. My second chapter assesses the relationship between SIF and crop yields. I developed a mechanism understanding between SIF and crop photosynthesis using ground measurements at corn and soybean experimental sites. Then I applied the mechanism into county-level crop yield estimates with satellite-derived SIF in the United States. I showed that these estimates agree well with the United States Department of Agriculture (USDA) reported annual crop statistics. The third chapter examines how three

dominant crops in China, including rice, corn, and wheat, respond to climate change and air quality. I developed a crop yield prediction model, based on a large volume of historical crop yield datasets in China since 1980. Using the developed crop model, I quantified the sensitivity of crop yields to four climate and air pollution factors. Using global climate models, I further predicted the crop yield variations under future warming scenarios by 2050. My fourth chapter disentangles the drivers of different ecosystems in contributing to the enhanced atmospheric CO_2 seasonal amplitude. I developed a 20-year global photosynthesis dataset based on satellite observations. Then I used an atmospheric transport model to examine the contribution of the individual ecosystem (e.g., forest, cropland, grassland) to reshape the atmospheric CO_2 seasonality at NOAA surface CO_2 sites.

Chapter 2

TRACKING SEASONAL AND INTERANNUAL VARIABILITY IN PHOTOSYNTHETIC DOWNREGULATION IN RESPONSE TO WATER STRESS AT A TEMPERATE DECIDUOUS FOREST

He, L., Wood, J.D., Sun, Y., Magney, T., Dutta, D., Köhler, P., Zhang, Y., Yin, Y. and Frankenberg, C., 2020. Tracking seasonal and interannual variability in photosynthetic downregulation in response to water stress at a temperate deciduous forest. *Journal of Geophysical Research: Biogeosciences*, *125*(8), p.e2018JG005002. DOI: https://doi.org/10.1029/2018JG005002

2.1 Abstract

The understanding and modeling of photosynthetic dynamics affected by climate variability can be highly uncertain. In this paper, we examined a well-characterized eddy covariance site in a drought-prone temperate deciduous broadleaf forest combining tower measurements and satellite observations. We find that an increase in spring temperature usually leads to enhanced spring gross primary production (GPP), but a GPP reduction in late growing season due to water limitation. We evaluated how well a coupled fluorescence-photosynthesis model (SCOPE) and satellite datasets track the interannual and seasonal variations of tower GPP from 2007 to 2016. In SCOPE, a simple stress factor scaling of Vcmax as a linear function of observed predawn leaf water potential (ψ_{pd}) shows a good agreement between modeled and measured interannual variations in both GPP and solar-induced chlorophyll fluorescence (SIF) from the Global Ozone Monitoring Experiment-2 (GOME-2). The modeled and satellite-observed changes in SIF_{yield} are ~30% smaller than corresponding changes in light use efficiency (LUE) under

severe stress, for which a common linear SIF to GPP scaling would underestimate the stress reduction in GPP. Overall, GOME-2 SIF tracks interannual tower GPP variations better than satellite vegetations indices (VIs) representing canopy "greenness". However, it is still challenging to attribute observed SIF variations unequivocally to greenness or physiological changes due to large GOME-2 footprint. Higher resolution SIF datasets (e.g., TROPOMI) already shows the potential to well capture the downregulation of late-season GPP and could pave the way to better disentangle canopy structural and physiological changes in the future.

2.2 Introduction

Accurate estimates of gross primary production (GPP) are important for tracking the response of plants to environmental stress and have important applications for crop and forest management (Beer et al., 2010). In recent decades, growing-season length and peak vegetation growth have increased due to the global climate change and human activities, which have a potential positive impact on terrestrial carbon uptake (Chen et al., 2019; Park et al., 2019; Huang et al., 2018; Zhu et al., 2016; Buitenwerf et al., 2015). However, late growing-season photosynthesis is highly uncertain and sensitive to climate (Zhang et al., 2020; Buermann et al., 2018; Wolf et al., 2016). In a warming climate, water availability plays an increasingly important role as a limiting factor for late growing-season terrestrial photosynthesis (Lian et al., 2020; Zhang et al., 2020). Therefore, it is crucial to evaluate the impact of water availability on photosynthesis, and how well observations and photosynthesis models can track late growing-season photosynthesis, with a particular focus on responses to water stress.

Satellite observations have been widely used to monitor vegetation growth status and estimate GPP at global scales (Schimel et al., 2015). Traditional reflectance-based vegetation indices (VIs) such as the Normalized Difference Vegetation Index (NDVI) (Tucker, 1979) and Enhanced Vegetation Index (EVI) (Huete et al., 2002) are appropriate for tracking canopy "greenness", but are sometimes insensitive to

environmental stress on diurnal and/or short time scales (e.g. heat waves and water stress) (Rossini et al., 2015; Dobrowski et al., 2005). At longer time-scales, changes in pigment composition associated with environmental stress can be detected from space, such as the carotenoid:chlorophyll index (CCI, Gamon et al., 2016), but it is unclear how responsive this signal is to rapid changes in photosynthesis. A potential solution to track dynamic and reversible adaptation of plants to stress is to monitor changes in the chlorophyll *a* fluorescence yield, which typically decreases following a rapid increase in non-photochemical quenching (NPQ) and reduction in photosynthetic efficiency.

To model GPP from greenness indices, the light use efficiency (LUE) based model (Monteith, 1972) with remote sensing observations of absorbed light has been developed to derive GPP (Running et al., 2004):

$$GPP = PAR \times fPAR \times LUE = APAR \times LUE \quad (1)$$

where PAR is incident photosynthetically active radiation, fPAR is the fraction of photosynthetically active radiation absorbed by plants (usually inferred by VIs) and LUE is the efficiency of the plant's conversion of absorbed radiation to CO_2 uptake, which responds dynamically to changes in temperature, water stress and/or the light environment. Calculating LUE mostly relies on simple scaling functions based on air temperature and vapor pressure deficit (VPD) (Myneni et al., 2015; Yuan et al., 2007; Turner et al., 2006; Running et al., 2004), which is associated with large uncertainties.

Another strategy to relate remote sensing measurements to photosynthetic efficiencies arises from the light reactions of photosynthesis. There are three primary dissipation pathways for the energy absorbed by chlorophyll molecules in the antenna system (Porcar-Castell et al. 2014): photochemical quenching (PQ), fluorescence and heat dissipation.

At scales relevant to satellite remote sensing, the emission of steady-state fluorescence illumination is referred to as solar-induced chlorophyll fluorescence (SIF), the emission of red and near-infrared light in the 650 to 850 nm spectral range. Recent global satellite products of SIF from the Greenhouse Gases Observing Satellite (GOSAT) (Guanter et al., 2012; Frankenberg et al., 2011; Joiner et al., 2011), Global Ozone Monitoring Experiment-2 (GOME-2) (Joiner et al., 2013; Köhler et al., 2015), SCanning Imaging Absorption spectroMeter for Atmospheric CHartographY (SCIAMACHY) (Köhler et al., 2015), Orbiting Carbon Observatory-2 (OCO-2) (Sun et al., 2018; Sun et al., 2017; Frankenberg et al., 2014), Chinese global carbon dioxide monitoring satellite (TanSat) (Liu et al., 2018) and TROPOspheric Monitoring Instrument (TROPOMI) (Köhler et al., 2018; Guanter et al., 2015) have shown promise to constrain large-scale carbon fluxes from space (Li et al., 2018; MacBean et al., 2018; Song et al., 2018; Sun et al., 2017; Zhang et al., 2016; Sun et al., 2015).

Analogous to the LUE model for GPP, SIF emission from the canopy can be described according to:

$$SIF = PAR \times fPAR \times \Phi_F \times \Omega = APAR \times SIF_{yield} \quad (2)$$

where Φ_F is the actual fluorescence yield, defined as the emitted fluorescence per unit of radiation absorbed, neglecting potential re-absorption of far-red light within the canopy; Ω is the probability of fluorescence photons escaping the canopy; and SIF_{yield} is the effective fluorescence yield (Guanter et al., 2014) and is computed as the product of actual fluorescence yield and escape probability.

Since SIF is emanating from the light reaction centers during photosynthesis, it is expected to be related to the electron transport rate, and thus a proxy of photosynthesis (Gu et al., 2019; Perez-Priego et al., 2015). Recent studies show robust empirical linear scaling between GPP and SIF for different vegetation types at the canopy scale (He et al., 2020; Magney et al., 2019; Li et al., 2018; Sun et al.,

2018; Smith et al., 2018; Song et al., 2018; Verma et al., 2017; Wood et al., 2017; Guan et al., 2016; Zhang et al., 2016; Guanter et al., 2014; Frankenberg et al., 2011). The primary reason for such strong relationships is that APAR acts as a common variable in both equations, driving GPP and SIF. The 2nd order effect is that the SIF_{yield} correlates with LUE at the canopy scale in most cases (Magney et al., 2019; Yang et al. 2015). This indicates that SIF not only contains information on light interception, but also physiological responses to environmental stress, which are reflected in changes in photosynthetic yields. Therefore, SIF is expected to correlate better with GPP than VIs. However, the SIF_{yield}–LUE relationship is complex, causing deviations from a simple linear scaling and is only empirically represented in models (van der Tol et al., 2014). Positive relationships between SIF_{yield} and LUE have been reported at the canopy scale across different ecosystems (Song et al., 2018; Zhang et al., 2016; Yang et al., 2015; Porcar-Castell et al., 2014; van der Tol et al., 2014), but there is limited understanding of the covariation of the SIF_{yield} and LUE under different environmental conditions.

The potential of satellite SIF to track drought has been reported in some recent papers. For example, *Sun et al.* (2015) explored the potential of GOME-2 SIF to monitor the drought spatial and temporal dynamics; *Verma et al.* (2016) showed that the relationship between OCO-2 SIF and GPP is robust at canopy scale under different environmental conditions in grasslands; *Yoshida et al.* (2015) found that SIF_{yield} and fPAR both decline during the drought, and GPP losses in mixed forest is mainly due to LUE reduction, while GPP losses in croplands and grasslands are mostly driven by changes in fPAR. However, few studies have focused on evaluating the performance of photosynthesis models and long-term satellite SIF and VI observations to track flux tower GPP during the late growing-season, when vegetation is exposed to varying stress intensities. Also, it remains unclear how the SIF_{yield}–LUE relationship responds to different levels of water stress in forest ecosystem.

Here, we address this knowledge gap by using long-term observations at the Missouri Ozark AmeriFlux site (US-MOz), a drought-prone, temperate deciduous forest site located in central Missouri, to examine the relationships among eddy covariance GPP, satellite SIF and VIs, as well as LUE based satellite GPP products and a detailed coupled photosynthesis and SIF modeling exercise. The study site regularly experiences seasonal drought in later summer, allowing us to investigate the complex relationship between SIF_{yield} and GPP under varying degrees of stress. The US-MOz site also provides a unique set of predawn leaf water potential (ψ_{pd}) measurements, which enable us to link efficiency changes directly to plant water status. Our main questions are: 1) What are the drivers of interannual variations in late growing-season GPP and are these related to systematic changes in the seasonal cycle? 2) How well does a biophysical process-based model track the interannual variations in both flux tower GPP and measured SIF? 3) How well can SIF track the seasonal and interannual variation of GPP compared with MODIS VIs and the MODIS GPP product?

2.3 Materials and methods

2.3.1 Field Site and Measurements

The AmeriFlux site US-MOz (38.744 N, 92.200 W) is a second growth upland oak-hickory forest, located in the transitional zone between the central hardwood and central grassland regions in the United States (Wood et al., 2018; Gu et al., 2016a; Gu et al., 2015). The dominant tree species at the site are white oak (*Quercus alba* L.), black oak (*Q. velutina* Lam.), shagbark hickory (*Carya ovata* (Mill.) K. Koch), sugar maple (*Acer saccharum* Marsh.) and eastern redcedar (*Juniperus virginiana* L.). The site lies in a warm, humid and continental climate zone, with an average annual temperature of about 13 °C, and average annual precipitation around 1140 mm. Physiological water stress is common during the growing season (Gu et al., 2015) and is tightly controlled by within-season precipitation variability (Gu et al., 2016b), because plant available water in the comparatively shallow soils can be

quickly depleted. Water stress is therefore a strong regulator of ecosystem carbon and water fluxes (Wood et al., 2018; Gu et al., 2016a; Yang et al., 2010), the partitioning of available energy into sensible and latent heat (Gu et al., 2006), and is related to tree mortality (Wood et al., 2018; Gu et al., 2015).

In this study, we used half-hourly net ecosystem exchange (NEE), GPP and evapotranspiration (ET) derived from continuous eddy covariance measurements from 2007 to 2016. The reader is referred to Gu et al. (2012, 2016a) for a more complete description of the instrumentation on the 32 m walk-up tower used to observe ecosystem fluxes and the eddy covariance flux calculations. Briefly, the moving point threshold test developed by *Gu et al.* (2005), was used to objectively estimate friction velocity thresholds for screening nighttime NEE data for periods of low turbulence. Data gaps were filled using the mean diurnal variation approach (Gu et al., 2016a). GPP was estimated by subtracting daytime observations of NEE from soil respiration measured using flow through non-steady state chambers (Yang et al. 2010), noting that soil respiration is often the largest component of ecosystem respiration (Li et al., 2012; Hermle et al., 2010; Tang et al., 2008). We also point out that there are uncertainties and potential biases with any partitioning method (Wohlfahrt and Gu, 2015), and indeed, recent evidence points to potentially large biases in the common NEE partitioning methods (Keenan et al., 2019; Wehr et al., 2016).

We also used records of incident photosynthetically active radiation (PAR), air temperature (Ta), vapor pressure deficit (VPD), precipitation, volumetric soil water content (SWC) at 10 cm depth, and ψ_{pd}. Predawn leaf water potential is measured before sunrise and is a useful indicator of plant and ecosystem physiological water stress, as it reflects the root zone soil water potential and the degree to which leaves are able to rehydrate overnight (Wood et al., 2018; Gu et al., 2016b; Gu et al., 2015). At weekly to stem abundance before dawn and ψ_{pd} was determined using the

pressure chamber technique (Pallardy et al., 2008, 1991). An overview of the long-term GPP, Ta and precipitation can be found in **Supplementary Figure S1**.

2.3.2 Satellite datasets

2.3.2.1 GOME-2 SIF

We used GOME-2 SIF (~ 80 km × 40 km footprint before July 2013, ~ 40 km x 40 km after) at 740 nm retrieved using a statistical approach (Köhler, Guanter, and Joiner, 2015), and applied a daily correction factor to convert the instantaneous SIF signal to a daily average SIF. GOME-2 SIF soundings with center longitudes/latitudes within 0.75° from the US-MOz were extracted from 2007 to 2016. Figure 2.1(a) shows an example of extracted footprint on 16 June, 2013 in the direct vicinity of the tower. SIF observations were filtered by removing soundings with cloud fractions larger than 20%, and then aggregated to monthly averages.

2.3.2.2 MODIS NDVI, EVI, NIRv, fPAR and GPP

We derived commonly used VIs (including NDVI, EVI and near infrared reflectance of terrestrial vegetation (NIRv)) from the MODIS MCD43A4 v006 using the following formulas (Badgley et al., 2017; Didan et al., 2015; Huete et al., 1997; Liu & Huete, 1995):

$$NDVI = \frac{NIR-R}{NIR+R} \quad (3)$$

$$EVI = G \times \frac{NIR-R}{NIR+C_1 \times R-C_2 \times B+L} \quad (4)$$

$$NIRv = NIR \times NDVI \quad (5)$$

where NIR, R and B stand for the spectral reflectance acquired in the near-infrared, red and blue bands, respectively; G is a scaling factor; C_1 and C_2 are constants to

account for atmospheric scattering; L is the coefficient of canopy background adjustment. For MODIS EVI derivation, G, C_1, C_2 and L are set to 2.5, 6, 7.5 and 1. MCD43A4 provides daily "nadir" 500 m pixel size reflectance data corrected by using a bidirectional reflectance distribution function model, which minimizes the bias in reflectance measurements introduced by different illumination and observation geometries. The MODIS MCD15A3H fPAR product, a 4-day composite dataset with 500 m spatial resolution, was also used in this study to estimate the relative contribution of fPAR to the GPP–SIF relationship. We also included the MODIS MYD17A2H V006 8-day GPP product with 500 m spatial resolution in the analysis to evaluate its performance compared to flux tower GPP and SIF. MODIS products were aggregated at 0.02° within the flux tower in the study, which contain a large proportion of homogeneous forests (Figure 2.1(b)).

2.3.2.3 GOSIF dataset

To reconcile the large footprint of GOME-2 SIF, we also used the machine-learning generated GOSIF dataset at 0.05° spatial resolution, aggregated at monthly averages from 2007 to 2016. GOSIF is trained using OCO-2 SIF and co-located MODIS MCD43C4 (Collection 6, 0.05°) BRDF-corrected EVI, and meteorology variables (including PAR, VPD and Ta) obtained from the NASA reanalysis MERRA-2 dataset (Li et al., 2019).

2.3.2.4 TROPOMI SIF

To explore the potential of new satellite SIF at higher spatiotemporal resolution in the drought monitoring, we also evaluated the performance of TROPOMI SIF, with ~7 km × 3.5 km spatial resolution and near-global daily coverage (Köhler et al., 2018). The TROPOMI instrument onboard the European Sentinel-5 Precursor satellite was launched on 13 October 2017. As for GOME-2, the daily correction factor was also applied to TROPOMI SIF to convert instantaneous SIF to a daily

average. In this study, we aggregated TROPOMI SIF monthly at 0.05° in 2018 to investigate its seasonal variation at US-MOz.

2.3.2.5 Spatial aggregation of the remote sensing data

In the fine-scale analysis, we tried to make the raw satellite data (at native resolution) comparable to the flux tower GPP. Therefore, we used the GOME-2 SIF footprints with the central longitude/latitude 0.75° nearby the flux tower, as well as MODIS data 0.02° within the flux tower. Note that the footprints of GOME-2 are quite large and composed of different landcovers other than forests, such as croplands and grasslands. This makes it hard to fairly compare the GOME-2 SIF and MODIS products. To deal with this problem, we also conducted an analysis gridding both GOME-2 and MODIS products at 0.25°, and then examined these two at the same spatial aggregation.

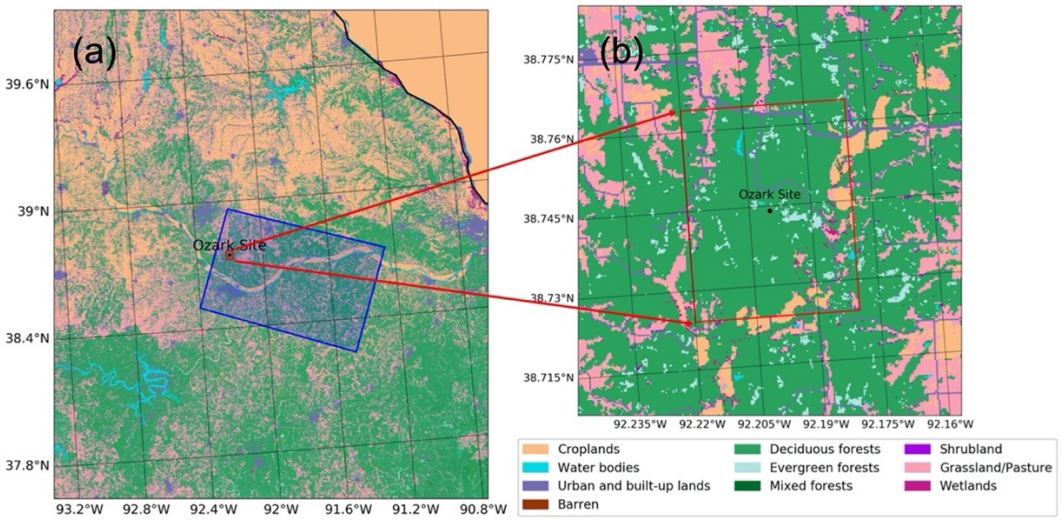

Figure 2.1: An example of a GOME-2 footprint relative to MODIS aggregation used in the analysis: (a) The transparent light blue polygon represents a GOME-2 footprint from an overpass on 16 Jun 2013. All GOME-2 footprints with the distance between central longitude/latitude and US-MOz less than 0.75° are used in the analysis. Red boundaries indicate the 0.02° fine-resolution of MODIS products aggregated in this study. (b) The enlarged map shows the location of the flux tower and surrounding land cover. The 30-m Cropland Data Layer (CDL) by

United States Department of Agriculture (USDA) in 2016 is used for land cover classification.

2.3.3 GPP and SIF simulations

The Soil Canopy Observation, Photochemistry and Energy fluxes (SCOPE) model is a 1D integrated radiative transfer and energy balance model, which simulates photosynthesis, fluorescence, the surface energy balance and reflectance/emission spectra (van der Tol et al., 2009). Within SCOPE, empirical models of the rate coefficients of NPQ and SIF_{yield} are used, which are based on leaf level experiments (van der Tol et al., 2014), and parameterized as a function of the photosynthetic PSII yield (ΦP) computed by the Farquhar, von Caemmerer, Berry (FvCB) model (Farquhar et al., 1980). SCOPE provides two different parameterizations of the leaf-level SIF_{yield} (ΦF)–ΦP relationship. The first (SCOPE 1) is derived from measurements of leaves of various species experiencing progressive drought (Flexas et al. 2002), and the second, (SCOPE 2) is derived from cotton leaves with less exposure to stress (van der Tol et al. 2014). The parameterizations diverge towards lower photosynthetic yields (i.e. at high light and generally more stressed conditions) (Magney et al. 2017; van der Tol et al. 2014). We used half-hourly meteorological variables measured at the US-MOz from 2007 to 2016 for the SCOPE simulations. The important meteorological drivers include incoming shortwave and longwave radiation, air temperature, atmospheric pressure, actual vapor pressure and wind speed. Leaf area index (LAI) measured at the site, as well as typical values of leaf biochemical parameters (e.g. Vcmax25 = 80u mol m^{-2} s^{-1} mol m^{-2} s^{-1} and Chl content =100u mol m^{-2} s^{-1} g/cm^2) are used for the simulations. The key biochemical parameter Vcmax is scaled by a stress factor ([0-1]), which is a common way of implementing soil moisture stress in land surface models (Oleson et al., 2013). Further, the model also incorporates detailed calculation of temperature dependence of the photosynthetic biochemical parameters (Dutta et al., 2019). The rationale for using SCOPE simulations is to 1) model GPP and SIF changes at the canopy level with proper parameterization of Vcmax; 2) compare

the measured SIF_{yield}–LUE at the canopy level with expectations from the SCOPE parameterization ΦF–ΦP at the leaf level, with an emphasis on the fractional change of each term under stress (LUE, SIF_{yield}, ΦF, ΦP).

2.3.4 Singular value decomposition (SVD) analysis

To extract the coherent patterns contributing to the seasonal and interannual variations of GPP, we perform an SVD analysis to obtain the principal components (PCs) that explain the time series of eddy covariance GPP. We assemble monthly flux tower GPP from 2007 through 2016 into matrix A with m rows and n columns, where m=10 is the number of years and n=12 is the number of months. Using SVD, we factorize A into three matrices $A = USV^T$, where the columns of U (m by m) and V (n by n) are left and right singular vectors, and S (m by n) is a diagonal matrix with non-negative real numbers in descending order. The matrix A with both seasonal and interannual information can then be reconstructed by

$$A = \sum_{i=1}^{m} u_i \times s_i \times v_i^T \quad (3)$$

where u_i is the i^{th} singular vector with length m, containing temporal loadings for individual year; v_i is the i^{th} singular vector with length n, containing the i^{th} principal component (PCi, equivalent to seasonal dynamics of GPP); and s_i is the singular value of i^{th} component. In other words, monthly GPP of each year can be reconstructed as the linear combination of PCs weighted by the corresponding temporal loadings. In our study, we found that the first three PCs are sufficient to explain most of the variance (around 90%).

2.4 Results

2.4.1 Long-term analysis of flux tower observations and satellite remote sensing

2.4.1.1 Interannual variations of GPP, NDVI, EVI, NIRv, fPAR and SIF

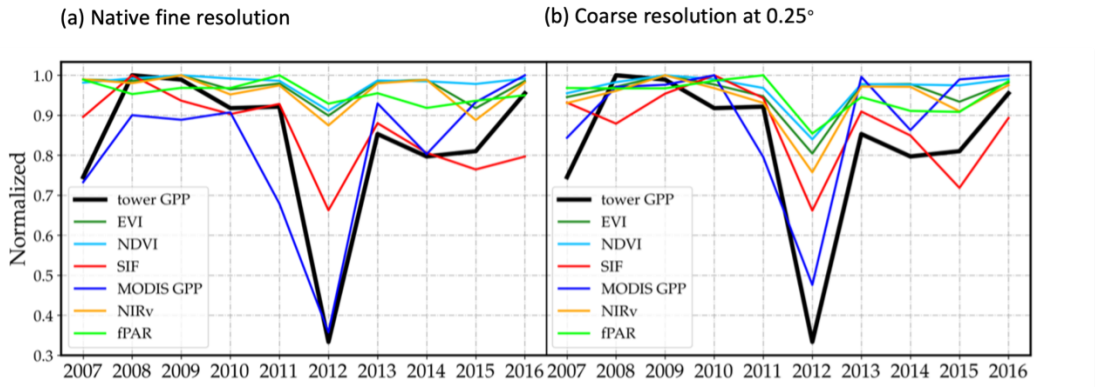

Figure 2.2: Average flux tower GPP, MODIS EVI, NDVI and NIRv, and GOME-2 SIF during JJA from 2007 to 2016. (a) MODIS products are aggregated at 0.02° and native GOME-2 SIF footprints of the central longitude and latitude within 0.75° from the flux tower are used. (b) MODIS products and GOME-2 SIF are aggregated at 0.25°. All variables are scaled by the corresponding maximum value. RMSE and R^2 between flux tower GPP and SIF, NDVI, EVI, NIRv, fPAR, MODIS GPP, NDVI*PAR, EVI*PAR, NIRv*PAR and fPAR *PAR are reported in **Table 2-1**. Raw data of flux tower GPP, SIF, MODIS GPP, NDVI, EVI, NIRv, fPAR are reported in **Table 2-2.**

To evaluate the performance of MODIS VIs, MODIS GPP, and GOME-2 SIF in tracking interannual variation (IAV) of flux tower GPP during JJA, we normalized each variable by its maximum value (Figure 2.2). At both fine and coarse aggregations, MODIS GPP and GOME-2 SIF capture the magnitude of the IAV of flux tower GPP better than NDVI, EVI and NIRv. In 2012 U.S. Drought (Parazoo et al., 2015; Sun et al., 2015; Hoerling et al., 2014; Boyer et al., 2013; Mallya et al., 2013; Karl et al., 2012), flux tower GPP decreased by nearly 70% compared to 2008, the most productive year. Meanwhile, MODIS GPP decreased by around 55% and SIF dropped by around 33%, whereas only a 10% decline of VIs and fPAR were observed at the fine scale 0.02° aggregation (Figure 2.2(a)). Little fluctuation

in VIs and fPAR in JJA from 2007 to 2016 indicates that this ecosystem maintains a relatively stable canopy structure during the peak growing season, which is supported by measurement of LAI in the field (**Supplementary Figure 2.18**). Therefore, a substantial part of the summer interannual GPP variations can be attributed to changes in LUE, which are better reflected in MODIS GPP and GOME-2 SIF observations.

We also recognize a larger decrease of VIs and fPAR found at the coarser aggregation at 0.25° (Figure 2.2(b)) in 2012, implying that the structure of non-forest ecosystems in the vicinity (crops and grasslands) might be influenced more strongly than forest ecosystems during the drought. This confounding factor makes it difficult to evaluate whether the stronger reduction in observed SIF is supporting the claim that SIF reacts more strongly to dynamic environmental stress or whether the large GOME-2 pixels just include more information from crops and grasslands, which reacted more strongly. Therefore, we studied the spatial pattern of the anomalies of GOME-2 SIF, MODIS NDVI and NIRv at 0.25° to in 2012 drought from the normal years. The fractional anomaly at each grid was computed as:

$$X_{anomaly} = \frac{X_{JJA_{2012}}}{X_{JJA_{mean}}}$$

where X represents the variable (such as SIF, NIRv and NDVI). $X_{JJA_{2012}}$ is the average of X during JJA in 2012, while $X_{JJA_{mean}}$ is the multi-year average of X during JJA from 2007 to 2016.

This analysis was necessary to: 1) examine whether the spatial pattern of SIF and NDVI/NIRv anomalies is consistent using the dataset aggregated at the same resolution; and 2) explore SIF–NDVI/NIRv relation across different types of biomes during the drought.

The CDL 30-meter landcover map around Ozark is shown in Figure 2.3(a). Figure 2.3(c) and (e) show the spatial pattern of $NIRv_{anomaly}$ and $NDVI_{anomaly}$ at native fine resolution (500m), whereas Figure 2.3(b), (d) and (f) are based on coarse resolution (0.25°). At the fine resolution, only a few areas actually show enhancements, mostly aligned along rivers. In general, we find a larger reduction of NIRv compared to NDVI in most regions. At the coarse resolution (0.25°), around 30% reduction was observed for SIF and NIRv at the Ozark grid cell, while only a 10% reduction was found for NDVI, which could be due to NDVI saturation effects.

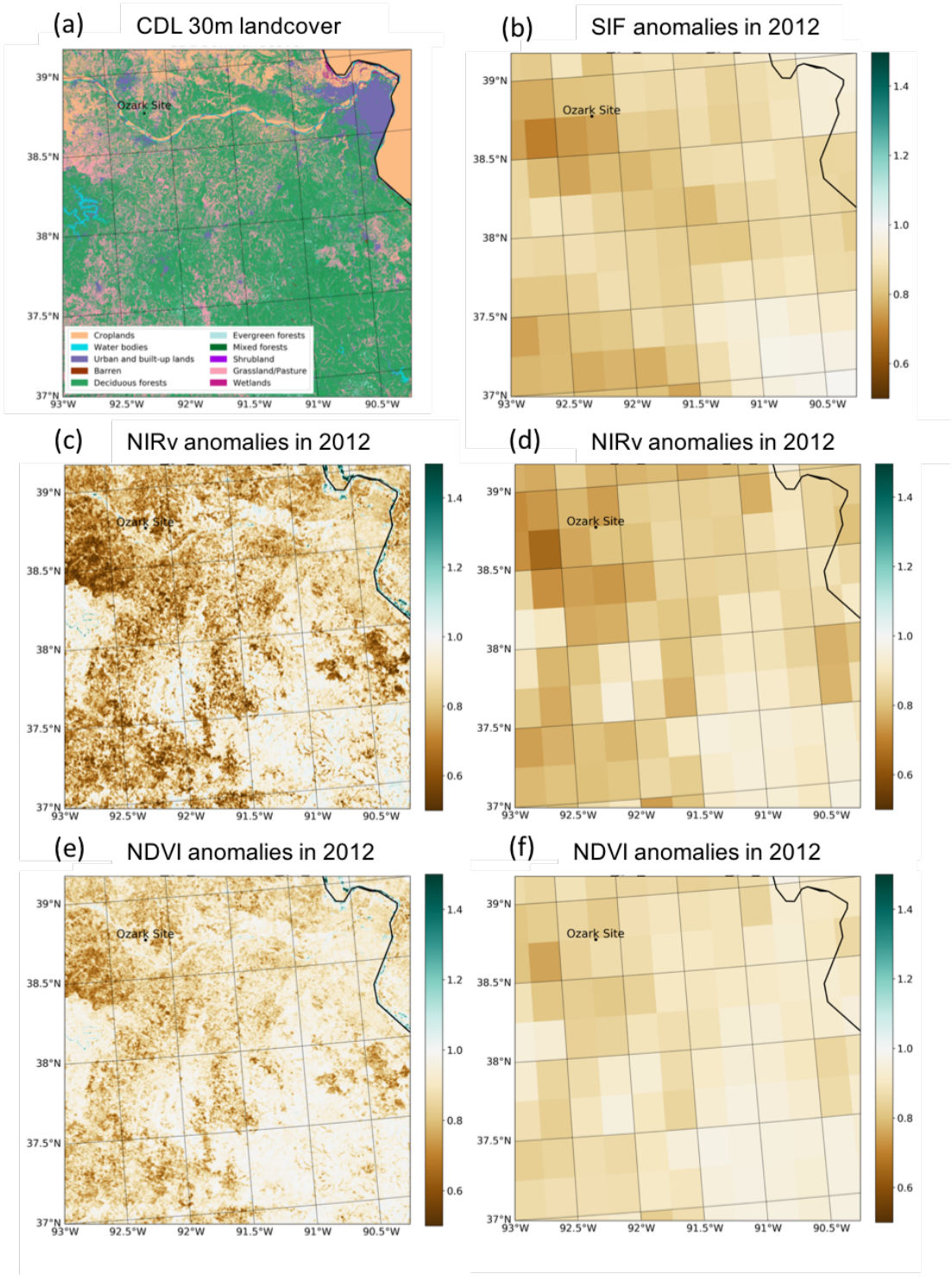

Figure 2.3: (a) The landcover map based on the USDA CDL dataset in 2016. The spatial distributions of NIRv and NDVI anomalies at native fine resolution (500 m)

are shown in (c) and (e). The spatial distributions of SIF, NIRv and NDVI anomalies at coarse resolution (0.25°) are shown in (b), (d) and (f).

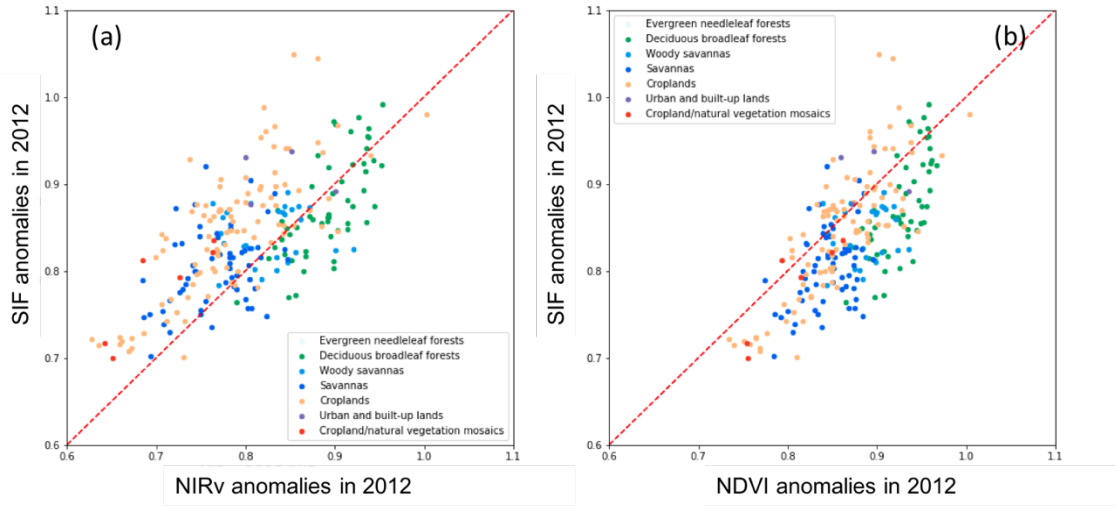

Figure 2.4: The anomalies of (a) SIF–NIRv (b) SIF–NDVI during 2012 drought. Different colors represent different land types.

We also quantified the relationship of $SIF_{anomaly}$–$NIRv_{anomaly}$ and $SIF_{anomaly}$–$NDVI_{anomaly}$ corresponding to different land covers using all the data in the state of Missouri gridded at 0.25° (Figure 2.4). In general, the spatial patterns in the IAV of all remotely sensed datasets are tightly correlated. However, we find that the relationship also depends on the land cover, with more fractional reduction observed for SIF than NIRv and NDVI in forests during the 2012 drought, which corroborates that some of the stress related reduction in GPP over forests is captured by SIF. This analysis underscores the importance of considering the spatial heterogeneity in the complex natural ecosystem when interpreting remote sensing data.

2.4.1.2 Seasonal variations of GPP, NDVI, EVI, NIRv, fPAR and SIF

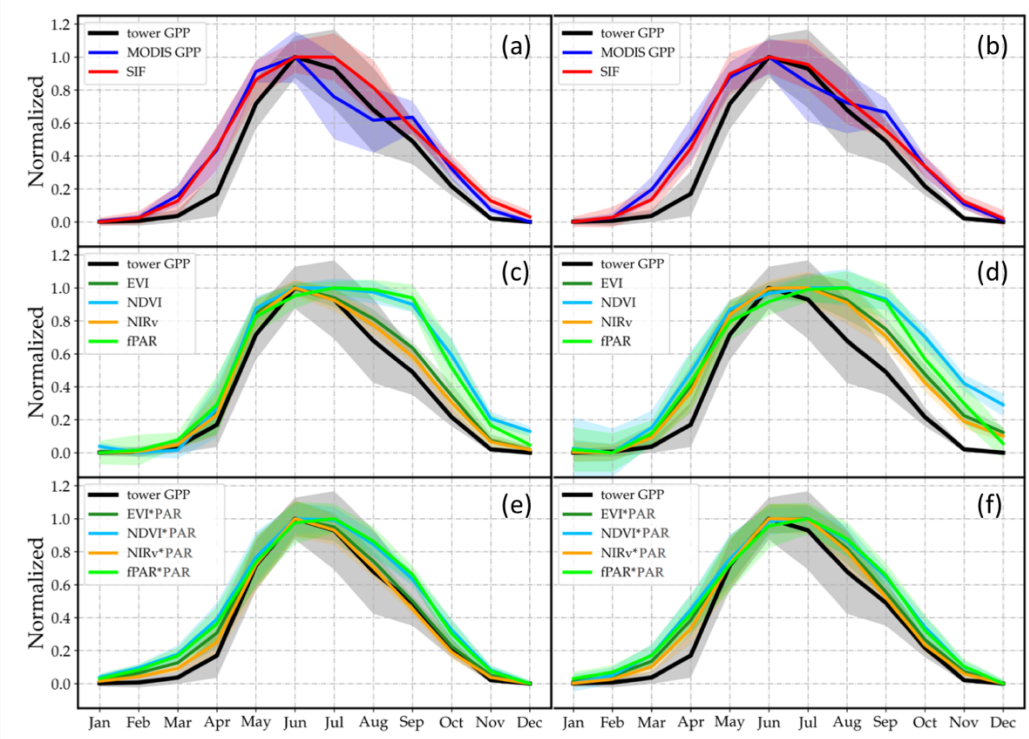

Figure 2.5: Seasonal cycles of monthly mean flux tower GPP, MODIS GPP, GOME-2 SIF, MODIS EVI, NDVI, NIRv and fPAR, EVI*PAR, NDVI*PAR, NIRv*PAR and fPAR*PAR with the shadow regions representing ±1 standard deviation from 2007 to 2016. In (a), (c) and (e), MODIS products are aggregated at 0.02°, and native GOME-2 SIF footprints of the central longitude and latitude within 0.75° from the flux tower are used. In (b), (d) and (f), MODIS products and GOME-2 SIF are gridded at 0.25°. All variables are linearly normalized based on min-max scaling to fall in [0,1]. RMSE and R^2 between flux tower GPP and SIF, NDVI, EVI, NIRv, fPAR, MODIS GPP, NDVI*PAR, EVI*PAR, NIRv*PAR and fPAR *PAR are reported in **Table 2-3**.

Figure 2.5(a), (c) and (e) show the seasonal variations at the fine spatial scale, with MODIS products aggregated at 0.02°, and GOME-2 SIF of the central longitude and latitude within 0.75° from the flux tower. Figure 2.5(b), (d) and (f) show the seasonal variations with MODIS products and GOME-2 SIF gridded at 0.25°. All variables are normalized based on min-max scaling from [0,1]. For both spatial aggregations, NDVI and fPAR do not track the GPP seasonality during the mid-to-

late growing season (i.e., Jul, Aug and Sep). Flux tower GPP decreases by 50% from Jul to Sep, however, NDVI and fPAR remain almost constant. To evaluate whether this discrepancy can be caused by changes in available light, we used PAR measured at the flux tower to scale the vegetation indices to estimate APAR, which was calculated as fPAR*PAR (Figure 2.5(e) and (f)). We found a closer agreement between NIRv*PAR and EVI*PAR with flux tower GPP seasonality. This indicates that in general, the seasonal cycle of GPP at the US-MOz site is mostly dominated by changes in absorbed light and not photosynthetic efficiencies, and thus the accurate estimate of absorbed light is important to obtain the accurate GPP estimate at the seasonal scale. Using NDVI, the relationship is weaker, with a pronounced broadening in the seasonal cycle compared to GPP. The MODIS fPAR algorithm is similar to NDVI, only considering the reflectance at red and near infrared bands (Myneni et al., 2015), thus showing strong similarity to NDVI. Other VIs, such as the EVI, reduce the saturation problem and the effects of atmospheric interferences and soil background brightness (Huete et al., 2002). In addition, NIRv contains the information of the pixel reflectance attributed to vegetation and mitigates the mixed-pixel problem (Badgley, Field, and Berry, 2017). Here, NIRv and EVI perform best at the seasonal scale, while SIF increases earlier than reflectance-based VIs at the onset of growing season. An explanation for this could be that GOME-2 observations are obtained with large footprints that are influenced by the mixed forest and crops or grasslands in the vicinity of the flux tower.

Interestingly, MODIS GPP appears to closely follow GOME-2 SIF in the early part of the season but deviates from a typical seasonality in July and August, with persistent reductions in GPP. This is mainly related to the LUE parameterization in the MODIS model, which appears to strongly overestimate the sensitivity to VPD or temperature. In fact, the LUE parameterization in MODIS GPP appears to worsen the agreement compared to the raw vegetation indices multiplied by PAR.

2.4.1.3 Diurnal variations of LUE

Diurnal LUE changes may introduce bias when we intend to estimate daily average SIF (and GPP) using an instantaneous SIF signal. Here we evaluate the potential bias in the daily GPP estimate using the LUE at GOME-2 and OCO-2 overpass times. The average diurnal cycle of LUE in the summer period (DOY 150-240) from 2007 through 2016 is shown in Figure 2.6(a). Here, the apparent LUE is approximated by GPP/PAR, with the assumption that fPAR is almost constant within the growing season and not changing within a day, which is supported by fPAR measurements in the field. LUE is higher in the morning and late afternoon, and lower around solar noon. A diurnal hysteresis in LUE was observed, with higher LUE in the morning than afternoon for the same Earth-Sun geometry. This is usually caused by increases in temperature and vapor pressure deficit during the day, causing an LUE asymmetry in the diurnal cycle. This temporal variation of LUE may cause a bias for upscaling instantaneous GPP (GPP_{inst}) to daily GPP (GPP_{daily}), which depends on the time chosen to infer daily GPP. In a similar fashion, there may be similar biases when scaling instantaneous satellite SIF observations to daily averages. This analysis gives insights into interpreting SIF observations at different times of satellite overpasses, as well as quantifying bias of temporal scaling of SIF from snapshots taken at a certain time of a day to an estimate of daily average.

Then, we evaluated the reconstructed diurnal GPP pattern based on the LUE at 9:30 and 13:30 local time, the overpass times of GOME-2 and OCO-2, respectively. The reconstruction was performed by multiplying the instantaneous LUE by an average diurnal PAR pattern in the summer period including both sunny and cloudy observations. The reconstructed GPP and flux tower GPP measurements in summer using different instantaneous LUE are shown in Figure 2.6(b) and (c). There was no significant bias in upscaling GPP based on LUE at 9:30 because the instantaneous value was a good estimator of the daily average. However, daily GPP

was largely underestimated when using LUE at 13:30, since the instantaneous value was almost at the minimum daily value. Therefore, based on the seasonal averaged diurnal shape of GPP at this site, we expect less bias in the GOME-2 daily normalized SIF compared to OCO-2 under the assumption that i) the SIF_{yield} is correlated with LUE; and ii) instantaneous SIF is scaled to daily SIF using the Earth-Sun geometry. However, we have to consider that the variability of SIF_{yield} is dampened compared to LUE, which might reduce this bias at mid-day.

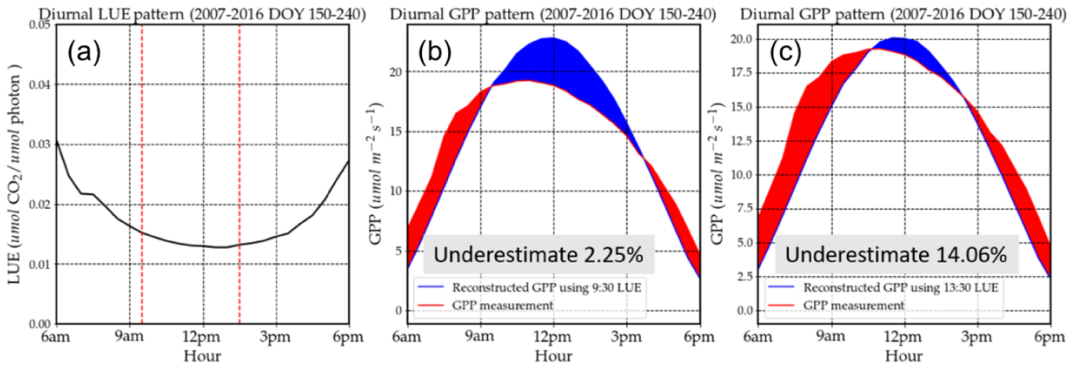

Figure 2.6: (a) Average diurnal GPP/PAR pattern during JJA including both sunny and cloudy observations from 2007 to 2016. The red dashed lines represent different GOME-2 and OCO-2 overpasses, ~ 9:30 and 13:30at local time, respectively. In (b) and (c), the diurnal patterns of GPP from measurements and the LUE upscaling approach are represented by the red and blues lines, respectively. Blue and red shaded regions represent overestimation by upscaled and measured GPP, respectively.

2.4.2 Impact of spring temperature on annual GPP

Here, we investigated the control of late growing-season GPP at the US-MOz site. Specifically, we aim to isolate specific variations of GPP seasonality that might be related to the interannual variability of GPP. The SVD analysis of eddy covariance GPP provides us with a pattern of three leading PCs scaled by corresponding singular values, i.e. computed as $s_1 \times v_1^T$, $s_2 \times v_2^T$ and $s_3 \times v_3^T$ in Figure 2.7(a)-(c). The first three PCs explain 90% of the seasonal variability across 10 years. As expected, the shape of $s_1 \times v_1^T$ reflects the mean seasonal GPP cycle, while the

following PCs reflect deviations from the mean. $s_2 \times v_2^T$ increases rapidly in early spring, and remains positive until summer, representing a "trade-off" between spring gain and summer loss. $s_3 \times v_3^T$ follows a "W" pattern (see Fig 7 (c)) and can be interpreted as a widening or narrowing of the overall growth period. Total GPP (the integration of GPP over 12 months) of the three PCs is 124.0, 4.0 and -3.2, respectively, and denoted as r_1, r_2, r_3. Total annual GPP can thus be approximated by the sum of $u_1 r_1$, $u_2 r_2$ and $u_3 r_3$. Since r_1 is significantly larger than r_2 and r_3, annual total GPP is mainly controlled by u_1.

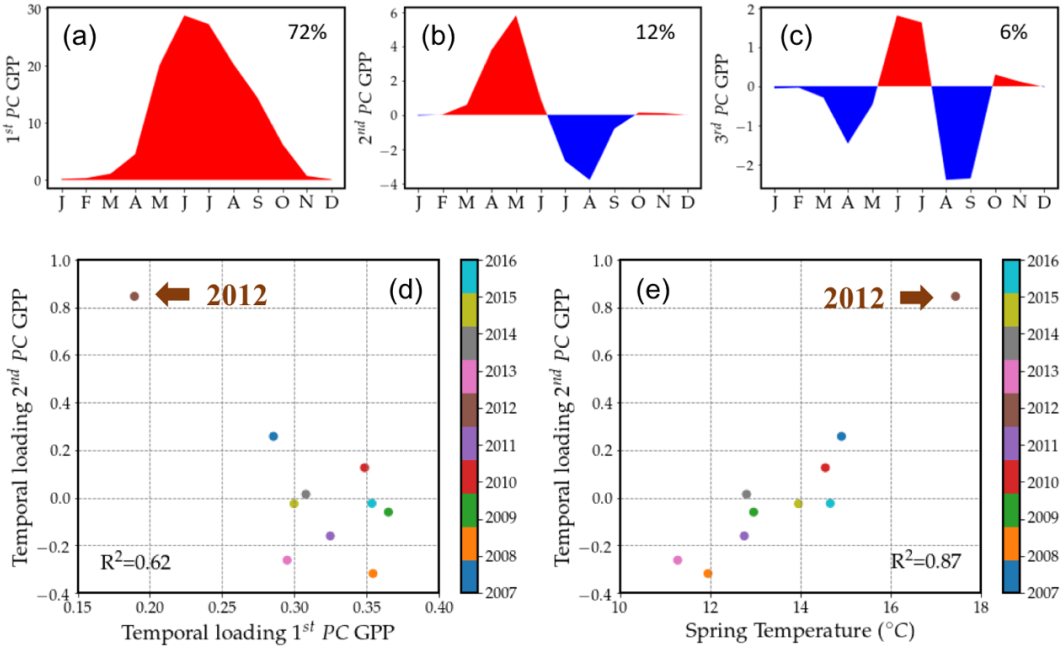

Figure 2.7: Three leading PCs scaled by corresponding singular value $s_1 \times v_1^T$, $s_2 \times v_2^T$ and $s_3 \times v_3^T$ are shown in (a), (b) and (c), explaining 72%, 12% and 6% of variability in monthly GPP. Negative correlation between temporal loading u_1 and u_2 is shown in (d) and positive correlation between average spring temperature and temporal loading u_2 is shown in (e), with different color representing different years.

A strong negative correlation is observed for u_1 and u_2 (Figure 2.7(d)). Meanwhile, u_2 is strongly correlated with annual spring temperature (Figure 2.7(e)), even if the more extreme drought years of 2007 and 2012 are excluded. This indicates that in

years with higher spring temperature, $s_2 \times v_2^T$ captures the seasonal change with an increase in spring GPP but a decrease in the summer. As this feature correlates negatively with u_1, there is an overall decrease in annual GPP during all years with an early spring.

We found that spring GPP, SIF and NEE are strongly driven by spring temperature (Figure 2.8 (a) and (b)). Larger spring GPP, SIF and more net ecosystem CO_2 uptake (i.e., more negative NEE) are observed for years with warmer spring (Figure 2.8(c) and (d)). However, warmer springs do not guarantee an increase in annual GPP and net ecosystem CO_2 uptake (e.g., in 2007 and 2012), which is due to higher evapotranspiration during the onset of the growing season or low precipitation throughout the growing season. In addition, higher spring temperature is consistently associated with lower net ecosystem CO_2 uptake and GPP in the summer (Figure 2.8(e) and (f)), which might be attributed to less photosynthetic efficiency due to water limitation as well as more active respiratory processes at higher temperature and will be discussed in Section 4.1.

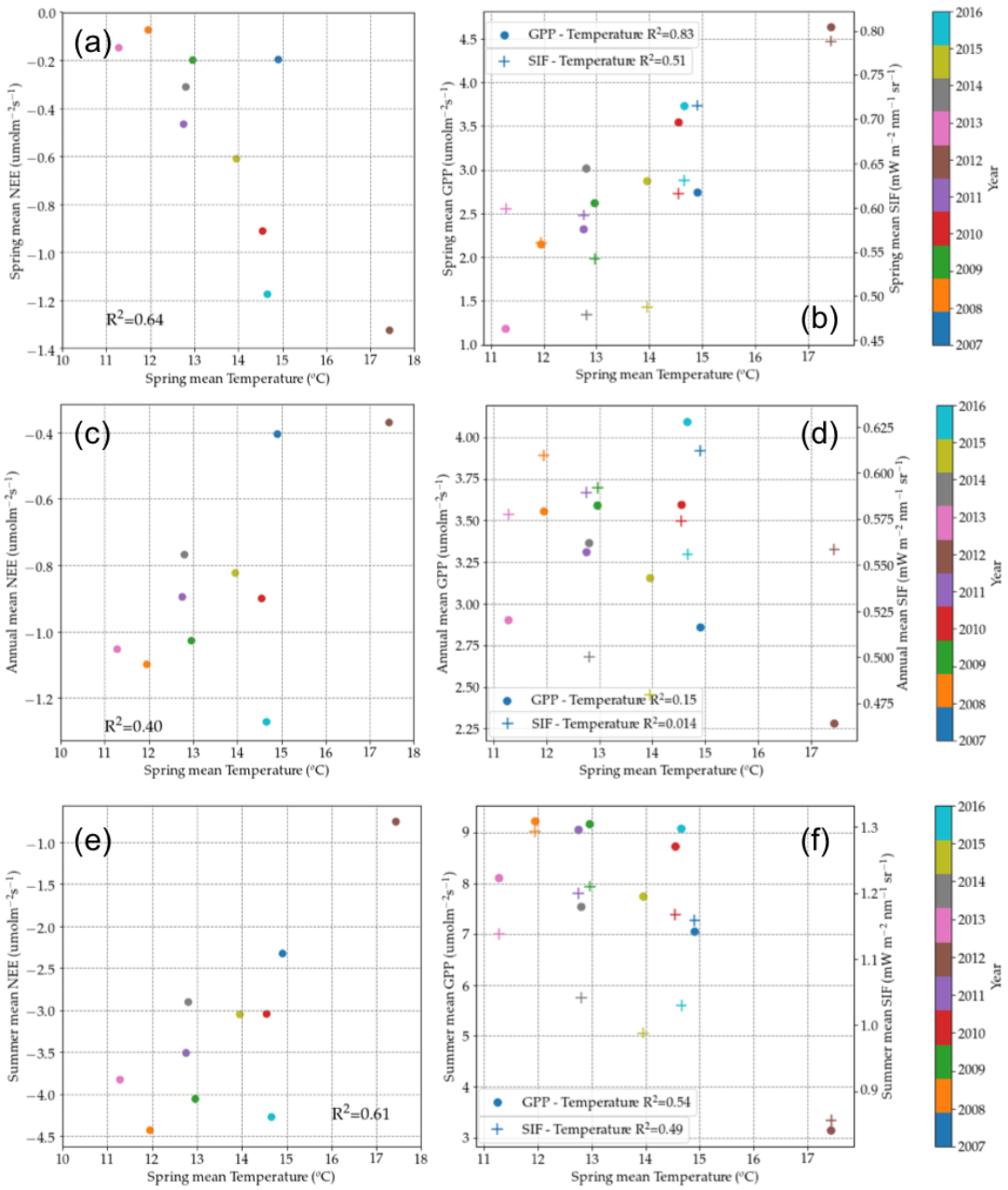

Figure 2.8: The relationship between spring temperature with spring mean NEE, GPP and SIF (a and b), annual mean NEE, GPP and SIF (c and d), and summer NEE, GPP and SIF (e and f). Different colors represent different years. Spring months are defined as March, April and May.

To investigate whether the other parameters follow similar principal components in the SVD decomposition, we performed the same SVD analysis for flux tower ET

measurements, satellite VIs and SIF (Figure 2.9). The analysis including tower measurements and satellite observations consistently shows that the second PC is similar to the one for GPP, especially for SIF and ET. Since ET is linked with stomatal conductance and water use efficiency, it is expected to covary with GPP, explaining strong correlations among all the three PCs of ET and GPP. For remote sensing data, SIF performs most similar to the tower GPP in higher orders, with three leading PCs explaining 78%, 8% and 5% of variability, and all shapes having high similarity to the PCs for GPP. In contrast, NDVI is largely dominated by the first PC, which explains 92% variability, and only 4% and 2% variability can be explained by the second and third PC. This implies that SIF is more sensitive in capturing the signal of stress-induced GPP "seasonal-shifted" dynamics than VIs, and thereby helps better estimate the inter-annual GPP change patterns.

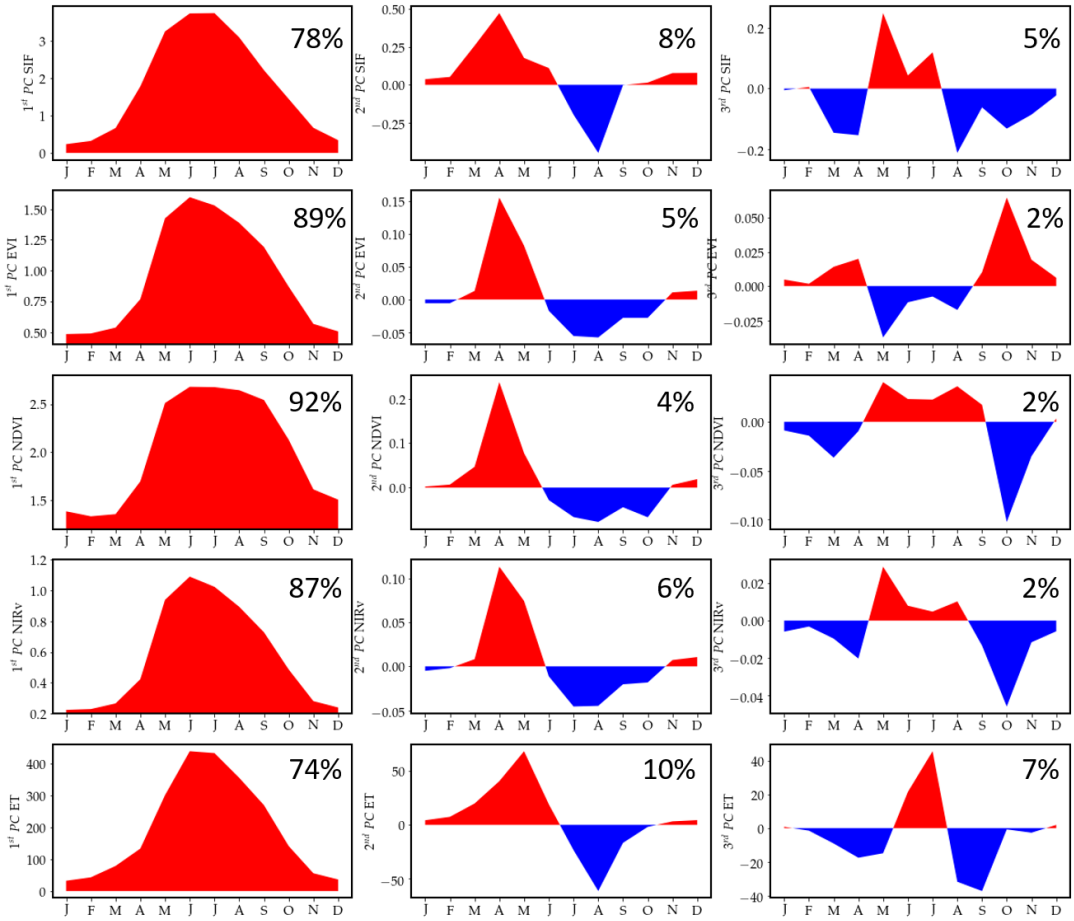

Figure 2.9: Three leading PC's of SIF, EVI, NDVI, NIRv and ET (top to bottom rows, respectively) scaled by corresponding singular value $s_1 \times v_1^T$, $s_2 \times v_2^T$ and $s_3 \times v_3^T$, with the fraction of explained variance shown for each.

2.4.3 SCOPE modeled GPP and SIF track flux tower GPP

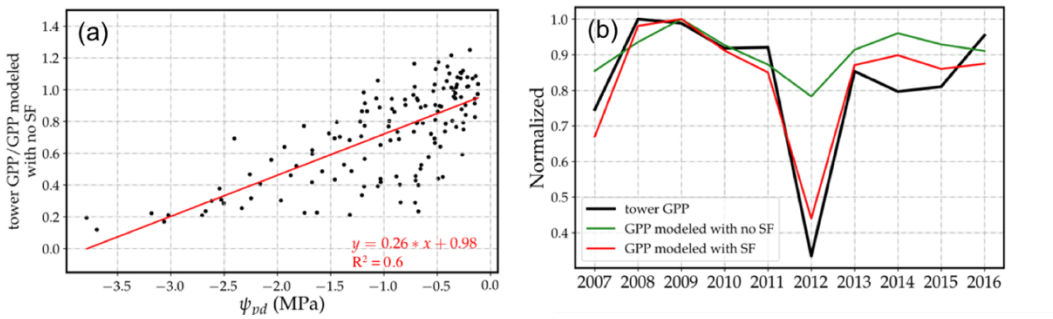

Figure 2.10: a) The ratio of flux tower GPP (bi-weekly average) to GPP modeled by SCOPE (bi-weekly average) with no scaling factor (SF) introduced as the function of ψ_{pd} (MPa). (b) Average of flux tower GPP, GPP modeled by SCOPE with/without SF during JJA from 2007 to 2016. All variables are scaled by the corresponding maximum value.

To better understand the underlying mechanisms, we simulate the interannual variations of GPP and SIF using the SCOPE model and evaluate how well SCOPE captures flux tower GPP variations with proper parameterization. During drought, plants may experience a combination of both canopy structural changes and physiological stress, imposed by atmospheric conditions such as elevated temperature and VPD but also through soil moisture deficits. Usually, the structural change is reflected in VIs, however, capturing physiological changes is challenging. Disentangling these two effects is important to determine the information SIF can provide for quantifying physiological stress beyond canopy structural changes. In this section, we show the effects of incorporating physiological stress on both primary production and fluorescence with SCOPE simulations. In SCOPE, environmental stress affects photosynthesis and fluorescence purely through changes in humidity and temperature, as a soil moisture model is missing. As in many models, the drought stress through soil moisture variations is incorporated

through a stress factor [0, 1] (SF) to scale the maximum carboxylation rate (Vcmax at 25 °C) effectively reducing photosynthesis and thus also stomatal conductance, which is equivalent to the soil water stress parameter (BTRAN) in the Community Land Model (Oleson et al., 2013). We performed two simulations: 1) without any soil moisture stress (SF =1), and 2) with variable SF as a time series computed as a function of pre-dawn leaf water potential ψ_{pd} (Figure 2.10(a)). We found that the ratio of observed flux tower GPP to the GPP modeled using SCOPE (case 1), $\frac{towerGPP}{GPPmodeledwithnoSF}$, is correlated with ψ_{pd} (Figure 2.10(a)), and proportional to the stress experienced by the plant. The SF is calculated from this relationship based on the first order linear regression of $\frac{towerGPP}{GPPmodeledwithnoSF}$ and ψ_{pd}, which is used for the simulations of case 2. In both cases, we used LAI and meteorological data (including air temperature, VPD, radiation, wind speed, etc.) collected at the flux tower to drive the model. Thus, a basic inter-annual variation of stress due to changing atmospheric conditions is already included in simulation 1.

The 1st case (green line in Figure 2.10(b)), with no soil moisture driven physiological stress, can be interpreted as the GPP of plants around Ozark, only considering atmospheric variations across different years. The 2nd case (red line in Figure 2.10(b)), with SF, indicates the effect of soil moisture availability on GPP. In the 2012 drought, higher air temperature and larger VPD only account for a 20% reduction in GPP. However, we found an additional 35% reduction in GPP upon introduction of SF in the model, leading to a 55% total reduction in GPP, close to the 65% reduction in GPP observations, underlining that our ad-hoc SF parameterization worked well. Overall, comparing the two cases (with and without the stress factor) using the SCOPE model provides a good way to decouple canopy structural changes and physiological stress on GPP. The latter was found to contribute more in the 2012 drought, which underscores the importance of a physiology related signal to monitor terrestrial GPP changes using remote sensing.

To evaluate how SIF might change within a modeling framework, we look into the IAV of modeled SIF (with and without SF introduced) at three different timescales (daily average, 9:30 and 13:30), and compare its magnitude against the corresponding IAV of GPP. In the SCOPE framework, GPP and ΦP are first simulated by the FvCB model (Farquhar et al., 1980), and then ΦF is derived based on the leaf-level empirical ΦF–ΦP relationship (Lee et al., 2015; van der Tol et al., 2014). Finally, SIF is computed based on the ΦF and APAR estimated from the multi-layer canopy radiative transfer model within SCOPE. The goal of this section is to 1) evaluate the IAV of SIF using different ΦF–ΦP and SF parameterizations; 2) examine the IAV magnitude of modeled SIF and modeled GPP; 3) compare the IAV of modeled instantaneous SIF at different overpass times with the daily average. The analysis including the daily average, as well as sampling at other times of day is necessary, because it helps to evaluate theoretically how well the IAV of daily-averaged GPP and SIF can be captured from instantaneous satellite observations at different overpass times.

Figure 2.11(a) shows the IAV of modeled daily average GPP and SIF with/without SF using the two different SCOPE versions. When SF is introduced as a ψ_{pd}, SIF modeled by SCOPE 1 can capture the 2012 drought to some extent, with a 17% decrease in SIF; whereas no reduction is observed for SIF modeled by SCOPE 2. This underscores the significance of choosing between two ΦF–ΦP options, which may lead to very different IAV patterns of SIF. When SF is fixed to 1, the IAV of SIF with both parameterizations hardly reflect the 2012 drought.

Figure 2.11(b) and (c) show the IAV of modeled GPP and SIF with different parameterizations of ΦF–ΦP and SF sampled at 9:30 and 13:30, respectively. During both times, SIF modeled by SCOPE 1 with SF introduced captures the 2012 drought best. A reduction of around 18% was observed at 9:30 in 2012, the magnitude of which is similar to the reduction observed for daily averages in Figure

2.11(a), while a reduction over 25% was simulated at 13:30 since plants are usually more stressed in the afternoon due to higher VPD.

The magnitude of modeled SIF reductions (18%) in 2012 gives a theoretical reference, which we can compare against the observed SIF reductions of around 33%. We thus conclude that the large footprint of GOME-2 caused an over-estimation for the forest SIF reductions because of the presence of non-forest cover within the footprints. However, the SCOPE simulations underline that we expect reductions in SIF owing to dynamic variations in plant stress, which are also comparable with the observed changes in GOME-2 SIF (about half of the reduction). It should be noted that the modeled SIF variations are always smaller than the modeled GPP variations during the 2012 drought, which is in line with our observations. A linear scaling approach for SIF–GPP would thus largely underestimate interannual variations in GPP, which is an important caveat for using SIF to study stress driven IAV in GPP. In addition, our findings underline the need to better represent the stress impact on the ΦF, as we find that the SCOPE 2 parameterization can lead to increases in ΦF at low photosynthetic yields, which is unlikely to happen for plants adapted to their environment, which we will outline in the following LUE–SIF_{yield} section.

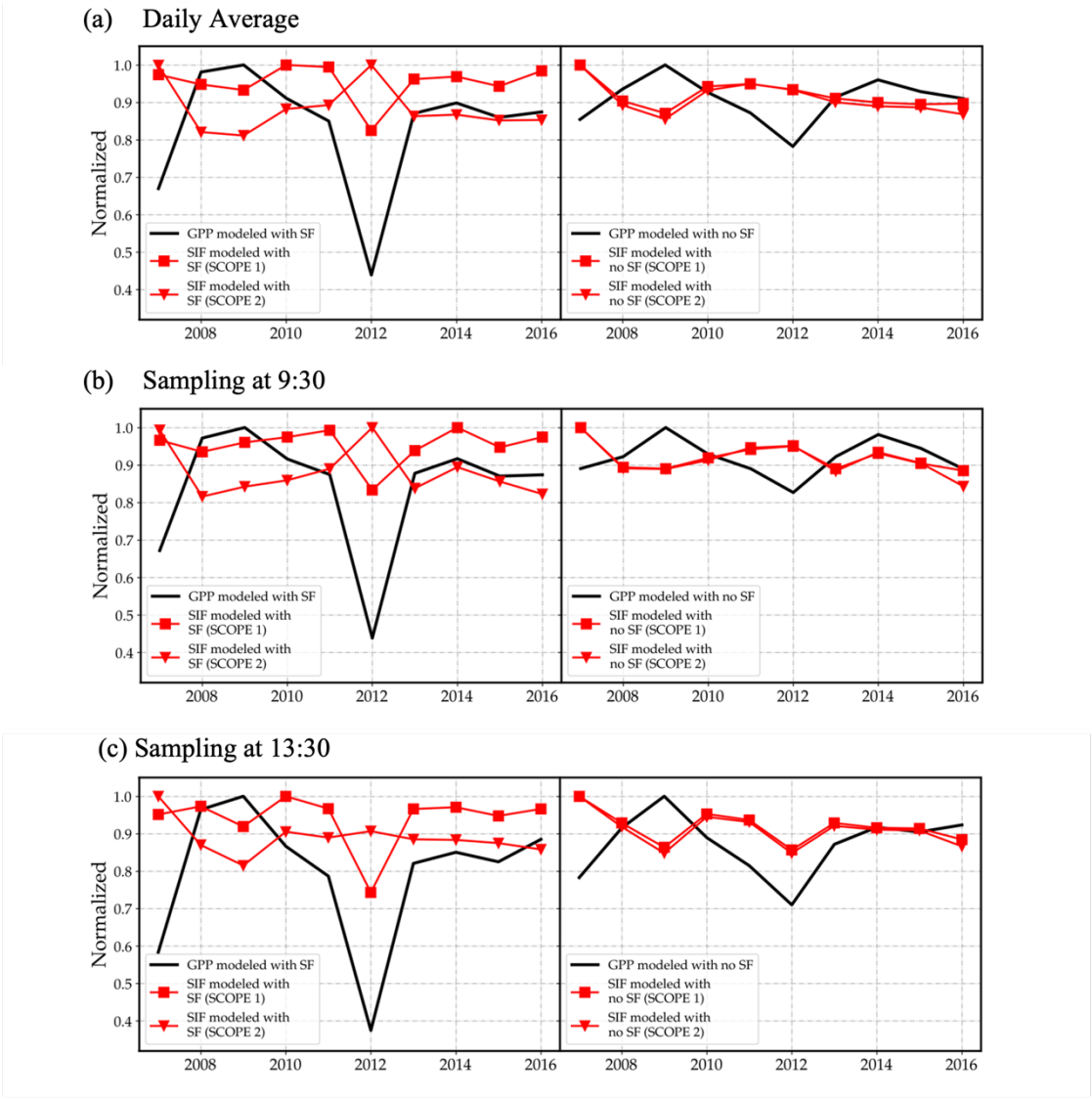

Figure 2.11: Average of GPP, SIF modeled by SCOPE with/without SF using two different parameterizations of ΦF vs ΦP during JJA from 2007 to 2016. All variables are scaled by the corresponding maximum value. Note that SCOPE 1 refers to empirical leaf-level ΦF–ΦP relationship based on various leaf samples experienced progressive drought (Flexas et al., 2002) and SCOPE 2 refers to ΦF–ΦP relationship experimented on healthy cotton leaves (van der Tol et al., 2014).

2.4.4 Smaller variations in SIF_{yield} than LUE

Both satellite and SCOPE modeled SIF showed a significant decrease in the 2012 drought, but with a smaller fractional change in SIF compared to GPP. This

addresses the question of the covariation between LUE and SIF_{yield} across different stress levels. As we observed low inter-annual variability in VIs during JJA, we can use this time-period to better understand the connection between LUE and SIF_{yield} because these two terms should have a larger impact on overall GPP and SIF than changes in APAR. fPAR aggregated at 0.02° shows little variation across JJA from 2007 to 2016 (Figure 2.2(a)), indicating that the interannual GPP-SIF relationship in JJA is indeed mainly driven by SIF_{yield} changes, not APAR. Consequently, we approximated LUE and SIF_{yield} as GPP/PAR and SIF/PAR. In Figure 2.12(a), we found that there is a positive correlation between LUE and SIF_{yield} (R^2=0.66, Figure 2.12(a)), whereas fPAR shows little variations across different LUE levels. Color coded by ψ_{pd}, both LUE and SIF_{yield} decrease in water-stressed period when ψ_{pd} is low. We also evaluated whether the SIF_{yield}–LUE changes observed at the canopy are consistent with leaf-level ΦF–ΦP employed in the SCOPE model. We found that the SCOPE 1 agrees well with our canopy measurements, with positive SIF_{yield}–LUE pattern and very similar changes in terms of magnitude. However, the negative SIF_{yield}–LUE relationship at high stress levels shown by SCOPE 2 is not observed with GOME-2. This suggests that the extreme behavior at low ΦP modeled in SCOPE 2 might be rarely observed in nature, as it would require stress levels that greatly exceed the capacity of NPQ for plants. Under this condition, SIF_{yield} would have to increase at higher stress levels when NPQ is saturated. This might have to do with the experimental setup, where leaf data have been used under stress conditions that go beyond what they typically experience in nature. Under these conditions, plants might lack the dissipative pathways for enhanced NPQ, which results in longer excited state lifetimes and thus higher SIF_{yields} at lower photosynthetic yields. For global modeling, the use of SCOPE 2 parametrization might thus lead to erroneous results. In the future, more studies on ΦF–ΦP relationships under different environmental stresses across a variety of plant species will be important to achieve more accurate estimate of SIF.

In Figure 2.12(b), we found both LUE and SIF_{yield} are positively correlated with ψ_{pd} (R^2=0.83 and R^2=0.60, respectively). However, the relative change is not the same for LUE and SIF_{yield}. For example, when ψ_{pd} dropped from −0.5 MPa (unstressed periods) to nearly −3.5 MPa (severe drought in 2012), LUE dropped from 0.0175 to 0.0025 — an 85% decrease — while we only see a 42% decrease from 0.00225 to 0.0013 for SIF_{yield}. This indicates that the SIF_{yield} is not as sensitive as LUE to water stress; and consequently, a ~40% fractional difference is missing with the assumption of linear SIF_{yield}–LUE relationship. One potential reason might be that GOME-2 SIF is measured at 9:30 am when plants tend to be subjected to comparatively less stress versus the afternoon. The other reason is attributed to the systematic lower fractional reduction in SIF than GPP under the stress, which is confirmed by the SCOPE in Section 3.3. Therefore, the latter one should be considered as the dominant factor explaining the smaller relative changes in the observed SIF compared to GPP. Additionally, as was previously noted, we have to bear in mind that the SIF yield changes are likely overestimated due to the large GOME-2 footprints.

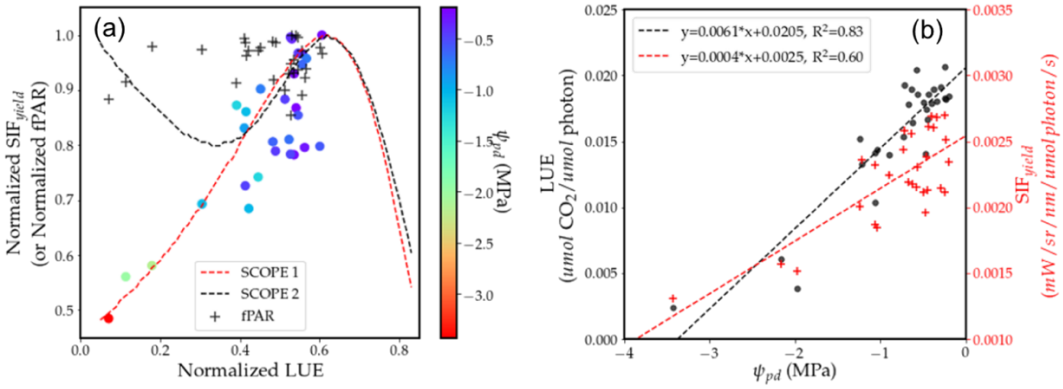

Figure 2.12: (a) Relative changes in LUE (or GPP/PAR) and SIF_{yield} (or SIF/PAR) in JJA from 2007 to 2016 overlain with modeling results of ΦF–ΦP relationship from the SCOPE 1 and SCOPE 2. To better compare the canopy scale observations with the modeled leaf scale, we normalize SIF_{yield} by its maximum and normalize LUE with the maximum at 0.6, which is the largest photochemical yield for plants exposed at normal light range. The color of the circular symbols represents ψ_{pd} (MPa), with red indicating more water stressed conditions. MODIS fPAR

aggregated at 0.02° is shown and also normalized by its maximum. (b) GPP/PAR or SIF/PAR as a function of ψ_{pd}. Black and red dashed lines represent least squares linear fits to the observations.

2.5 Discussion

2.5.1 Seasonal compensation of warm spring

A warmer spring would lengthen the photosynthetically active period, and thus increase annual GPP (Sippel et al., 2017; Keenan et al., 2014; Richardson et al., 2013; Buermann et al., 2013; Grippa et al., 2005). However, we observed the opposite at the Ozarks: an early spring tends to enhance productivity and thus depletion of the soil water storage that available for the later growing season, leading to increased reliance on precipitation and higher probability of water stress and vulnerability of GPP in summer (Ummenhofer et al., 2017; Wolf et al., 2016). Here we compared the water budget in 2008 (the most productive year) and 2012 (the most water stressed year) by accumulated precipitation, accumulated evapotranspiration, accumulated precipitation – accumulated evapotranspiration, and soil moisture in Figure 2.13. Compared to 2008, the evapotranspiration increases much more rapidly in 2012 due to the warmer spring, leading to a significant decrease of precipitation – evapotranspiration as well as soil moisture in the beginning of summer (~ DOY 150) , indicating that there is less water available for plants in the late growing season.

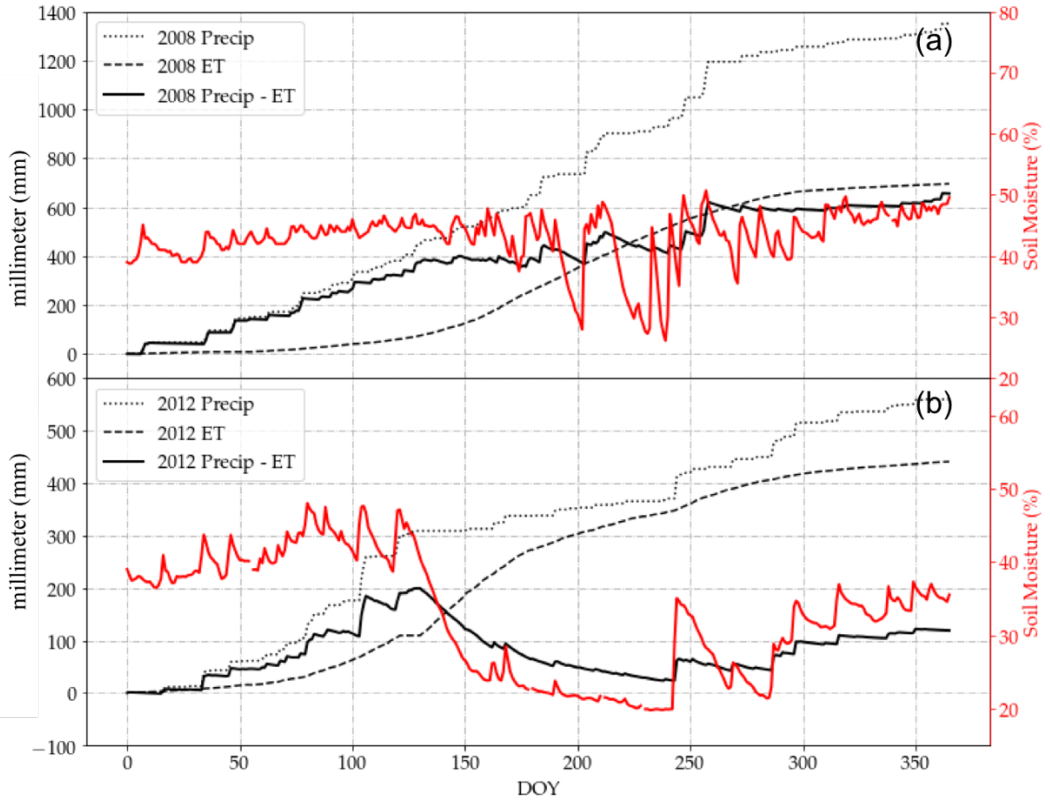

Figure 2.13: The water budget in (a) 2008 and (b) 2012. The black dotted line, dashed line and solid line represent accumulated precipitation, accumulated evapotranspiration, and accumulated precipitation – accumulated evapotranspiration in the unit of millimeter (left-axis). The red line represents soil moisture in the unit of percentage (right-axis).

The 2008 and 2012 cases help to explain the "spring GPP gain" and "summer GPP loss" pattern shown in Figure 2.7, and both compensate each other in terms of annual total GPP (Figure 2.8(d)). This points to a strong coupling of the carbon and water cycles, as well as a climate–carbon feedback. Higher spring temperature with moderate VPD is accompanied with an increase in GPP and ET, which can rapidly deplete soil water available for the summer (Buermann et al., 2018; Grippa et al., 2005; Sippel et al., 2017). Therefore, during the subsequent summer, GPP is significantly reduced due to less water availability, and is accompanied with a decrease in latent heat and increase in sensible heat fluxes, which ultimately leads to larger VPD and higher air temperature. This can act as a positive feedback loop,

exacerbating the water and heat stress in summer. There is also a possibility that land-atmosphere coupling (Koster et al., 2006) could cause the correlation of spring-time temperature (and associated ET increases) and water deficits in summer. Although answering the question of causality of this intriguing correlation is beyond the scope of the current study, at least we found a strong correlation between spring temperature and ψ_{pd} (R^2=0.52).

With regard to changes in the seasonal cycle driven by spring-time temperature, it should be noted that the sensitivity of assimilatory and respiratory processes to spring temperature change differs by ecosystem type (Caignard et al., 2017; Wang et al., 2011; Welp et al., 2007). For example, deciduous forests are found to be more sensitive to increased spring temperature and summer drought than evergreen forests (Welp et al., 2007). More flux tower-based analyses are needed to fully understand the response of different kinds of vegetation to temperature changes. In a warming climate, there are two competing effects: increasing temperature and vapor pressure deficits, as well as increased water use efficiency of photosynthesis due to CO_2 fertilization (Yuan et al., 2019; Keenan et al., 2013). On the other hand, reduced transpiration due to CO_2 fertilization can also result in positive feedback, further amplifying surface temperature increases and heat stress (Swann et al., 2016). For future projections, it will be important to understand the site-specific response and how it scales spatially. Also, process-based carbon cycle models need to better estimate the response of the ecosystem to changes in spring temperature, and the consequent energy partitioning later in the summer.

2.5.2 Less reduction in SIF than GPP in drought events

Both observations and SCOPE simulations show less variations in the SIF_{yield} than in LUE across different water stress levels (Figure 2.12), which explains the reduced IAV observed in SIF compared to GPP (Figure 2.2 and 2.11). Some recent studies suggest that SIF is more linked with chlorophyll APAR than GPP since SIF directly emanates from the light reactions of photosynthesis (Li et al., 2020; Gu et

al., 2019; Yang et al., 2018; Porcar-Castell et al., 2014). In a drought period, it is expected that plants will absorb more light due to increased downwelling radiation. Meanwhile, plants are more likely to experience stomatal closure due to higher VPD and less soil water, which strongly depresses the photosynthetic efficiency. This would lead to a strong reduction in LUE while reductions in the SIF_{yield} are muted.

2.5.3 Promises of high-resolution SIF products

Current long-term SIF studies are challenged by relatively large footprints of GOME-2, especially in heterogeneous landscapes. Recently, some machine-learning based SIF products of high spatiotemporal resolution have been generated (e.g., CSIF, GOSIF, RSIF, SIF_{oco2}) based on satellite SIF, high-resolution spectral information, and meteorology data (Gentine et al., 2018; Yu et al., 2018; Zhang et al., 2018; Li et al., 2019; Turner et al., 2020; Wen et al., 2020). In addition, TROPOMI SIF, with both high spatial and temporal resolution has been available since early 2018 (Köhler et al., 2018). All of these datasets show promise to better understand long-term GPP:SIF relationships in different ecosystems.

We used 0.05°-monthly aggregated GOSIF and extract 2×2 pixels (as shown by the red boundary in Figure 2.14(a) and (b)) around the US-MOz which cover 70% forests, 5% croplands and other landcovers (mainly grass/savannas). The choice of using four nearby pixels rather than the single pixel where the flux tower lies is that i) uncertainties will be reduced, and ii) more importantly, the US-MOz site is dominated by southeast wind in the summer period (see https://ameriflux.lbl.gov/sites/siteinfo/US-MOz#windroses). Figure 2.14(c) shows the interannual variations of GOSIF vs. flux tower GPP from 2007 to 2016. We observe a 30% reduction in GOSIF during the 2012 drought, which is similar to the 33% decrease in GOME-2 SIF.

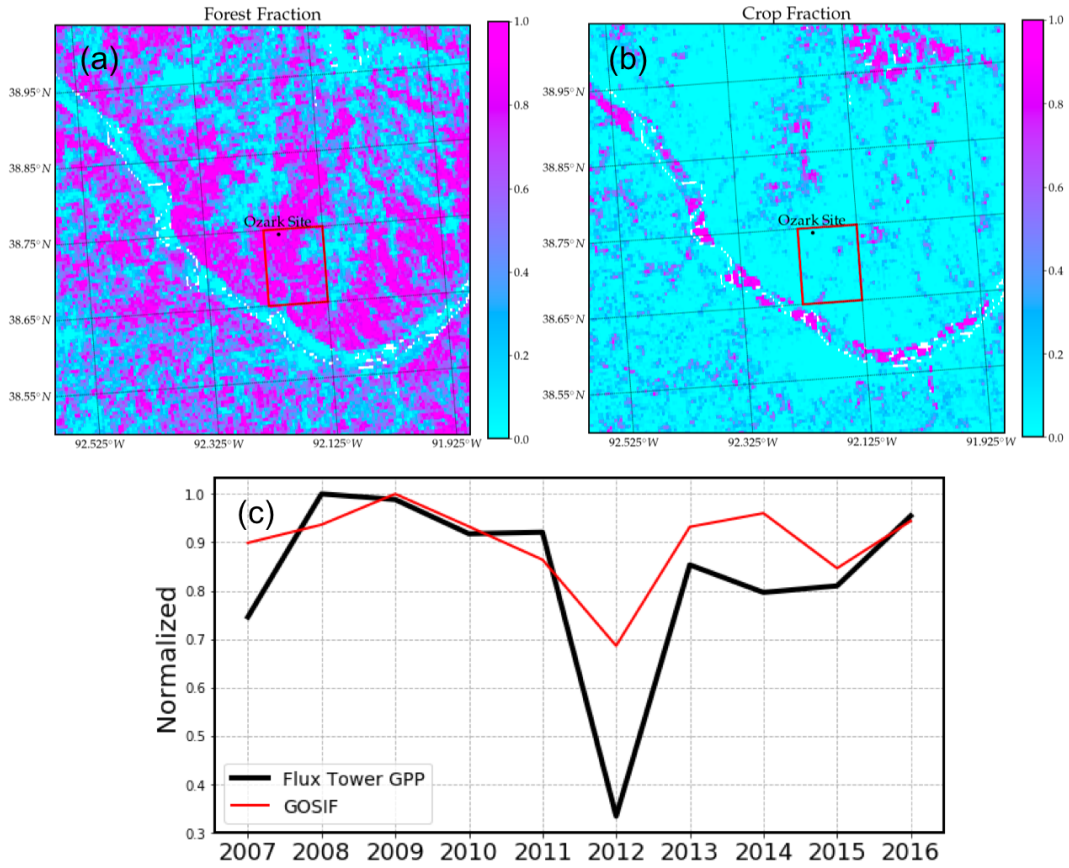

Figure 2.14: (a) Forest and (b) crop fraction based on the USDA CDL dataset. (c) Interannual flux tower GPP, and GOSIF during JJA scaled by the corresponding maximum value from 2007 to 2016. The red boxes in (a) and (b) represent the domain for GOSIF results in (c).

We also leveraged 0.05°-monthly aggregated TROPOMI SIF in 2018 and 2019 over the same region to explore its seasonal and interannual variations. The Ozarks experience strong water stress in 2018 as the ψ_{pd} dropped to ~ −3.5 MPa in mid-Aug (**Supplementary Figure 2.19**), as compared to a more normal year, 2019. Figure 2.15 shows the seasonality of TROPOMI SIF, GOSIF, MODIS NDVI, EVI, NIRv and flux tower GPP in 2018. TROPOMI SIF tracks the seasonality of flux tower GPP much better than GOSIF and all MODIS VIs, with a significant decrease in July and August. As for the interannual comparison, we visualized the fractional difference of TROPOMI SIF and MODIS NDVI, EVI and NIRv in July 2018 and 2019 (Figure 2.16). It shows that TROPOMI SIF over forest regions is more

sensitive to water stress than all VIs, while nearby crops actually increased, either due to the proximity to rivers or watering.

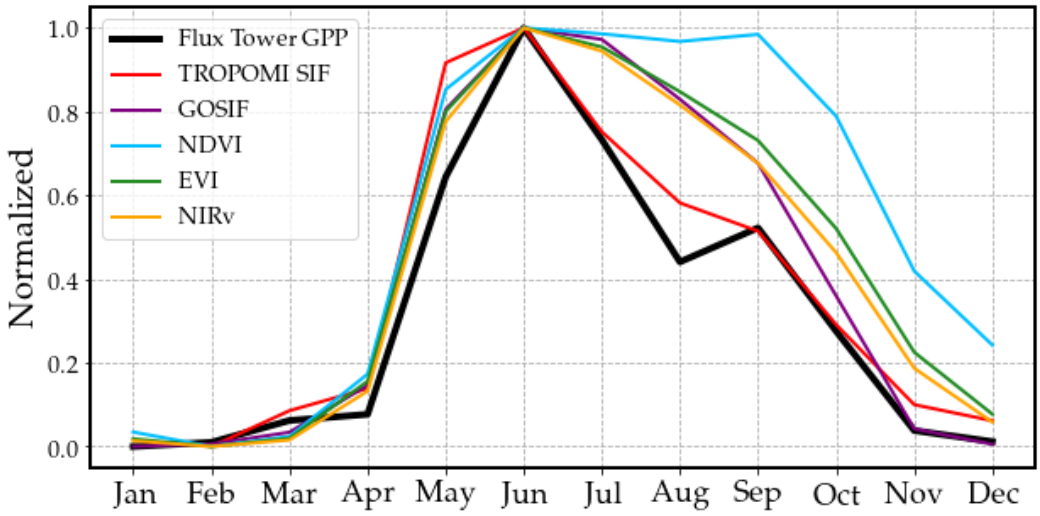

Figure 2.15: Monthly averaged flux tower GPP, TROPOMI SIF, GOSIF and MODIS NDVI, EVI and NIRv in 2018. All variables are linearly normalized based on min-max scaling to fall in [0,1].

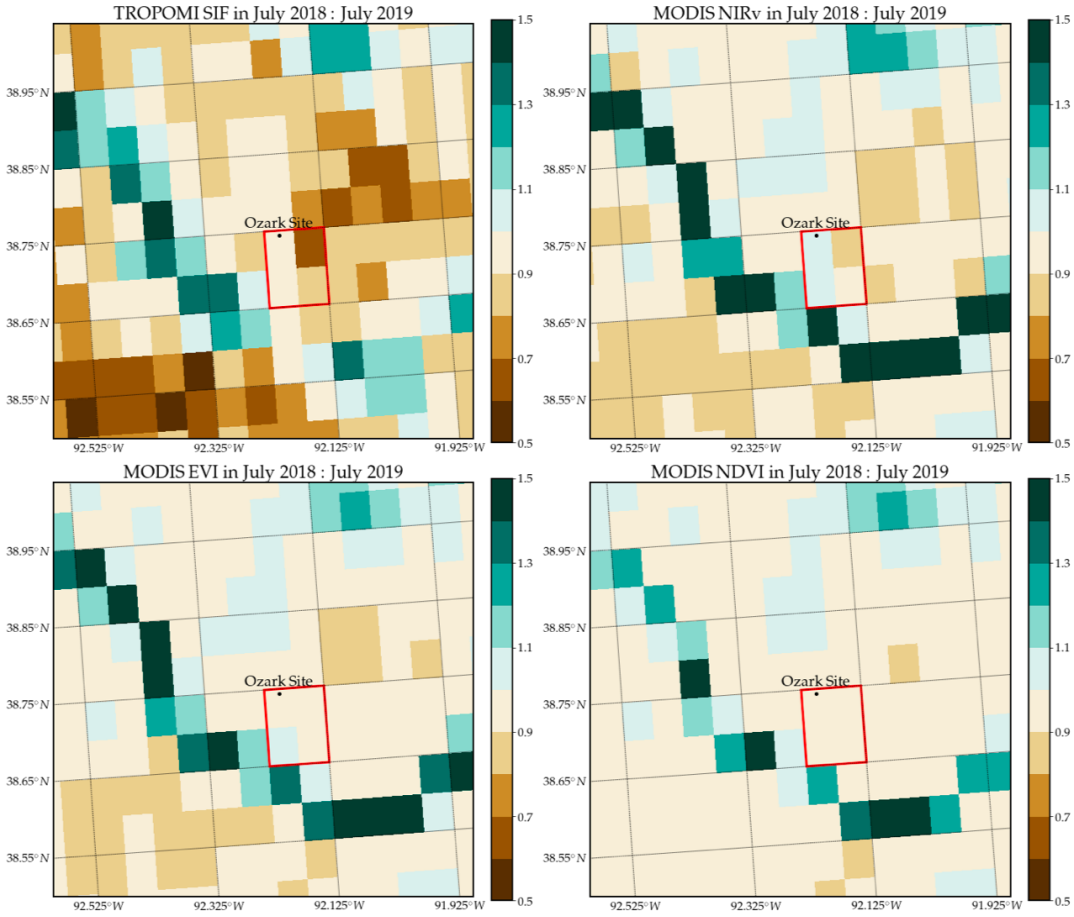

Figure 2.16: The spatial distributions of TROPOMI SIF, NDVI, EVI and NIRv fractional differences in July 2018 and 2019 at 0.05° are shown in (b), (d) and (f). The full seasonal cycle for all remote sensing variables averaged over the red boundary in 2018 and 2019 is reported in **Figure 2.20**.

2.6 Acknowledgements

The GOME-2 SIF product is publicly available on ftp://fluo.gps.caltech.edu/data/Philipp/GOME-2/. The predawn leaf water potential data at the MOFLUX site are obtained from https://tes-sfa.ornl.gov/node/80. Flux data used in the paper are available in the AmeriFlux database (https://ameriflux.lbl.gov) before 2016, and flux data in 2016 are provided by Dr. Jeffrey D. Wood in University of Missouri, which will eventually be available through the AmeriFlux portal. All the MODIS products are obtained from Google

Earth Engine (https://developers.google.com/earth-engine/datasets/catalog/modis). GOSIF data is available at http://globalecology.unh.edu/data/GOSIF.html.TROPOMI SIF can be downloaded from ftp://fluo.gps.caltech.edu/data/tropomi. Y.Z. is supported by International Cooperation and Exchange Programs between NSFC and DFG (41761134082). J.D.W. acknowledges support for the MOFLUX site from the U.S. Department of Energy, Office of Science, Office of Biological and Environmental Research Program, through Oak Ridge National Laboratory's Terrestrial Ecosystem Science - Science Focus Area; ORNL is managed by UT-Battelle, LLC, for the U.S. DOE under contract DE-AC05-00OR2272. Y.S. acknowledge the USDA-NIFA Hatch Project Award 1014740, the Cornell Initiative for Digital Agriculture Research Innovation Fund, the NASA Earth Science Division MEaSUREs program, and the NSF MacroSystem Biology (1926488).

2.7 Appendix

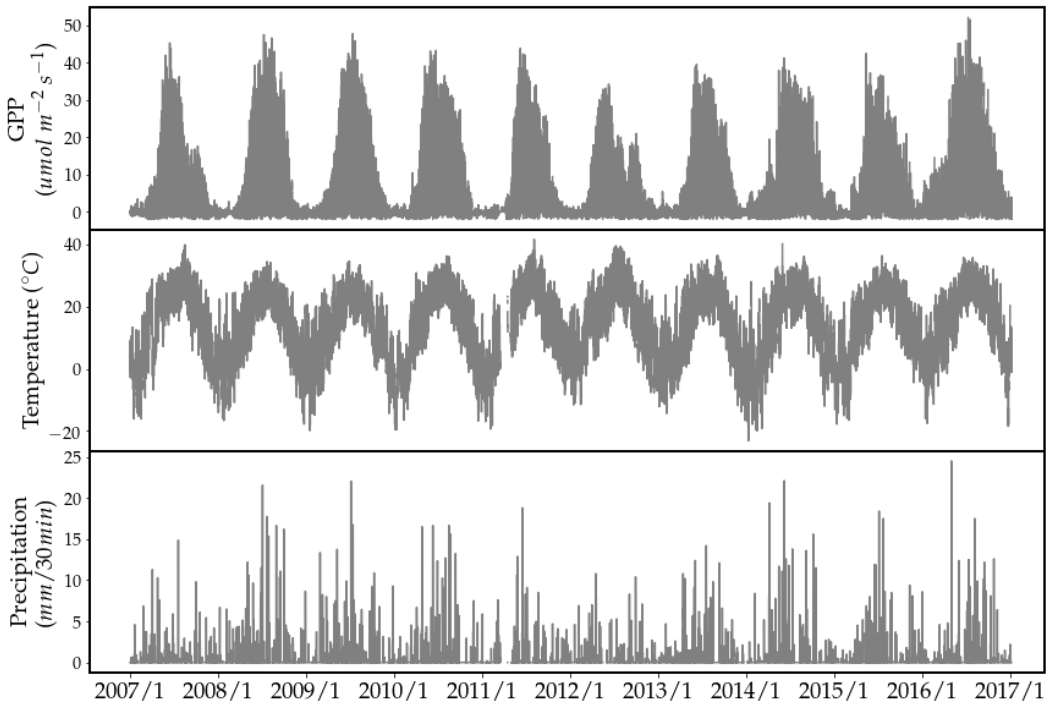

Figure 2.17: Time series of 30-min flux tower observations from Jan 2007 to Dec 2016. Ozark Site lies in a typical subtropical climate zone, with hot summer and cold winter. Plants largely relies on summer precipitation for the growth. Large interannual precipitation is consistent and robust under different stress levels.

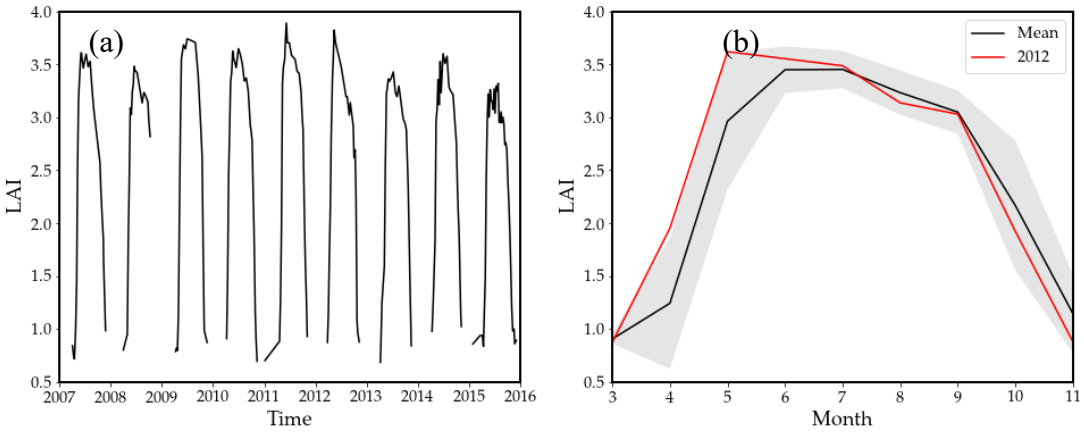

Figure 2.18: (a) Time series of monthly LAI and (b) the 2012 seasonal cycle compared to the ensemble mean (+/- 1SD) seasonal cycle LAI data from years 2007 through 2015 are summarized. On each day that observations were made the following was done: 1) LAI measured non-destructively on 5 transects, each with 5 plots except for one transect with 4 (24 plots total); 2) the mean LAI for each transect based on 4 sub-canopy measurements on each plot; 3) transect means were averaged to obtain a grand mean for the forest; 4) monthly mean LAI was then calculated.

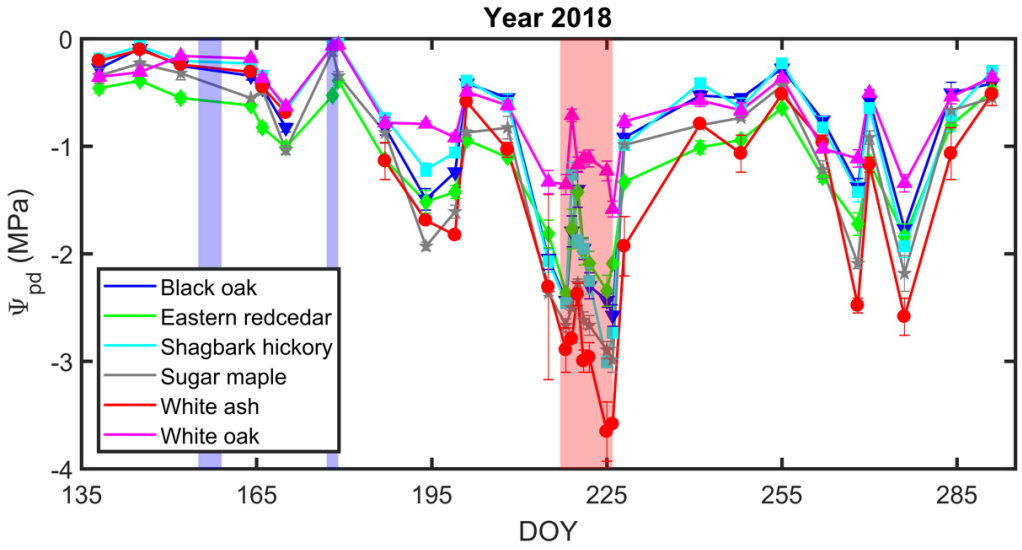

Figure 2.19: Predawn leaf water potential of different species measured at the US-MOz during the growing season in 2018.

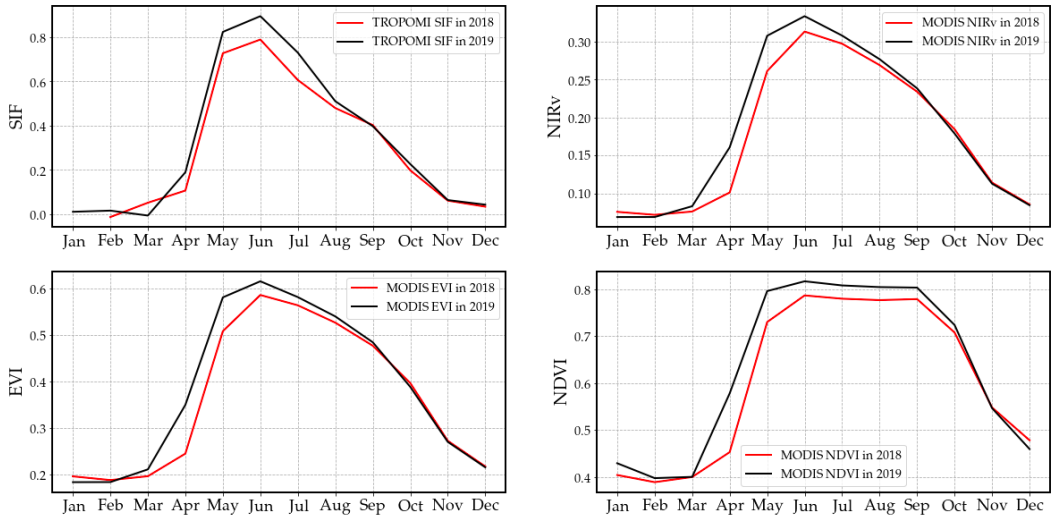

Figure 2.20: Monthly averaged TROPOMI SIF in 2018 and 2019. Larger reduction in SIF than MODIS VIs from peak to late growing season in 2018 is observed.

Table 2-1: RMSE and R2 between flux tower GPP and SIF, MODIS GPP, NDVI, EVI, NIRv, fPAR at the inter-annual scale corresponding to Figure 2. PAR is also included here for comparison.

a) At native fine resolution

	SIF (mW m^{-2} sr^{-1} nm^{-1})	**NDVI**	**EVI**	**NIRv**	**fPAR**	**MODIS GPP (umol m^{-2} s^{-1})**	**Tower PAR (umol m^{-2} s^{-1})**
RMSE	0.11	0.05	0.12	0.13	0.17	0.10	0.17
R^2	0.62	0.93	0.56	0.49	0.16	0.72	0.15

b) At coarser resolution of 0.25°

	SIF (mW m^{-2} sr^{-1} nm^{-1})	**NDVI**	**EVI**	**NIRv**	**fPAR**	**MODIS GPP (umol m^{-2} s^{-1})**	**Tower PAR (umol m^{-2} s^{-1})**
RMSE	0.12	0.05	0.07	0.07	0.10	0.09	0.17
R^2	0.55	0.91	0.86	0.85	0.69	0.77	0.15

Table 2-2: Raw data of flux tower GPP, SIF, MODIS GPP, NDVI, EVI, NIRv, fPAR used in Figure 2.2. PAR is also included here for comparison. These variables were computed as the average during JJA in the individual year.

a) At native fine resolution

	Tower GPP (umol m^{-2} s^{-1})	**SIF (mW m^{-2} sr^{-1} nm^{-1})**	**MODIS GPP (umol m^{-2} s^{-1})**	**NDVI**	**EVI**	**NIRv**	**fPAR**	**Tower PAR (umol m^{-2} s^{-1})**
2007	7.06	1.16	6.43	0.84	0.49	0.33	0.86	521.03
2008	9.47	1.29	7.90	0.85	0.48	0.32	0.83	503.60
2009	9.36	1.21	7.80	0.86	0.49	0.33	0.84	485.62
2010	8.69	1.17	7.97	0.85	0.47	0.31	0.84	519.99
2011	8.72	1.20	5.96	0.85	0.48	0.32	0.87	532.72
2012	3.16	0.86	3.14	0.78	0.44	0.29	0.81	539.13
2013	8.08	1.14	8.16	0.85	0.48	0.32	0.83	499.61
2014	7.54	1.04	7.05	0.85	0.49	0.33	0.80	486.01
2015	7.67	0.99	8.19	0.84	0.45	0.29	0.81	451.79
2016	9.04	1.03	8.78	0.85	0.48	0.32	0.83	492.67

b) At coarse resolution of 0.25°

	Tower GPP (umol m^{-2} s^{-1})	SIF (mW m^{-2} sr^{-1} nm^{-1})	MODIS GPP (umol m^{-2} s^{-1})	NDVI	EVI	NIRv	fPAR	Tower PAR (umol m^{-2} s^{-1})
2007	7.06	1.14	5.61	0.73	0.53	0.27	0.66	521.03
2008	9.47	1.08	6.46	0.75	0.54	0.28	0.66	503.60
2009	9.36	1.17	6.49	0.77	0.56	0.29	0.66	485.62
2010	8.69	1.23	6.65	0.76	0.55	0.28	0.68	519.99
2011	8.72	1.16	5.29	0.74	0.53	0.27	0.69	532.72
2012	3.16	0.81	3.17	0.65	0.45	0.22	0.59	539.13
2013	8.08	1.11	6.62	0.75	0.55	0.29	0.65	499.61
2014	7.54	1.04	5.74	0.75	0.55	0.29	0.63	486.01
2015	7.67	0.88	6.58	0.75	0.52	0.27	0.62	451.79
2016	9.04	1.09	6.64	0.76	0.55	0.29	0.68	492.67

Table 2-3: RMSE and R^2 between flux tower GPP and SIF, NDVI, EVI, NIRv, fPAR, MODIS GPP, NDVI*PAR, EVI*PAR, NIRv*PAR and fPAR *PAR at the seasonal scale corresponding to Figure 2.5. PAR is also included here for comparison.

a) At native fine resolution

	SIF (mW m^{-2} sr^{-1} nm^{-1})	**NDVI**	**EVI**	**NIRv**	**fPAR**	**MODIS GPP (umol m^{-2} s^{-1})**
RMSE	0.07	0.13	0.05	0.04	0.13	0.11
R^2	0.96	0.88	0.98	0.99	0.88	0.91

	Tower PAR (umol m^{-2} s^{-1})	**NDVI*PPFD**	**EVI*PAR**	**NIRv*PAR**	**fPAR*PAR**
RMSE	0.14	0.07	0.04	0.03	0.07
R^2	0.85	0.97	0.99	0.99	0.96

b) At coarse resolution of 0.25°

	SIF (mW m^{-2} sr^{-1} nm^{-1})	NDVI	EVI	NIRv	fPAR	MODIS GPP (umol m^{-2} s^{-1})
RMSE	0.08	0.17	0.10	0.08	0.15	0.11
R^2	0.96	0.79	0.93	0.95	0.84	0.92

	Tower PAR (umol m^{-2} s^{-1})	NDVI*PAR	EVI*PAR	NIRv*PAR	fPAR*PAR
RMSE	0.14	0.08	0.06	0.05	0.08
R^2	0.85	0.95	0.97	0.98	0.95

C h a p t e r 3

FROM THE GROUND TO SPACE: USING SOLAR-INDUCED CHLOROPHYLL FLUORESCENCE (SIF) TO ESTIMATE CROP PRODUCTIVITY

He, L., Magney, T., Dutta, D., Yin, Y., Köhler, P., Grossmann, K., Stutz, J., Dold, C., Hatfield, J., Guan, K. and Peng, B., 2020. From the ground to space: Using solar-induced chlorophyll fluorescence to estimate crop productivity. *Geophysical Research Letters*, *47*(7), p.e2020GL087474. DOI: https://doi.org/10.1029/2020GL087474

H.L participated in project conceptualization, literature collection, data analysis, and manuscript writing. All co-authors contributed to the writing of the paper.

3.1 Abstract

Timely and accurate monitoring of crops is essential for food security. Here we examine how well solar-induced chlorophyll fluorescence (SIF) can inform crop productivity across the United States. Based on tower-level observations and process-based modeling, we find highly linear GPP:SIF relationships for C4 crops, while C3 crops show some saturation of GPP at high light when SIF continues to increase. C4 crops yield higher GPP:SIF ratios (30~50%) primarily because SIF is most sensitive to the light reactions (does not account for photorespiration). Scaling to the satellite, we compare SIF from the TROPOspheric Monitoring Instrument (TROPOMI) against tower-derived GPP and county-level crop statistics. Temporally, TROPOMI SIF strongly agrees with GPP observations upscaled across a corn and soybean dominated cropland (R^2 = 0.89). Spatially, county-level TROPOMI SIF correlates with crop productivity (R^2 = 0.72; 0.86 when accounting for planted area and C3/C4 contributions), highlighting the potential of SIF for reliable crop monitoring.

3.2 Introduction

Cropping systems not only provide sustenance for the world's human population and livestock but they also have a major impact on both local climate (Mueller et al., 2016) and the carbon cycle (Peters et al., 2007). Hence, large-scale crop monitoring and yield forecasting is necessary to support food security, and to quantify the overall impact on the climate and carbon cycle.

Crop productivity is reliant upon its ability to convert light energy into sugar via photosynthesis. Therefore, a reliable measure of gross primary production (GPP) is a key step towards crop monitoring. Satellite observations have the potential to provide GPP estimates from regional to global scales (Running et al., 2004; Zhao et al., 2005; Turner et al., 2006; Yuan et al., 2007; Ryu et al., 2019). Most remote-sensing based GPP estimates use spectral information in the visible and near infrared (NIR) regions that are related to greenness (Huete et al., 2002) or thermal (Anderson et al., 2012), and microwave bands, which are sensitive to vegetation/soil water content (Konings et al., 2016; Guan et al., 2017). In most cases, predicting GPP largely depends on empirical estimates of light use efficiency (LUE, efficiency with which absorbed light is used for CO_2 fixation), which is highly uncertain.

The emission of red and far-red light from excited chlorophyll-a molecules, denoted solar-induced chlorophyll fluorescence (SIF), offers a physiologically based GPP proxy, potentially avoiding the need for LUE parameterizations. In fact, an empirical linear scaling between SIF and GPP across various vegetation types under different environmental conditions has already been shown in many studies (Frankenberg et al., 2011; Guanter et al., 2014; Guan et al., 2016; Zhang et al., 2016; Verma et al., 2017; Wood et al., 2017; Li et al., 2018; Sun et al., 2018; Smith et al., 2018; Song et al., 2018; Zuromski et al., 2018; Magney et al., 2019a), revealing the potential of SIF to monitor GPP across all spatial scales.

The rationale of linking SIF with crop productivity can be shown using the following equations (Guan et al., 2016):

$$\sum NPP = \sum GPP - \sum Ra = CUE \cdot \sum GPP \quad (1)$$

$$Crop\ Productivity = \sum NPP \cdot fAG \cdot HI \quad (2)$$

$$\sum SIF \sim \sum GPP \quad (3)$$

where $\sum$ means the temporal integration of the variable over the growth period. NPP refers to net primary production, calculated as GPP minus the amount of carbon consumed by plants by autotrophic respiration (Ra), which includes maintenance and growth respiration. During the growing period, we can assume that growth respiration dominates the Ra term, which in theory should scale with GPP. CUE is the carbon use efficiency, which varies across species and environmental conditions (Amthor, 1989; DeLUCIA et al., 2007). fAG is the fraction of the aboveground to total biomass and HI is the harvest index − the mass of harvested grain divided by total aboveground biomass. Both fAG and HI are related to the crop type and environmental conditions but are usually treated as constant parameters for individual crops. These equations exhibit the underlying relationship among SIF, NPP, GPP and crop productivity and show that even if GPP and SIF are perfectly correlated, variations in CUE, fAG and HI can still impact the relationship of SIF to crop productivity.

Some efforts have been made to explore the potential of satellite SIF in estimating crop productivity. Guanter et al. (2014) found that the highest SIF values observed from the Global Ozone Monitoring Experiment-2 (GOME-2) satellite are associated with the Corn Belt in the United States (US) Midwest. In addition, SIF captured the photosynthetic activity over highly productive croplands, while traditional VIs show saturation effects in dense canopies. In some cropping systems, however, the use of NIRv (Badgeley et al., 2017) might track productivity quite

well (Dechant et al., 2019), but may be less sensitive to rapid changes in PSII operating efficiency. Thus, SIF has its own unique advantage to track crop photosynthesis over vegetation indices (VIs). Guan et al. (2016) used GOME-2 SIF as an approximation of photosynthetic electron transport rate (ETR) to derive GPP and crop yield, which has shown a significant improvement in county-level crop yield estimates. Zhang et al. (2014) proposed the utility of space-based SIF measurements, combined with a process-based model, to estimate the photosynthetic capacity over six crop flux sites in the US. However, direct comparisons of SIF and crop yields have been restricted by the coarse spatial resolution of available satellite SIF measurements. In the US, the average area of counties that are predominantly agricultural is ~1700 km^2, with the smallest one ~430 km^2. A single GOME-2 footprint (80 km x 40 km) thus covers several counties, making it challenging to compare SIF with the benchmark of county-level annual crop statistics from the National Agricultural Statistics Service (NASS) of the US Department of Agriculture (USDA). Fine spatial resolution (1.3 km x 2.25 km) SIF data from the Orbiting Carbon Observatory (OCO-2) has been available since September 2014 (Frankenberg et al., 2014, Sun et al., 2018), but does not provide contiguous spatial coverage. To fill this knowledge gap, we leverage SIF inferred from measurements of the TROPOspheric Monitoring Instrument (TROPOMI), with an unprecedented spatial resolution (up to 7 km × 3.5 km) and near-global daily coverage (Köhler et al., 2018), which allows us to achieve robust SIF averages for individual counties.

A thorough understanding of the relationship between SIF and GPP, and how it might vary depending on photosynthetic pathway (C3, C4) is important to achieve accurate estimates of crop photosynthesis from SIF. Some studies found stronger relationships between SIF and absorbed light by chlorophyll, than GPP (Yang et al., 2018; Li et al., 2020). As SIF emanates from the light reactions of photosynthesis, it is expected to be more closely related to the electron transport rate in photosystem II than to GPP (Frankenberg et al. 2011; Porcar-Castell et al.,

2014; Gu et al., 2019). Thus, the GPP:SIF ratio should vary between C3 and C4 photosynthetic pathways (Porcar-Castell et al., 2014; Guan et al., 2016; Gu et al., 2019), because it is important to know how efficiently electrons from the light reactions are used for carbon fixation. This is fundamentally different for C3 and C4 plants, with the latter inhibiting photorespiration, which generally leads to a higher and less variable efficiency. Typical C3 crops include soybeans, wheat, barley, oats and rice, whereas typical C4 crops include corn, sugarcane and sorghum. Several recent studies point to a different GPP:SIF ratio for C3 and C4 plants (Liu et al., 2017; Wood et al., 2017; Liu et al., 2017; Li et al., 2018); however, there is still limited understanding of how exactly these mechanisms influence the GPP:SIF relationship across time and space. To fill this knowledge gap, we include both field measurements and a biophysical model to explain the discrepancies of GPP:SIF of C3 and C4 crops, and use this to inform our interpretation of the satellite data.

In this paper, the objectives are to (i) compare observed and modeled GPP:SIF relationships for C3 and C4 crops at site level, (ii) examine whether aggregated TROPOMI SIF at local (10 km) scales can represent the seasonality of GPP observations over homogenous croplands, and (iii) evaluate how well aggregated TROPOMI SIF at the county level can be used to estimate crop productivity and NPP in the US.

3.3 Data and Methods

3.3.1 Site-level SIF and GPP observations

3.3.1.1 Eddy-covariance (EC) GPP

In this paper, EC data were collected at long-term and well characterized USDA agricultural flux towers within C3 (soybeans, *Glycine max* L. Merr.) and C4 (corn, *Zea mays* L.) cropping systems in central Iowa. Specific sites are Brooks field (41.974536°N, -93.693711°W) and Coles field (42.488414°N, -93.522582°W) for the PhotoSpec comparison in 2017 as well as two nearby towers at Coles field

covering soy (42.488414°N, -93.522582°W) and corn (42.481677°N, -93.523521°W) for the TROPOMI comparison in 2018. These farming systems are typical for those in the Upper Midwest corn belt (more details in Dold et al., 2017, 2019). Data were excluded under unfavorable weather conditions (e.g., rainfall, low wind turbulence and high humidity) (Baker el al., 2015), screened for outliers (Dold et al., 2017), and gap-filled. Turbulent CO_2 fluxes were computed using the EC method (Burba, 2013), and then net ecosystem exchange (NEE) was partitioned into GPP and ecosystem respiration (Re). Note that we do not have overlapping datasets of TROPOMI, PhotoSpec and EC systems, thus the EC to PhotoSpec comparison is limited to 2017 and the EC to TROPOMI comparison to 2018.

3.3.1.2 PhotoSpec SIF

We installed two PhotoSpec instruments in a soybean (Brooks field, 41.974203°N, -93.695839°W) and corn field (Coles field, 42.48655°N, -93.52641°W) in central Iowa following planting in late May 2017 and measured SIF until harvest in September 2017 (Magney et al., 2019b). PhotoSpec consists of a 2D scanning telescope to guide reflected radiances into a set of high resolution spectrometers (Grossmann et al., 2018) to infer SIF using the solar Fraunhofer line in-filling technique, similar to all current satellite retrievals. The scanning telescope was placed atop a 7-m tower and we calculate a "canopy average" of all viewing angles at an hourly time step to match the temporal resolution of flux tower data (following Magney et al., 2019b). Because the scanning telescope revisits every measuring point within an hour, this canopy average is more representative of a hemispherical sensor with a footprint of a few meters around the tower (an average of all viewing directions). Due to the narrow field-of-view of PhotoSpec, we can isolate between vegetation and non-vegetation signals, where we have determined NDVI at 0.6 to be sufficient for the definition of the peak growing season − when our analysis was conducted (as can be seen in **Supplementary Figure 3.5**, where the rows can be seen early in the season). Notably, while the escape ratio and angular dependencies

are an important consideration for tower-based SIF measurements (Zeng et al., 2019), this makes little difference in our study for the canopy structure is relatively stable during the peaking growing season. More details on PhotoSpec retrievals and instrument specifications can be found in Grossmann et al. (2018) and Magney et al. (2019b).

3.3.2 TROPOMI SIF

On October 13, 2017, the TROPOMI instrument onboard the European Sentinel-5 Precursor satellite was launched. TROPOMI is a multi-band push-broom imaging grating spectrometer, which also covers the far-red part of the SIF emission spectrum (Köhler et al. 2018). The SIF retrieval window ranges from 743 to 758 nm, a subset of TROPOMI's band 6 (725-775 nm). A daily correction factor is applied to convert instantaneous SIF to a daily average (following Frankenberg et al., 2011).

For the comparison with GPP observations, we extracted TROPOMI SIF within +/-10 km of two nearby flux towers, and applied a +/-4 day moving average, sampled every 4 days. The agricultural cover is quite homogeneous within +/-10 km, with ~58% corn and ~30% soybeans derived from the 30-meter cropland data layer (CDL; https://nassgeodata.gmu.edu/CropScape/) (**Supplementary Figure 3.6**). Since TROPOMI SIF represents an average of all crops within the sampling area, we assume a ⅔:⅓ weighted average of flux tower GPP for corn and soy, respectively.

For the comparison with county-level crop statistics reported by USDA NASS, we aggregated SIF at the county scale, yielding on average 700 TROPOMI soundings per month for counties with > 45% planted areas. The planted ratio of each county is shown in **Supplementary Figure 3.7**.

3.3.3 Crop statistics from USDA NASS

We obtained the county-level total crop production and planted area for individual crop types from the USDA NASS Quick Stats Database (quickstats.nass.usda.gov). In most studies, crop yield refers to the amount of grain per unit of harvested land area per crop (Fischer, 2014). Therefore, it is associated with accumulated NPP weighted by aboveground biomass during the crop growth season (Lobell et al., 2002). Thus, NPP acts as a bridge to link crop statistics with satellite observations (Smith et al., 2014).

We used crop production and acreage for individual crop types to calculate county-level crop productivity as $\frac{total\ crop\ production}{total\ county\ area}$. From a physical perspective, this definition is more comparable with the county-level aggregated satellite TROPOMI SIF, since satellite SIF records represent the entire footprint, regardless of land type.

Following Lobell et al. (2002), Guan et al. (2016) and Guan et al. (2017), we converted crop productivity to NPP at the county level:

$$NPP(\frac{gC}{m^2}) = \sum_{i=1}^{N} \frac{P_i \cdot MRP_i \cdot (1-MC_i) \cdot 0.45\frac{gC}{C}}{HI_i \cdot fAG_i} / total\ county\ area \quad (4)$$

$$= \sum_{i=1}^{N} \frac{Y_i \cdot MRP_i \cdot (1-MC_i) \cdot 0.45\frac{gC}{C}}{HI_i \cdot fAG_i} \quad (5)$$

where i represents the crop type (dominated by corn and soybean here), P the reported crop production, MRP the mass per unit of report production, MC the moisture content, and Y the crop productivity based on the definition given before. The list of fAG and HI of common crops can be found in Lobell et al. (2002) and Guan et al. (2016) (see **Supplementary Table S1**).

3.3.4 Site-level GPP and SIF modeling

We use the Soil Canopy Observation, Photochemistry and Energy fluxes (SCOPE) model, a 1D integrated radiative transfer and energy balance model, to simulate photosynthesis, fluorescence, the surface energy balance and reflectance/emission

spectra at leaf and canopy scales (van der Tol et al., 2009). This mechanistic model helps to understand the connection between SIF, GPP, quantum yield of photosystem II (PSII) ($PSII_{yield}$) and actual electron transport rate (Ja) under different environmental conditions for C3 and C4 plants. We modeled GPP and SIF at nadir viewing using SCOPE at two flux tower sites with concurrent PhotoSpec and GPP observations. We used available meteorological data from the flux tower (i.e., incoming shortwave and longwave radiation, air temperature, ambient atmospheric pressure, vapor pressure and wind speed), and optimized canopy parameters (LAI, V_{CMAX}, Chl content) via a Bayesian inversion system (Dutta et al., 2019).

3.4 Results and Discussion

3.4.1 Observed and modeled GPP:SIF for C3 and C4 at the site level

We compared ground-based PhotoSpec SIF measurements throughout the peak growing season in both C3 (soybean) and C4 (corn) crops with flux tower GPP as well as PAR (**Figure 3.1(a), (b) and (c)**). The peak growing season is defined as DOY 210-235 for soybean and DOY 175-190 for corn. Here, hourly SIF is linearly correlated with PAR for soybean (R^2=0.87) and corn (R^2=0.84), with negligible differences in the SIF:PAR ratio (**Figure 3.1(a)**). This indicates that during the peak growing season in both agricultural sites, SIF is mostly driven by incident radiation and exhibits negligible differences due to the fluorescence yield. To first order, we expect SIF to be tightly related to PAR in systems where there is little stress (i.e. low variations in SIF_{yield}), which can be expected in highly efficient agricultural areas. Little apparent stress is also indicated by the canopy-scale light response curve of GPP vs. PAR (**Figure 3.1(b)**), with a near-linear relationship for corn and some saturation effects for soybean at higher light levels. Consequently, we found that hourly averaged SIF is strongly correlated with GPP in both soybean (R^2=0.51) and corn (R^2=0.64), however, with a larger GPP:SIF ratio observed for corn - leading to roughly a 30% higher GPP per unit SIF in corn at higher light levels

(**Figure 3.1(c)**). This implies that the light-use efficiency of corn is higher than that of soybean, due to the evolved mechanism to concentrate CO_2 at the rubisco site and thereby minimize photorespiration as well as the occurrence of carboxylation limited photosynthetic rates in C4 plants.

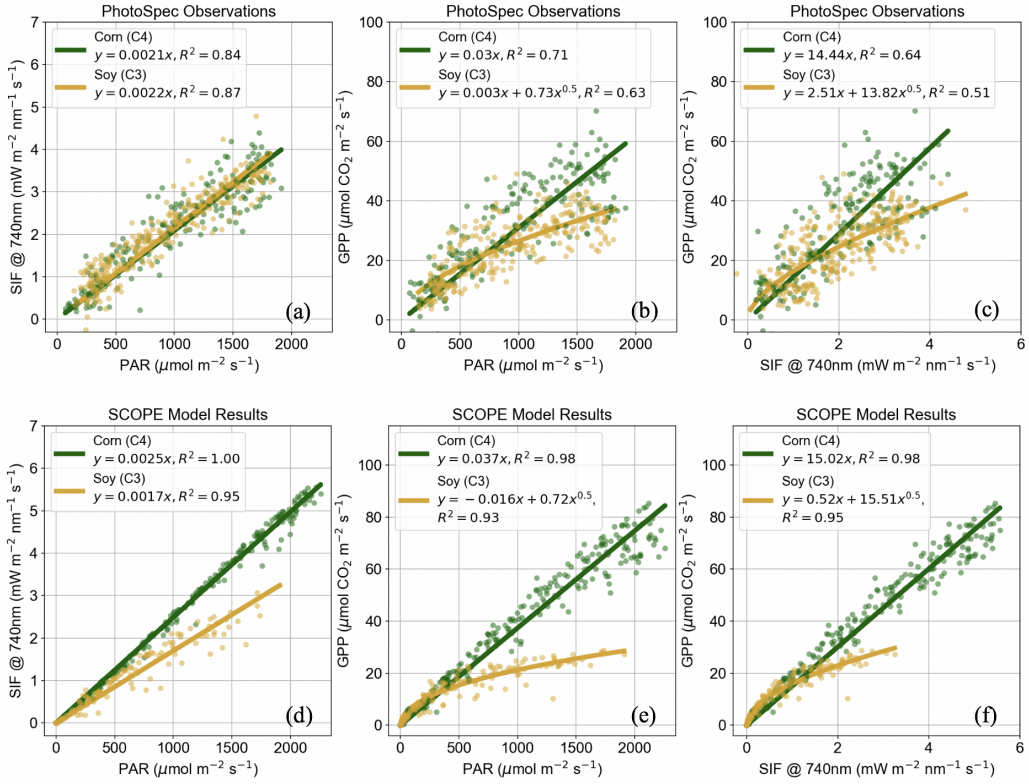

Figure 3.1: Canopy-scale relationships in the peak growing season (DOY 175-190 for corn and 210-235 for soybean) based on hourly averaged data from PhotoSpec for soybean (gold) and corn (green): (a) SIF:PAR, (b) GPP:PAR, (c) GPP:SIF for both soybeans and corn. SCOPE modeled relationships are for the same time-periods and based on hourly averaged data for soybean and corn: (d) SIF:PAR, (e) GPP:PAR and (f) GPP:SIF. The results of Photospec-measured relative SIF, which is normalized by incoming NIR reflected radiance to reduce the effects of structural and bidirectional reflectance of the signal (Yang et al., 2018), is shown in **Figure 3.8**.

To test whether the GPP:SIF relationship observed in the field is consistent with what is expected from biophysical models, we compared the simulated far-red SIF at 740nm and GPP against PAR using SCOPE (**Figure 3.1(d), (e) and (f)**). For both

soybean and corn, the PAR:SIF relationship is highly linear, yet with slightly different slopes (**Figure 3.1(d)**). In the light response curve for GPP (**Figure 3.1(e)**), soybean GPP saturates at higher light levels, when the rate of photosynthesis is limited by the carboxylation rate. Corn remains highly linear even at high light levels, resulting in a more linear GPP:SIF relationship. Apart from the high SIF values modeled for corn leading to diverging SIF:PAR relationships between corn and soy, these simulations are broadly consistent with our observational evidence. We found that the high SIF to PAR slope for C4 is likely related to how SCOPE computes the $PSII_{yield}$ for C4 plants, which are in the range of a maximum SIF_{yield} given by the $PSII_{yield}$:SIF_{yield} parameterization (van der Tol et al., 2014). Our canopy spectrometer data supports this, as we observe similar SIF yields for C3 and C4 crops. The overly high modeled SIF values as well as the inconsistency with our field measurements point to an overestimation in the SIF_{yield} for C4 plants in the SCOPE model. Apart from that, the measurement and modeling perspective agree very well.

Both our observations at the site level as well as the SCOPE modeling results showed that the GPP:SIF relationship is more linear for C4 than C3 plants. It is well established that SIF is a better proxy for the actual electron transport rate (Ja) than for GPP, which requires us to separate C3 and C4 photosynthetic mechanisms if we use Ja to estimate GPP. The explicit relationships among the four variables, SIF, Ja, $PSII_{yield}$ and SIF_{yield} can be described as follows (Gu et al., 2019; Porcar-Castell et al., 2014):

$$Ja = \Phi_{PSII} \cdot \beta \cdot APAR_{green} \qquad (6)$$

$$SIF = \Phi_{SIF} \cdot \beta \cdot \varepsilon \cdot APAR_{green} \qquad (7)$$

where Φ_{PSII} and Φ_{SIF} is the quantum yield of PSII and SIF, respectively; $APAR_{green}$ is absorbed photosynthetically active radiation by green elements (Gitelson & Gamon, 2015); β is the fraction of $APAR_{green}$ allocated to PSII; ε is

the escape probability of fluorescence from the canopy (Zeng et al., 2019). Here, we neglect variations in the canopy structure and thus ε as we focus on the peak growing season, where we observe little structural change (**Supplementary Figure 3.5**).

Combing (6) and (7) we obtain:

$$\frac{Ja}{SIF} \sim \frac{\Phi_{PSII}}{\Phi_{SIF}} \qquad (8)$$

which demonstrates that Ja:SIF is determined by Φ_{PSII} and Φ_{SIF}, which is dependent on environmental conditions (e.g., light intensity, drought and heat stress). The less Φ_{PSII} is varying − as is often the case for highly efficient crops − the more constant and linear the SIF to Ja relationship is. Leaf-level measurements have been used to derive the empirical relationship between Φ_{PSII} and Φ_{SIF} (Lee et al., 2013; van der Tol et al., 2014). For example, Flexas et al. (2002) found that for under stress, Φ_{PSII} and Φ_{SIF} are usually positively correlated if substantial non-photochemical quenching (NPQ) exists. At the canopy level, Φ_{PSII} and Φ_{SIF} are mostly positively correlated at the seasonal scale (Song et al., 2018; Verma et al., 2017; Zhang et al., 2016; Yang et al., 2015; Porcar-Castell et al., 2014), mainly due to averaging effects of the canopy, which integrates over a variety of Φ_{PSII} and Φ_{SIF} values for all leaves (similar to our PhotoSpec observations).

The linkage between GPP and Ja depends on the photosynthetic pathway (Farquhar et al., 1980; Collatz et al., 1992):

$$GPP = \frac{Ja \cdot (C_c - \Gamma^*)}{4C_c + 8\Gamma^*} \text{ for C3} \qquad (9)$$

$$GPP \approx \frac{Ja}{6} \text{ for C4} \qquad (10)$$

where C_c is chloroplast CO_2 partial pressure and Γ^* is chloroplastic photorespiratory CO_2 compensation point. Comparing (9) and (10), for C3 plants,

an additional nonlinearity in GPP:Ja arises, which is attributed to the varying fraction of electrons used in photorespiration. Due to the lack of photorespiration in C4 plants, the relationship between Ja and GPP is strictly linear. For the same reason, the conversion factor from Ja to GPP is mostly higher for C4 than C3 plants, as about ⅓ of the electron transport rate is wasted in photorespiration in C3 plants. Since SIF is mostly proportional to Ja, (9) and (10) directly explain the more linear behavior and steeper GPP:SIF slope for C4 versus C3 plants. It should be noted that at high C_c values, the slope for C3 plants can be steeper (e.g., at low light levels). In general, variations in the GPP:SIF scaling at the leaf scale can thus be attributed to two different effects: i) variations in the ratio of Φ_{PSII} and Φ_{SIF} in the light reactions as well as ii) the scaling from Ja to GPP, which depends on the photosynthetic pathway.

3.4.2 Consistent seasonal cycle seen by TROPOMI SIF and field GPP measurements

Here, we evaluate how well TROPOMI SIF represents local GPP patterns in a corn/soybean dominated area in Iowa during the growing season of 2018. The seasonal cycle of footprint-level TROPOMI SIF and flux tower GPP at both soybean and corn sites is shown in **Figure 3.2**. Corn GPP increases more rapidly and reaches its maximum of ~25 gC/m^2/day around July 10, while soybean GPP approaches maximum of ~15g C/m^2/day more gradually, around July 20. As mentioned in **Section 3.3**, TROPOMI SIF represents an average of all crops in the area, for which we calculate the weighted average of GPP assuming a ⅔:⅓ contribution of corn and soy, respectively. There is strong agreement between TROPOMI SIF and the weighted area-averaged GPP estimate (R^2=0.89) (**Figure 3.2**), motivating our use of TROPOMI SIF in large-scale crop monitoring. In particular, the GPP:SIF ratio at both satellite and flux tower scales is consistent – around 12 (gC/m^2/d)/(W/m^2/μm/sr). While there is close correspondence between SIF and GPP during senescence, there is a small mismatch early in the growing

season, which could be explained by 1) fewer TROPOMI observations due to increased cloud cover during this time of year (see **Supplementary Figure 3.9**), 2) different planting and emergence dates within the satellite footprint and 3) potentially higher SIF escape probabilities at the beginning of the season as the canopy is more open at that stage. We also did not find any apparent viewing angle dependent behavior in the TROPOMI datasets (see **Supplementary Figure 3.9**). Importantly, it should be noted that this is the first time that satellite-based SIF can be compared with GPP at weekly temporal resolution and ~10km spatial scales – a significant improvement over previous satellites providing monthly data at 0.5-degree resolution.

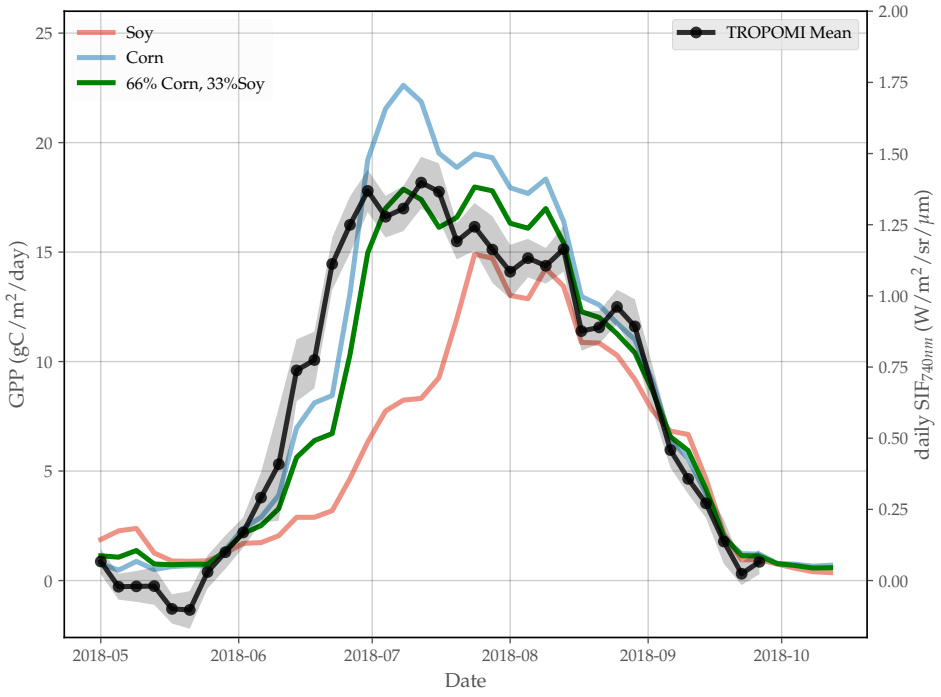

Figure 3.2: The 2018 seasonal cycle of flux tower GPP for soybeans and corn in Iowa and TROPOMI SIF (within +/-0.1° latitude and longitude, shaded area showing 2sigma uncertainty range). A moving average of +/- 4 days and 4 day sampling interval is applied to both datasets. The upscaled GPP (green) is approximated by a weighted average of ⅔ corn and ⅓ soy contributions, determined by computing crop fraction within +/-0.1° (in total, 88% of this area is covered by either corn and soybean).

Tower-level SIF was not included in this comparison as there was no temporal overlap between tower SIF data and TROPOMI in 2018. In recent years, more ground-based SIF measurements have become available (Yang et al., 2015; Miao et al., 2018; Grossmann et al., 2018; Yang et al., 2018; Dechant et al. 2019; Du et al., 2019; Magney et al., 2019b; Zhang et al., 2019; Li et al., 2020), which will help disentangle various factors (e.g., view angles, canopy structure and overpass times) that might also impact the SIF to GPP relationship.

3.4.3 Spatial correlation between county-level TROPOMI SIF and crop productivity

Here we focus on the county level in the US to evaluate the capability of using TROPOMI SIF to predict crop productivity. We define the growth period for each county as the period in which SIF exceeds 10% of its peak value within the year. The spatial pattern of crop productivity and the average growing-season TROPOMI SIF of 2018 is shown in **Figure 3.3(a) and (c)**. The SIF map closely matches the NASS yield-based NPP pattern in the Corn Belt, the most dominant region of corn/soybean staple crop production in the US. For counties with > 45% planted areas, we found that crop productivity and converted NPP are both highly correlated with SIF, with R^2=0.72 and R^2=0.71, respectively (**Figure 3.3(b) and (d)**). As discussed previously, crop productivity:SIF and NPP:SIF relationships are not identical for C3 and C4 crops. At the same level of SIF, higher crop productivity and NPP are observed for counties with more C4, which is expected based on the ground-based measurements and modeling results (**Sections 3.4.1**). In contrast to the nonlinear pattern observed for temporal variations at the site level, spatial variations in the county-level analysis are more linear. The main reason is that the non-linear pattern is only apparent at high light levels. In contrast, the spatial correlation is discussed for seasonal averages, in which the impact of high light levels is smoothed out.

In theory, crop productivity is associated with temporally integrated net photosynthesis over the growing season. Therefore, we also tested the correlation between crop productivity and the corresponding NPP against integrated SIF over the growing period. We found that the crop productivity:integrated SIF and NPP:integrated SIF correlations are still consistent and robust, yet weaker than when using the average growing season SIF (see **supplementary Figure 3.11**).

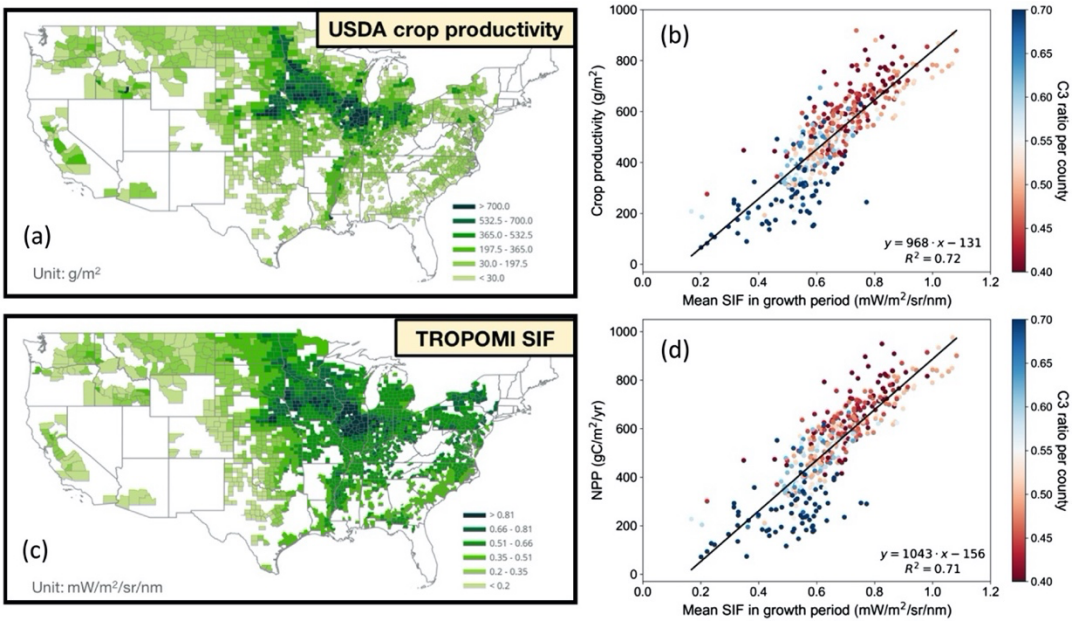

Figure 3.3: Spatial pattern of county-scale (a) crop productivity derived from USDA NASS and (c) average TROPOMI SIF during the growth period of 2018. In counties with planted area >45%, the relationship of (b) crop productivity:SIF and (d) NPP:SIF. The color scheme represents the relative fraction of C3 crops, with blue meaning more C3 and red means more C4. The maps of C3 and C4 crops distributions are shown in **Figure 3.10**. The growth period here is defined as the time when SIF exceeds 10% of Max(SIF) within a year. The results are robust with different thresholds defining the growing season (see **Figure 3.11)** and TROPOMI relative SIF (see **Figure 3.12).**

Overall, the crop productivity (NPP):SIF relationship at the county level is almost linear. This is likely due to the high efficiency of crops (generally high photosynthetic yields) as well as large contributions from C4 crops, where the relationship is more linear. In addition, crop productivity (NPP):SIF ratio is 25~50% higher for C4 than C3, which is consistent with ground-based measurements and

modeling outputs in **Sections 3.2**. Including results from field measurements (PhotoSpec) and a biophysical model (SCOPE) gives us more confidence in explaining the discrepancies between C3 and C4 crops and the associated GPP:SIF relationship. A more detailed understanding of the GPP:SIF slope for different crops at different environmental conditions based on field-level measurements would help us to better estimate NPP:SIF for a variety of crops, and ultimately improve the prediction of crop productivity at the global scale, where ground based measurements are lacking.

3.4.4 Improving the productivity prediction performance using additional information

Although crop productivity can be estimated with SIF observations alone, we can further improve the performance by adding two other explanatory variables, which are easily accessible: planted area fraction per county ($Crop_{fraction}$) and fraction of C3 plants per county ($C3_{ratio}$). The SIF signal from crops will be dampened if the planted area fraction is low and a correction factor should be considered between C4 and C3, since higher productivity is expected for C4 at the same level of SIF. Here, we fit the two multiple linear regression models for crop productivity based on (i) SIF and $Crop_{fraction}$ (ii) SIF, $Crop_{fraction}$ and $C3_{ratio}$, (**Figure 3.4**). With the added information of $Crop_{fraction}$, R^2 improved from 0.72 to 0.79, and adding the $C3_{ratio}$, R^2 improved to 0.86 (**Figure 3.3 and 3.4**), which also converges into a more normal distribution of the residuals for C3 and C4 dominated counties around the line of best fit. This behavior is consistent with our field-level measurements and modeling, giving us mechanistic confidence in such an approach.

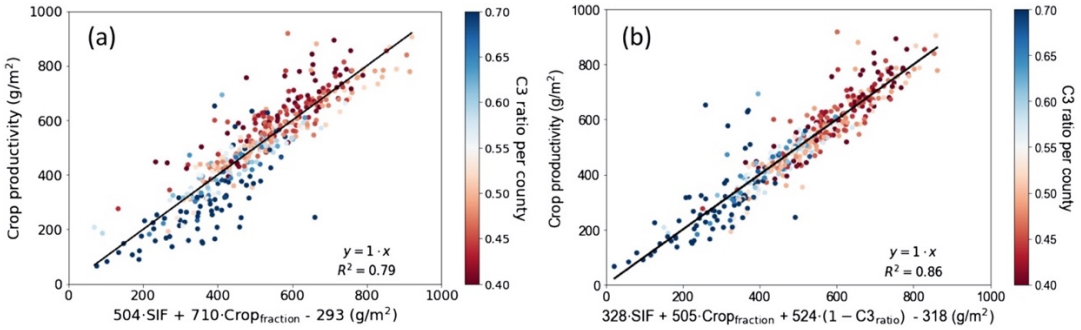

Figure 3.4: The relationships between true crop productivity and predicted crop productivity using multiple linear regression based on variables (a) SIF and crop fraction per county (b) SIF, crop fraction and relative C3 ratio per county.

It should be noted that we currently use several assumptions and do not use any model information for this upscaling approach. For instance, we assume that respiration scales with GPP, which results in a linear scaling of GPP to NPP. Notably, other growing season environmental conditions (temperature, VPD, soil moisture) as well as canopy structure and associated variations in the escape probability of SIF could have an impact on our interpretation of the SIF signal. Theoretically, however, SIF contains the information on environmental conditions and tracks GPP variations better than traditional reflectance-based vegetation indices (e.g., NDVI), though its response to stress is weaker than for GPP (or LUE) (Magney et al., 2017; van der Tol et al., 2014). Additionally, HI, the process of plant NPP converting to ultimate grain yield, which is also controlled by reproductive processes and environmental conditions during grain fill, is an important consideration. Despite this, it is hard to justify adding more complexity to the analysis given the already strong empirical linear relationship between crop NPP and SIF.

3.4.5 Towards finer-resolution crop productivity estimates

Our SIF-only based crop productivity proxy approach achieved robust and reliable performance over agriculture dominated counties in the US. To fully exploit the potential of this approach in other regions of the world, especially for small-scale,

diverse, and fragmented agricultural fields, high spatially and temporally resolved remote sensing datasets will be required. This is still challenging for current satellite SIF products (e.g., short record of TROPOMI, sparse spatiotemporal sampling of OCO-2 and large footprint of GOME-2). Recently, some machine-learning based long-term SIF products of high spatio-temporal resolution have been developed (e.g., CSIF, GOSIF, RSIF, SIF_{oco2}) based on satellite SIF, high-resolution spectral information, and meteorology data (Gentine et al., 2018; Yu et al., 2018; Zhang et al., 2018; Li et al., 2019; Turner et al., 2020). Future work across all scales will be needed to test the long-term performance of SIF products on the global scale, particularly as we link these measurements to photosynthesis (Ryu et al., 2019). A combination of high-resolution reflectance based remote sensing products and crop models (Lobell et al., 2015; Jin et al., 2017) have already shown great potential in fine-scale yield estimates.

3.5 Conclusions

We investigated the GPP:SIF relationship of crops from ground-based measurements and validated the biophysics with model runs for C3 and C4 crops at two field sites in the Upper Midwest corn belt of the US during the 2017 growing season. Generally, we find a linear GPP:SIF relationship except for high-light levels when GPP starts to saturate whereas SIF still increases, especially for C3 crops. This is attributed to two effects: 1) $\frac{PSII_{yield}}{SIF_{yield}}$ of crops varies less than in other ecosystems, since crops in this region rarely experienced severe stress conditions, which would lead to a strong reduction of $\frac{PSII_{yield}}{SIF_{yield}}$. Thus, the correspondence between SIF and actual electron transport rate Ja is highly linear for crops; 2) Ja:GPP varies between C3 and C4, which is determined by the number of electrons required for carboxylation. The latter consideration also results in a different GPP:SIF relationship between C3 and C4 crops, with a steeper GPP:SIF slope for C4 plants − an important consideration when using SIF as a proxy for crop

productivity. A direct comparison of satellite SIF measurements against two flux tower sites in a highly agricultural area in Iowa further supports this finding at larger spatial scales. At the county scale, we found that SIF is highly correlated with crop productivity derived from the USDA NASS database (R^2=0.72). Using ancillary information on crop-planted fraction and relative C3 crop ratio per county, we can further improve our estimate using a multiple linear regression model to R^2=0.86. Our model-free SIF-based crop productivity estimation framework appears promising and can provide insights to monitor the crop productivity globally outside the US, especially in developing agricultural countries. A validation approach against well documented productivity estimates in the US represented a necessary proof of concept before applying the method to less well monitored agricultural areas.

3.6 Acknowledgements

Part of this research was funded by the NASA Carbon Cycle Science program (grant NNX17AE14G). L.H. thanks the Resnick Sustainability Institute at Caltech for fellowship support. TROPOMI SIF data generation by P.K. and C.F. is funded by the Earth Science U.S. Participating Investigator program (Grant NNX15AH95G). TROPOMI SIF product is available at ftp://fluo.gps.caltech.edu/data/tropomi/. County-level crop statistics is available at the USDA NASS Quick Stats Database (quickstats.nass.usda.gov). Crop-specific land cover data layer

CDL can be accessed at https://nassgeodata.gmu.edu/CropScape/.

3.7 Appendix

Table 3-1: The conversion factors used for NPP (g C/m^2) for individual crop type (modified based on Guan el al., (2016)). Light grey represents the ones involved in our analysis after the filtering of total crop planted area > 45% per county.

Crop	Published production unit	kg per production unit	Moisture content (%)	Harvest Index	Fraction of production allocated to aboveground (fAG)
Corn for Grain	**Bushel**	**25.401**	**11**	**0.45**	**0.85**
Soybean	**Bushel**	**27.216**	**10**	**0.4**	**0.87**
Hay (other)	**Ton**	**907**	**15**	**1**	**0.53**
Wheat	**Bushel**	**27.216**	**11**	**0.4**	**0.83**
Hay (alfalfa)	**Ton**	**907**	**15**	**1**	**0.53**
Cotton	**Lb**	**0.453**	**8**	**0.4**	**0.8**
Sorghum for grain	**Bushel**	**25.401**	**10**	**0.4**	**0.8**
Corn for silage	**Ton**	**907**	**65**	**1**	**0.85**
Barley	**Bushel**	**21.772**	**12**	**0.4**	**0.67**

Durum Wheat	**Bushel**	**27.216**	**12**	**0.4**	**0.83**
Sunflowers	**Lb**	**0.453**	**10**	**0.35**	**0.94**
Oats	**Bushel**	**14.515**	**11**	**0.4**	**0.71**
Peanuts	**Lb**	**0.453**	**9**	**0.4**	**0.8**
Sugarbeets	**Ton**	**907**	**85**	**0.4**	**0.8**
Canola	**Lb**	**0.453**	**10**	**0.35**	**0.94**
Rice	**Lb**	**0.453**	**9**	**0.4**	**0.8**
Potatoes	**Hundred Weight**	**50.8**	**80**	**0.5**	**0.8**

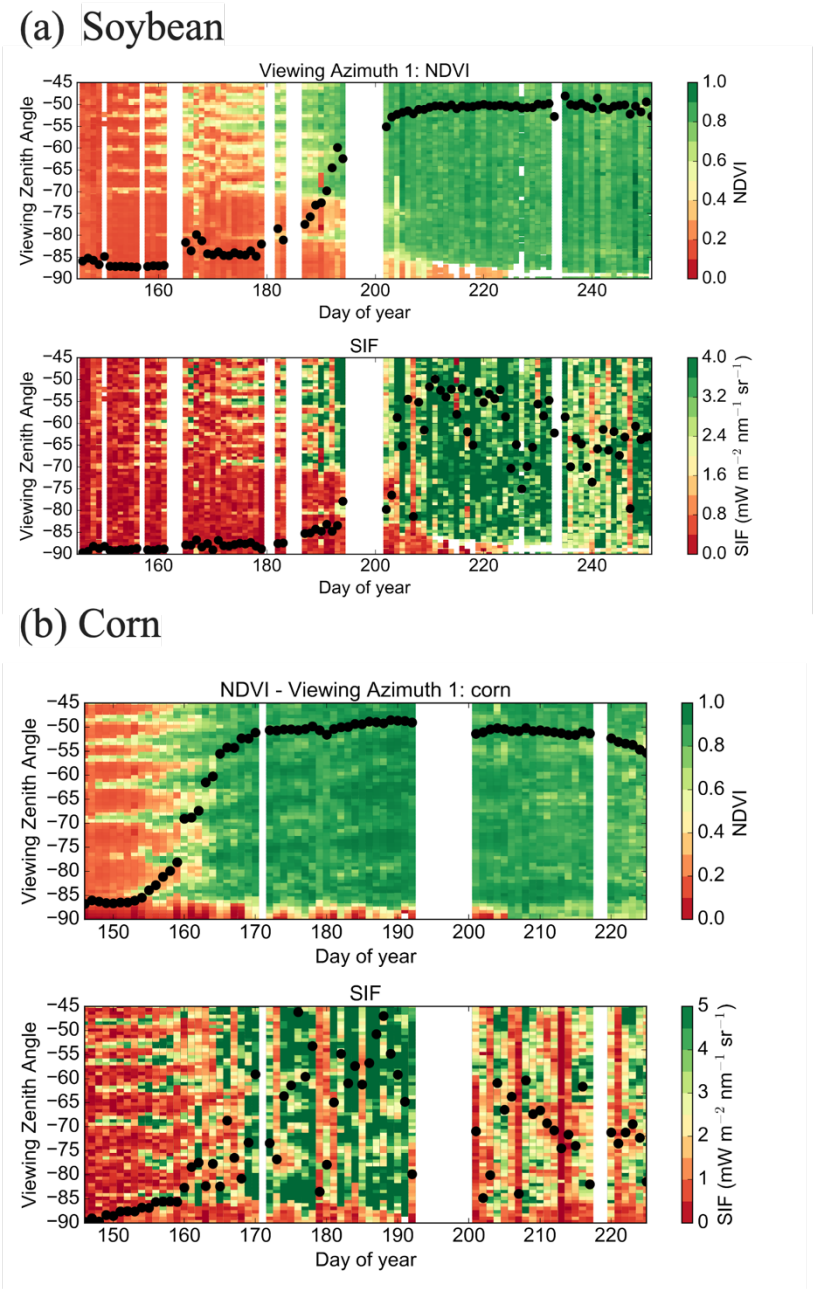

Figure 3.5: The impact of viewing geometry on both (a) soybean and (b) corn sites. Note that NDVI is invariant when NDVI > 0.6, which can be used as the indicator of the peak growth season, whereas far-red SIF at 740nm shows dynamic response during the same period.

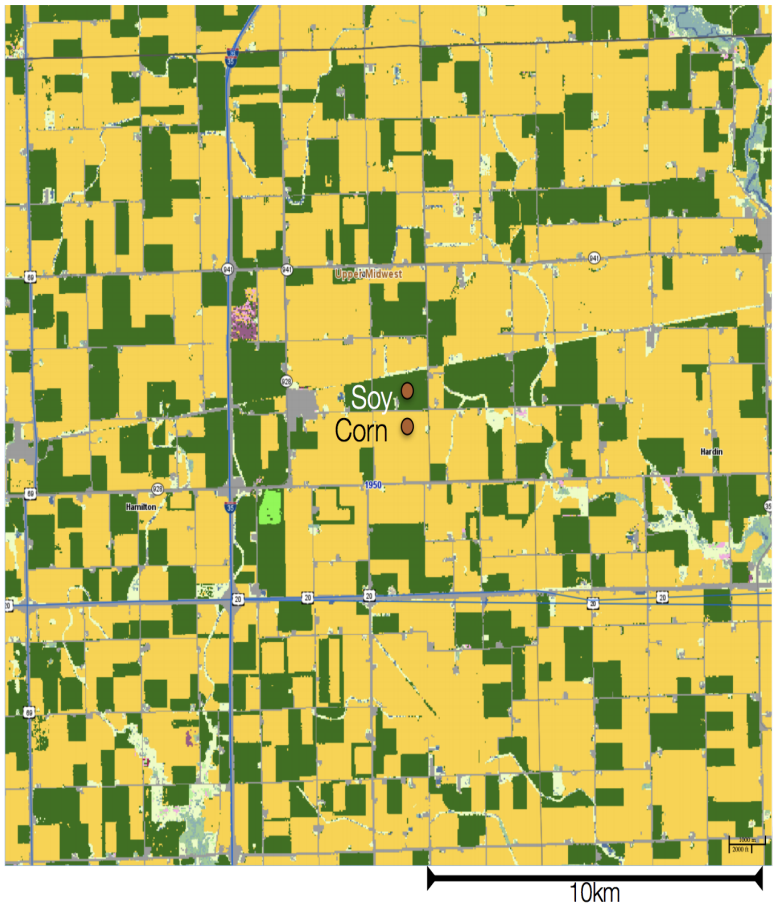

Figure 3.6: The location of USDA flux towers of C3 (42.488414°N, -93.522582°W; soybeans, *Glycine max* L. Merr.) and C4 (42.481677°N, -93.523521°W; corn, *Zea mays* L.), surrounded by homogeneous soybean and corn fields used in the 2018 satellite/flux tower comparison. Green represents soybean and yellow represents corn. Within +/-10 km from the flux towers, there are ~58% corn and ~30% soybeans derived from the 30-meter crop-specific land cover data layer (CDL; https://nassgeodata.gmu.edu/CropScape/).

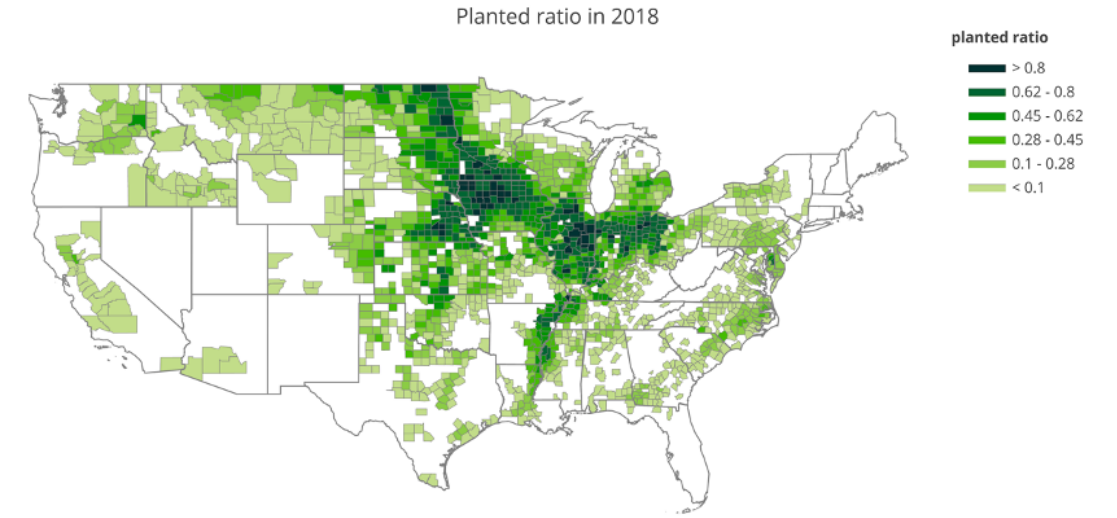

Figure 3.7: The fraction of total planted area of each county in 2018. The planted area for individual crop type in each county is obtained from USDA NASS Quick Stats Database (quickstats.nass.usda.gov), and the total area of each county is obtained from the United States Census Bureau (https://factfinder.census.gov/).

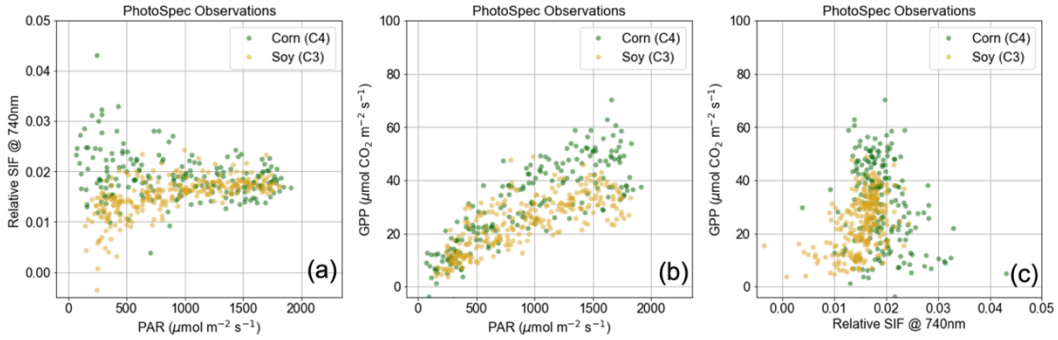

Figure 3.8: Canopy-scale relationships in the peak growing season based on hourly averaged data from PhotoSpec for soybean (gold) and corn (green): (a) relative SIF:PAR, (b) GPP:PAR, (c) GPP:relative SIF for both soybeans and corn. Relative SIF cancels out radiation and can be considered as a proxy of SIF yield. Thus, there is no obvious correlation with PAR or GPP. Since relative SIF is quite stable, this implies that the canopy structure is quite stable and PAR we used in the peak growing season is almost chlorophyll-absorbed APAR.

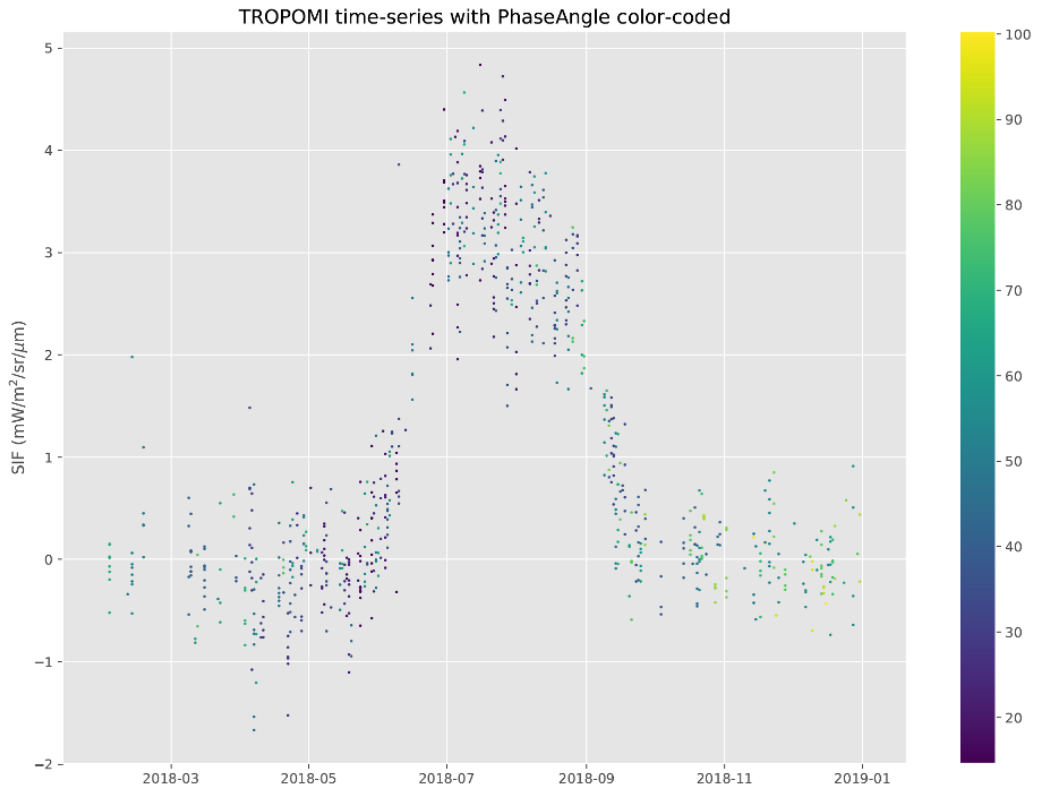

Figure 3.9: Footprint-level TROPOMI time series colored by the phase angle within +/-10 km from the flux towers used in **Figure 3.2**. Fewer TROPOMI observations are due to increased cloud cover at the beginning of the growing season. In addition, there is no apparent viewing angle dependent behavior in the TROPOMI datasets over the growing season.

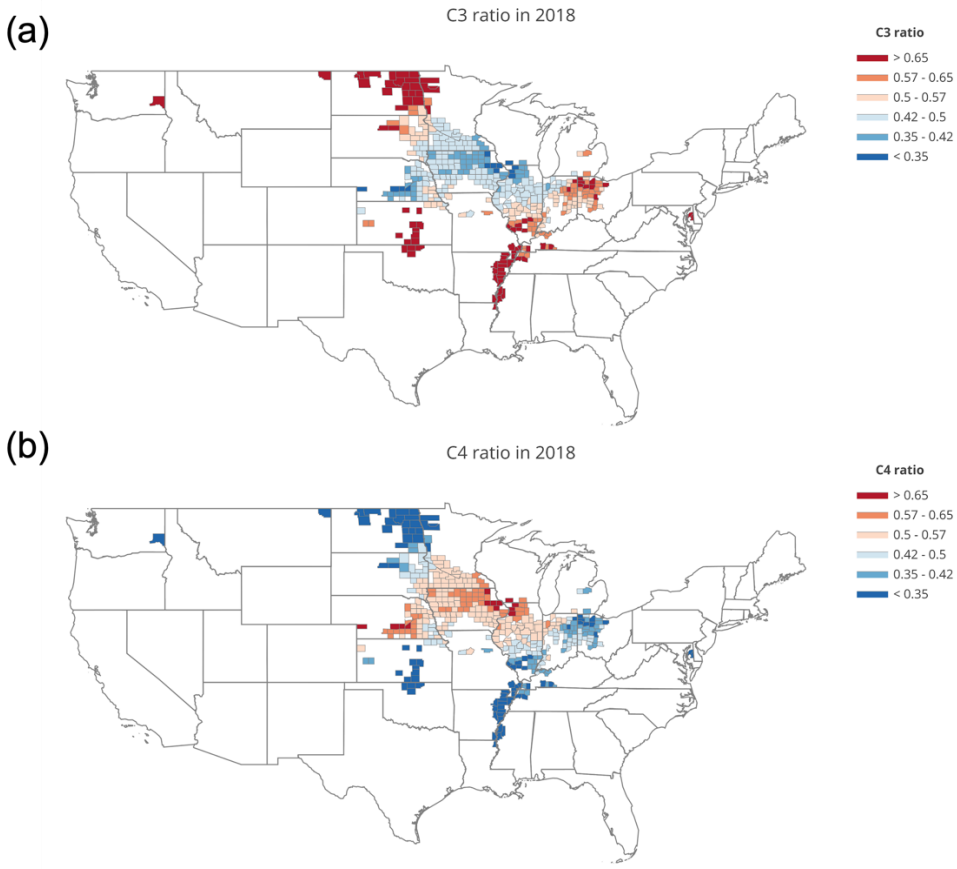

Figure 3.10: The fraction of (a) C3 and (b) C4 crops over the total planted areas for agricultural dominated counties, which have > 45% planted areas.

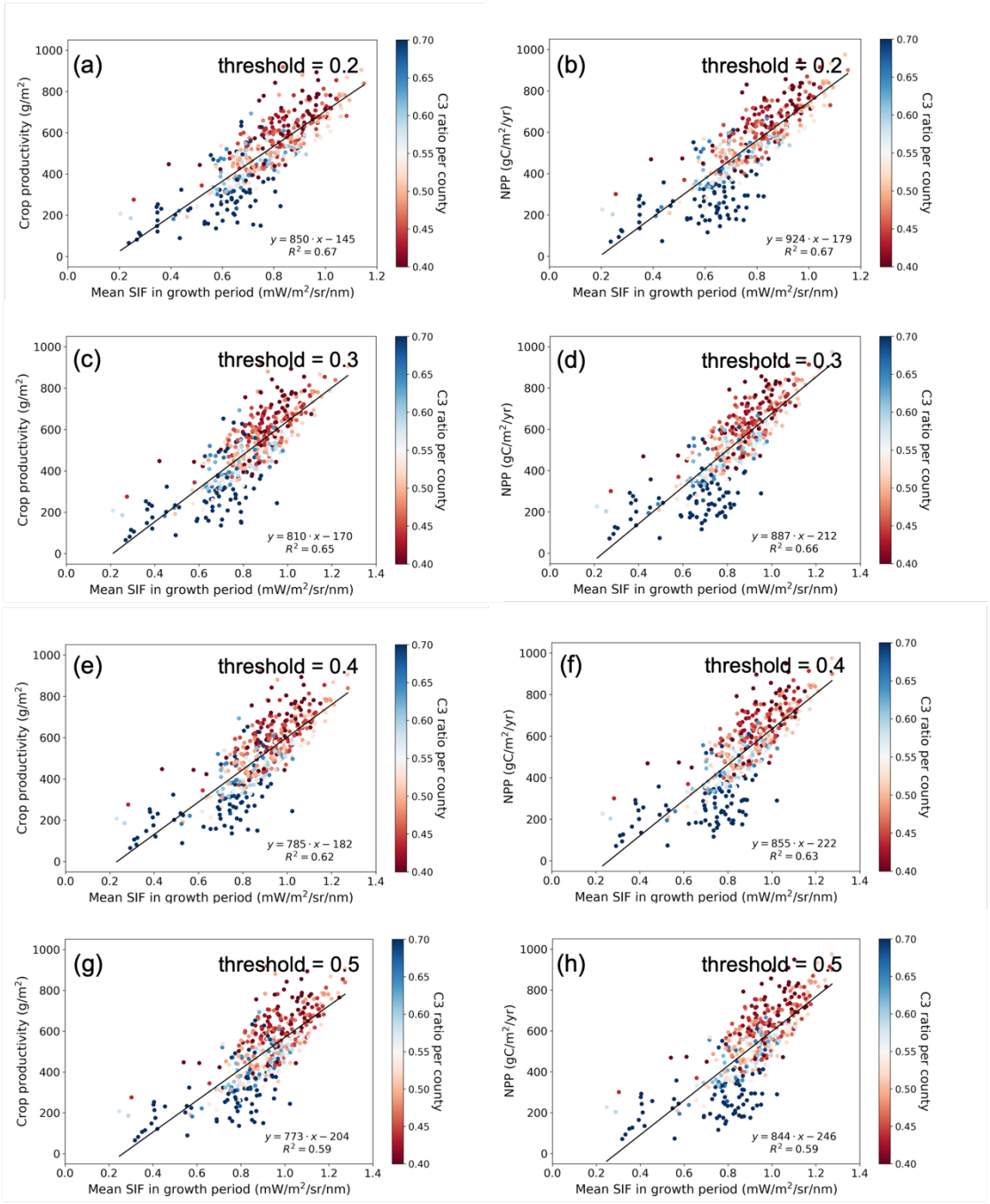

Figure 3.11: In counties with planted area > 45%, the relationship of crop productivity and NPP against average TROPOMI SIF during the growth period of 2018. The growth period for each county is defined when SIF is larger than some proportion of its maximum SIF. In the main text, we choose the threshold as 0.1, and here we represent the results with the varying threshold from 0.2 to 0.5. The color scheme represents the relative fraction of C3 crops, where blue means more C3 and red means more C4.

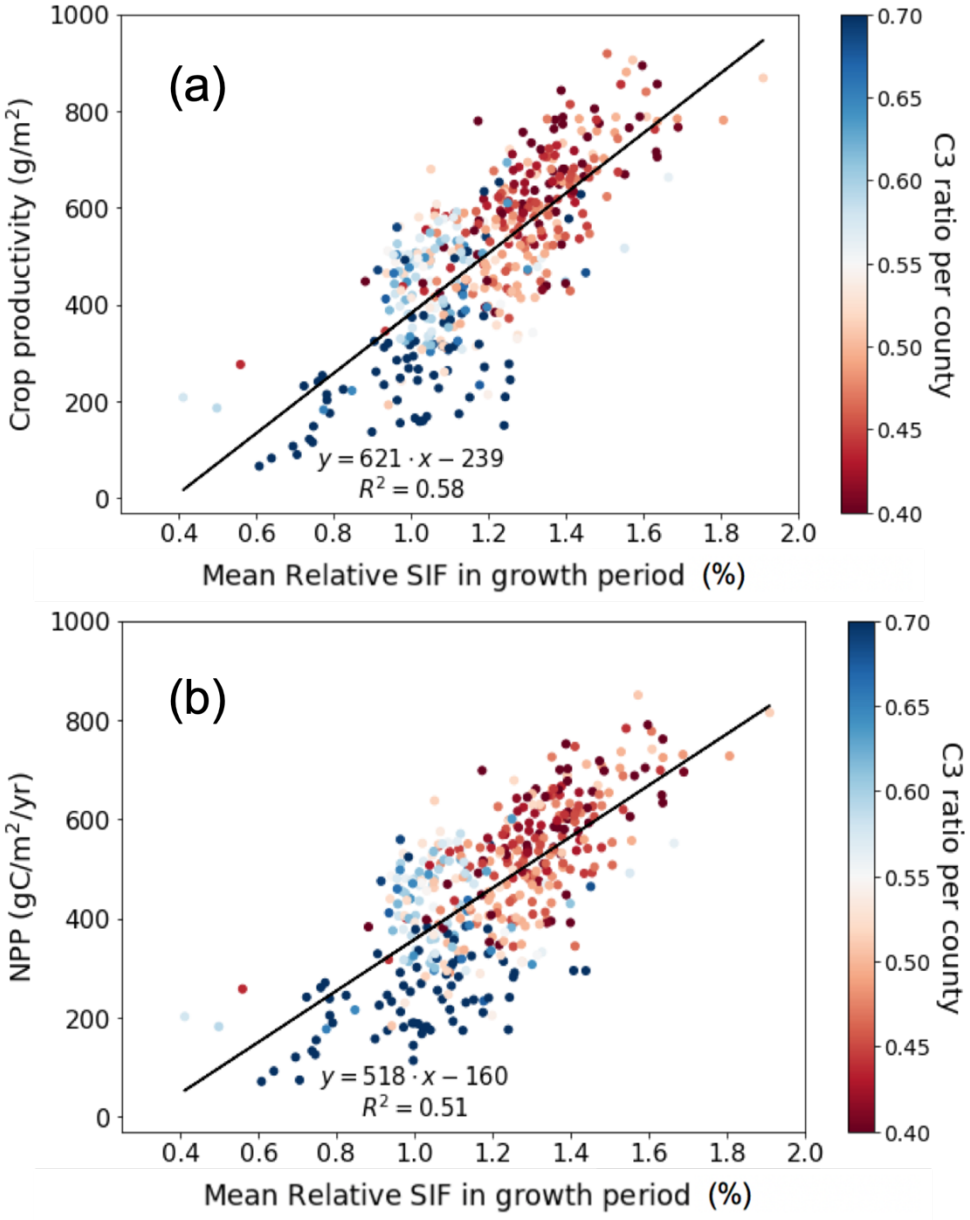

Figure 3.12: Spatial pattern of county-scale (a) crop productivity derived from USDA NASS and (c) average TROPOMI SIF during the growth period of 2018. In counties with planted area >45%, the relationship of (b) crop productivity:relative SIF and (d) NPP:relative SIF. The color scheme represents the relative fraction of C3 crops, where blue meaning more C3 and red means more C4.

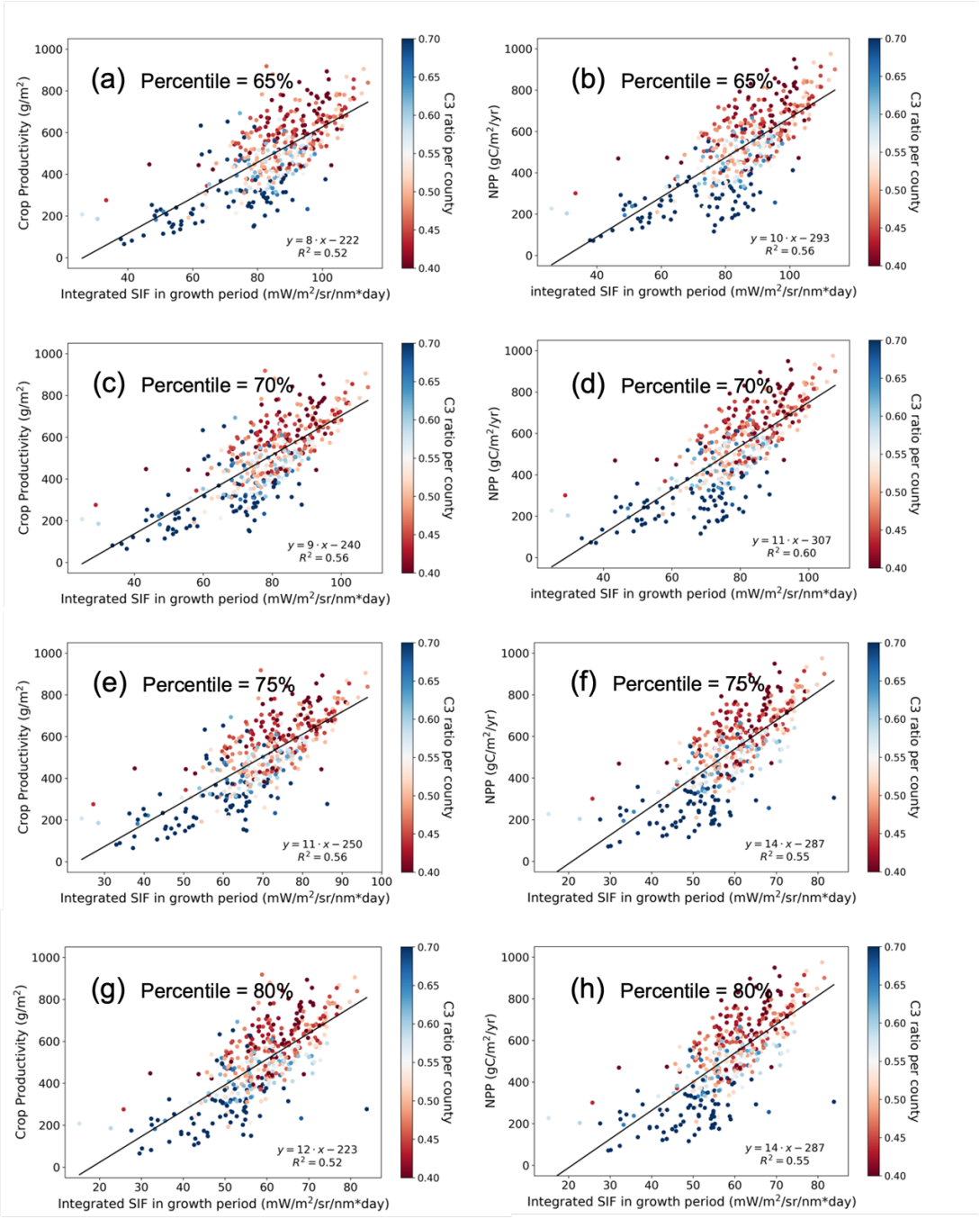

Figure 3.13: In counties with planted area > 45%, the relationship of crop productivity and NPP against integrated TROPOMI SIF during the growth period of 2018. The growth period for each county is defined as the time when SIF is larger than some percentile (from 60% to 80%) of the total observations. The color scheme represents the relative fraction of C3 crops, where blue means more C3 and red means more C4.

Chapter 4

MARKED IMPACTS OF POLLUTION MITIGATION ON CROP YIELDS IN CHINA

He, L., Wei, J., Wang, Y., Shang, Q., Liu, J., Yin, Y., Frankenberg, C., Jiang, J.H., Li, Z. and Yung, Y.L., 2022. Marked impacts of pollution mitigation on crop yields in China. *Earth's Future*, *10*(11), p.e2022EF002936. DOI: https://doi.org/10.1029/2022EF002936

4.1 Abstract

Plant growth and crop harvest are impacted by both climate change and air pollution. However, their relative importance in crop yields remains elusive, especially in heavily polluted regions. Here we develop a crop yield prediction model, based on a large volume of historical crop data, as well as climate and pollution records in China since 1980. A long-term surface ozone concentration dataset is developed from a machine-learning model and various observations. An assessment of four climate and pollution factors reveals the critical role of particulate and ozone pollution in regulating interannual variations of crop yields in China. During 2010-2018, we find that the particulate pollution mitigation outweighs the negative impacts of concurrent climate change, resulting in 0.5-1.9% net yield increases nationwide, despite of the ozone increases in the North China Plain. Looking to the future, the impacts of climate change, particularly from surface temperature increase, will dominate over pollution factors and profoundly reduce future maize and rice yields by −0.6 to −2.8% $10yr^{-1}$ by 2050. Our findings call for the attention on the threat to future global food security from the absence of pollution mitigation and the persistence of global warming.

4.2 Introduction

Crop yields are strongly influenced by regional climate and air quality (Wang et al., 2020). Temperature increase and resultant enhancement of the crop respiration have caused a global yield loss in recent decades (Lobell et al., 2011; Zhao et al., 2017), and such a trend is expected to be amplified over the next century as air temperature exceeds the tipping point in the crop-temperature relationship (Schlenker & Roberts, 2009). Precipitation exerts impacts on crop yield by altering soil and air moisture (Kimm et al., 2020) but in a non-monotonic manner (Li et al., 2019; Rosenzweig et al., 2002). Meanwhile, atmospheric pollutants such as anthropogenic aerosols and near-surface ozone exert detectable impacts on regional crop yields by changing physical, biochemical, and physiological processes during plant growth (Ainsworth, 2017; Chameides et al., 1999). Two of the pronounced aerosol effects on crop yields are the decrease in total solar radiation reaching the ground for plant photosynthesis (Gerstl & Zardecki, 1982) as well as the increase in diffuse radiation and light use efficiency (Hemes et al., 2020). The former is generally more significant, leading to a net negative effect (Tie et al., 2016). As a strong oxidant, ozone near the surface reduces photosynthesis by entering leaves via the stomata, producing damaging radicals, and consequently accelerating plant senescence (Felzer et al., 2007). Tropospheric ozone is mainly produced by photochemical reactions between nitrogen oxides (NO_x) and volatile organic compounds (VOCs) in the presence of sunlight. Both precursor gases are of significant anthropogenic origin. On the global scale, regions with high levels of aerosol and ozone pollution are always collocated with croplands in rapidly developing countries. Therefore, effective controls of pollutant emissions in these regions have the great potential of alleviating crop yield loss due to air pollution (Burney & Ramanathan, 2014; Chameides et al., 1999). Meanwhile, it remains highly uncertain how air pollution and climate change compete or work together over the world's pollution centers with characteristic pollution evolutions in the past few decades (Wang et al., 2015).

China produces the largest amounts of rice and wheat in the world, and contributes approximately 28% and 17% of global production, respectively (Deng et al., 2019;

Li et al., 2019). China is also the second-largest maize producer behind the United States, with more than an 18% share of production in the world maize economy (Meng et al., 2016). In the recent four decades, yields for staple crops in China have experienced decades of increases, mainly owing to technological innovation. Nevertheless, during the same period, there was about a 1°C increase in growing-season temperature over major crop regions globally, reducing relative yields by several percent (Zhao et al., 2017). The rapid urbanization, industrialization, and economic growth also led to serious regional haze in the majority of the country (Huang et al., 2015; Le et al., 2020). However, the recent decade starting from 2010 witnessed an unprecedented reduction in particulate pollution after a series of emission control policies and environmental protection laws by the Chinese government (Li, 2020; Sogacheva et al., 2018; Tie et al., 2016; Zhao et al., 2018). Particularly in 2013, China issued the nation's most stringent policy named as "Air Pollution Prevention and Control Action Plan". Since then, the particulate matter (PM) concentration has dropped by up to 50% (Wei et al., 2021; Zhang et al., 2019). Several studies using ground observations and crop models showed that yields significantly suffered from climate warming and increasing aerosols and surface ozone in northern and eastern China (Tie et al., 2016; Wang et al., 2007; Yi et al., 2018; Yi et al., 2020; Zhao et al., 2020). However, a systematic understanding of the crop yield response to climate and air pollution is limited due to the sparse and short records of ground observations.

This paper assesses the individual and joint impacts of climate and air pollution on both historical and future crop yields. We focus on three most important staple crops in China, including rice, maize, and wheat. A robust statistical model is established that accounts for the spatiotemporal variations of surface air temperature, precipitation, aerosol optical depth (AOD), and surface ozone (O_3) exposure, aiming to estimate the relative yield change (RYC) due to the individual and joint effects of those four factors. Similar yield models have also been used to study the response of yield to climate or pollution (Burney & Ramanathan, 2014;

Butler et al., 2018; Hong et al., 2020; Lobell et al., 2011, 2020; McGrath et al., 2015; Tack et al., 2015). To our best knowledge, this study is the first effort to assess the yield benefit due to effective emission controls in China after 2010. We use long-term province-level yield annual reports with climate variables and air pollution data from various sources from 1980 to 2018. Lack of long-term surface ozone measurements has been an outstanding issue faced by large-scale data analysis studies. Here we employ the recently developed surface ozone dataset in China, which is derived from a machine learning model that takes in ozone surface monitor data since 2013 as well as long term climate, emissions, and other auxiliary dataset. Future yield changes by 2050 are assessed by feeding predicted climate and air pollution variations from the ensemble climate model projections to the established crop prediction models.

4.3 Materials and Methods

4.3.1 Observational data

The annual crop production, harvested area, and yield data are from the National Bureau of Statistics of China (http://data.stats.gov.cn/). We use historical monthly temperature and total precipitation of 0.25° × 0.25° obtained from the fifth generation ECMWF reanalysis for the global climate and weather (ERA5) from 1980 to 2018 (Bell et al., 2019 a&b). The monthly surface maximum daily average 8 hours (MDA8) O_3 product of 0.1° × 0.1° is obtained from the China High Air Pollutants (CHAP) dataset, which was predicted from the solar radiation intensity and surface temperature, together with other big data including observations, satellites, and models, by employing the space-time extremely randomized trees (STET) machine learning model (Wei et al., 2021). For surface ozone, we adopt a widely used MDA8 index to reflect ozone exposures on crops over the growing season. Such an index is highly correlated with the ozone cumulative index AOT40, which is a cumulative indicator of hourly ozone concentrations exceeding 0.04 ppm. Based on the ground-based observations, MDA8 are highly correlated with AOT40

on the monthly basis, with R^2 of 0.92 (SI Appendix, Figure 4.6). The historical monthly AOD at 550 nm data of 0.625° × 0.5° is obtained from the Modern-Era Retrospective analysis for Research and Applications version 2 (MERRA-2) (Global Modeling and Assimilation Office, 2015), as there is no satellite record providing continuing AOD measurements on the monthly basis since 1980. We validate the MERRA2 AOD by the retrieved AOD from AVHRR (Advanced Very High Resolution Radiometer) which is one of the earliest satellite instruments, whenever the product is available (SI Appendix, Figure 4.7). AOD measures the extinction of solar radiation by aerosol particles, e.g., smoke, pollution, and dust. We hypothesize that aerosols exert impacts on crops mainly through the interference with atmospheric radiative fluxes, so the column-integrated quantity AOD is appropriate to be used in our analysis. The planted distribution of each crop is generated by Spatial Production Allocation Model for 2010 (SPAM 2010) (International Food Policy Research Institute, 2019). Province-level temperature, precipitation, AOD, and surface ozone are averaged over grids with planted fraction greater than 2.5% of each crop.

4.3.2 Statistical yield model

To explore crop responses to the various factors, we develop a statistical yield model for each crop using the following panel regression approach (Equation 1):

$$\log\left(crop\ yield_{i,y}\right) = \beta_0 + \beta_{temp} \cdot temp_{i,y} + \beta_{precip} \cdot precip_{i,y} + \beta_{AOD} \cdot AOD_{i,y} + \beta_{O_3} \cdot O_{3_{i,y}} + f_1(y) + f_2(i) + \varepsilon_{i,y} \quad \text{(Equation 1)}$$

where $temp$, $precip$, AOD and O_3 are the growing-season averaged 2-m temperature, daily precipitation, AOD, and MDA8 O_3, respectively, during 1980-2018 (SI Appendix, Figure 4.8). Following the crop calendar for China reported by the United States Department of Agriculture (USDA), the growing season is defined as three months before the harvest season, which refers to June – August

for single-season rice, July – September for maize and January – April for winter wheat. The subscripts i and y are indices for province and year. β_{temp}, β_{precip}, β_{AOD} and β_{O_3} are slope coefficients for each corresponding variable. β_0 is the regression intercept. We use the growing-season averaged climate and pollution variables instead of monthly averages to avoid the collinearity among monthly variables, which will lead to large uncertainty in the model fitting. There are steady increases in yearly yields throughout recent decades, which is likely due to the technological innovation in seeding, irrigation, and planting skills, as well as policy practices (SI Appendix, Figure 4.9). To account for the abovementioned time-varying factors contributing to the increasing yields, we introduce a set of yearly variables $f_1(y)$. In addition, to account for the spatial heterogeneity of some other impacts (e.g., soil and water qualities), provincial variables $f_2(i)$ are used. ε is the residual term.

We use *linearmodels* package in Python to fit the yield model, which also reports the significant levels (p-value) of regression coefficients and the model performance (R^2) (See details in SI Appendix, Table S1). The predicted crop yields by the regression models generally agree well with the reported yield (Figure 4.1), with the correlation coefficient square (R^2) being 0.79, 0.81, and 0.89 for rice, maize, and winter wheat, respectively. There are no obvious patterns between residuals versus fitted values, which validates the good performance of the chosen model (SI Appendix, Figure 4.10). It should be noted that our model assumes equal weight to different provinces regardless of their share in the national crop production. Therefore, our estimation is interpreted as an overall average impact.

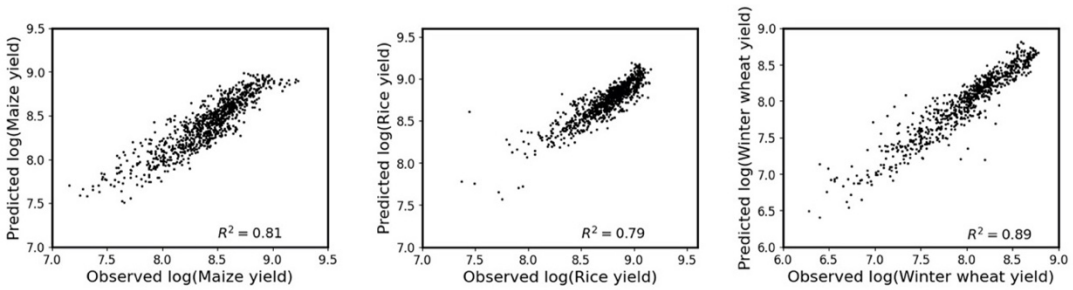

Figure 4.1: The correlation between predicted yield vs. observed yield for maize (left), single-season rice (middle) and winter wheat (right).

We calculate 90% confidence intervals (CIs) of each coefficient are derived from the 5th and 95th percentiles by repeating the model 1,000 times using 75% bootstrap sampling of provinces for each year. We also use *dominance-analysis* package in Python to calculate the fractional contribution of different factors based on the residuals of the base model, which only includes yearly and provincial dummies. Dominance analysis calculates the dominance of one predictor over another by comparing their additional contributions to model performance in terms of R^2 across all subset models (Budescu, 1993).

4.3.3 Relative yield changes due to climate and pollution factors

We estimate relative yield changes (RYC, unit: %) in 2006-2010 (or 2014-2018) compared to 1980-1984 (or 2006-2010) due to individual factors for the largest 10 production provinces of each crop. We choose 2010 as a breakpoint because of the increasing trend of AOD before 2010 and the reversed pattern afterward, which motivates us to quantify the different impacts of aerosol pollutants to crop yields before and after 2010. RYC is derived from the modeled yield difference between the predictors using the averaged historical level during 2006-2010 (or 2014-2018) and the hypothetical scenario with the same level during 1980-1984 (or 2006-2010). The 90% CIs of these RYC estimates are the 5th and 95th percentiles determined using the bootstrapping method, with 1,000 crop models generated from 75% observations each year.

The country-averaged yield predictions are estimated by the statistical yield model holding at the current technology stage, which is denoted as S0. To evaluate the contribution of a certain factor, we simulate the yield by fixing this factor at the same level as in 2015-2020, represented by S1. Then, we can isolate the corresponding contribution using the difference S1-S0. The uncertainty of future

projections is obtained by resampling 1,000 times the yield model with bootstrapping from historical observations.

4.3.4 Possible interaction terms and non-linear fitting in the statistical model

Previous literatures have demonstrated that there may exist interactive relationships among the variables in our model (Burney & Ramanathan, 2014; Hong et al., 2020). For example, the change of temperature may positively affect the level of O_3, while AOD could decrease when precipitation increases due to the wash-out effect. Therefore, we add interaction terms in our base model (Equation 2), and the results are shown in SI Appendix, Table S2. There is no significant increase in R^2 after adding interaction terms across all three crops in Equation 2, implying the predictability cannot be enhanced by considering the two interactive relationships mentioned above.

$$\log(crop\ yield_{i,y}) = \beta_0 + \beta_{temp} \cdot temp_{i,y} + \beta_{precip} \cdot precip_{i,y} + \beta_{AOD} \cdot AOD_{i,y}$$
$$+ \beta_{O_3} \cdot O_{3_{i,y}} + \beta_{inter1} \cdot (AOD_{i,y} \times precip_{i,y}) +$$
$$\beta_{inter2} \cdot (O_{3_{i,y}} \times temp_{i,y}) + f_1(y) + f_2(i) + \varepsilon_{i,y} \quad \text{(Equation 2)}$$

The second alternative model we choose is to add nonlinear trend variables into the regression (Equation 3). Instead of using yearly dummy variables, we test the model performance of representing the technological innovation and other time-varying effect as a combination of 1st and 2nd order of polynomials regarding to $year$. The rationale is that these time-varying impacts may not be linear across years. When new technology is adopted to crop planting, its positive impact on RYC usually increases at first couple of years and then saturates. The corresponding results are presented in SI Appendix, Table S3. We find that the 1st order polynomial year variable is positive, indicating that the yield is increasing along the time. The quadratic year variable is negative for all crops, which implies that the increasing rate of the yield is becoming leveled off.

$$\log(crop\ yield_{i,y}) = \beta_0 + \beta_{temp} \cdot temp_{i,y} + \beta_{precip} \cdot precip_{i,y} + \beta_{AOD} \cdot AOD_{i,y}$$

$$+ \beta_{O_3} \cdot O_{3_{i,y}} + \beta_{year} \cdot y + \beta_{year2} \cdot y^2 + f(i) + \varepsilon_{i,y} \quad \text{(Equation 3)}$$

We find that these two alternative models do not make a significant difference in the model's predicting capability, lending support to the robustness of the modeled crop responses. To reduce the arbitrariness of the fitting form and to better interpret the result, we keep one variable in one term of the regression model.

4.4 Results

4.4.1 Historical yield response to climate and pollution factors

Annual production and yields (production per area) of the three most important staple crops are analyzed in the thirty-one provinces of China from 1980 to 2018. There are two rice cropping systems in China, single-season, and double-season. The single-rice system (referred to as rice hereafter), which accounts for more than 65% of total rice production in China, is the main focus of our study. Figure 4.2A shows that a high planted fraction of rice is concentrated in southeastern China, particularly in the Yangtze River Basin. During 1980-2018, there is a quasi-linear increase in the rice production in China, which is believed to be mainly driven by the technological advancement (Peng et al., 2009). Maize is mainly planted in the North China Plain and Northeast of China (Figure 4.2A). The time evolution of total maize production exhibits two stages, and it experienced a faster increase in maize production after 2005 than before. Both spring wheat and winter wheat are planted in China, and winter wheat production accounts for around 90% of total China wheat production (Sun et al., 2018). The North China Plain is the major wheat planted area (Figure 4.2A), which produces more than 60% of total national wheat production (Lu & Fan, 2013). Even though the winter wheat total production also increased along with time, the earlier time period in the 1980s had an even larger increase rate than in recent years. There was even a decline of production in

the early 2000s, due to the reduction in harvest area for winter wheat after 2000 (SI Appendix, Figure 4.9).

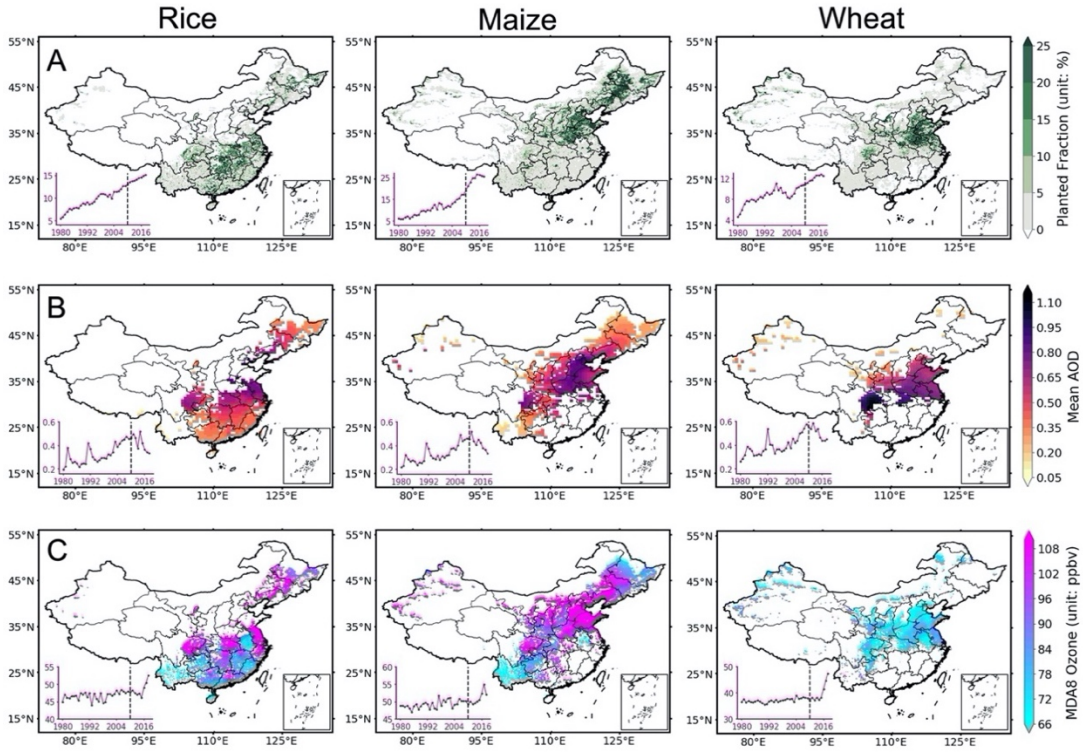

Figure 4.2: Geospatial maps and interannual trends of different crop types and corresponding pollution levels for peak growing seasons in China. (A) Planted fraction (unit: %) of each 10km x 10km cell for rice (left), maize (middle) and wheat (right). (B) The climatology of MERRA2 aerosol optical depth (AOD) at 550 nm for peak growing seasons during 2006 to 2010. (C) The climatology of the surface ozone MDA8 for peak growing seasons during 2006 to 2010. The peak growing season is defined as June-August for rice, July-September for maize and January-April for winter wheat. The inserts show the times series of the total crop production (unit: × 10 Megatonnes) (A), AOD (B), and near surface ozone (C) for individual crop type during the peak growing season from 1980 to 2018. The time series of peak growing-season temperature, precipitation and annual total harvested area and country-averaged yields for three crops can be found in SI Appendix, **Figure 4.8** and **Figure 4.9**.

We further analyze spatial maps and temporal evolutions of the AOD and surface O_3 during the growing season of each crop type during 1980-2018. As shown in Figure 4. 2B, the areas of high crop fractions are always accompanied by high AOD,

such as the Yangtze River Basin for rice, North China Plain and Northeast China for maize, and central East China for wheat. The mean AOD during the growing season is 0.34, 0.35, and 0.42 for rice, maize, and wheat, respectively. Similarly, surface O_3 and crop fraction covary spatially, implying the potential influence of pollution on crop production. The mean daily maximum 8-hour surface ozone concentration (MDA8) during the growing season is 47.1, 49.7, and 37.8 ppbv for rice, maize, and wheat, respectively. The historical changes of AOD over different crop-dominant regions share the same key feature: a general increasing trend during 1980-2010, followed by a reduction in the recent decade. Such an AOD evolution characteristic reflects the implementations of emission control policies at different time periods in China. The trends of surface ozone are complicated (Figure 4.2C). Generally, there are small increasing trends before 2013, followed by an abrupt and steep increase since 2014. The most recent abrupt increases have been well observed (Lobell & Burney, 2021), but the main cause remains elusive, owing to the fact that O_3 production involving non-linear atmospheric chemistry can be at different regimes in urban and rural areas, and O_3 formation has a complex relationship with aerosols (Wu et al., 2020).

The crop yield models (Equation 1) derived from historical data show significant impacts from both air pollution and climate change (Figure 4.3). The crop yield is reduced by 1.7-5.9% per 0.1 increase in AOD (Figure 4.3A), corroborating the hypothesis that particulate pollution reduces the solar radiation reaching the surface and lowers plant photosynthesis (Lobell & Burney, 2021; Tie et al., 2016). The winter wheat exhibits the largest sensitivity to particulate pollution, likely because northern China is more polluted in the wintertime when AOD variation is larger. Both maize and rice show significant yield reduction by ozone, and the reduction rate per 5ppbv MDA8 ozone increase is larger for maize. The response of wheat to ozone bears a large uncertainty bar, likely due to the fact that the NCP, where wheat is mainly planted, experienced dramatic ozone change in recent years. A warmer near-surface air temperature results in yield loss for all crop types, with the largest

response for winter wheat and the smallest and least significant sensitivity for rice. Our predicted magnitude of crop yield responses to temperature increase are consistent with previous assessments based on field warming experiments in China (Zhao et al., 2016) as well as a chemistry-crop-climate coupled model (Zhang et al., 2021). The crop responses to precipitation are complicated. Our result shows that every 1 mm precipitation per day can result in about 5.4% winter wheat yield loss during the growing season. Further analyses reveal that there are diverse responses of winter wheat to precipitation in the top six provinces in term of total yield. Our reduced regression models ran on individual provinces with time-fixed effects removed (SI Appendix, Table S4) show that, in the relatively wet provinces such as Anhui and Jiangsu in southern China, the precipitation has significantly negative impact on winter wheat yield (Li et al., 2010; Song et al., 2019). Precipitation provides moisture in the air and soil needed by plants, but is also accompanied with enhanced cloud cover and reduced radiation reaching the surface. Excessive precipitation can further cause devastating fungal pathogens for winter wheat near the end of the growing season (Wiik & Ewaldz, 2009). Such effects can be profound in Eastern China, since the end of the winter wheat growing season overlaps with the onset of the East Asian Summer Monsoon (Li et al., 2016). In contrast, maize and rice are less sensitive to precipitation changes, showing a small enhancement in yields.

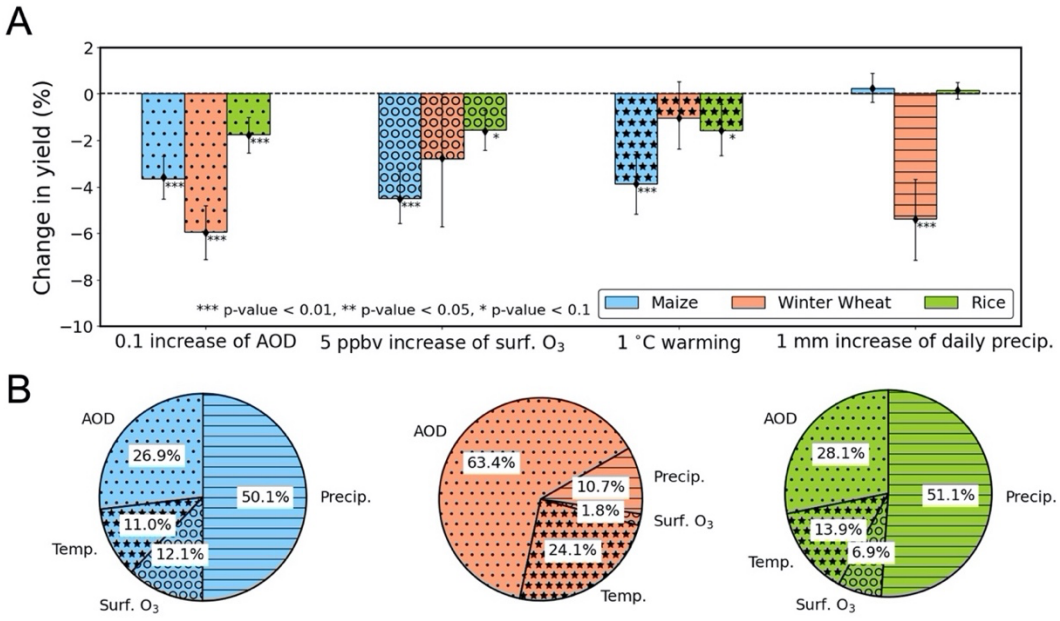

Figure 4.3: (A) Crop yield responses to air pollution and climate variables. The average yield response to unit change, i.e., 0.1 increase of AOD, 5 ppbv increase of surface zone, 1 °C warming and 1mm increase of daily precipitation over the peak growing season from 1980 to 2018. The bar chart is plotted with diamond symbols (median estimates) and error bars (90% confidence intervals, CIs) by bootstrap resampling the model 1,000 times. (B) The percentage contribution of AOD, surface ozone, temperature, and precipitation to the spatial variation of yields for each crop using the dominance analysis. Blue, orange, and green color corresponds to maize, winter wheat, and rice, respectively.

To further reveal the relative importance of each factor with respect to the interannual variation of each crop, we conduct a dominance analysis and calculate the percentage contributions of different factors of interest to the residual of the base model. Among four targeted factors, precipitation is the most important one for maize and rice, accounting for about 50% of interannual variability in the detrended yield data (Figure 4.3B). The large fluctuation of precipitation over the agricultural regions in China are closely linked with the characteristics of East Asia Summer Monsoon, whose intensity is subject to many climate variabilities, such as El Niño–Southern Oscillation. Aerosol is the predominant factor for the winter wheat yield by explaining 63.4% of the interannual variability in the detrended data. Temperature and ozone pollution are relatively less important factors. Together,

they can explain the rest 20-25% variability. The results reinforce the notion that air pollution, particularly through anthropogenic aerosols, is crucial for crop production.

4.4.2 Agricultural benefits from pollution mitigation after 2010

The year 2010 apparently represents a tipping point of particulate pollution in China because of the increasing/decreasing trend of AOD before/after that year. We focus on this recent pollution transition period and estimate RYC by different factors for the whole nation as well as the largest ten production provinces of each crop. We group the responses to surface temperature and precipitation into the climate effect and the responses to AOD and ozone concentration into the pollution effect. RYC is calculated by the predicted yields under different hypothetical climate and pollution scenarios in our panel regression models. For example, to assess the influence of the recent pollution mitigation, we contrast the predicted crop yields using different AOD and ozone concentrations between two time periods, 2014-2018 and 2006-2010 and hold all other variables unchanged at the 2006-2010 levels. As shown in Figure 4.4, from 1980 to 2010, both climate and pollution factors resulted in the reduction of the yields, but the impact of pollution is more pronounced than that of climate variations. Three crop types generally share the same responses. Nationwide, pollution caused by the RYC is –4.8%, –8.5%, and –17.1% for rice, maize, and winter wheat, respectively, while climate induced RYC is only –1.4%, –1.8%, and –1.6% for three crops accordingly. The top ten productive provinces for each crop also agree with each other on the signs of the effects but differ slightly in magnitude. In contrast, the effects of both pollution and climate were drastically changed in the second decade of the 21st century.

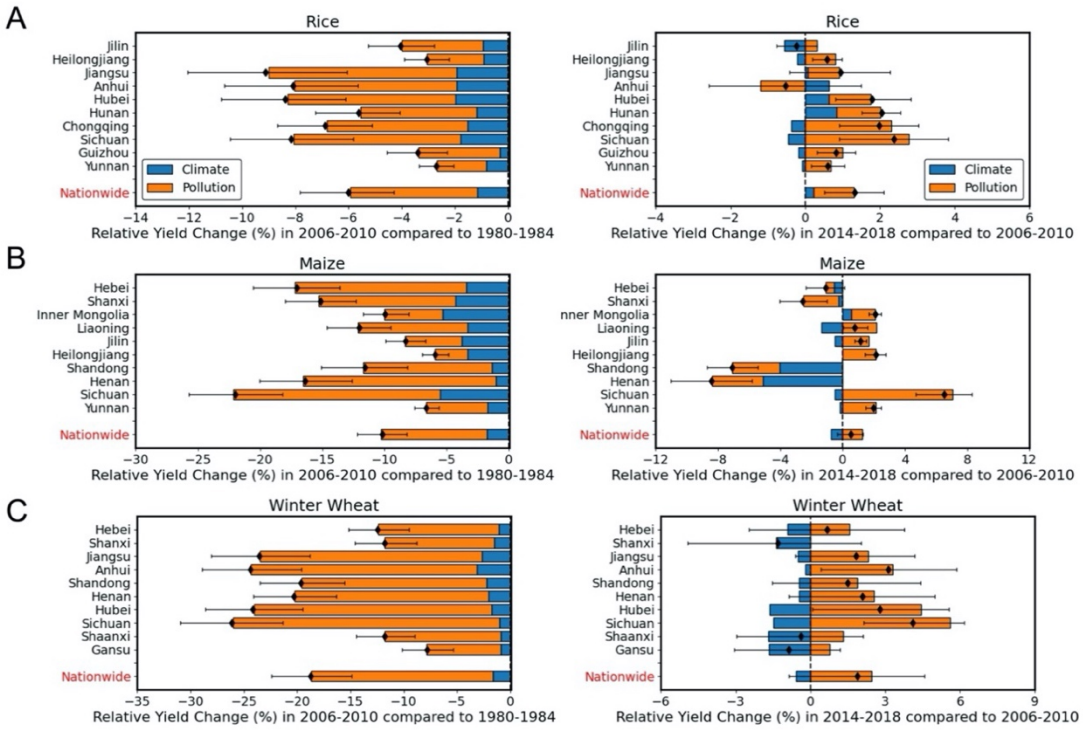

Figure 4.4: Relative yield change (RYC) attributed to climate and pollution changes for (A) rice, (B) maize and (C) winter wheat. The climate change is the net effect of temperature and precipitation variations, and the pollution change concerns AOD and surface ozone together. For left panels, RYC is calculated as ($Model_{2006–2010\ avg}$ − $Baseline_{2006–2010\ avg}$)/$Baseline_{2006–2010\ avg}$. $Model_{2006–2010\ avg}$ is the estimated crop yield from the panel regression model using the historical 2006-2010 averaged climate and pollution records, and $Baseline_{2006–2010\ avg}$ is estimated from the actual pollution (climate) levels but held with the same climate (pollution) scenario in 1980-1984. Nationwide estimates are calculated as the sum of province values weighted by harvested area. RYC is plotted as black diamonds (median estimates), with dark 5-95% percentile error bars calculated by bootstrapping the model 1,000 times.

Owing to the effective emission control in China, the particulate pollution level significantly dropped in the growing seasons of three crops, resulting in increases in the national crop yield when comparing 2014-2018 to 2006-2010. However, due to the deteriorated ozone pollution after 2013 in the North China Plain, the crop yield gain by the PM mitigation was largely offset. Nationwide, the RYC induced

by pollution mitigation is still positive, about 1.1%, 1.3%, and 2.4% for rice, maize, and wheat, respectively. For those provinces located in the North China Plain, such as Henan, Shandong, and Shanxi, a net reduction of maize yield by pollution factors is found after 2010, as the ozone pollution impacts outweigh that of the PM reduction. Climate-induced changes in crop yield during the same periods are insignificant for rice and winter wheat regions, leaving the pollution mitigation effects to dominate the crop yield variations. Most wheat-prevalent provinces experienced a moderate reduction in yield under climate change during 2006-2018, but the corresponding RYC is generally smaller than 2%. Overall, the reduction in aerosols in recent years stands out as a key driver of the crop variations on the interannual time scale.

4.4.3 Predicted yield changes by 2050

Capitalizing on the crop prediction models, we assess the impacts of future climate and pollution variations on the crop yields by 2050. Global climate simulations with various emission scenarios have been widely used to assess the societal and economic impacts by climate change (Shindell et al., 2021). Here the ensemble means of different models of Coupled Model Intercomparison Project (Phase 6, CMIP6) with the emission scenario SSP5-8.5 are used to reflect the future climate and pollution scenarios (SI Appendix, Figure 4.11-4.13 & Table 4-5). The SSP5-8.5 represents the scenario with rapid and unconstrained growth with a fossil fuel-based economy, and will lead to ~2 °C increase in global temperature in the 2050s compared to 1995-2014 (Li et al., 2018). The future projections aim to isolate the effects of temperature, precipitation, aerosol, and surface ozone levels on future yields under the assumption that the technology is held as equivalent to the current years (2015–2020). Note that hourly surface O_3 concentrations are not available from the CMIP6 models to calculate MDA8. According to the ground-based observations, O_3 MDA8 is linearly correlated with the O_3 monthly mean with R^2 at about 0.92 (SI Appendix, Figure 4.14), so we convert the O_3 monthly mean (MM)

in the CMIP6 model outputs to MDA8 following the empirical relationship: MDA8 = MM×1.3+6.2.

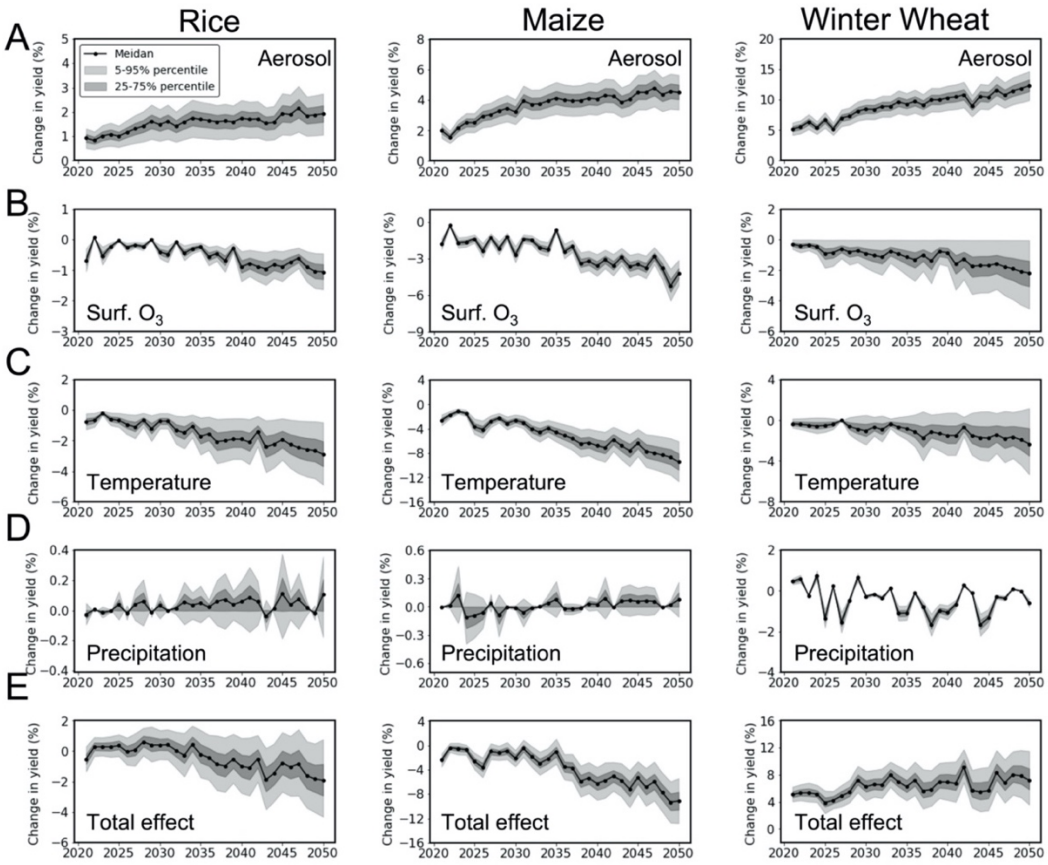

Figure 4.5: The projected future changes in country-level yield of rice, maize and winter wheat in response to four individual factor changes as well as their total effects under RCP8.5. The future change in yield is estimated from the difference between projected growing-season climate or pollution scenarios in 2021-2050 and the averaged scenarios in 2015-2020. The yield change is plotted as points (median estimates), with dark and light shaded areas (25-75% and 5-95% percentile estimates) calculated by bootstrapping the model 1,000 times.

Anthropogenic aerosols are projected to be continuously reduced in China by 2050. Thus, three crops all show a significant increasing trend in response to the aerosol variations (Figure 4.5A). Surface ozone level is projected to increase in the near

future (Figure 4.5B), likely due to the reduction in the ozone precursor NO_x and consequent ozone enhancement via the non-linear ozone chemistry (Le et al., 2020) as well as the effect of temperature increase. For rice by 2050, the ozone-induced yield loss (−1.1%) is close to the aerosol-induced yield gain (+1.9%). Future temperature increase is found to be the most critical factor for all three crop types (Figure 4.5C). It can cause trends of –0.8% $10yr^{-1}$, –2.5% $10yr^{-1}$, and –0.6% $10yr^{-1}$ for rice, maize, and wheat, respectively. Future precipitation changes will not impose a noticeable influence on the crops (Figure 4.5D). Taking four factors together, for rice and maize, the temporal evolutions and trends under the total effects largely resemble those of the temperature changes during 2020-2050 (Figure 4.5E). Therefore, the regime shifts after 2020 in the way that the climate variability, particularly the global warming, dominates over the pollution factors and profoundly determines the future rice and maize yields. For winter wheat, as it exhibits large sensitivity to aerosols (Figure 4.3B), its net yield trend during 2020-2050 is positive, mainly determined by the future aerosol reduction.

4.5 Conclusion and Discussion

In the present study, we develop a robust statistical model to predict three predominant crops in China, i.e., rice, maize, and winter wheat. Four key factors are taken into account when predicting crop yields, including the temperature, precipitation, AOD, and surface ozone over the growing seasons. To overcome the sparsity of the ground-level ozone observations over the 40-year time period, we employ a machine learning model and multiple sources of ozone, meteorological factors, as well as emissions since 1980. The ozone prediction from the ML model is reliable according to the cross-evaluation by the reserved ozone measurements. The statistical model exhibits high fidelity in reproducing the yields of three prevalent crops in China. With moderate uncertainty, the model helps us quantify the crop yield responses to different climate and pollution factors during different time periods in the past and future. We find the critical role of particulate pollution

in regulating interannual variations of crop yields in China. Moreover, the recent abatement of anthropogenic emission results in a net crop gain, which masks the crop loss due to the increased temperature and precipitation.

The findings of alternative models with different mathematical formats are consistent with our main conclusions derived from previous model. Moreover, we assessed the collinearity of all variables in SI Appendix, Table 4-6. These correlations are not strong to undermine our conclusions. Overall, our findings in this alternative model are consistent with previous models, AOD and O_3 negatively affect RYC for all three crops.

Some other factors related to crop yield deserve further investigations, such as CO_2 fertilization effect and nitrogen deposition. With the elevated atmospheric CO_2 concentrations, plant photosynthesis and crop yield is expected to increase (Ainsworth & Long, 2004). Meanwhile, C3 crops (i.e., rice and wheat) typically show larger increase in water use efficiency than C4 crops (i.e., maize) with higher surrounding CO_2 concentrations. Meanwhile, nitrogen deposition is also likely to increase crop yields to a lesser extent (Lombardozzi et al., 2018). Additional reactive nitrogen has been created due to human activities and contributed to the increase of terrestrial carbon sink (Wang et al., 2017). Since CO_2 concentrations and regional nitrogen availability has increased with time in the recent four decades, the yield benefit due to CO_2 fertilization and nitrogen deposition can then be captured by $f_1(y)$ in our statistical model. However, it remains unclear how the rate of CO_2 fertilization and nitrogen deposition will change in different regions in the future. Therefore, a better understanding of both effects in different cropping systems under various environmental conditions are needed to constrain our future predictions.

Our future predictions are based on historical response of crop yield to pollution and climate changes. Some papers have reported that the sensitivity of yield is becoming larger to drought accompanied with higher planting density under global

warming (Lobell et al., 2020; Lobell & Burke, 2008). Meanwhile, the uncertainties in the future yield response to the warming is expected to be larger than precipitation due to the greater magnitude of temperature change relative to the year-to-year variations in precipitation (Lobell & Burke, 2008). Future studies are needed to combine yield and temperature data of different scales, i.e., site and region, to explore explicitly the relationships between warming and yield to close the yield gap in the changing climate.

In summary, our finding demonstrates the co-benefit of the recent air pollution control policy from an agriculture and food perspectives. However, such a benefit will be significantly offset or even outweighed by the exacerbated global warming. Hence, it will pose a great threat to global food security in the future, along with the growth of the world population. Our study calls for full consideration of air pollution impacts on the agriculture and crop yield on both interannual and decadal time scales when projecting future food production. Additionally, accurate long-term projections of particulate and ozone pollution are also in a pressing need to assess the future crop yield and to develop adaptation strategies.

4.6 Acknowledgements

The monthly temperature and precipitation products used in this study are publicly available at Copernicus Climate Change Service (https://cds.climate.copernicus.eu/). The monthly AOD reanalysis product is available at Goddard Earth Sciences Data and Information Services Center (https://disc.gsfc.nasa.gov/). The monthly surface ozone dataset is from the ChinaHighAirPollutants (CHAP) dataset (https://weijing-rs.github.io/product.html). The SPAM crop spatial distribution is available at https://www.mapspam.info/data/. The annual province-level crop statistics are from National Bureau of Statistics of China (https://data.stats.gov.cn/english/).

L.H. acknowledges the fellowship supported by the Resnick Sustainability Institute at California Institute of Technology. Y.W, J.L., C.F., J.H.J. and Y.L.Y. acknowledge the support of the Jet Propulsion Laboratory, California Institute of Technology, under contract with NASA. J.W. and Z.L. acknowledge the NASA Applied Science program (number: 80NSSC21K1980). We thank Drs. Xu Yue, Chao Liu, and Zhenong Jin for helpful discussions.

4.7 Appendix

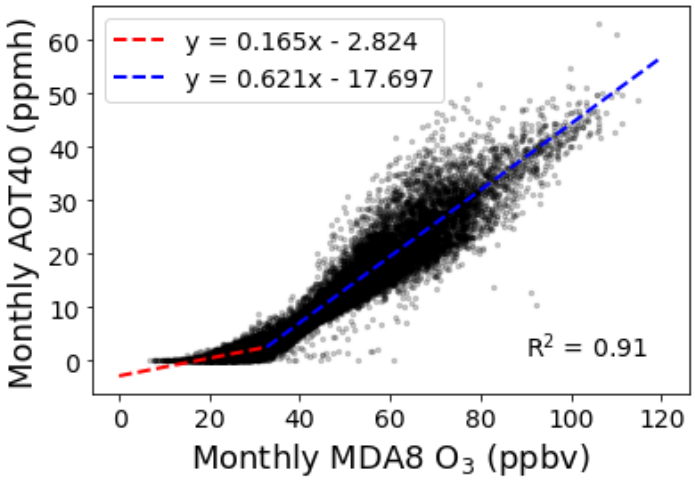

Figure 4.6: Relationship between monthly AOT40 and monthly MDA8 O3 from ground-based observations.

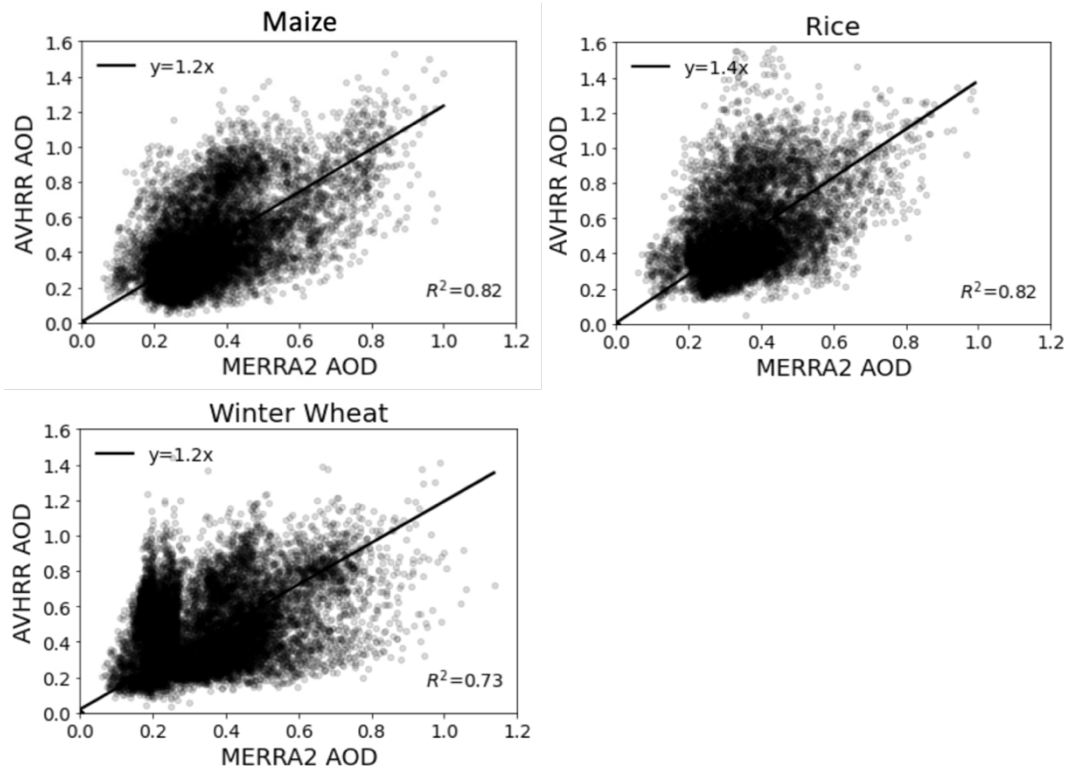

Figure 4.7: MERRA2 monthly AOD validation by AVHRR AOD during1982-2005.

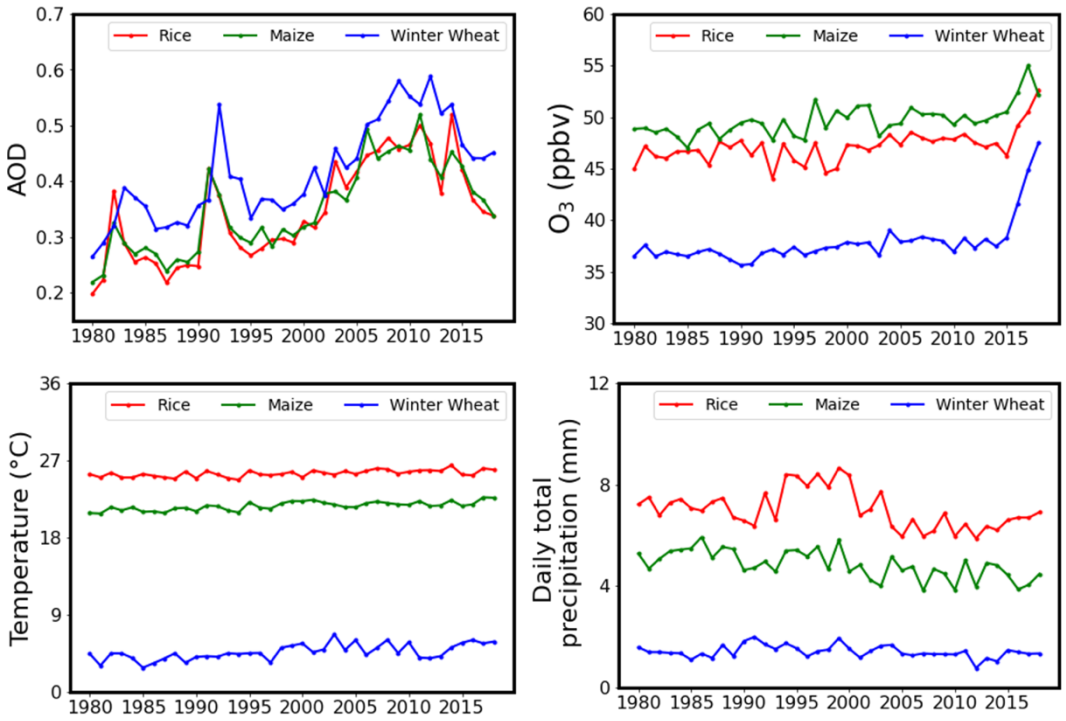

Figure 4.8: Trend of growing-season averaged AOD, surface O3, temperature, and precipitation for maize, single-season rice, and winter wheat.

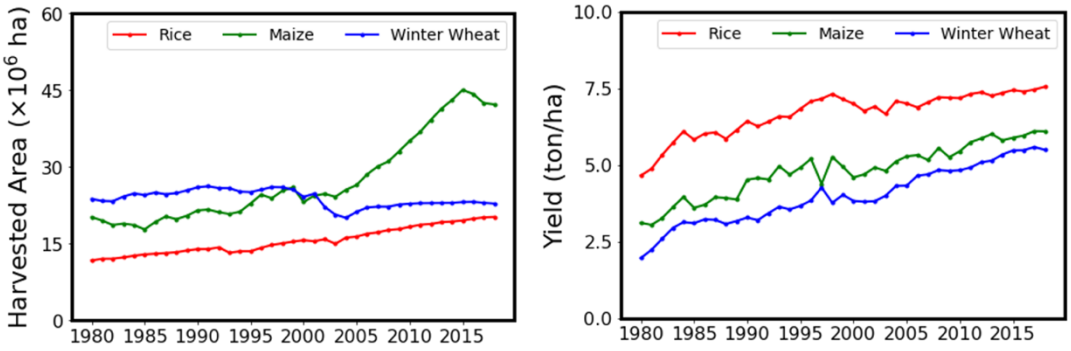

Figure 4.9: Trend of growing-season average annual total harvested area and country-averaged yields for maize, single-season rice and winter wheat.

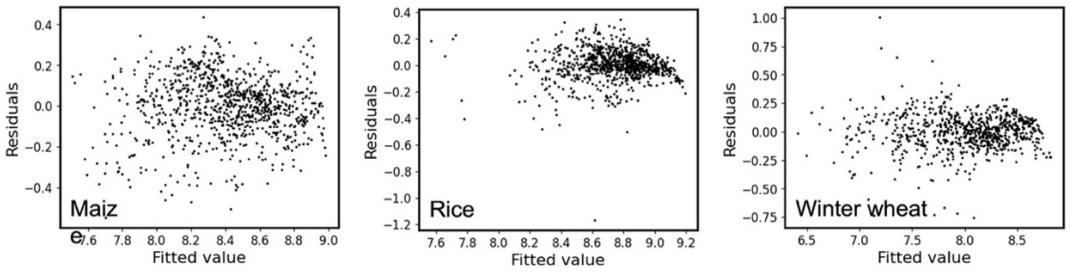

Figure 4.10: Residuals versus model fitted values for maize (left), single-season rice (middle) and winter wheat (right).

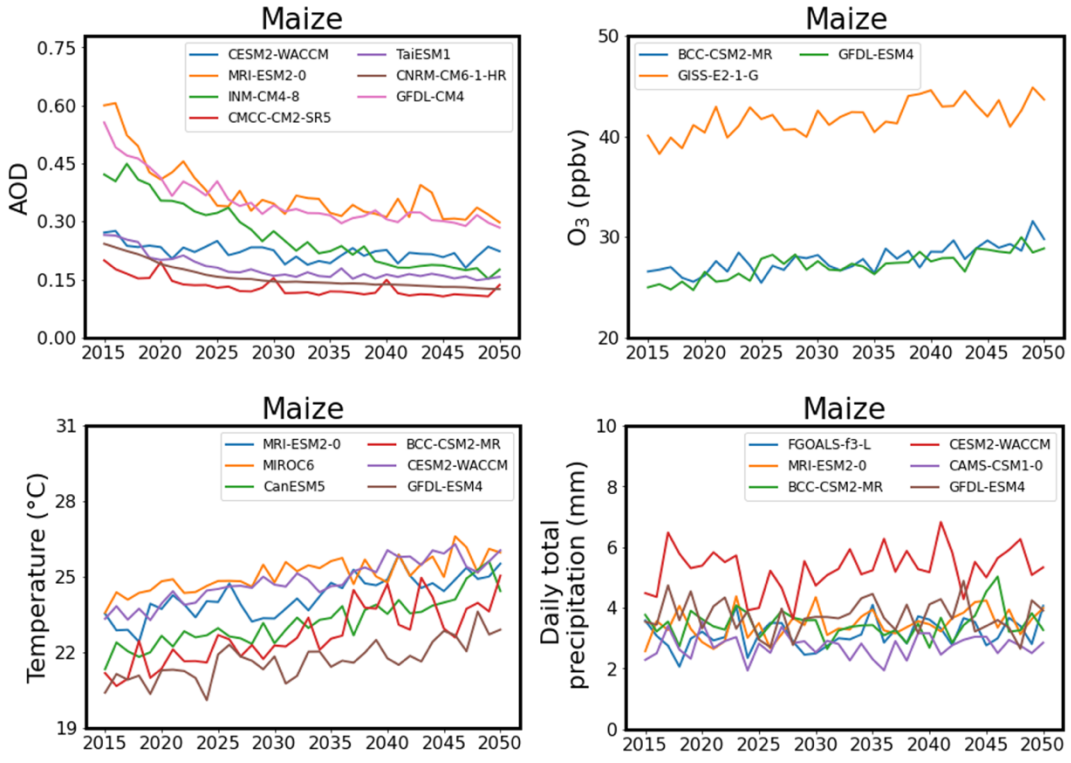

Figure 4.11: Trend of growing-season averaged AOD, surface O3, temperature and precipitation for maize of individual CMIP6 model (Table. S4) up to 2050.

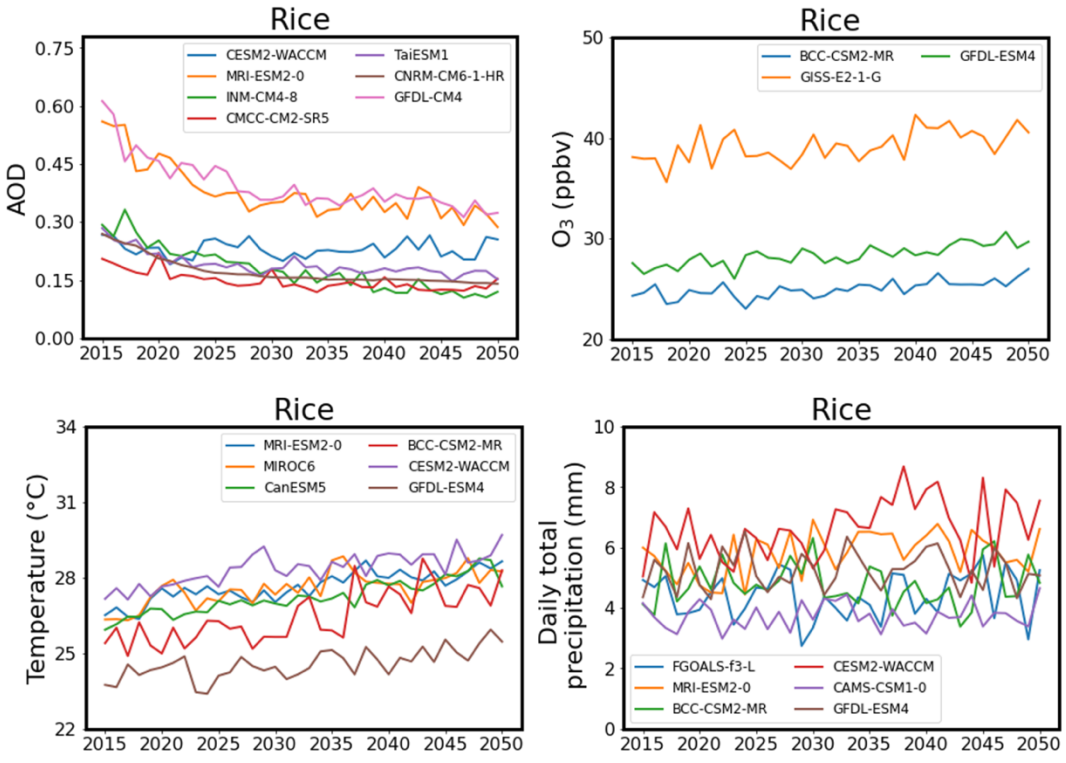

Figure 4.12: Trend of growing-season averaged AOD, surface O3, temperature and precipitation for single-season rice of individual CMIP6 model (Table. S4) up to 2050.

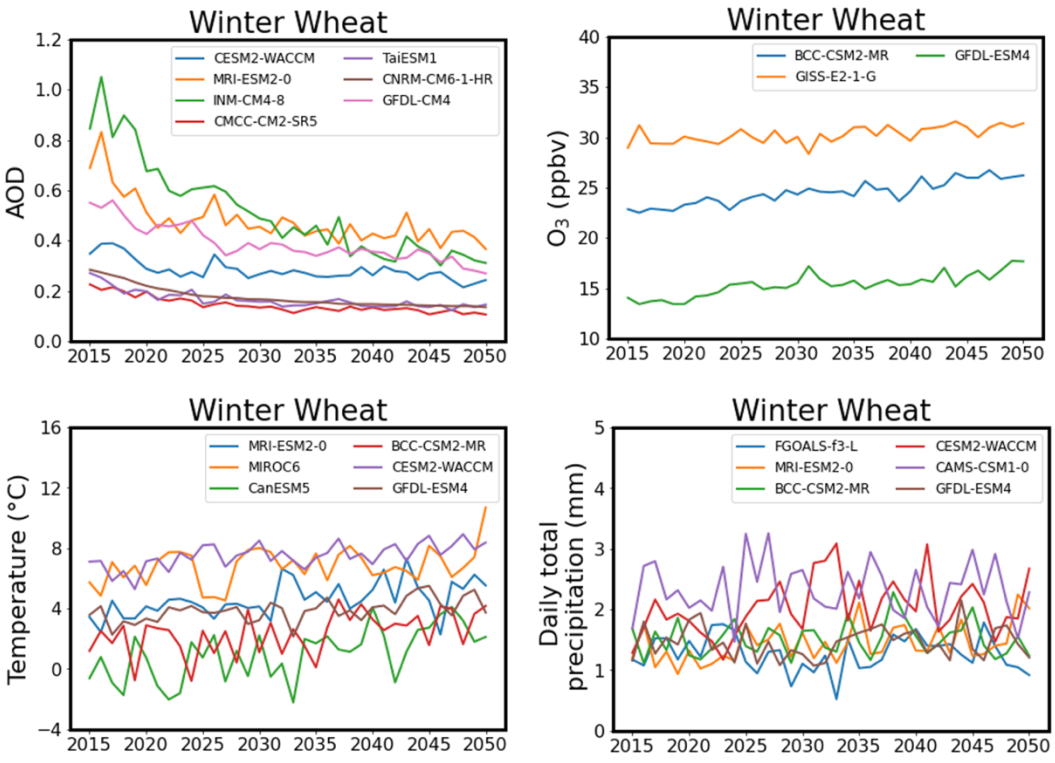

Figure 4.13: Trend of growing-season averaged AOD, surface O3, temperature and precipitation for winter wheat of individual CMIP6 model (Table. S4) up to 2050.

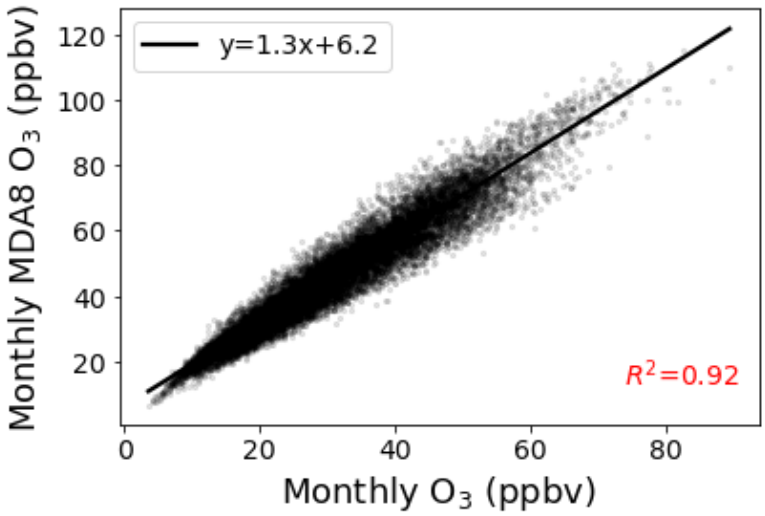

Figure 4.14: Monthly MDA8 vs. monthly mean O3 from ground-based observations in China.

Table 4-1: Regression specifications based on the default models

	Dependent Variable: *ln(yield)*		
	Maize	*Rice*	*Winter Wheat*
Temperature	-0.039***(0.013)	-0.016*(0.010)	-0.010(0.013)
Precipitation	0.003(0.006)	0.001(0.004)	-0.054***(0.020)
AOD	-0.364***(0.090)	-0.175***(0.068)	-0.594***(0.115)
O_3	-0.009*** (0.002)	-0.003(0.002)	-0.006(0.006)
Year	0.574**(0.048)	0.401***(0.040)	0.760***(0.062)
Province	0.007(0.074)	-0.047*(0.048)	-0.393*(0.099)
Constant	9.282***(0.380)	8.969***(0.283)	8.199***(0.212)
R^2	0.812	0.786	0.893
Observations	939	938	795
Year Dummies	Y	Y	Y
Province Dummies	Y	Y	Y

Notes: Standard errors are presented in parentheses; ***P < 0.01, **P < 0.05, *P < 0.1. The year(province) variable in this table is an average across of all yearly (provincial) dummies. The 1st year (1980) in our sample is the base year for yearly dummies, and the base entity for provincial dummies is randomly selected by the software. The key coefficients will not change regardless of the dummy variable base year and province selection in the model.

Table 4-2: Regression specifications based on the model (1) with interaction terms

	Dependent Variable: *ln(yield)*		
	Maize	*Rice*	*Winter Wheat*
Temperature	-0.135***(0.035)	-0.037(0.032)	-0.053*(0.028)
Precipitation	-0.021**(0.011)	0.011(0.007)	-0.013(0.032)
AOD	-0.691***(0.153)	-0.042(0.107)	-0.318**(0.162)
O_3	-0.055***(0.015)	0.022(0.014)	-0.007 (0.007)
AOD: Precipitation	0.059**(0.025)	-0.021(0.016)	-0.096**(0.051)
O_3: Temperature	0.002***(0.001)	-0.001*(0.0006)	-0.002***(0.0007)
Year	0.569**(0.048)	0.405**(0.038)	0.739***(0.062)
Province	-0.020(0.075)	-0.036*(0.051)	-0.384*(0.100)
Constant	11.761***(0.880)	7.555***(0.854)	7.631***(0.282)
R^2	0.815	0.787	0.894
Observations	939	938	795
Year Dummies	Y	Y	Y
Province Dummies	Y	Y	Y

Notes: Standard errors are presented in parentheses; ***P < 0.01, **P < 0.05, *P < 0.1. The year variable in this table is an average across of all yearly dummies. The 1st year (1980) in our sample is the base year for yearly dummies, and the base entity for provincial dummies is randomly selected by the software. The key coefficients will not change regardless of the dummy variable base year and province selection in the model.

Table 4-3: Regression specifications based on the models (2) with nonlinear

	Dependent Variable: *ln(yield)*		
	Maize	*Rice*	*Winter Wheat*
Temperature	-0.021**(0.010)	-0.004(0.008)	-0.008(0.008)
Precipitation	0.006(0.005)	0.005(0.003)	-0.023(0.016)
AOD	-0.217***(0.064)	-0.191***(0.048)	-0.251***(0.085)
O_3	-0.008***(0.002)	-0.003*(0.002)	-0.002(0.004)
Year	1.979***(0.181)	1.651***(0.149)	1.406***(0.257)
$Year^2$	-0.0005***(0.00005)	-0.0004***(0.00004)	-0.0003***(0.00006)
Province	0.085(0.059)	-0.027*(0.044)	-0.340*(0.077)
Constant	-1990.2***(181.07)	-1654.5***(148.80)	-1417.3***(256.41)
R^2	0.797	0.767	0.876
Observations	939	938	795
Year Dummies	N	N	N
Province Dummies	Y	Y	Y

Notes: Standard errors are presented in parentheses; ***P < 0.01, **P < 0.05, *P < 0.1. The year variable in this table is an average across of all yearly dummies. Instead of dummies, we directly use the year and its quadratic term as of our explanatory variables. The base entity for provincial dummies is randomly selected by the software. The key coefficients will not change regardless of the dummy variable base province selection in the model.

Table 4-4: The growing-season (January-April) averaged daily total precipitation (unit: mm) and relative yield change (RYC, unit: %) corresponded to 1mm increase of daily total precipitation.

Province	daily precipitation (mm)	RYC (%)
Hebei	0.47	0.7%
Shanxi	0.76	8.4%
Jiangsu	1.86	-12%***
Anhui	2.02	-17%***
Shandong	0.72	-2%
Henan	1.03	-9%***

Table 4-5: CMIP6 monthly models and experiments using in this study.

Variable	Modelling Group	ESM	Model Variant	Experiment ID	Nominal Resolution	Table ID
Surface Temperature (ts)	MRI	ESM2-0	r1i1p1f1	ssp585	100km	Amon
	MIROC	MIROC6	r1i1p1f1		250km	
	CCCma	CanESM5	r11i1p1f1		500km	
	BCC	CSM2-MR	r1i1p1f1		100km	
	CESM2	WACCM	r1i1p1f1		100km	
	GFDL	ESM4	r1i1p1f1		100km	
Precipitation flux (pr)	BCC	CSM2-MR	r1i1p1f1		100km	
	CAMS	CSM1-0	r1i1p1f1		100km	
	CESM2	WACCM	r2i1p1f1		100km	
	FGOALS	fe-L	r1i1p1f1		100km	
	GFDL	ESM4	r1i1p1f1		100km	
	MRI	ESM2-0	r1i1p1f1		100km	
AOD at 550nm (od550aer)	TaiESM1	TaiESM1	r1i1p1f1		100km	
	CMCC	CM-2-SR5	r1i1p1f1		100km	
	MRI	ESM2-0	r1i1p1f1		100km	
	CNRM	CM6-1	r1i1p1f2		250km	
	CESM2	WACCM	r2i1p1f1		100km	
	INM	CM4-8	r1i1p1f1		100km	
	GFDL	CM4	r1i1p1f1		100km	
ozone (o3)	BCC	CSM2	r1i1p1f1		100km	
	GISS	E2-1	r1i1p3f1		250km	
	GFDL	ESM4	r1i1p1f1		100km	

Table 4-6: Variables Correlations of maize, rice and winter wheat from 1980 to 2018.

Maize

	Year	ln(yield)	Temperature	Precipitation	AOD	O_3
Year	1					
ln(yield)	0.582	1				
Temperature	0.083	-0.139	1			
Precipitation	-0.168	-0.416	0.179	1		
AOD	0.438	0.319	0.478	-0.013	1	
O_3	0.108	0.424	-0.339	-0.395	0.522	1

Rice

	Year	ln(yield)	Temperature	Precipitation	AOD	O_3
Year	1					
ln(yield)	0.517	1				
Temperature	0.075	0.186	1			
Precipitation	-0.109	-0.210	-0.184	1		
AOD	0.449	0.451	0.187	-0.283	1	
O_3	0.094	0.451	-0.148	-0.512	0.601	1

Winter Wheat

	Year	ln(yield)	Temperature	Precipitation	AOD	O_3
Year	1					
ln(yield)	0.430	1				
Temperature	0.096	-0.200	1			
Precipitation	-0.070	-0.315	0.664	1		
AOD	0.380	0.195	0.727	-0.489	1	
O_3	0.338	0.311	-0.236	-0.085	-0.212	1

C h a p t e r 5

MARKED IMPACTS OF POLLUTION MITIGATION ON CROP YIELDS IN CHINA

He, L., Byrne, B., Yin, Y., Liu, J. and Frankenberg, C., 2022. Remote-Sensing Derived Trends in Gross Primary Production Explain Increases in the CO2 Seasonal Cycle Amplitude. *Global Biogeochemical Cycles*, *36*(9), p.e2021GB007220. DOI: https://doi.org/10.1029/2021GB007220

5.1 Abstract

An increase in the seasonal cycle amplitude (SCA) of atmospheric CO_2 since the 1960s has been observed in the Northern Hemisphere (NH). However, dominant drivers of the amplified CO_2 seasonality are still debated. The peak of CO_2 uptake by vegetation is critical in shaping the seasonality of atmospheric CO_2. Using satellite-upscaled gross primary production (GPP) from both FLUXCOM and satellite-derived near-infrared reflectance of vegetation (NIR_V) since 2001, we demonstrate that peak season GPP has increased across the northern extratropics over the last two decades. We relate this productivity increase to changes in the SCA of CO_2 using an atmospheric chemical transport model. This increased photosynthesis carbon uptake has strongly contributed to CO_2 SCA trends, but with substantial latitudinal and longitudinal variations. Despite a general increase in the CO_2 SCA across the NH, there are distinct regional differences. These differences are mainly controlled by regional biosphere carbon fluxes, and the remainder explained by non-biome factors, which include large-scale atmospheric transport, changes in fossil fuel combustion, biomass burning and oceanic fluxes. Using the global network of flask and in situ CO_2 measurement sites, we find that SCA trends at high latitude sites, such as Barrow (BRW) and Alert (ALT), are mainly driven by increasingly productive natural ecosystems, whereas mid latitude sites around the Midwest United States are mainly impacted by intensified agriculture as well as atmospheric transport. Averaging across the 15 long-term surface CO_2 sites,

forests contribute 26% (7%) to the SCA trends, while crops contribute 17% (24%) and the combined shrubland, grassland and wetland regions contribute 23% (37%) for simulations driven by NIRv (FLUXCOM) ecosystem fluxes. Our findings demonstrate that satellite inferred trends of ecosystem fluxes can capture the observed CO_2 SCA trend.

5.2 Introduction

The seasonal cycle of atmospheric CO_2 in the Northern Hemisphere (NH) is mainly driven by seasonal changes in the net ecosystem change (NEE), which is the difference between photosynthetic carbon uptake (gross primary production, GPP) and ecosystem respiration (TER) (Randerson et al., 1997). Surface and air-borne measurements have shown a 30~50% increase in the seasonal cycle amplitude (SCA) of lower tropospheric CO_2 north of 45°N since the 1960s (Bacastow et al., 1985; Keeling et al., 1996; Forkel et al., 2016; Graven et al., 2013). The amplified CO_2 seasonality has been suggested to be driven by increasing productivity of high-latitude forests in the Northern Hemisphere, mainly from Arctic and boreal regions (Forkel et al., 2016; Graven et al., 2013; Lin et al., 2020; J. Liu et al., 2020; Piao et al., 2018; Yin et al., 2018). Meanwhile, Gray et al. (2014) and Zeng et al. (2014) reported that increasing cropland productivity linked with land use change and management has a non-negligible impact on the CO_2 seasonality trend. Despite a general SCA increase observed at most surface sites across the NH, the magnitude and range of trends and interannual variations differ from site to site (Forkel et al., 2016; Graven et al., 2013; Piao et al., 2018; Yuan et al., 2018). This suggests that both atmospheric circulation and heterogeneity in regional fluxes play an important role in trends at different locations.

Current earth system models generally underestimate the CO_2 SCA increase and disagree on the underlying mechanisms of whether rising CO_2, climate change, land use change or atmospheric transport is the dominant factor of such an increase (Bastos et al., 2019; Graven et al., 2013; Piao et al., 2018; Thomas et al., 2016;

Yuan et al., 2018; Zhao et al., 2016). This suggests that some key biophysical or biochemical processes are missing or underrepresented in these models.

In this study, we employ space-based remote sensing to track spatial and temporal changes in peak season GPP and then, using a chemical transport model, examine whether these changes can explain the observed SCA trends at surface CO_2 measurement sites across the northern extratropics. Remote sensing of reflectance-based vegetation indices (VIs) has been widely used to track regional to global changes in ecosystem productivity. Previous studies have found that most regions of the global lands show a persistent and widespread increase of VIs (greenness) during the growing season since the 1980s, while only limited regions exhibit browning (Anav et al., 2015; Chen et al., 2019; Zhu et al., 2016). This greening trend is consistent with increased peak growing season uptake (Huang et al., 2018), which might explain CO_2 SCA changes. In this study, we aim to directly link remote sensing-based vegetation trends to atmospheric CO_2. Remote sensing-based variations in ecosystem uptake can be coupled with an atmospheric transport model to explain variations in atmospheric CO_2 (Fung et al., 1987), but only now are space-based GPP datasets long enough to examine long-term trends in the SCA amplitude.

The Normalized Difference Vegetation Index (NDVI)-weighted near-infrared reflectance of vegetation (NIR_V), has shown great potential to capture global photosynthesis changes (Badgley et al., 2017, 2019), especially over crop regions, which are likely underestimated in process-based photosynthesis models (Guanter et al., 2014; Sun et al., 2021). Meanwhile, semi-empirical data-driven approaches have been established to upscale GPP from eddy-covariance fluxes to the globe. For example, the state-of-art global GPP product FLUXCOM ($GPP_{Fluxcom}$) is upscaled from flux tower observations, driven by a variety of machine learning methods and remote sensing observations, such as NDVI and the Enhanced Vegetation Index (EVI) (Jung et al., 2020). Hence, $GPP_{Fluxcom}$ is considered to

predict GPP well in regions with representative flux tower observations. Combined with FLUXCOM TER ($TER_{FLUXCOM}$) datasets, these two novel datasets provide bottom-up NEE estimates at high spatiotemporal resolutions and allow us to track interannual changes of land biosphere carbon fluxes.

Seasonal NEE changes drive variations in atmospheric CO_2, and consequently the CO_2 seasonal amplitude. Here, we test whether the NIRv-based and FLUXCOM NEE datasets, when applied in an atmospheric transport model, are capable of tracking changes in atmospheric CO_2, including trends and interannual variations in the observed CO_2 SCA. To test our hypothesis, we first investigate the trend of peak growing season FLUXCOM GPP and satellite NIRv during the 2001-2018 period. Then we simulate surface CO_2 seasonality with a global atmospheric transport model, driven by NIRv-based and FLUXCOM NEE of individual ecosystems (e.g., cropland, forest, and other vegetation types) and other flux components (e.g., fossil fuel, biomass burning and air-sea fluxes). Then we compare the simulated CO_2 seasonal amplitude with observations at 15 surface CO_2 sites (including 5 coastal sites and 10 continental sites) of 12-year or longer records in the NH, and further quantify the relative contribution of different land cover types at these sites. Previous studies have mostly relied on limited remote coastal stations located primarily offshore, which are far away from large terrestrial signals and reflect well-mixed air masses, mainly to avoid the complexities of atmospheric boundary layer dynamics and topography in transport modeling (Forkel et al., 2016; Graven et al., 2013; Keeling et al., 1996). With more continuous in-situ CO_2 measurements available across the globe, as well as the improvement of atmospheric transport models and meteorological reanalysis data, we can now better understand the spatiotemporal pattern of CO_2 signals (Bauer et al., 2015; Gaubert et al., 2019; Gelaro et al., 2017). In this study, we aim to incorporate both long-run coastal and continental sites to explore the dominant fluxes on the observed CO_2 signal changes at different locations.

5.3 Materials and Method

5.3.1 Bottom-up biosphere carbon flux estimate

For bottom-up estimates of spatially and temporally resolved biosphere carbon fluxes, we use two Moderate Resolution Imaging Spectroradiometer (MODIS) reflectance-based datasets, FLUXCOM (Jung et al., 2020) and NIRv-based NEE estimates (as explained in detail later).

5.3.1.1 FLUXCOM carbon fluxes

FLUXCOM uses machine learning to merge carbon flux measurements from FLUXNET eddy covariance (EC) towers with remote sensing and meteorological data to estimate net ecosystem exchange, gross primary productivity, and terrestrial ecosystem respiration and their uncertainties. Here, we use the 8-day 0.083° FLUXCOM remote sensing-based (RS) GPP and TER products, which have been found to have more realistic interannual variations in GPP than FLUXCOM remote sensing and meteorological -based (RS+METEO) products (Jung et al., 2020). The ensemble products of FLUXCOM-RS encompass estimates of different machine learning estimates and flux partitioning variants for GPP and TER (Jung et al., 2020). For each ensemble member, fluxes are estimated from MODIS NDVI and EVI, land surface temperature, plant functional type and incoming global radiation (Jung et al., 2020). NEE is calculated as the difference between TER and GPP.

5.3.1.2 NIRv-based carbon fluxes

The NIRv-based global GPP estimate is derived from the relationship between GPP and NIRv at 105 EC towers covering a variety of vegetation types across different climate zones (**Table 5-2**), using the FLUXNET2015 dataset (Pastorello et al., 2020). We calculate daily tower GPP values (GPP_{site}) as the mean of both daytime (Lasslop et al., 2010) and night-time partition (Reichstein et al., 2005) approaches. NIRv was computed from MODIS MCD43A4 v006 BRDF corrected reflectance.

For training against flux tower measurements, we aggregate MODIS data within a 1km radius of the flux tower, deriving site-level NIRv ($NIRv_{site}$).

Some field experiments have found that taking incoming radiation into account further improves NIRv-based GPP estimates, especially for croplands (Dechant et al., 2020; Liu et al., 2020; Wu et al., 2020). Consequently, a new proxy, NIRv-radiance (NIRvRad), is defined as the product of NIRv and photosynthetically active radiation (PAR). Recent effort has been made to develop a high spatiotemporal resolution of the GPP dataset covering the Contiguous United States based on NIRvRad (Jiang et al., 2020). To account for changes in radiation, we use PAR estimates from the Breathing Earth System Simulator (BESS, Ryu et al., 2018). Here, we use site-level PAR (PAR_{site}) extracted from BESS for the corresponding grid cell that the selected tower falls in. Then, site-level NIRvRad ($NIRvRad_{site}$) can be derived using $NIRv_{site}$ and PAR_{site}.

Here, we propose a biome-specific relationship between GPP_{site} with $NIRv_{site}$ and PAR_{site} as follows:

$$NIRvRad_{site} = (NIRv_{site} - B_{soil}) \times PAR_{site}$$

$$GPP_{site} = a \times NIRvRad_{site} + b$$

$$GPP_{site} = a \times (NIRv_{site} - B_{soil}) \times PAR_{site} + b$$

where B_{soil} is a NIRv adjustment parameter for the soil background; a and b represent slope and intercept of the regression, respectively. We then derive biome specific regression parameters (a, b and B_{soil}) based on 16-day aggregated flux measurements and remote sensing datasets at 105 EC sites. **Figure 5.7** shows that our NIRv-based GPP estimates generally perform well with R^2 from 0.6 to 0.9 to capture tower GPP variation across different species. We find that the slope of croplands is larger compared to other vegetation types, underlining higher light use efficiency of crops, which can be related to the C4 photosynthetic pathway as well

as fertilization and irrigation. For comparison, we extract FLUXCOM GPP at these sites and find it agrees well with EC GPP observations (**Figure 5.8**).

We upscale the NIRv-GPP relationships derived at the site level to generate 8-day 0.083° global NIRv-based GPP estimates. First, we grid both daily 500-meter MODIS NIRv and daily 0.083° BESS PAR to 8-day 0.083°. Second, we calculate biome fractions at each 0.083° grid cell using the MODIS MCD12Q1 V6 data product, which provides the International Geosphere-Biosphere Programme (IGBP) biome type classification at 500-meter resolution after 2001. Third, we derive an averaged GPP at each grid cell using site-level NIRv-GPP relationships weighted by the corresponding biome fractions. The latitudinal distribution of NIRv-inferred GPP and FLUXCOM GPP are shown in **Figure 5.9**, both with peaks in tropics and regions around 50°N. NIRv-based NEE is obtained as the difference between FLUXCOM TER and NIRv-based GPP.

5.3.1.3 Trend of peak season vegetation growth

Here we look at the trend of peak values of annual FLUXCOM GPP and MODIS NIRv from 2001 to 2018. We aggregate daily 500-m MODIS NIRv to 8-day averages with a spatial resolution of 0.083° to match the spatial and temporal resolution of the FLUXCOM dataset. The annual peak season FLUXCOM GPP (GPP_{peak}) and MODIS NIRv ($NIRv_{peak}$) are defined as the 95%-percentile value of the same year for each grid cell. We calculate the spatial patterns of the long-term trend ($Trend_{absolute}$) from 2001 to 2018 of GPP_{peak} and $NIRv_{peak}$ using ordinary least squares linear regression for each grid. We derive the long-term relative trend ($Trend_{relative}$, unit: % $year^{-1}$) by normalizing $Trend_{absolute}$ by the 5-year average GPP (GPP_{peak}) or NIRv ($NIRv_{peak}$) over 2001 to 2005.

We also calculate the frequency of the greening/browning trends north of 15°N grouped by land cover, including forest, crop, the combination of shrubland, grassland and wetland north of 23°N ($SGW_{>23°}$) and all biomes south of 23°N

($Veg_{<23°}$). For each 0.083° grid cell, different vegetation fractions are calculated based on the MODIS MCD12Q1 V6 IGBP data product of 500-meter resolution in 2018. The definition of each land cover is followed in **Table 5-1**. We use a latitude threshold of 23°N here, mainly to separate tropical regions and south from other NH ecosystems. Then, for each pixel at 0.083°, the dominant vegetation type is identified, and the spatial distribution of land cover is shown in **Figure 5.1**.

Table 5-1: Definition of different land cover based on MODIS MCD12Q1 V6 IGBP data product.

Label	**Biome**	**Extent**
Cropland	cropland + cropland/natural veg mosaics	North of 23° with India cropland
Forest	evergreen needle + evergreen broadleaf + deciduous needle + deciduous broadleaf + mixed forest + savannas + woody savannas	North of 23°
$SGW_{>23°}$	open shrubland + closed shrubland + grassland + wetland	North of 23°
$Veg_{<23°}$	all biomes	South of 23° except for India cropland

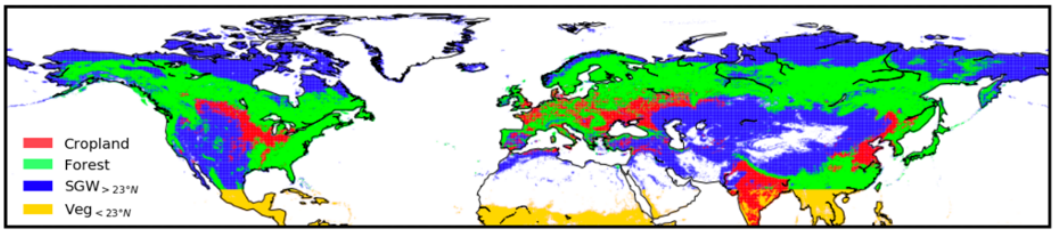

Figure 5.1: Spatial distribution of cropland, forest, SGW>23° and Veg<23° followed by the definition in Table 1.

5.3.2 Bottom-up biosphere carbon flux estimate Simulations of atmospheric CO_2

To relate trends in ecosystem carbon fluxes to atmospheric CO_2, we use an atmospheric chemical transport model (CTM) (**Sec 5.3.2.1**) to model 3D global CO_2 distributions in time. We sample modeled CO_2 at the times and locations of surface observations (**Sec 5.3.2.2**). The SCA trends are then calculated for collocated simulations and measurements (**Sec 5.3.2.3**). Comparing observed versus simulated SCA trends allows us to evaluate whether modeled GPP variations can explain the observed SCA trends and major factors drive the observed trends at different sampling sites (**Sec 5.3.2.4**).

5.3.2.1 Atmospheric transport model

NEE can be related to atmospheric CO_2 measurements through a CTM. Here we simulate atmospheric CO_2 fields and measurements using the Greenhouse Gas Framework - Flux (GHGF-Flux) transport model. GHGF-Flux is a flux inversion system developed under the NASA Carbon Monitoring System Flux (CMS-Flux) project (https://cmsflux.jpl.nasa.gov) and is based on the GEOS-Chem atmospheric chemistry transport model (Henze et al., 2007; Liu et al., 2014). Atmospheric transport is driven by the Modern Era Retrospective Analysis for Research and Applications, Version 2 (MERRA-2) meteorology produced with version 5.12.4 of the Goddard Earth Observing System (GEOS) atmospheric data assimilation system (Gelaro et al., 2017). To perform tracer transport, these fields are regridded

to 2° latitude by 2.5° horizontal resolution and archived with a temporal resolution of three hours except for surface quantities and mixing depths, which have a temporal resolution of one hour. Transport is performed with a 15-min dynamical time step from 2001 to 2018.

Several different surface flux datasets are utilized for the experiments performed here. Fossil fuel emissions are obtained from the "Miller" emissions dataset (Jacobson et al., 2020). The Miller emission dataset maps country total fossil fuel emissions from CDIAC (Boden et al., 2017) onto a 1x1 degree map according to the spatial patterns from EDGAR v4.2 inventories (Janssens-Maenhout et al., 2011). As Boden et al. (2017) only covers emissions through 2014, fossil fuel emissions are estimated through 2018 by extrapolating the percentage change for each fuel type for each country from British Petroleum (Ersoy et al., 2019). Biomass burning (BB) emissions of CO_2 (including small fires) are obtained from version 4 of the Global Fire Emissions Database (GFED4.1s) (Giglio et al., 2013; Randerson et al., 2012; Van Der Werf et al., 2017). GFED4.1s provides estimates of biomass burning using MODIS 500 m burned area (Giglio et al., 2013), 1 km thermal anomalies, and 500 m surface reflectance observations to statistically estimate burned area associated with small fires (Randerson et al., 2012). We incorporate the diurnal cycle in biomass burning based on Mu et al. (2011). Daily ocean fluxes spanning 2001-2019 are obtained from the ECCO-Darwin-V4 model (Brix et al., 2015; Dutkiewicz et al., 2009; Menemenlis et al., 2008). ECCO-Darwin-V4 model is an ocean biogeochemistry general circulation model based on combining the following components: (i) a full-depth, eddying, global-ocean configuration of the Massachusetts Institute of Technology general circulation model (MITgcm), (ii) an adjoint-method-based estimate of ocean circulation from the Estimating the Circulation and Climate of the Ocean, Phase II (ECCO2) project, (iii) the MIT ecosystem model “Darwin”, and (iv) a marine carbon chemistry model.

To separate the impact of atmospheric transport, we generate a climatological seasonal cycle of NEE that is annually repeated over 2001-2018 ($NEE_{seasonality}$). These climatological experiments are calculated as the mean of 2010-2015 NEE for the three GOSAT+surface+TCCON inversions of (Byrne et al., 2020a&b). The anomalies of FLUXCOM GPP (ΔGPP_{Fluxom}), NIRv-inferred GPP (ΔGPP_{NIRv}) and FLUCOM TER ($\Delta TER_{Fluxcom}$) are deseasonalized by subtracting the corresponding averaged seasonality during 2001 to 2018. We only incorporate anomalies of these fluxes rather than their mean seasonality because FLUXCOM NEE overestimates the magnitude of global annual total NEE significantly (-17 Pg C $year^{-1}$), suggesting a bias in spatial sampling of flux towers, some missing components related to carbon release from ecosystem to the atmosphere and large uncertainties in scaling (Jung et al., 2020; Keenan & Williams, 2018).

Seven forward simulations are performed over the 2001-2018 period by applying different sets of surface fluxes. A one-year spin-up simulation was performed over 2000. This spin up was run from the optimized CO_2 fields for Jan 1, 2015, from Byrne et al. (2020a). The global mean difference between the one-year spin-up and in situ measurements was then subtracted. $S_{Baseline}$ is driven by time-varying FF, BB and ocean fluxes, but with constant NEE seasonality. This simulation estimates changes in the SCA amplitude in the absence of trends in NEE. When variations in biosphere carbon fluxes are taken into account, we include anomalies (or deseasonalized, with the removal of the mean seasonal cycle from 2001 to 2018) of $GPP_{Fluxcom}$, TER_{Fluxom} and GPP_{NIRv} for the baseline run, named as $S_{Fluxcom}$ and S_{NIRv}, respectively. **Figure 5.2** shows a more detailed illustration of constructing $S_{Baseline}$, $S_{Fluxcom}$ and S_{NIRv} based on CO_2 fluxes from multiple sources.

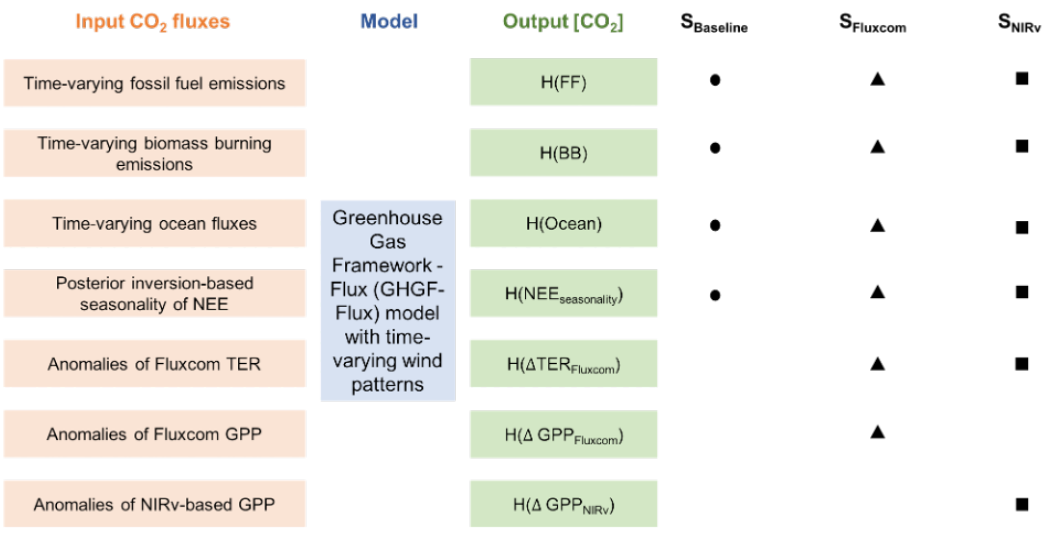

Figure 5.2: Diagram of the $S_{Baseline}$, $S_{Fluxcom}$ and S_{NIRv} simulations based on CO_2 fluxes from multiple sources. [CO_2] represents the atmospheric CO_2 concentrations. Mathematically, [CO_2] simulated in $S_{Baseline}$, $S_{Fluxcom}$ and S_{NIRv} can be formulated as H(FF) + H(BB) + H(Ocean) + $H(NEE_{seasonality})$, H(FF) + H(BB) + H(Ocean) + $H(NEE_{seasonality})$ + $H(\Delta TER_{Fluxcom})$ + $H(\Delta GPP_{Fluxcom})$ and H(FF) + H(BB) + H(Ocean) + $H(NEE_{seasonality})$ + $H(\Delta TER_{Fluxcom})$ + $H(\Delta GPP_{NIRv})$, where H(X) denotes the application of a forward atmospheric model to simulate CO_2 concentrations driven by fluxes X.

5.3.2.2 Surface atmospheric CO_2 measurements

To examine whether trends in FLUXCOM and NIRv-GPP can explain measured SCA trends, we use atmospheric CO_2 measurements at 15 surface sites, which have 12-year or longer records, including 5 coastal sites and 10 continental sites in the NH. The list of selected sites can be found in **Table 5-3**. We extracted the hourly surface CO_2 observations at the selected sites from Observation Package (ObsPack) data (Schuldt et al., 2020). For sites other than MLO and IZO, we filter the data by using afternoon measurements from 12pm to 4pm local time to ensure that the boundary layer is well mixed.

5.3.2.3 SCA trend calculations

The seasonal cycle amplitude (SCA) is defined as the magnitude of the peak to trough of the detrended seasonal cycle, after detrending the timeseries using the NOAA fitting package "ccgcrv" (Thoning & Tans, 1989). Daily gridded output and in-situ observations are aggregated into 14-day averages before curve-fitting.

For the CO_2 SCA calculation at each site, we conduct an uncertainty analysis of the derived SCA by applying the perturbation to the measurements as follows:

$$CO_{2_{pseudo}}(t) = CO_2(t) + \varepsilon(t) \times CO_{2_{uncertainty}}(t)$$

where t represents the index of time step;ε follows a standard uniform distribution; $CO_{2pseudo}$, CO_2 and $CO_{2uncertainty}$ refer to the perturbed CO_2 measurements, simulated (including $S_{Baseline}$, $S_{Fluxcom}$ and S_{NIRv}) CO_2 measurements and the uncertainties of modeled CO_2, respectively. $CO_{2uncertainty}$ is an estimate of observation, model transport, and representation errors. In other words, it is the standard deviation of the data-model mismatch for CarbonTracker CT2019B simulation (Jacobson et al. 2020), which is a widely used estimate of the error in assimilating these data into a transport model (e.g., OCO-2 MIP inversions). $CO_{2uncertainty}$ is usually small in coastal sites compared to continental sites. We run the curve-fitting algorithm 1,000 times with sampling ε from the standard normal distribution. Then we have the ensemble mean and standard deviation, which represents uncertainties in the derived SCA for each year. The SCA of observed and simulated CO_2 time series at 15 sampling sites is shown in **Figure 5.10**.

For individual runs, we calculate the SCA trend using 75% samples over the observed period using ordinary least squares linear regression. To make sure that the derived trend is not influenced by the sampling bias at the beginning of the measurement, we drop the SCA in the first year which does not cover the whole growing season. Then we compute ensemble mean and standard deviation of the SCA trend across all 1,000 samples, which also provides an uncertainty estimate of

the derived SCA trend. We apply a similar procedure to gridded GEOS-Chem outputs to derive the spatial pattern of CO_2 SCA trend of simulations $S_{Baseline}$, $S_{Fluxcom}$ and S_{NIRv}.

5.3.2.4 Separate different factors on CO_2 SCA trends

To identify the contribution of the observed CO_2 SCA trend from different regions, we separate the global terrestrial ecosystems into four tagged regions defined in **Table 5-1** and run GHGF-Flux driven by anomalies of GPP_{Fluxom}, GPP_{NIRv} and $TER_{Fluxcom}$ in each region independently. This enables the separation of regional CO_2 tracers, which can be summed to derive the total CO_2 response to all impact factors. The effects of transport, FF, BB, ocean, cropland, forest, $SGW_{>23^\circ}$ and $Veg_{<23^\circ}$ on seasonal CO_2 changes are differentiated by designing the following five transport simulations. S1 uses time-varying wind patterns with constant NEE seasonality, so that it can be interpreted as the effect of wind. Then, time-varying non-biome fluxes of BB, FF and air-sea fluxes are added to S1 in order to separate their individual contributions, with corresponding simulations named as S2, S3 and S4, respectively. Then, anomalies of biome fluxes including $SGW_{>23^\circ}$ and $Veg_{<23^\circ}$, forest and cropland are added in order to S4 to disentangle their individual contributions, named as S5, S6, S7 and S8, respectively. Differences between simulations can thus be used to quantify the contribution of various factors.

5.4 Results

5.4.1 Widespread increase of peak growing season vegetation growth across the Northern Hemisphere

Here we investigate the trend of peak growing season vegetation activity using photosynthesis estimate and proxy, namely $GPP_{Fluxcom}$ and MODIS NIRv respectively. We derive the 95%-percentile of seasonal variations of both datasets at 8-day intervals in each year to represent annual peak photosynthesis, which is denoted as GPP_{peak} and $NIRv_{peak}$. Overall, both GPP_{peak} and $NIRv_{peak}$ exhibit a

consistent widespread increase across the NH over 2001-2018 (**Figure 5.3**). A positive trend in GPP_{peak} is observed in most regions, with a large trend in croplands and some Arctic regions (**Figure 5.3A**). The mean GPP_{peak} trend for crops is 0.7 %/year. This trend is dominated by strong increases for croplands in North America (mean 1.1 %/year), northern China (mean 1.0 %/year) and India (mean 0.71 %/year), while a more modest trend is found for Europe (mean 0.5 %/year). The $SGW_{>23^\circ}$ biomes, composed primarily of high-latitude shrublands and mid-latitude grasslands also show a strong positive mean trend of 0.7 %/year despite a strong decrease in Kazakhstan. Subdividing these, this is a result of a strong trend in high-latitude shrublands (mean 0.7 %/year), mid-latitude grasslands (mean 0.8 %/year), and modest trends elsewhere (mean 0.4 %/year). The trend of $NIRv_{peak}$ (**Figure 5.3B**) has similar spatial patterns with large increases in croplands, but also shows some differences, such as a large positive trend in Southeast China (mean 1.0 %/year) and less positive or even browning in high-latitude shrublands (mean 0.1 %/year).

The peak season TER also increases (**Figure 5.11**), with mean trends of 0.4, 0.1, 0.3 and 0.6 %/year for crops, forests, high-latitude shrublands and mid-latitude grasslands, respectively. The magnitude of these increases is smaller compared to that of GPP and NIRv, which implies an increasing maximum rate of carbon sequestration due to increased photosynthesis over the past two decades.

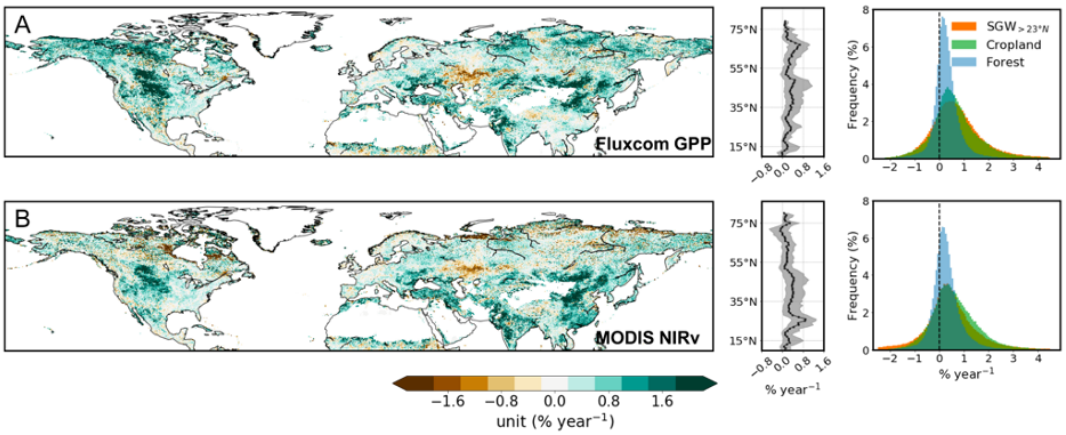

Figure 5.3: The trend of 95%-percentile 8-day Fluxcom GPP (A) and MODIS NIRv (B) (unit: % $year^{-1}$) from 2001 to 2018, including the spatial pattern, latitudinal distributions, and frequency plots. The grids are grouped into cropland, forest and $SGW_{>23°}$, and the definition can be found in **Table 5-1** and **Figure 5.1**. The difference between these two maps is shown in **Figure 5.12**. The trend of 95%-percentile 8-day Fluxcom GPP (unit: gC m^{-2} $year^{-1}$) from 2001 to 2018 is shown in **Figure 5.13**. The trend of annual mean 8-day Fluxcom GPP (unit: % $year^{-1}$) from 2001 to 2018 is shown in **Figure 5.14**.

5.4.2 Temporal changes of biosphere carbon fluxes shape the spatial pattern of the increase in CO_2 SCA

To test whether the observed enhancement of peak season vegetation growth has changed the CO_2 seasonal amplitude we examine the CO_2 trends from the model simulations. The baseline simulation, $S_{Baseline}$, which intends to isolate the CO_2 SCA trend that is not due to changes in NEE by using a climatological NEE seasonal cycle but time-varying BB, FF, and ocean fluxes, shows a wide-spread negative trend of the simulated CO_2 SCA across the NH (**Figure 5.4A**). The most negative trend with around -0.3ppm/year is observed in Central Europe due to reductions in fossil fuel emissions (**Figure 5.15**), as well as in central Siberia likely driven by increased biomass burning during spring and summer (Bondur et al., 2020; Kharuk et al., 2008, 2021; Kukavskaya et al., 2016; Ponomarev et al., 2016, 2019). In contrast, East China exhibits strong positive trends of approximately +0.3ppm/year. This is mainly due to increased fossil fuel emissions especially in winter, and hence enhanced seasonal cycle amplitude (**Fig. S9**). The zonal mean trend in $S_{Baseline}$ is most negative at higher latitudes, with a trend below -0.07 ppm/year between 60°N and 70°N.

Including changes in NEE, both $S_{Fluxcom}$ and S_{NIRv} show a predominantly positive trend of the CO_2 SCA across the NH (**Figure 5.4B & 5.4C**). The Midwest of the United States (US) exhibits more than +0.3ppm/year due to the enhanced peak season crop productivity (**Figure 5.3**). In India, S_{NIRv} results in a larger CO_2 SCA trend compared to $S_{Fluxcom}$, mainly because NIRv has a more pronounced increase

than FLUXCOM GPP over these regions (**Figure 5.3**). Clearly, temporal changes of biosphere carbon fluxes play an important role in shaping the spatial patterns of CO_2 SCA trends across the NH. Without these, SCA trends would even have been mostly negative in the northern hemisphere.

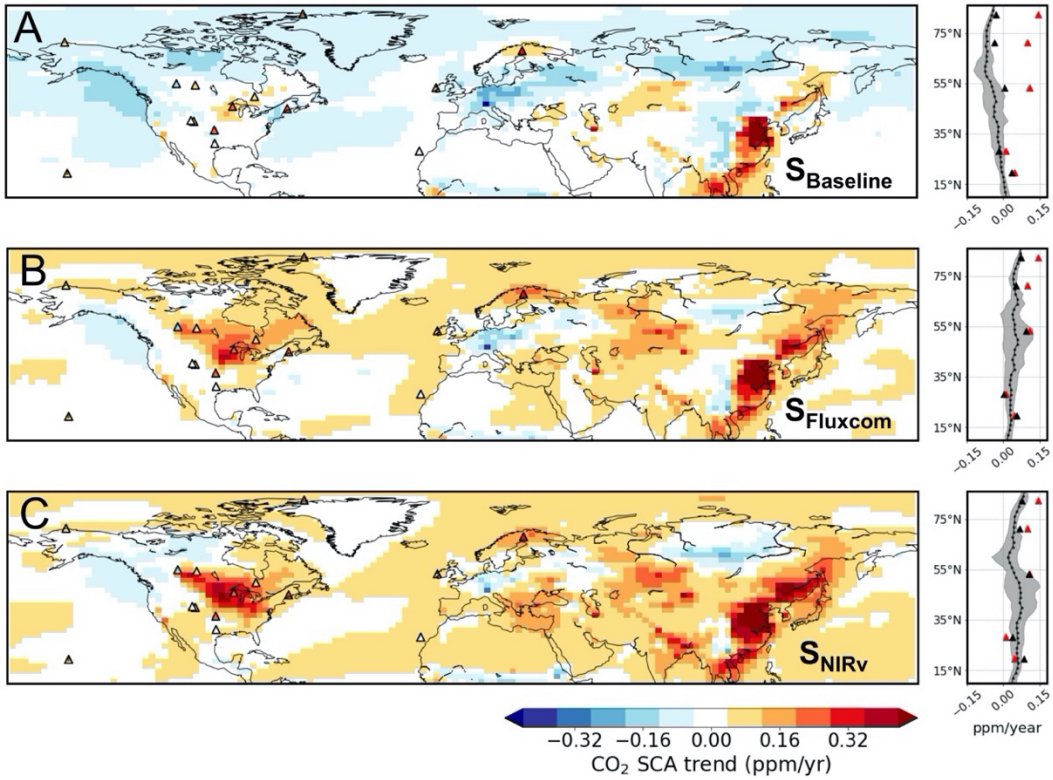

Figure 5.4: Spatial pattern and latitudinal distribution of simulated CO_2 SCA trend based on $S_{Baseline}$ (A), $S_{Fluxcom}$ (B) and S_{NIRv} (C) (unit: ppm/year). In the spatial map, the selected 15 surface sites are overlaid and colored by the observed trend. The latitudinal distribution shows the median of the simulated CO_2 SCA in bins of 1° latitude, with the shaded area representing 25–75% percentile trend estimates. Black and red triangles represent the simulated and observed CO_2 SCA trend at 5 coastal sites, including MLO, IZO, MHD, BRW and ALT, from low to high latitude.

5.4.3 Simulated GPP-driven CO_2 SCA trends consistent with observations

In comparison to $S_{Baseline}$, the $S_{Fluxcom}$ and S_{NIRv} runs show much better agreement with the observed CO_2 SCA. Compared against coastal background sites, $S_{Fluxcom}$ and S_{NIRv} capture an increase in the SCA trend with latitudes, which is in fact

negative for the baseline simulation. $S_{Baseline}$ only agrees well with observations at the two low latitude coastal sites, MLO and IZO (**Figure 5.4**). For mid-high latitude coastal sites, MHD, BRW and ALT, a significant positive CO_2 SCA trend of +0.11 to +0.14 ppm/year is observed (p-value < 0.01). However, $S_{Baseline}$ trends are negative at these sites, with -0.01 to -0.04 ppm/year, which shows that additional flux changes are required to explain observed positive changes in the CO_2 SCA. In contrast, $S_{Fluxcom}$ and S_{NIRv} provide estimates much closer to the observations, which underscores the important role of ecosystem flux variations in driving the observed increasing CO_2 SCA trend at mid-high latitude sites in the NH.

The coastal sites capture large-scale variations while continental sites are more influenced by regional fluxes. Here we investigate whether the simulated trends in the CO_2 SCA across 15 surface sites, including both continental and coastal sites, are consistent with observed trends. **Figure 5.5A** shows the simulated CO_2 SCA trends against observed trends. Across the sites, the observed CO_2 SCA trend ranges from -0.1 to +0.3 ppm/year. $S_{Baseline}$ largely underestimated the SCA trend with a slope of 0.49, with a range across sites of -0.20 to +0.15 ppm/year ($R^2 = 0.5$). According to **Figure 5.5B** & **5.5C**, $S_{Fluxcom}$ and S_{NIRv} better capture the observed CO_2 SCA trend with linear regression slopes of 0.80 and 0.99, respectively (both with $R^2 = 0.71$), explaining the overall magnitude of observed SCA trends. Overall, $S_{Fluxcom}$ and S_{NIRv} reproduce the observed CO_2 SCA trend across both coastal and continental sites well, whereas $S_{Baseline}$ consistently underestimates the trend. This suggests that the bottom-up estimates of FLUXCOM and NIRv-based NEE are capable of tracking changes in atmospheric CO_2, including the trend magnitude in the observed CO_2 SCA, in particular for NIR_v-based NEE.

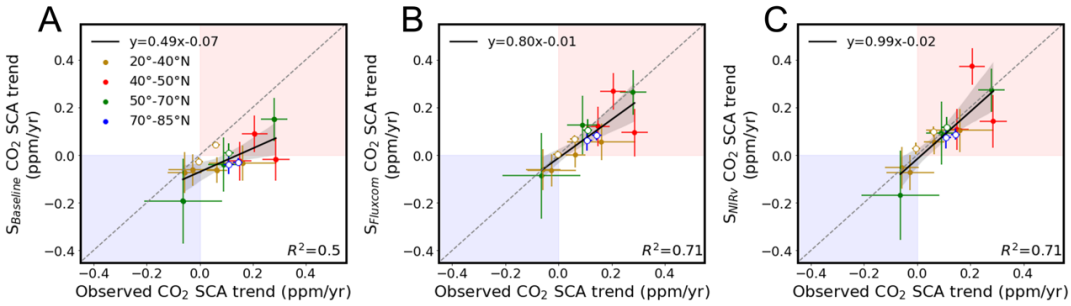

Figure 5.5: The comparison between observed and simulated CO_2 SCA trend derived from $S_{Baseline}$ (A), $S_{Fluxcom}$ (B) and S_{NIRv} (C). Filled (open) circles represent continental (coastal) surface CO_2 sites. Coastal sites include MLO, IZO, MHD, BRW and ALT. The point with error bars represents the ensemble mean and standard deviation of the derived CO_2 SCA trend using the bootstrapping the model uncertainties 1,000 times. **Table 5-4** reports the ensemble mean, median, standard deviation, 5%-tile and 95%-tile of the derived CO_2 SCA trend using the bootstrapping the model uncertainties 1,000 times. The time series of observed and simulated CO_2 SCA at individual sites can be found in **Figure 5.10**. The comparison between the observed and simulated CO_2 SCA at each sampling site and year can be found in **Figure 5.16**.

5.4.4 Regional contributions to the site-level CO_2 SCA trend

The peak season GPP trends show remarkable differences between regions and ecosystem, with particularly strong trends in croplands and Arctic ecosystems, for both the GPP and NIRv estimate (**Figure 5.3**). Here we examine the contribution of different regions and ecosystems to SCA trends.

Figure 5.6 shows the contributions of individual factors to the observed CO_2 SCA trend. For both $S_{Fluxcom}$ and S_{NIRv}, all biome types produce positive trends (bar above the zero-line), except for the forest impact on Lac La Biche, Alberta, Canada (LLB) with S_{NIRv}. Positive trends in the mid-latitudes are primarily constituted by croplands, forests and $SGW_{>23°}$. Although the estimated CO_2 SCA trends from $S_{Fluxcom}$ and S_{NIRv} are comparable with observations, the source regions driving these trends are quite different. S_{NIRv} generally has a larger estimate of agricultural contributions while $S_{Fluxcom}$ has a larger contribution from forests. For mid-latitude sites near the Northern America cropland (e.g., SGP and LEF), agricultural

contributions are comparable or even larger than other vegetation types. Forests and $SGW_{>23^\circ}$ also have quite strong impacts on mid-high latitude sites, whereas the relative importance of the two depends on the bottom-up ecosystem fluxes used.

In addition to biome driven trends, SCA trends from biomass burning emissions, fossil fuel emissions, and the mean seasonal cycle of NEE coupled with interannual variations (IAV) in transport had non-trivial impacts on the inferred trends in SCA. For mid-latitude sites, atmospheric circulation has comparable or even larger impacts than NEE changes. For example, atmospheric transport can explain around 50% CO_2 SCA trends at MLO, LEF and PAL. This highlights the potential impact of changes in atmospheric circulation patterns on observed trends in CO_2 SCA.

Biomass burning has a consistent negative impact on all sampling sites (more pronounced for sites north of 50°), which is related to increasing wildfires over boreal regions during summer in recent decades and hence reducing CO_2 drawdown in the peak growing season (Wang et al., 2021). Fossil fuel can exert either positive or negative influences, depending on the site location and assumed timing of fossil fuel emissions. Ocean has generally a small negative impact on most sites, except for BRW and ALT, with around -0.04 ppm/year.

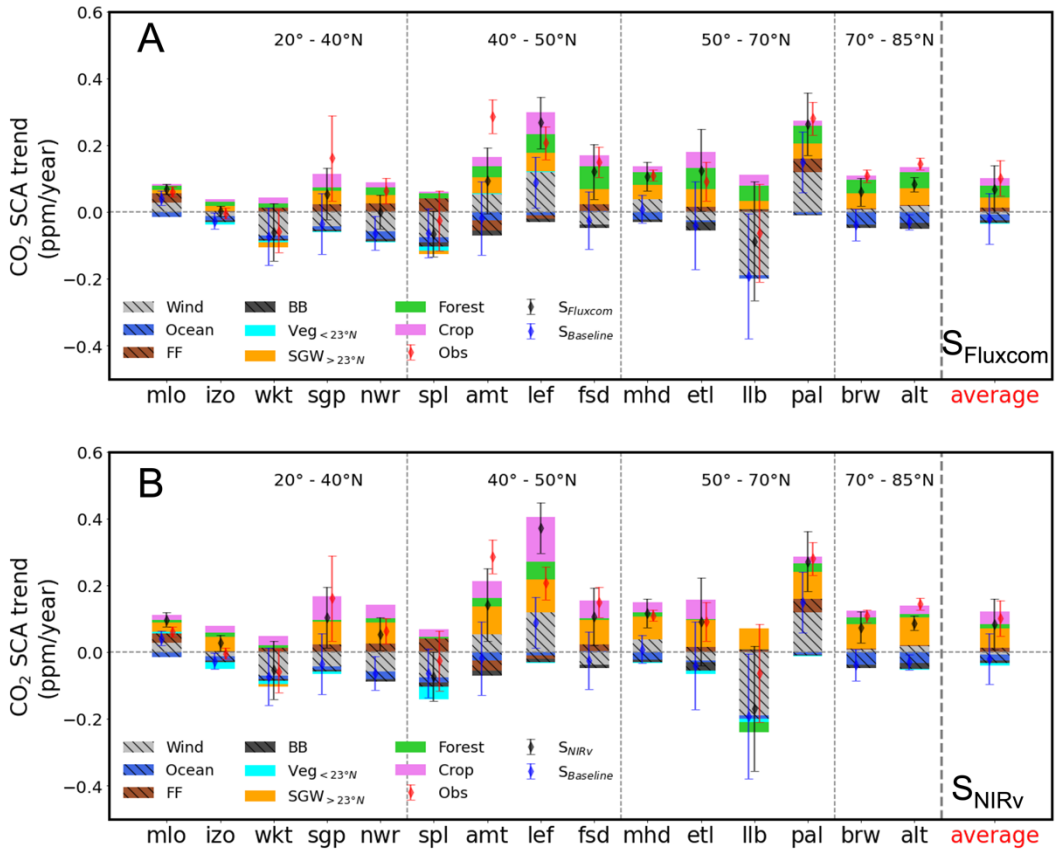

Figure 5.6: The contribution of individual drivers to CO_2 SCA trend at the surface CO_2 sites based on flux anomalies inferred from FLUXCOM (A) and MODIS NIRv (B). The average contribution of individual drivers is also calculated using 15 selected surface CO_2 sites. The drivers include wind, fossil fuel, biomass burning, ocean, cropland, forest, $SGW_{>23^\circ}$ and $Veg_{<23^\circ}$. The sites are ordered in latitude. Hatched bars are used to represent non-biome drivers. The simulated observed and $S_{Baseline}$ CO_2 SCA trends are also overlaid for reference. **Table 5-5** reports the value of individual drivers.

5.5 Discussion

Our results show a broad increase in peak growing season and annual GPP across the northern extratropics from 2001 to 2018, suggesting that a variety of factors – both through direct human management of crop systems and natural response to climate change – are driving trends in GPP. In crop regions, changes in agricultural

practices, such as hybridization, irrigation or fertilization, are main drivers of increased yields (Chen et al., 2019; Huang et al., 2018; Zeng et al., 2014), whereas inter-annual climate variations accounts for roughly a third of the observed yield variability (Ray et al., 2015). Positive trends in high-latitude shrublands may be due to warming. High-latitude shrublands are usually temperature limited, so that warming in recent decades has increased their productivity (Liu et al., 2020). Mid-latitude grasslands usually lie in arid regions with strong water limitation, so that the enhancement of water use efficiency induced by CO_2 fertilization is likely to play a role in the strong trend in these areas (Winkler et al., 2021). Forests show more varied responses, with temperate forest showing increasing productivity, possibly related to CO_2 fertilization and reforestation, whereas boreal forests can exhibit either greening or browning, owing to mixed effects of climate change and more frequent and intense disturbances such as droughts and wildfires (Goetz et al., 2005; Seidl et al., 2017; Verbyla, 2011; Winkler et al., 2021).

Despite major differences in biome specific NEE trends between FLUXCOM and NIRv-GPP, both datasets, the simulated CO_2 SCA trends driven by these datasets performed well in capturing observations across the surface sites examined in this study. Despite a general increase in the CO_2 SCA across the NH, there are distinct regional differences due to different dominant drivers. By averaging the 15 surface CO_2 sites, we estimate that forest, crop, and $SGW_{>23^\circ}$ contribute +0.01-0.04 ppm/year (7-26%), +0.02-0.04 ppm/year (17-24%) and +0.03-0.06 ppm/year (23-37%) on SCA trends. However, there are still limitations of a sparse network of surface sites in unambiguously distinguishing specific regions and biomes for the large-scale trends. The recent expansion of the number of surface sites and introduction of satellite missions retrieving total-column dry-air mole fractions of CO_2 (X_{CO2}), such as GOSAT (2009-present) and OCO-2 (2014-present), has dramatically increased the spatial extent of CO2 measurements in recent years (Jacobs et al., 2021; Ishizawa et al., 2016; Parazoo et al., 2013; Peiro et al., 2022), however, we are limited in examining SCA trends with these data due to the short

records. Still, this expanded observational coverage will be critical for isolating biome-specific contributions to the CO_2 SCA changes.

Most previous studies have attributed the amplified CO_2 seasonality to the enhanced photosynthesis of temperate and boreal forests of the NH due to warming effects and CO_2 fertilizations (Barnes et al., 2016; Forkel et al., 2016; Graven et al., 2013; Lin et al., 2020; Liu et al., 2020; Piao et al., 2018). However, current terrestrial biosphere models generally underestimate the CO_2 SCA trend by solely adjusting vegetation fluxes in high latitudes, which implies that such mechanisms cannot explain the full range and magnitude of the observed increasing CO_2 SCA trend (Zeng et al., 2014). The inability of models to reproduce the trend of the CO_2 seasonal amplitude could be due to the inaccurate sensitivity to CO_2 fertilization and climate changes (Rollinson et al., 2017; Schimel et al., 2015; Smith et al., 2016), underrepresentation of land use change, and underestimate of cropland flux seasonality in mid-latitudes in the NH (Ito et al., 2016; Piao et al., 2018; Sun et al., 2021; Zeng et al., 2014; Zhao et al., 2016). Our spatial pattern of CO_2 SCA trends (**Figure 5.4**) shows that crop regions, including North America, north China and India have experienced large CO_2 SCA increases since 2001. In addition, our site-level analysis reveals a strong impact of cropland fluxes on surface sites, especially around 40°N to 50°N near the Midwest United States. Though these point to the importance of agricultural activities in amplifying the CO_2 seasonality, different studies still disagree on their roles (Forkel et al., 2016; Piao et al., 2018; Lin et al., 2020). An improved implementation of land use management and crop-specific flux simulations is needed to fully understand their role on the seasonal characteristics of CO_2.

It should be noted that inferred GPP trends from both NIRv and FLUXCOM are based on MODIS surface spectral reflectance. Instead of using NIRv as a predictor of vegetation absorbed photosynthetic solar radiation, FLUXCOM uses MODIS NDVI to estimate spatiotemporal patterns of GPP. Therefore, these two GPP

datasets inherited similar deficiencies from MODIS surface reflectance measurements. GPP is determined by both absorbed photosynthetic solar radiation linked with canopy structural changes and light use efficiency (LUE) related to physiological changes (Bradford et al., 2005; Coops et al., 2010; Running et al., 2000; Turner et al., 2003). The reflectance-based GPP estimates are primarily sensitive to canopy structural changes in ecosystems, but are less sensitive to physiological changes induced by environmental changes, such as variations in air temperature, soil moisture, vapor pressure deficit, and atmospheric rising CO_2 (Dobrowski et al., 2005; Gamon et al., 1995; He et al., 2020a&b; Huete et al., 2002; Rossini et al., 2015; Song et al., 2018; Sun et al., 2017; Frankenberg et al., 2021). This could partially explain the weaker trends seen in forest ecosystems. It is also noticeable that the MODIS instrument was first on board the Terra satellite, launched in December 1999. Then a similar instrument was launched on the Aqua satellite in May 2002. To avoid any artificial trend introduced when only the MODIS Terra data are available, we examine the trend starting in 2003 for FLUXCOM and NIRv (**Figure 5.17**), and its spatiotemporal pattern is consistent with the trend starting in 2001(**Figure 5.3**).

The interpretation of measured spectral vegetation indices from satellite sensors is challenging at high latitudes. Measurements in these regions are often influenced by patchy snow, cloud covers, and shadows caused by low sun angles (Myers-Smith et al., 2020), which makes accurate GPP estimates difficult. Satellite-derived vegetation indices have revealed divergent responses of high-latitude ecosystems in the NH in the warming climate (Myers-Smith et al., 2020; Alcaraz-segura et al., 2010). Depending on vegetation indices from different satellite products, the high latitude ecosystems have experienced greening (Forbes et al., 2010; Jia et al., 2003; Jia et al., 2009; Macias-Fauria et al., 2012; Zhang et al., 2017; Zhu et al., 2016; Arndt et al., 2019; Berner et al., 2020; Keenan & Riley, 2018; Myneni et al., 1997; Zhang et al., 2008) or browning (Bhatt et al., 2013; Phonex et al., 2016; Lara et al., 2018; Miles et al., 2016; Parent & Verbyla, 2010; Verbyla, 2011). Fire disturbances

may explain ecological variability and regional differences of vegetation productivity (Goetz et al., 2005; Beck & Goetz, 2011). Satellite-based models mostly do not explicitly consider the difference in photosynthetic capacity between moss and higher plants when estimating regional GPP in the boreal region, resulting in a substantial overestimation. With a lower photosynthetic capacity, mosses can generate only about one-third of the GPP that vascular plants at the same NDVI (Yuan et al., 2014). In addition, the sparse network of flux tower sites at high latitudes in the NH results in high uncertainties in ecosystem carbon flux estimates (Jung et al., 2020; Schimel et al., 2015). Some efforts have been made to improve observational coverage for these high latitudes. For example, Virkkala et al. (2021) develops a standardized monthly database of Arctic-Boreal carbon fluxes based on chamber, snow diffusion and eddy covariance measurements. This can be used to improve understanding of the regional and temporal variations of ecosystem carbon fluxes.

Observed CO_2 SCA trends are found to be consistent with the modeled trends driven by NEE anomalies from FLUXCOM and NIRv, but with some underestimation at mid-high latitude sites. Residual biases could be due to several factors. First, this could be due to an underestimate of trends and interannual variations of global GPP and NEE in the underlying fluxes. As most remote sensing based GPP estimates, FLUXCOM and NIRv-derived GPP are driven by climate and greenness, and do not account for direct physiological benefits on plants via CO_2 fertilization effects (Jung et al., 2020). This may lead to an underestimate of GPP trends, especially in mid-high arid and semi-arid regions. FLUXCOM products have also been found to underestimate interannual variations in NEE and GPP compared to inversions and process-based global dynamic vegetation models (Jung et al., 2020). Second, systematic errors in the transport model could contribute to residual biases. GEOS-Chem (from which GHGF-Flux inherits transport) has been found to systematically underestimate vertical transport in the northern extratropics (Schuh et al., 2019; Stanevich et al., 2020; Yu et al., 2018).

Third, biases in the in meteorological reanalysis used to drive the transport have been noted (Parazoo et al., 2012). However, quantifying the impact of these biases on the simulations presented here is challenging. The impact of these errors could be better characterized by re-running these experiments with a different chemical transport model, such as TM5, but this is computationally expensive and beyond the scope of the current study.

5.6 Conclusion

Atmospheric CO_2 measurements provide powerful tools to understand biosphere-atmosphere carbon interactions. The variations in the CO_2 SCA indicate underlying changes in biosphere carbon fluxes. Our study illustrates that the observed increasing CO_2 SCA trend in the last two decades is mainly driven by the widespread enhanced vegetation carbon uptake over the NH. Both FLUXCOM and NIRv-based terrestrial carbon flux estimates better account for trends in SCA across a range of in situ sites (slope of 0.80 and 0.99) relative to climatological NEE (slope of 0.49).

Trends in FLUXCOM and NIRv-based GPP are widespread across the northern extratropics, with positive trends found in many biomes. Agricultural areas have among the strongest positive trends in GPP, suggesting changes in agricultural practices, such as hybridization, irrigation or fertilization, are significantly increasing the productivity of these regions. However, strong positive trends are also found across a mosaic of natural ecosystems, particularly high-latitude shrublands and mid-latitude grasslands, but also in many forest regions. These positive trends in natural ecosystems are likely due to both CO_2 fertilization and warming, in high latitude regions.

Although these large-scale features are captured by both FLUXCOM and NIRv-based GPP, these datasets show regional and biome-specific differences. Despite this, both datasets perform well in simulation SCA CO_2 trends for 15 surface sites.

Furthermore, the SCA trends at individual surface sites are strongly impacted by interannual variations in transport, as well as trends in biomass burning, ocean fluxes, and fossil fuel emissions. This suggests that the relatively sparse sampling of surface sites over 2001-2018 is insufficient to distinguish between NEE trends produced by FLUXCOM and NIRv.

5.7 Acknowledgement

L.H. thanks the Resnick Sustainability Institute at Caltech for fellowship support. B.B. and J.L. were supported by the NASA OCO2/3 science team program NNH17ZDA001N-OCO2. Part of this research was carried out at the Jet Propulsion Laboratory, California Institute of Technology, under a contract with the National Aeronautics and Space Administration (80NM0018D004). Resources supporting this work were provided by the NASA High-End Computing (HEC) Program through the NASA Advanced Supercomputing (NAS) Division at Ames Research Center. We thank the discussion with Dr. Martin Jung from Max Planck Institute for Biogeochemistry and data products from the FLUXCOM initiative. We thank J. B. Miller for providing the FF emission dataset, which can be downloaded from https://gml.noaa.gov/ccgg/carbontracker/. CarbonTracker CT2019B results provided by NOAA ESRL, Boulder, Colorado, USA from the website at http://carbontracker.noaa.gov. FLUXNET2015 data can be obtained from the FLUXNET website (https://fluxnet.org). MCD43A4 Version 6 BRDF adjusted Reflectance dataset can be obtained from https://lpdaac.usgs.gov/products/mcd43a4v006/. GFED4.1s biomass burning emissions can be obtained from https://www.globalfiredata.org/. NEE fluxes of Byrne et al. (2020a) can be downloaded from https://cmsflux.jpl.nasa.gov/. The introduction of time-series curve fitting tool “ccgcrv” can be found in https://gml.noaa.gov/ccgg/mbl/crvfit/crvfit.html with Python package obtained from https://gml.noaa.gov/aftp/user/thoning/ccgcrv/.

5.8 Appendix

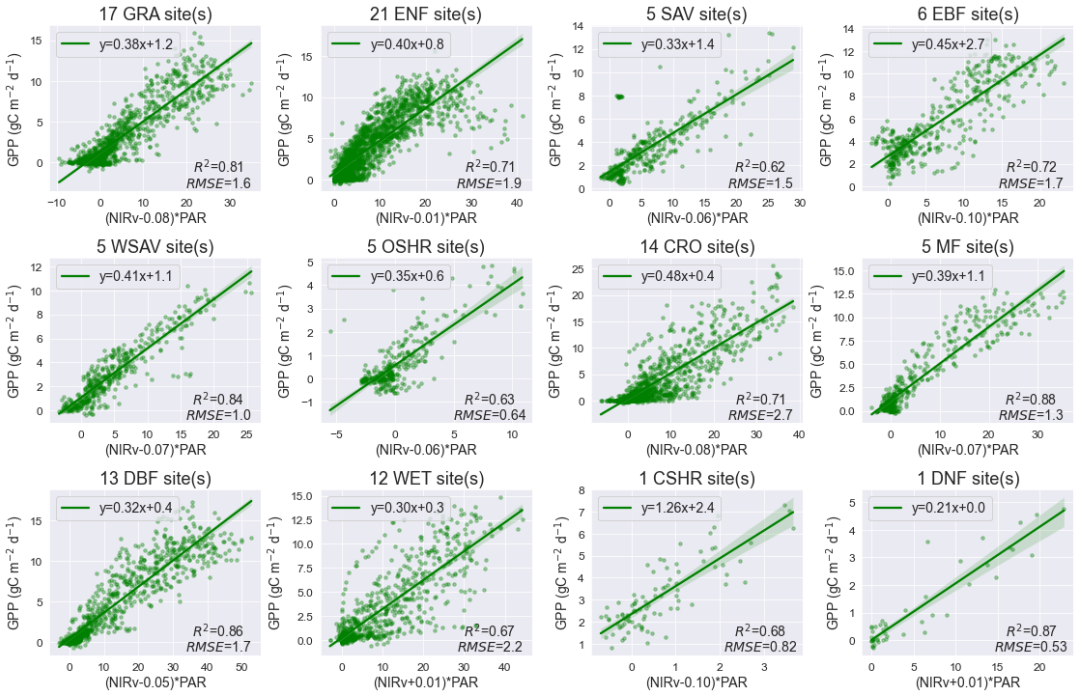

Figure 5.7: The relationship among GPP, NIRv and PAR across different vegetation types. In each subplot, individual points represent a 16-day average of corresponding measurements. Due to limited sites in CSHR, the derived slope seems an outlier compared to other vegetation types. Therefore, we apply the slope and intercept derived from OSHR into CSHR when we estimate the spatiotemporal patterns of GPP from MODIS NIRv datasets.

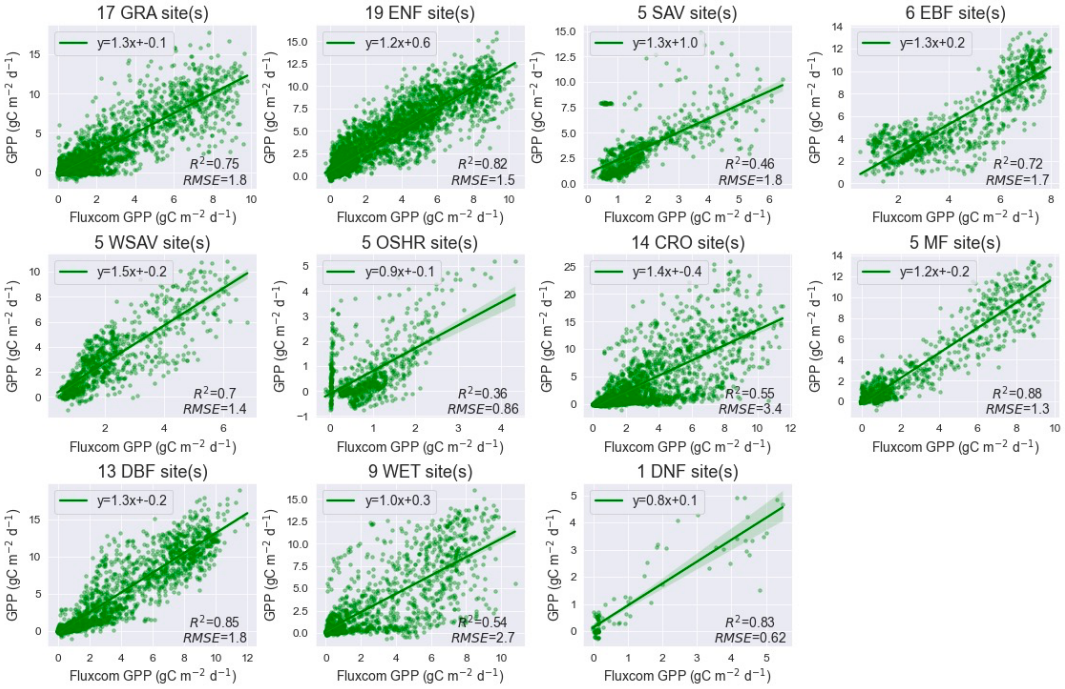

Figure 5.8: The comparison between 8-day 0.083° FLUXCOM and eddy covariance GPP across different vegetation types. Eddy covariance GPP is aggregated at 8-day to match the temporal resolution of FLUXCOM products. Please note that FLUXCOM has empty value at the grid cell that the CSHR site falls in. The CSHR site used in this study is IT-Noe (8.15°E, 40.61°N).

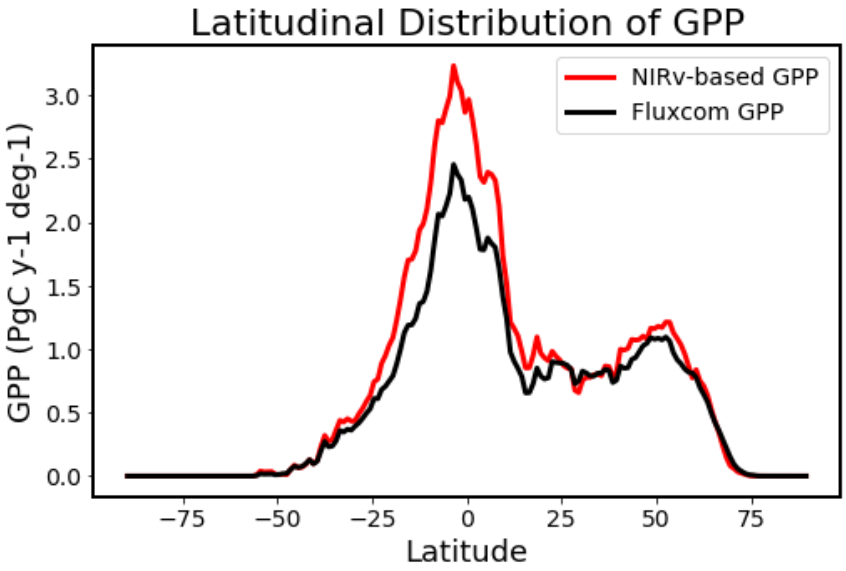

Figure 5.9: Averaged latitudinal distribution of NIRv-inferred GPP and FLUXCOM GPP during 2001 to 2018.

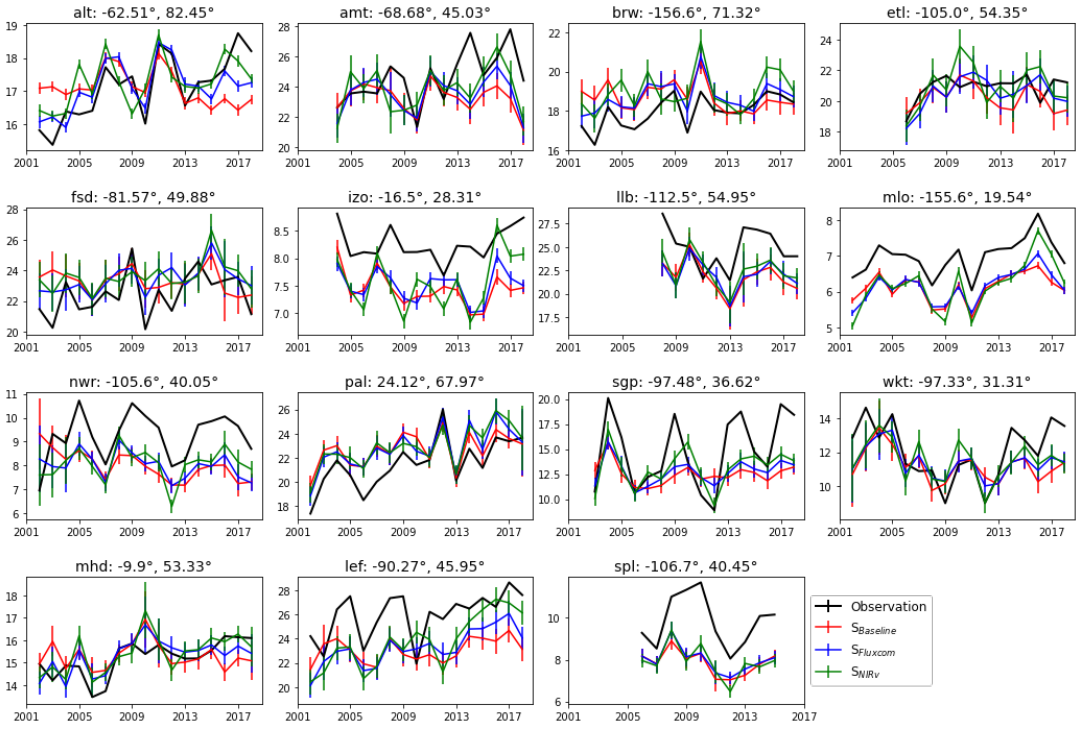

Figure 5.10: The time series of CO_2 SCA (unit: ppm) at 15 selected sites. The ensemble mean with standard deviation is shown using the bootstrapping the model uncertainties 1,000 times.

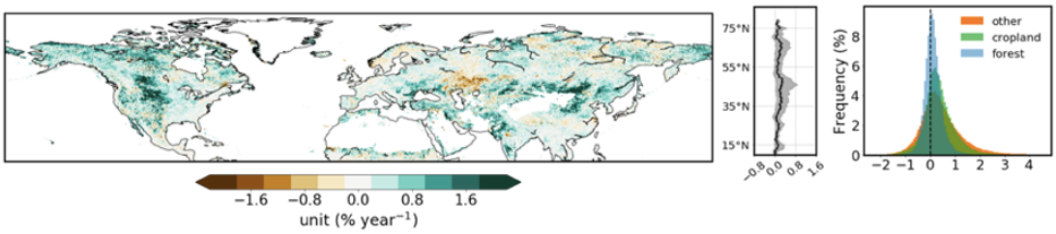

Figure 5.11: Peak season (95%-tile) 8-day Fluxcom TER trend from 2001 to 2018.

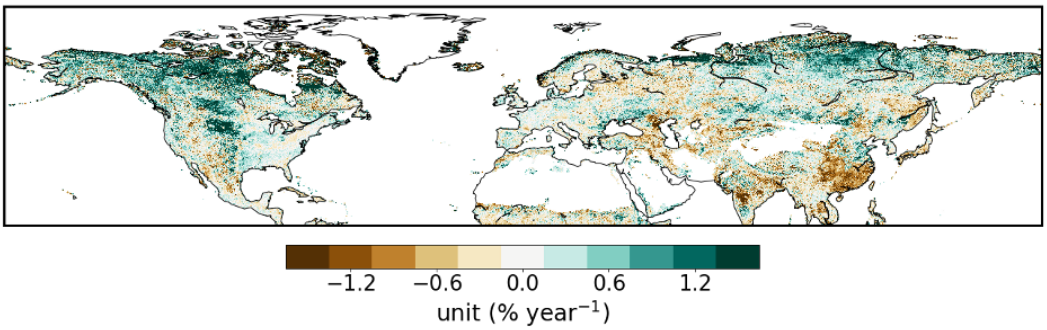

Figure 5.12: Difference between 95%-tile 8-day Fluxcom GPP trend and 95%-tile 8-day MODIS NIRv trend in Fig. 3.

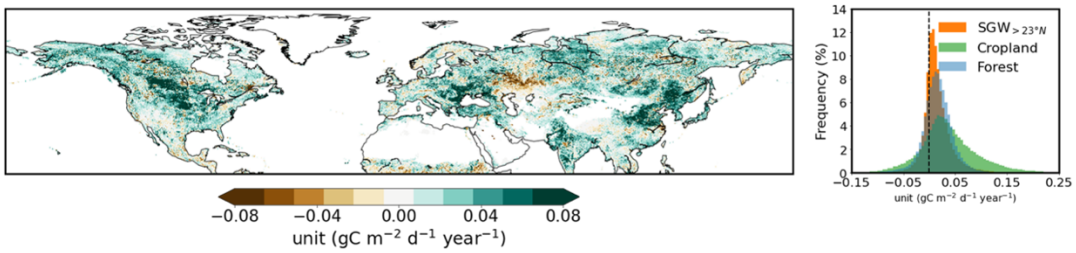

Figure 5.13: The actual trend of 95%-percentile 8-day Fluxcom GPP (unit: gC m^{-2} d^{-1} $year^{-1}$) from 2001 to 2018 is shown.

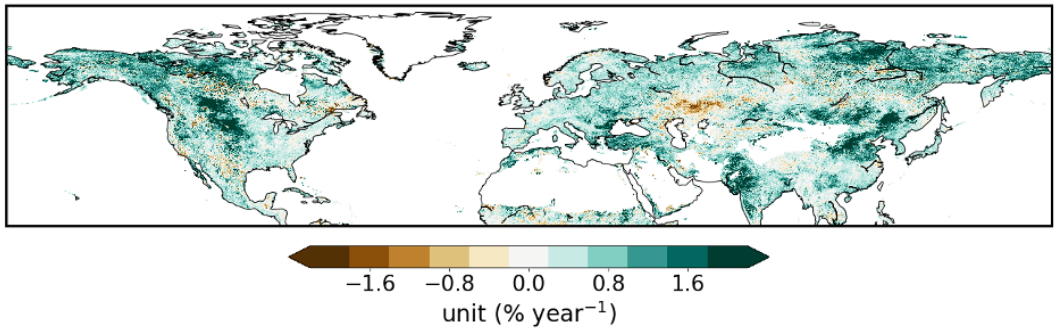

Figure 5.14: The trend of annual mean 8-day Fluxcom GPP (unit: % year-1) from 2001 to 2018.

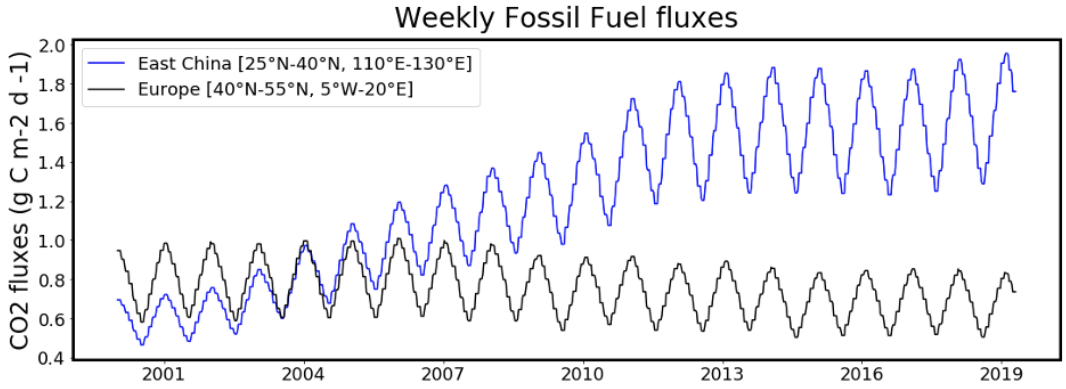

Figure 5.15: Weekly fossil fuel emissions since 2000 in East China and Europe.

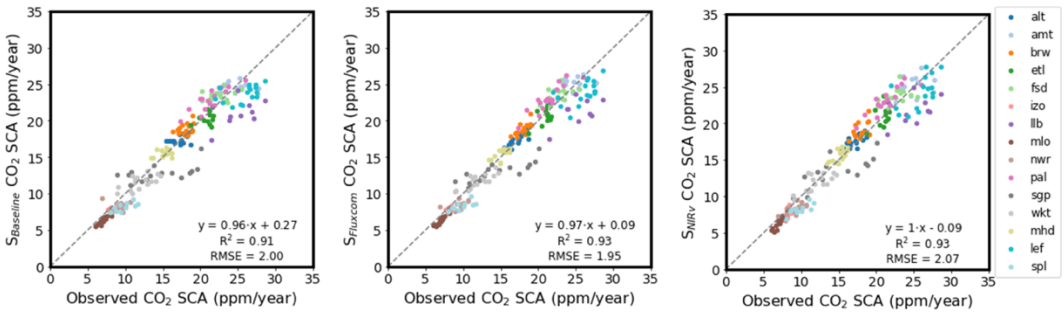

Figure 5.16: The comparison between the observed and simulated CO2 SCA at each sampling site and year can be found in Fig. S3.

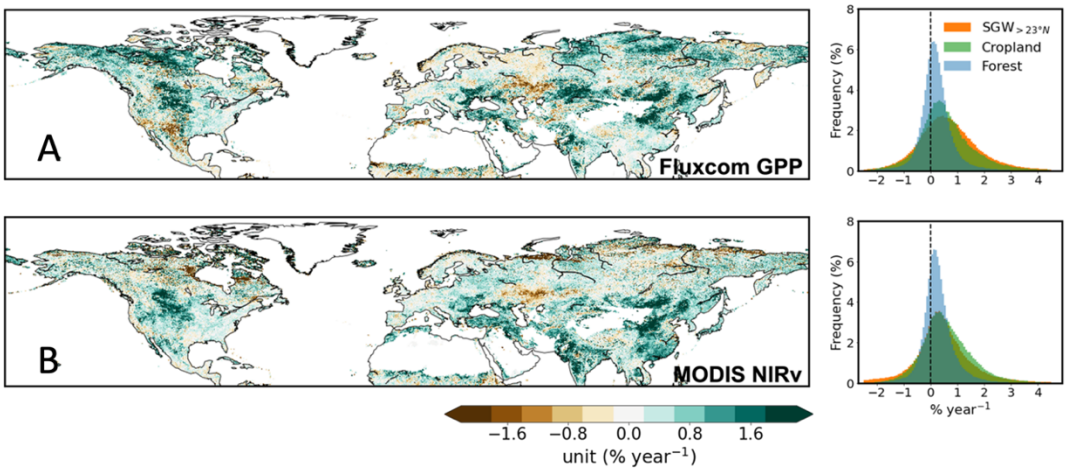

Figure 5.17: The trend of 95%-percentile 8-day Fluxcom GPP (A) and MODIS NIRv (B) (unit: % year^{-1}) from 2003 to 2018.

Table 5-2: Sites used to derive NIRv-GPP relationships.

Site	Longitude	Latitude	IGBP
BE-Lon	4.7461	50.5516	CRO
CH-Oe2	7.7343	47.2863	CRO
DE-Geb	10.9143	51.1001	CRO
DE-Kli	13.5224	50.8931	CRO
FR-Gri	1.9519	48.8442	CRO
IT-BCi	14.9574	40.5238	CRO
IT-CA2	12.026	42.3772	CRO
US-ARM	-97.4888	36.6058	CRO
US-Ne1	-96.4766	41.1651	CRO
US-Ne2	-96.4701	41.1649	CRO
US-Ne3	-96.4397	41.1797	CRO
US-Tw2	-121.6433	38.1047	CRO
US-Tw3	-121.6467	38.1159	CRO
US-Twt	-121.6526	38.1071	CRO
IT-Noe	8.1512	40.6062	CSHR
CA-TPD	-80.5577	42.6353	DBF
DE-Hai	10.453	51.0792	DBF
DE-Lnf	10.3678	51.3282	DBF
DK-Sor	11.6446	55.4859	DBF
IT-CA1	12.0266	42.3804	DBF
IT-CA3	12.0222	42.38	DBF
IT-Col	13.5881	41.8494	DBF
US-Ha1	-72.1715	42.5378	DBF
US-MMS	-86.4131	39.3232	DBF
US-Oho	-83.8438	41.5545	DBF
US-UMB	-84.7138	45.5598	DBF
US-UMd	-84.6975	45.5625	DBF
US-WCr	-90.0799	45.8059	DBF
RU-SkP	129.168	62.255	DNF
AU-Cum	150.7236	-33.6152	EBF
AU-Whr	145.0294	-36.6732	EBF
AU-Wom	144.0944	-37.4222	EBF
FR-Pue	3.5957	43.7413	EBF
GF-Guy	-52.9249	5.2788	EBF

IT-Cp2	12.3573	41.7043	EBF
AU-ASM	133.249	-22.283	ENF
CA-TP1	-80.5595	42.6609	ENF
CA-TP3	-80.3483	42.7068	ENF
CA-TP4	-80.3574	42.7102	ENF
CH-Dav	9.8559	46.8153	ENF
CZ-BK1	18.5369	49.5021	ENF
DE-Obe	13.7213	50.7867	ENF
DE-Tha	13.5652	50.9624	ENF
FI-Hyy	24.2948	61.8474	ENF
FI-Let	23.9595	60.6418	ENF
FI-Sod	26.6386	67.3624	ENF
IT-Lav	11.2813	45.9562	ENF
IT-Ren	11.4337	46.5869	ENF
IT-SR2	10.291	43.732	ENF
IT-SRo	10.2844	43.7279	ENF
NL-Loo	5.7436	52.1666	ENF
RU-Fyo	32.9221	56.4615	ENF
US-GLE	-106.2399	41.3665	ENF
US-Me2	-121.5574	44.4523	ENF
US-Me6	-121.6078	44.3233	ENF
US-NR1	-105.5464	40.0329	ENF
AT-Neu	11.3175	47.1167	GRA
AU-Emr	148.4746	-23.8587	GRA
AU-Rig	145.5759	-36.6499	GRA
AU-Stp	133.3502	-17.1507	GRA
AU-Ync	146.2907	-34.9893	GRA
CH-Cha	8.4104	47.2102	GRA
CH-Fru	8.5378	47.1158	GRA
CN-Sw2	111.8971	41.7902	GRA
CZ-BK2	18.5429	49.4944	GRA
DE-Gri	13.5126	50.95	GRA
DE-RuR	6.3041	50.6219	GRA
IT-Tor	7.5781	45.8444	GRA
NL-Hor	5.0713	52.2404	GRA
RU-Sam	126.4958	72.3738	GRA
US-AR2	-99.5975	36.6358	GRA

US-IB2	-88.241	41.8406	GRA
US-Var	-120.9507	38.4133	GRA
BE-Vie	5.9981	50.305	MF
CA-Gro	-82.1556	48.2167	MF
CH-Lae	8.365	47.4781	MF
US-SRC	-110.8395	31.9083	MF
US-Syv	-89.3477	46.242	MF
AU-TTE	133.64	-22.287	OSHR
ES-Amo	-2.2523	36.8336	OSHR
ES-LJu	-2.7521	36.9266	OSHR
RU-Cok	147.4943	70.8291	OSHR
US-Whs	-110.0522	31.7438	OSHR
AU-Cpr	140.5891	-34.0021	SAV
AU-DaS	131.3881	-14.1593	SAV
AU-Dry	132.3706	-15.2588	SAV
AU-GWW	120.6541	-30.1913	SAV
SN-Dhr	-15.4322	15.4028	SAV
CZ-wet	14.7704	49.0247	WET
DE-Akm	13.6834	53.8662	WET
DE-Spw	14.0337	51.8923	WET
DE-Zrk	12.889	53.8759	WET
DK-NuF	-51.3861	64.1308	WET
NO-Adv	15.923	78.186	WET
SE-St1	19.0503	68.3542	WET
US-Los	-89.9792	46.0827	WET
US-Myb	-121.7651	37.05	WET
US-Tw1	-121.6469	38.1074	WET
US-Tw4	-121.6414	38.103	WET
US-WPT	-82.9962	41.4646	WET
AU-Gin	115.7138	-31.3764	WSAV
AU-How	131.1523	-12.4943	WSAV
AU-RDF	132.4776	-14.5636	WSAV
US-SRM	-110.8661	31.8214	WSAV
US-Ton	-120.966	38.4316	WSAV

Table 5-3: Surface CO2 sites used in this study. Coastal sites are highlighted in red.

Station name	Station Code	Latitude	Longitude
Mauna Loa, Hawaii, United States	MLO	19.54	-155.6
Izana, Tenerife, Canary Islands, Spain	IZO	28.31	-16.5
Moody, Texas, United States	WKT	31.31	-97.33
Southern Great Plains, Oklahoma, United States	SGP	36.62	-97.48
Niwot Ridge, Colorado, United States	NWR	40.05	-105.6
Storm Peak Laboratory (Desert Research Institute), United States	SPL	40.45	-106.7
Argyle, Maine, United States	AMT	45.03	-68.68
Park Falls, Wisconsin, United States	LEF	45.95	-90.27
Fraserdale, Canada	FSD	49.88	-81.57
Mace Head, County Galway, Ireland	MHD	53.33	-9.9
East Trout Lake, Saskatchewan, Canada	ETL	54.35	-105
Lac La Biche, Alberta, Canada	LLB	54.95	-112.5
Pallas-Sammaltunturi, GAW Station, Finland	PAL	67.97	24.12
Barrow Atmospheric Baseline Observatory, United States	BRW	71.32	-156.6
Alert, Nunavut, Canada	ALT	82.45	-62.51

Table 5-4: Ensemble mean, median, standard deviation (std), 5%-tile and 95%-tile of the derived CO_2 SCA trend using the bootstrapping the model uncertainties 1,000 times.

unit (ppm /yr)	MLO	IZO	WKT	SGP	NWR	SPL	AMT	LEF	FSD	MHD	ETL	LLB	PAL	BRW	ALT
Mean of Obs	0.05	0.01	-0.02	0.21	0.04	-0.04	0.23	0.21	0.1	0.11	0.08	-0.07	0.28	0.1	0.14
Mean of $S_{Baseline}$	0.02	-0.03	-0.08	-0.02	-0.09	-0.08	-0.06	0.08	-0.04	-0.01	-0.04	-0.19	0.13	-0.05	-0.04
Mean of $S_{Fluxcom}$	0.04	-0.01	-0.07	0.05	-0.04	-0.09	0.02	0.24	0.09	0.08	0.09	-0.09	0.23	0.04	0.06
Mean of S_{NIRv}	0.07	0.03	-0.06	0.08	0.01	-0.09	0.08	0.36	0.08	0.1	0.07	-0.13	0.23	0.05	0.07
Median of Obs	0.05	0.01	-0.02	0.2	0.05	-0.03	0.23	0.21	0.1	0.11	0.09	-0.12	0.28	0.1	0.14
Median of $S_{Baseline}$	0.02	-0.03	-0.07	-0.02	-0.09	-0.08	-0.06	0.08	-0.04	-0.01	-0.04	-0.19	0.13	-0.04	-0.04
Median of $S_{Fluxcom}$	0.05	-0.01	-0.06	0.05	-0.04	-0.08	0.02	0.24	0.09	0.08	0.09	-0.1	0.23	0.04	0.07
Median of S_{NIRv}	0.07	0.03	-0.06	0.08	0.01	-0.09	0.08	0.36	0.07	0.1	0.07	-0.13	0.24	0.05	0.07
Std of Obs	0.02	0.02	0.06	0.13	0.04	0.09	0.05	0.05	0.04	0.02	0.06	0.15	0.05	0.02	0.02
Std of $S_{Baseline}$	0.01	0.02	0.09	0.07	0.05	0.07	0.09	0.07	0.09	0.04	0.11	0.18	0.09	0.04	0.02
Std of $S_{Fluxcom}$	0.02	0.02	0.09	0.07	0.05	0.07	0.1	0.07	0.08	0.04	0.12	0.19	0.1	0.04	0.02
Std of S_{NIRv}	0.02	0.02	0.09	0.09	0.05	0.07	0.1	0.07	0.09	0.04	0.13	0.19	0.09	0.05	0.02
5%-tile of Obs	0.02	-0.02	-0.11	0.02	-0.03	-0.24	0.15	0.13	0.03	0.09	-0.03	-0.25	0.19	0.07	0.11
5%-tile of $S_{Baseline}$	0	-0.06	-0.22	-0.13	-0.18	-0.2	-0.2	-0.04	-0.17	-0.07	-0.22	-0.49	-0.03	-0.11	-0.07
5%-tile of $S_{Fluxcom}$	0.02	-0.03	-0.21	-0.07	-0.12	-0.21	-0.14	0.12	-0.04	0.01	-0.11	-0.4	0.06	-0.03	0.02
5%-tile of S_{NIRv}	0.03	-0.01	-0.21	-0.07	-0.07	-0.21	-0.09	0.24	-0.07	0.03	-0.16	-0.44	0.07	-0.02	0.03
95%-tile of Obs	0.07	0.04	0.09	0.44	0.1	0.09	0.32	0.28	0.18	0.14	0.16	0.23	0.35	0.13	0.17
95%-tile of $S_{Baseline}$	0.05	0	0.06	0.1	-0.01	0.02	0.08	0.2	0.1	0.06	0.15	0.12	0.27	0.02	-0.01
95%-tile of $S_{Fluxcom}$	0.07	0.02	0.07	0.17	0.04	0.02	0.18	0.36	0.24	0.15	0.29	0.22	0.37	0.11	0.1
95%-tile of S_{NIRv}	0.1	0.07	0.07	0.24	0.09	0.02	0.25	0.47	0.23	0.16	0.28	0.21	0.38	0.13	0.1

Table 5-5: The contribution of individual drivers to the simulated CO_2 SCA trend (ppm/yr).

unit (ppm/yr)	MLO	IZO	WKT	SGP	NWR	SPL	AMT	LEF	FSD	MHD	ETL	LLB	PAL	BRW	ALT	average
Wind	0.03	-0.01	-0.07	-0.04	-0.06	-0.08	0.05	0.12	-0.04	0.04	-0.02	-0.19	0.12	0.01	0.02	-0.01
Ocean	-0.01	-0.01	-0.01	-0.01	-0.02	-0.02	-0.03	-0.01	0.00	-0.02	-0.01	-0.01	-0.01	-0.04	-0.03	-0.02
Fossil Fuel (FF)	0.03	0.00	0.01	0.02	0.03	0.04	-0.03	-0.01	0.02	0.00	0.01	0.00	0.04	0.00	0.00	0.01
Biomass Burning (BB)	0.00	-0.01	-0.01	-0.01	-0.01	-0.01	-0.02	-0.01	-0.01	-0.01	-0.02	0.00	0.00	-0.01	-0.02	-0.01
$S_{Fluxcom}$: Veg<23N°	0.00	-0.01	0.00	0.00	0.00	-0.01	0.00	0.00	0.00	0.00	0.00	0.00	0.00	0.00	0.00	0.00
$S_{Fluxcom}$: SGW>23N°	0.01	0.01	-0.02	0.04	0.03	-0.01	0.05	0.06	0.05	0.04	0.05	0.03	0.05	0.05	0.05	0.03
$S_{Fluxcom}$: Forest	0.01	0.02	0.01	0.01	0.02	0.02	0.04	0.06	0.07	0.04	0.06	0.05	0.05	0.04	0.05	0.04
$S_{Fluxcom}$: Crop	0.01	0.01	0.02	0.04	0.02	0.01	0.03	0.07	0.03	0.02	0.05	0.03	0.01	0.01	0.01	0.02
S_{NIRv}: Veg<23N°	0.00	-0.02	-0.01	-0.01	0.00	-0.04	0.00	0.00	0.00	0.00	-0.01	-0.01	0.00	0.00	0.00	-0.01
S_{NIRv}: SGW>23N°	0.03	0.04	-0.01	0.07	0.06	0.00	0.08	0.10	0.07	0.07	0.08	0.07	0.08	0.07	0.08	0.06
S_{NIRv}: Forest	0.01	0.01	0.01	0.01	0.01	0.01	0.03	0.06	0.01	0.01	0.00	-0.03	0.03	0.02	0.01	0.01
S_{NIRv}: Crop	0.02	0.02	0.03	0.07	0.04	0.02	0.05	0.13	0.05	0.03	0.06	0.00	0.02	0.02	0.03	0.04

Chapter 6

FINDINGS AND CLOSING THOUGHTS

Traditionally, field experiments are the standard way to study cause-and-effect relationships in biogeochemistry. However, a deluge of earth system data has become available with a higher density observation network, increased number of satellite missions and more advanced earth system models. Novel developments in statistics and computer science also allow machine learning approaches to reveal the underlying nonlinear physical patterns and important factors behind these huge volumes of datasets. In this thesis, I leveraged multi-source datasets (e.g., in-situ measurements, satellite remote sensing and reanalysis datasets), process-based models, and data-driven methods to conduct systematic research towards understanding cropping systems under climate change. Specifically, my dissertation integrates theories and methods from satellite remote sensing, ecological science, atmospheric science, and statistics to (i) measure plant photosynthesis, (ii) estimate crop yields, (iii) understand yield responses to climate change, and (iv) quantify intensified agriculture in reshaping atmospheric CO_2 seasonal cycle.

First, I developed a new approach for estimating crop yields from space using satellite solar-induced fluorescence (SIF) signals. In Chapter 2, I demonstrated that SIF can better capture plant photosynthesis downregulation than commonly used reflectance-based vegetation indices, such as NDVI and EVI, in tracking plant photosynthesis during water stress. In Chapter 3, I used satellite SIF to estimate crop yield benchmarked by USDA reported annual crop statistics. I also found different plants show varying SIF: photosynthesis (or crop yield) relationships, which implies crop species should be considered in accurate yield estimate. Second, I used data-driven approaches to understand how the crop yield is affected by climate change and air quality. In Chapter 4, I quantified the yield responses to

climate and air pollution factors based on a yield prediction model using historical records of crop yield. Using the established model, I further predicted future yield changes using climate and air pollution scenarios. Third, I investigated how intensified agriculture in recent decades influence atmospheric CO_2 seasonality. In Chapter 5, I developed a 20-year remote sensing-based ecosystem carbon flux dataset by integrating satellite and in-situ flux measurements. Using this dataset, I attributed the contribution of different ecosystems, such as cropland, forests, and grasslands to the observed increased atmospheric CO_2 seasonality in the Northern Hemisphere.

The approaches developed in the thesis have great potential to estimate and understand yield variations in developing countries (e.g., China, India, sub-Saharan African countries), in which yields are most vulnerable to climate change and poorly measured. With an improved estimate and understanding of crop yields at every piece of farmland on Earth, effective efforts can then be made to evaluate and target productivity-enhancing interventions. Therefore, the findings in my dissertation are relevant to agro-ecosystem management in the face of climate change and contribute to equitable solutions to climate challenges.

BIBLIOGRAPHY

Ainsworth, E. A. (2017). Understanding and improving global crop response to ozone pollution. *The Plant Journal*, *90*(5), 886–897.

Ainsworth, E. A., & Long, S. P. (2004). What have we learned from 15 years of free-air CO2 enrichment (FACE)? A meta-analytic review of the responses of photosynthesis, canopy properties and plant production to rising CO2. *New Phytologist*, *165*(2), 351–372.

Ainsworth, E. A., & Long, S. P. (2021). 30 years of free-air carbon dioxide enrichment (FACE): What have we learned about future crop productivity and its potential for adaptation? *Global Change Biology*, *27*(1), 27-49.

ALCARAZ-SEGURA, D., CHUVIECO, E., EPSTEIN, H. E., KASISCHKE, E. S., & TRISHCHENKO, A. (2010). Debating the greening vs. browning of the North American boreal forest: differences between satellite datasets. *Global Change Biology*, *16*(2), 760–770.

Amthor, J. S. (2012). *Respiration and crop productivity*. Springer Science & Business Media.

Anav, A., Friedlingstein, P., Beer, C., Ciais, P., Harper, A., Jones, C., et al. (2015). Spatiotemporal patterns of terrestrial gross primary production: A review. *Reviews of Geophysics*, *53*(3), 785–818.

Anderson, M. C., Allen, R. G., Morse, A., & Kustas, W. P. (2012). Use of Landsat thermal imagery in monitoring evapotranspiration and managing water resources. *Remote Sensing of Environment*, *122*, 50–65.

Arndt, K. A., Santos, M. J., Ustin, S., Davidson, S. J., Stow, D., Oechel, W. C., et al. (2019). Arctic greening associated with lengthening growing seasons in Northern Alaska. *Environmental Research Letters*, *14*(12), 125018.

Asseng, S., Ewert, F., Martre, P., Rötter, R. P., Lobell, D. B., Cammarano, D., et al. (2015). Rising temperatures reduce global wheat production. *Nature Climate Change*, *5*(2), 143–147.

Aunan, K., Berntsen, T. K., & Seip, H. M. (2000). Surface Ozone in China and its Possible Impact on Agricultural Crop Yields. *AMBIO: A Journal of the Human Environment*, *29*(6), 294–301.

Avnery, S., Mauzerall, D. L., Liu, J., & Horowitz, L. W. (2011). Global crop yield reductions due to surface ozone exposure: 2. Year 2030 potential crop production losses and economic damage under two scenarios of O3 pollution. *Atmospheric Environment*, *45*(13), 2297–2309.

Avnery, S., Mauzerall, D. L., Liu, J., & Horowitz, L. W. (2011). Global crop yield reductions due to surface ozone exposure: 1. Year 2000 crop production losses and economic damage. *Atmospheric Environment*, *45*(13), 2284–2296.

Bacastow, R. B., Keeling, C. D., & Whorf, T. P. (1985). Seasonal amplitude increase in atmospheric CO2 concentration at Mauna Loa, Hawaii, 1959 - 1982. *Journal of Geophysical Research*, *90*(D6), 10529–10540.

Badgley, G., Anderegg, L. D. L., Berry, J. A., & Field, C. B. (2019). Terrestrial gross primary production: Using NIRV to scale from site to globe. *Global Change Biology*, *25*(11), 3731–3740.

Badgley, G., Field, C. B., & Berry, J. A. (n.d.). *Canopy near-infrared reflectance and terrestrial photosynthesis*. *Science advances*, *3*(3), p.e1602244.

Baker, J. M., & Griffis, T. J. (2005). Examining strategies to improve the carbon balance of corn/soybean agriculture using eddy covariance and mass balance techniques. *Agricultural and Forest Meteorology*, *128*(3–4), 163–177.

Barnes, E. A., Parazoo, N., Orbe, C., & Denning, A. S. (2016). Isentropic transport and the seasonal cycle amplitude of CO2. *Journal of Geophysical Research*, *121*(13), 8106–8124.

Bastos, A., Ciais, P., Chevallier, F., Rödenbeck, C., Ballantyne, A. P., Maignan, F., et al. (2019). Contrasting effects of CO2 fertilization, land-use change and warming on seasonal amplitude of Northern Hemisphere CO2 exchange. *Atmospheric Chemistry and Physics*, *19*(19), 12361–12375.

Basu, S., Baker, D. F., Chevallier, F., Patra, P. K., Liu, J., & Miller, J. B. (2018). The impact of transport model differences on CO2 surface flux estimates from OCO-2 retrievals of column average CO2. *Atmospheric Chemistry and Physics*, *18*(10), 7189–7215.

Bauer, P., Thorpe, A., & Brunet, G. (2015). The quiet revolution of numerical weather prediction. *Nature 2015 525:7567*, *525*(7567), 47–55.

Beck, P. S. A., & Goetz, S. J. (2011). Satellite observations of high northern latitude vegetation productivity changes between 1982 and 2008: ecological variability and regional differences. *Environmental Research Letters*, *6*(4), 045501.

Beck, P. S. A., & Goetz, S. J. (2011). Satellite observations of high northern latitude vegetation productivity changes between 1982 and 2008: ecological variability and regional differences. *Environmental Research Letters*, *6*(4), 045501.

Beer, C., Reichstein, M., Tomelleri, E., Ciais, P., Jung, M., Carvalhais, N., et al. (2010). Terrestrial gross carbon dioxide uptake: global distribution and covariation with climate. *Science*, *329*(5993), 834–838.

Berner, L. T., Massey, R., Jantz, P., Forbes, B. C., Macias-Fauria, M., Myers-Smith, I., et al. (2020). Summer warming explains widespread but not uniform greening in the Arctic tundra biome. *Nature Communications 2020 11:1*, *11*(1), 1–12.

Bonal, D., Burban, B., Stahl, C., Wagner, F., & Hérault, B. (2016). The response of tropical rainforests to drought—lessons from recent research and future prospects. *Annals of Forest Science 2015 73:1*, *73*(1), 27–44.

Boyer, J. S., Byrne, P., Cassman, K. G., Cooper, M., Delmer, D., Greene, T., et al. (2013). The U.S. drought of 2012 in perspective: A call to action. *Global Food Security*, *2*(3), 139–143.

Bradford, J. B., Hicke, J. A., & Lauenroth, W. K. (2005). The relative importance of light-use efficiency modifications from environmental conditions and cultivation for

estimation of large-scale net primary productivity. *Remote Sensing of Environment*, *96*(2), 246–255. https://doi.org/10.1016/J.RSE.2005.02.013

Brix, H., Menemenlis, D., Hill, C., Dutkiewicz, S., Jahn, O., Wang, D., et al. (2015). Using Green's Functions to initialize and adjust a global, eddying ocean biogeochemistry general circulation model. *Ocean Modelling*, *95*, 1–14.

Brunner, L., Pendergrass, A. G., Lehner, F., Merrifield, A. L., Lorenz, R., & Knutti, R. (n.d.). Reduced global warming from CMIP6 projections when weighting models by performance and independence. *Earth System Dynamics, 11*(4), 995-1012.

Budescu, D. V. (1993). Dominance analysis: a new approach to the problem of relative importance of predictors in multiple regression. *Psychological Bulletin*, *114*(3), 542.

Buermann, W., Bikash, P. R., Jung, M., Burn, D. H., & Reichstein, M. (2013). Earlier springs decrease peak summer productivity in North American boreal forests. *Environmental Research Letters*, *8*(2), 24027.

Buermann, W., Forkel, M., O'sullivan, M., Sitch, S., Friedlingstein, P., Haverd, V., et al. (2018). Widespread seasonal compensation effects of spring warming on northern plant productivity. *Nature*, *562*(7725), 110–114.

Buermann, W., Lintner, B. R., Koven, C. D., Angert, A., Pinzon, J. E., Tucker, C. J., & Fung, I. Y. (2007). The changing carbon cycle at Mauna Loa Observatory. *Proceedings of the National Academy of Sciences of the United States of America*, *104*(11), 4249–4254.

Buitenwerf, R., Rose, L., & Higgins, S. I. (2015). Three decades of multi-dimensional change in global leaf phenology. *Nature Climate Change*, *5*(4), 364–368.

Bunn, A. G., Goetz, S. J., Kimball, J. S., & Zhang, K. (2007). Northern high-latitude ecosystems respond to climate change. *Eos, Transactions American Geophysical Union*, *88*(34), 333–335.

Burba, G. (2013). *Eddy covariance method for scientific, industrial, agricultural and regulatory applications: A field book on measuring ecosystem gas exchange and areal emission rates*. LI-Cor Biosciences.

Burney, J., & Ramanathan, V. (2014). Recent climate and air pollution impacts on indian agriculture. *Proceedings of the National Academy of Sciences of the United States of America*, *111*(46), 16319–16324.

Butler, E. E., Mueller, N. D., & Huybers, P. (2018). Peculiarly pleasant weather for US maize. *Proceedings of the National Academy of Sciences of the United States of America*, *115*(47), 11935–11940. https://doi.org/10.1073/pnas.1808035115

Byrne, B., Liu, J., Bloom, A. A., Bowman, K. W., Butterfield, Z., Joiner, J., et al. (2020). Contrasting Regional Carbon Cycle Responses to Seasonal Climate Anomalies Across the East-West Divide of Temperate North America. *Global Biogeochemical Cycles*, *34*(11), e2020GB006598.

Byrne, B., Liu, J., Lee, M., Baker, I., Bowman, K. W., Deutscher, N. M., et al. (2020). Improved Constraints on Northern Extratropical CO2 Fluxes Obtained by Combining Surface-Based and Space-Based Atmospheric CO2 Measurements. *Journal of Geophysical Research: Atmospheres*, *125*(15), e2019JD032029.

Byrne, B., Jones, D. B. A., Strong, K., Polavarapu, S. M., Harper, A. B., Baker, D. F., & Maksyutov, S. (2019). On what scales can GOSAT flux inversions constrain anomalies in terrestrial ecosystems? *Atmospheric Chemistry and Physics*, *19*(20), 13017–13035.

Caignard, T., Kremer, A., Firmat, C., Nicolas, M., Venner, S., & Delzon, S. (2017). Increasing spring temperatures favor oak seed production in temperate areas. *Scientific Reports*, *7*(1), 1–8.

Chameides, W. L., Yu, H., Liu, S. C., Bergin, M., Zhou, X., Mearns, L., et al. (1999). Case study of the effects of atmospheric aerosols and regional haze on agriculture: An opportunity to enhance crop yields in China through emission controls? *Proceedings of the National Academy of Sciences of the United States of America*, *96*(24), 13626–13633.

Chen, C., Park, T., Wang, X., Piao, S., Xu, B., Chaturvedi, R. K., et al. (2019). China and India lead in greening of the world through land-use management. *Nature Sustainability*, *2*(2), 122–129.

Collatz, G. J., Ribas-Carbo, M., & Berry, J. A. (1992). Coupled photosynthesis-stomatal conductance model for leaves of C4 plants. *Functional Plant Biology*, *19*(5), 519–538.

Crevoisier, C., Sweeney, C., Gloor, M., Sarmiento, J. L., & Tans, P. P. (2010). Regional US carbon sinks from three-dimensional atmospheric CO2 sampling. *Proceedings of the National Academy of Sciences*, *107*(43), 18348-18353.

Dechant, B., Ryu, Y., Badgley, G., Zeng, Y., Berry, J. A., Zhang, Y., et al. (2020). Canopy structure explains the relationship between photosynthesis and sun-induced chlorophyll fluorescence in crops. *Remote Sensing of Environment*, *241*, 111733.

DeLUCIA, E. H., Drake, J. E., Thomas, R. B., & Gonzalez-Meler, M. (2007). Forest carbon use efficiency: is respiration a constant fraction of gross primary production? *Global Change Biology*, *13*(6), 1157–1167.

Deng, N., Grassini, P., Yang, H., Huang, J., Cassman, K. G., & Peng, S. (2019). Closing yield gaps for rice self-sufficiency in China. *Nature Communications*, *10*(1), 1–9. https://doi.org/10.1038/s41467-019-09447-9

Didan, K., Munoz, A. B., Solano, R., & Huete, A. (2015). MODIS vegetation index user's guide (MOD13 series). *University of Arizona: Vegetation Index and Phenology Lab*.

Dobrowski, S. Z., Pushnik, J. C., Zarco-Tejada, P. J., & Ustin, S. L. (2005). Simple reflectance indices track heat and water stress-induced changes in steady-state chlorophyll fluorescence at the canopy scale. *Remote Sensing of Environment*, *97*(3), 403–414.

Dobrowski, S. Z., Pushnik, J. C., Zarco-Tejada, P. J., & Ustin, S. L. (2005). Simple reflectance indices track heat and water stress-induced changes in steady-state chlorophyll fluorescence at the canopy scale. *Remote Sensing of Environment*, *97*(3), 403–414.

Dold, C., Büyükcangaz, H., Rondinelli, W., Prueger, J. H., Sauer, T. J., & Hatfield, J. L. (2017). Long-term carbon uptake of agro-ecosystems in the Midwest. *Agricultural and Forest Meteorology*, *232*, 128–140.

Dold, C., Hatfield, J. L., Prueger, J. H., Moorman, T. B., Sauer, T. J., Cosh, M. H., et al. (2019). Upscaling gross primary production in corn-soybean rotation systems in the midwest. *Remote Sensing*, *11*(14), 1688.

Du, S., Liu, L., Liu, X., Guo, J., Hu, J., Wang, S., & Zhang, Y. (2019). SIFSpec: Measuring solar-induced chlorophyll fluorescence observations for remote sensing of photosynthesis. *Sensors*, *19*(13), 3009.

Dutkiewicz, S., Follows, M. J., & Bragg, J. G. (2009). Modeling the coupling of ocean ecology and biogeochemistry. *Global Biogeochemical Cycles*, *23*(4), 4017.

Dutta, D., Schimel, D. S., Sun, Y., Van Der Tol, C., & Frankenberg, C. (2019). Optimal inverse estimation of ecosystem parameters from observations of carbon and energy fluxes. *Biogeosciences*, *16*(1), 77–103.

Elmendorf, S. C., Henry, G. H. R., Hollister, R. D., Björk, R. G., Boulanger-Lapointe, N., Cooper, E. J., et al. (2012). Plot-scale evidence of tundra vegetation change and links to recent summer warming. *Nature Climate Change 2012 2:6*, *2*(6), 453–457.

Epstein, H. E., Raynolds, M. K., Walker, D. A., Bhatt, U. S., Tucker, C. J., & Pinzon, J. E. (2012). Dynamics of aboveground phytomass of the circumpolar Arctic tundra during the past three decades. *Environmental Research Letters*, *7*(1), 015506.

Fan, S., Gloor, M., Mahlman, J., Pacala, S., Sarmiento, J., Takahashi, T., & Tans, P. (1998, October 16). A large terrestrial carbon sink in North America implied by atmospheric and oceanic carbon dioxide data and models. *Science*, *282*(5388), 442-446.

Farquhar, G. D., von Caemmerer, S., & Berry, J. A. (1980). A biochemical model of photosynthetic CO2 assimilation in leaves of C3 species. *Planta*, *149*(1), 78–90.

Felzer, B. S., Cronin, T., Reilly, J. M., Melillo, J. M., & Wang, X. (2007). Impacts of ozone on trees and crops. *Comptes Rendus - Geoscience*, *339*(11–12), 784–798.

Fischer, R. A. (2015). Definitions and determination of crop yield, yield gaps, and of rates of change. *Field Crops Research*, *182*, 9–18.

Flexas, J., Escalona, J. M., Evain, S., Gulías, J., Moya, I., Osmond, C. B., & Medrano, H. (2002). Steady-state chlorophyll fluorescence (Fs) measurements as a tool to follow variations of net CO2 assimilation and stomatal conductance during water-stress in C3 plants. *Physiologia Plantarum*, *114*(2), 231–240. Retrieved from papers3://publication/uuid/D6A90549-D261-4A6E-BFE8-39ECC8F49F2D

Forkel, M., Carvalhais, N., Rödenbeck, C., Keeling, R., Heimann, M., Thonicke, K., et al. (2016). Enhanced seasonal CO2 exchange caused by amplified plant productivity in northern ecosystems. *Science*, *351*(6274), 696–699. https://doi.org/10.1126/science.aac4971

Frankenberg, C., Fisher, J. B., Worden, J., Badgley, G., Saatchi, S. S., Lee, J.-E. J.-E. J.-E., et al. (2011). New global observations of the terrestrial carbon cycle from GOSAT: Patterns of plant fluorescence with gross primary productivity.

Geophysical Research Letters, *38*(17), n/a-n/a. https://doi.org/10.1029/2011GL048738

Frankenberg, C., O'Dell, C., Berry, J. A., Guanter, L., Joiner, J., Köhler, P., et al. (2014). Prospects for chlorophyll fluorescence remote sensing from the Orbiting Carbon Observatory-2. *Remote Sensing of Environment*, *147*(0), 1–12. https://doi.org/10.1016/j.rse.2014.02.007

Frankenberg, C., Pollock, R., Lee, R. A. M., Rosenberg, R., Blavier, J.-F., Crisp, D., et al. (2015). The Orbiting Carbon Observatory (OCO-2): spectrometer performance evaluation using pre-launch direct sun measurements. *Atmospheric Measurement Techniques*, *8*(1), 301–313.

Frankenberg, C., Fisher, J. B., Worden, J., Badgley, G., Saatchi, S. S., Lee, J.-E., et al. (2011). New global observations of the terrestrial carbon cycle from GOSAT: Patterns of plant fluorescence with gross primary productivity. *Geophysical Research Letters*, *38*(17).

Frankenberg, C., Yin, Y., Byrne, B., He, L., & Gentine, P. (2021). Comment on "Recent global decline of CO2 fertilization effects on vegetation photosynthesis". *Science*, *373*(6562), p.eabg2947.

Fung, I. Y., Tucker, C. J., & Prentice, K. C. (1987). Application of Advanced Very High Resolution Radiometer vegetation index to study atmosphere-biosphere exchange of CO2. *Journal of Geophysical Research: Atmospheres*, *92*(D3), 2999–3015.

Gamon, J. A., Huemmrich, K. F., Wong, C. Y. S., Ensminger, I., Garrity, S., Hollinger, D. Y., et al. (2016). A remotely sensed pigment index reveals photosynthetic phenology in evergreen conifers. *Proceedings of the National Academy of Sciences*, *113*(46), 13087–13092.

Gamon, J. A., Field, C. B., Goulden, M. L., Griffin, K. L., Hartley, A. E., Joel, G., et al. (1995). Relationships Between NDVI, Canopy Structure, and Photosynthesis in Three Californian Vegetation Types. *Ecological Applications*, *5*(1), 28–41.

Gatti, L. V., Gloor, M., Miller, J. B., Doughty, C. E., Malhi, Y., Domingues, L. G., et al. (2014). Drought sensitivity of Amazonian carbon balance revealed by atmospheric measurements. *Nature*, *506*(7486), 76–80.

Gaubert, B., Stephens, B. B., Basu, S., Chevallier, F., Deng, F., Kort, E. A., et al. (2019). Global atmospheric CO2 inverse models converging on neutral tropical land exchange, but disagreeing on fossil fuel and atmospheric growth rate. *Biogeosciences*, *16*(1), 117–134.

Gentine, P., & Alemohammad, S. H. (2018). Reconstructed solar-induced fluorescence: A machine learning vegetation product based on MODIS surface reflectance to reproduce GOME-2 solar-induced fluorescence. *Geophysical Research Letters*, *45*(7), 3136–3146.

Gerstl, S. A. W., & Zardecki, A. (1982). Effects of aerosols on photosynthesis. *Nature*, *300*(5891), 436–437.

Gier, B. K., Buchwitz, M., Reuter, M., Cox, P. M., Friedlingstein, P., & Eyring, V. (2020). Spatially resolved evaluation of Earth system models with satellite column-averaged CO2. *Biogeosciences*, *17*(23), 6115–6144.

Giglio, L., Randerson, J. T., & Werf, G. R. van der. (2013). Analysis of daily, monthly, and annual burned area using the fourth-generation global fire emissions database (GFED4). *Journal of Geophysical Research: Biogeosciences*, *118*(1), 317–328. https://doi.org/10.1002/JGRG.20042

Goetz, S. J., Bunn, A. G., Fiske, G. J., & Houghton, R. A. (2005). Satellite-observed photosynthetic trends across boreal North America associated with climate and fire disturbance. *Proceedings of the National Academy of Sciences*, *102*(38), 13521–13525.

Goetz, S. J., Bunn, A. G., Fiske, G. J., & Houghton, R. A. (2005). Satellite-observed photosynthetic trends across boreal North America associated with climate and fire disturbance. *Proceedings of the National Academy of Sciences*, *102*(38), 13521–13525.

Graven, H. D., Keeling, R. F., Piper, S. C., Patra, P. K., Stephens, B. B., Wofsy, S. C., et al. (2013). Enhanced seasonal exchange of CO2by Northern ecosystems since 1960. *Science*, *341*(6150), 1085–1089.

Gray, J. M., Frolking, S., Kort, E. A., Ray, D. K., Kucharik, C. J., Ramankutty, N., & Friedl, M. A. (2014). Direct human influence on atmospheric CO 2 seasonality from increased cropland productivity. *Nature*, *515*(7527), 398–401.

Grippa, M., Kergoat, L., Le Toan, T., Mognard, N. M., Delbart, N., l'Hermitte, J., & Vicente-Serrano, S. M. (2005). The impact of snow depth and snowmelt on the vegetation variability over central Siberia. *Geophysical Research Letters*, *32*(21).

Grossmann, K., Frankenberg, C., Magney, T. S., Hurlock, S. C., Seibt, U., & Stutz, J. (2018). PhotoSpec: A new instrument to measure spatially distributed red and far-red Solar-Induced Chlorophyll Fluorescence. *Remote Sensing of Environment*, *216*, 311–327.

Gu, L., Falge, E. M., Boden, T., Baldocchi, D. D., Black, T. A., Saleska, S. R., et al. (2005). Objective threshold determination for nighttime eddy flux filtering. *Agricultural and Forest Meteorology*, *128*(3–4), 179–197.

Gu, L., Han, J., Wood, J. D., Chang, C. Y., & Sun, Y. (2019). Sun-induced Chl fluorescence and its importance for biophysical modeling of photosynthesis based on light reactions. *New Phytologist*, *223*(3), 1179–1191.

Gu, L., Massman, W. J., Leuning, R., Pallardy, S. G., Meyers, T., Hanson, P. J., et al. (2012). The fundamental equation of eddy covariance and its application in flux measurements. *Agricultural and Forest Meteorology*, *152*(1), 135–148.

Gu, L., Meyers, T., Pallardy, S. G., Hanson, P. J., Yang, B., Heuer, M., et al. (2006). Direct and indirect effects of atmospheric conditions and soil moisture on surface energy partitioning revealed by a prolonged drought at a temperate forest site. *Journal of Geophysical Research Atmospheres*, *111*(D16).

Gu, L., Pallardy, S. G., Hosman, K. P., & Sun, Y. (2015). Drought-influenced mortality of tree species with different predawn leaf water dynamics in a decade-long study of a central US forest. *Biogeosciences*, *12*(10), 2831–2845.

Gu, L., Pallardy, S. G., Hosman, K. P., & Sun, Y. (2016). Impacts of precipitation variability on plant species and community water stress in a temperate deciduous forest in the central US. *Agricultural and Forest Meteorology*, *217*, 120–136.

Gu, L., Pallardy, S. G., Yang, B., Hosman, K. P., Mao, J., Ricciuto, D., et al. (2016). Testing a land model in ecosystem functional space via a comparison of observed and modeled ecosystem flux responses to precipitation regimes and associated stresses in a Central U.S. forest. *Journal of Geophysical Research: Biogeosciences*, *121*(7), 1884–1902.

Guan, K., Berry, J. A., Zhang, Y., Joiner, J., Guanter, L., Badgley, G., & Lobell, D. B. (2016). Improving the monitoring of crop productivity using spaceborne solar-induced fluorescence. *Global Change Biology*, *22*(2), 716–726.

Guan, K., Wu, J., Kimball, J. S., Anderson, M. C., Frolking, S., Li, B., et al. (2017). The shared and unique values of optical, fluorescence, thermal and microwave satellite data for estimating large-scale crop yields. *Remote Sensing of Environment*, *199*, 333–349.

Guanter, L., Aben, I., Tol, P., Krijger, J. M., Hollstein, A., Köhler, P., et al. (2015). Potential of the TROPOspheric Monitoring Instrument (TROPOMI) onboard the Sentinel-5 Precursor for the monitoring of terrestrial chlorophyll fluorescence. *Atmos. Meas. Tech*, *8*, 1337–1352.

Guanter, L., Frankenberg, C., Dudhia, A., Lewis, P. E., Gómez-Dans, J., Kuze, A., et al. (2012). Retrieval and global assessment of terrestrial chlorophyll fluorescence from GOSAT space measurements. *Remote Sensing of Environment*, *121*, 236–251.

Guanter, L., Zhang, Y., Jung, M., Joiner, J., Voigt, M., Berry, J. A., et al. (2014). Global and time-resolved monitoring of crop photosynthesis with chlorophyll fluorescence. *Proceedings of the National Academy of Sciences*, *111*(14), E1327–E1333.

Guanter, L., Zhang, Y., Jung, M., Joiner, J., Voigt, M., Berry, J. A., et al. (2014). Global and time-resolved monitoring of crop photosynthesis with chlorophyll fluorescence. *Proceedings of the National Academy of Sciences of the United States of America*, *111*(14), E1327–E1333. https://doi.org/10.1073/pnas.1320008111

He, L., Magney, T., Dutta, D., Yin, Y., Köhler, P., Grossmann, K., et al. (2020). From the Ground to Space: Using Solar-Induced Chlorophyll Fluorescence to Estimate Crop Productivity. *Geophysical Research Letters*, *47*(7), e2020GL087474.

He, L., Wood, J. D., Sun, Y., Magney, T., Dutta, D., Köhler, P., et al. (2020). Tracking Seasonal and Interannual Variability in Photosynthetic Downregulation in Response to Water Stress at a Temperate Deciduous Forest. *Journal of Geophysical Research: Biogeosciences*, *125*(8), e2018JG005002.

Hemes, K. S., Verfaillie, J., & Baldocchi, D. D. (2020). Wildfire-Smoke Aerosols Lead to Increased Light Use Efficiency Among Agricultural and Restored Wetland Land Uses in California's Central Valley. *Journal of Geophysical Research: Biogeosciences*, *125*(2), e2019JG005380.

Henze, D. K., Hakami, A., & Seinfeld, J. H. (2007). Development of the adjoint of GEOS-Chem. *Atmospheric Chemistry and Physics*, *7*(9), 2413–2433.

Hermle, S., Lavigne, M. B., Bernier, P. Y., Bergeron, O., & Pare, D. (2010). Component respiration, ecosystem respiration and net primary production of a mature black spruce forest in northern Quebec. *Tree Physiology*, *30*(4), 527–540.

Hoerling, M., Eischeid, J., Kumar, A., Leung, R., Mariotti, A., Mo, K., et al. (2014). Causes and predictability of the 2012 Great Plains drought. *Bulletin of the American Meteorological Society*, *95*(2), 269–282.

Hong, C., Mueller, N. D., Burney, J. A., Zhang, Y., AghaKouchak, A., Moore, F. C., et al. (2020). Impacts of ozone and climate change on yields of perennial crops in California. *Nature Food*, *1*(3), 166–172.

Hu, L., Andrews, A. E., Thoning, K. W., Sweeney, C., Miller, J. B., Michalak, A. M., et al. (2019). Enhanced North American carbon uptake associated with El Niño. *Science Advances*, *5*(6), eaaw0076.

Huang, K., Xia, J., Wang, Y., Ahlström, A., Chen, J., Cook, R. B., et al. (2018). Enhanced peak growth of global vegetation and its key mechanisms. *Nature Ecology and Evolution*, *2*(12), 1897–1905.

Huang, R. J., Zhang, Y., Bozzetti, C., Ho, K. F., Cao, J. J., Han, Y., et al. (2015). High secondary aerosol contribution to particulate pollution during haze events in China. *Nature*, *514*(7521), 218–222.

Huang, R. J., Zhang, Y., Bozzetti, C., Ho, K. F., Cao, J. J., Han, Y., et al. (2015). High secondary aerosol contribution to particulate pollution during haze events in China. *Nature*, *514*(7521), 218–222.

Huete, A., Didan, K., Miura, T., Rodriguez, E. P., Gao, X., & Ferreira, L. G. (n.d.). Overview of the radiometric and biophysical performance of the MODIS vegetation indices. Retrieved from www.elsevier.com/locate/rse

Huete, A. R., Liu, H. Q., Batchily, K., & van Leeuwen, W. (1997). A comparison of vegetation indices over a global set of TM images for EOS-MODIS. *Remote Sensing of Environment*, *59*(3), 440–451.

Huete, A., Didan, K., Miura, T., Rodriguez, E. P., Gao, X., & Ferreira, L. G. (2002). Overview of the radiometric and biophysical performance of the MODIS vegetation indices. *Remote Sensing of Environment*, *83*(1–2), 195–213.

Jia, G. J., Epstein, H. E., & Walker, D. A. (2003). Greening of arctic Alaska, 1981–2001. *Geophysical Research Letters*, *30*(20), 2067.

Jin, Z., Azzari, G., & Lobell, D. B. (2017). Improving the accuracy of satellite-based high-resolution yield estimation: A test of multiple scalable approaches. *Agricultural and Forest Meteorology*, *247*, 207–220.

Joiner, J., Guanter, L., Lindstrot, R., Voigt, M., Vasilkov, A. P., Middleton, E. M., et al. (2013). Atmospheric Measurement Techniques Global monitoring of terrestrial chlorophyll fluorescence from moderate-spectral-resolution near-infrared satellite measurements: methodology, simulations, and application to GOME-2. *Atmos. Meas. Tech*, *6*, 2803–2823.

Joiner, J., Yoshida, Y., Vasilkov, A. P., & Middleton, E. M. (2011). First observations of global and seasonal terrestrial chlorophyll fluorescence from space. *Biogeosciences*, *8*(3), 637–651.

Jung, M., Schwalm, C., Migliavacca, M., Walther, S., Camps-Valls, G., Koirala, S., et al. (2020). Scaling carbon fluxes from eddy covariance sites to globe: Synthesis and evaluation of the FLUXCOM approach. *Biogeosciences*, *17*(5), 1343–1365.

Karl, T. R., Gleason, B. E., Menne, M. J., McMahon, J. R., Heim Jr, R. R., Brewer, M. J., et al. (2012). US temperature and drought: Recent anomalies and trends. *Eos, Transactions American Geophysical Union*, *93*(47), 473–474.

Keeling, C. D., Chin, J. F. S., & Whorf, T. P. (1996). Increased activity of northern vegetation inferred from atmospheric CO2 measurements. *Nature*, *382*(6587), 146–148.

Keeling, C. D., Whorf, T. P., Wahlen, M., & Plichtt, J. van der. (n.d.). Interannual extremes in the rate of rise of atmospheric carbon dioxide since 1980. *Nature*, *375*, 666–670.

Keenan, T. F., & Riley, W. J. (2018). Greening of the land surface in the world's cold regions consistent with recent warming. *Nature Climate Change 2018 8:9*, *8*(9), 825–828.

Keenan, T. F., & Williams, C. A. (2018). The Terrestrial Carbon Sink. *Annual Review of Environment and Resources*, *43*(1), 219-243.

Keenan, T. F., Hollinger, D. Y., Bohrer, G., Dragoni, D., Munger, J. W., Schmid, H. P., & Richardson, A. D. (2013). Increase in forest water-use efficiency as atmospheric carbon dioxide concentrations rise. *Nature*, *499*(7458), 324–327.

Keenan, T. F., Migliavacca, M., Papale, D., Baldocchi, D., Reichstein, M., Torn, M., & Wutzler, T. (n.d.). Widespread inhibition of daytime ecosystem respiration. *Nature Ecology & Evolution*, *3*(3), pp.407-415.

Keenan, T. F., Gray, J., Friedl, M. A., Toomey, M., Bohrer, G., Hollinger, D. Y., et al. (2014). Net carbon uptake has increased through warming-induced changes in temperate forest phenology. *Nature Climate Change*, *4*(7), 598–604.

Kimm, H., Guan, K., Gentine, P., Wu, J., Bernacchi, C. J., Sulman, B. N., et al. (2020). Redefining droughts for the US Corn Belt: The dominant role of atmospheric vapor pressure deficit over soil moisture in regulating stomatal behavior of Maize and Soybean. *Agricultural and Forest Meteorology*, *287*, 107930.

Köhler, P., Guanter, L., & Joiner, J. (2015). A linear method for the retrieval of sun-induced chlorophyll fluorescence from GOME-2 and SCIAMACHY data. *Atmos. Meas. Tech*, *8*, 2589–2608. https://doi.org/10.5194/amt-8-2589-2015

Köhler, P., Frankenberg, C., Magney, T. S., Guanter, L., Joiner, J., & Landgraf, J. (2018). Global retrievals of solar-induced chlorophyll fluorescence with TROPOMI: First results and intersensor comparison to OCO-2. *Geophysical Research Letters*, *45*(19), 10–456.

Köhler, P., Frankenberg, C., Magney, T. S., Guanter, L., Joiner, J., & Landgraf, J. (2018). Global Retrievals of Solar-Induced Chlorophyll Fluorescence With TROPOMI:

First Results and Intersensor Comparison to OCO-2. *Geophysical Research Letters*, *45*(19), 10,456-10,463.

Kolby Smith, W., Reed, S. C., Cleveland, C. C., Ballantyne, A. P., Anderegg, W. R. L., Wieder, W. R., et al. (2015). Large divergence of satellite and Earth system model estimates of global terrestrial CO2 fertilization. *Nature Climate Change 2015 6:3*, *6*(3), 306–310.

Konings, A. G., Piles, M., Das, N., & Entekhabi, D. (2017). L-band vegetation optical depth and effective scattering albedo estimation from SMAP. *Remote Sensing of Environment*, *198*, 460–470.

Koster, R. D., Sud, Y. C., Guo, Z., Dirmeyer, P. A., Bonan, G., Oleson, K. W., et al. (2006). GLACE: the global land–atmosphere coupling experiment. Part I: overview. *Journal of Hydrometeorology*, *7*(4), 590–610.

Lasslop, G., Reichstein, M., Papale, D., Richardson, A., Arneth, A., Barr, A., et al. (2010). Separation of net ecosystem exchange into assimilation and respiration using a light response curve approach: Critical issues and global evaluation. *Global Change Biology*, *16*(1), 187–208.

Lassoie, J. P., & Hinckley, T. M. (1991). *Techniques and approaches in forest tree ecophysiology*. CRC Press.

Le, T., Wang, Y., Liu, L., Yang, J., Yung, Y. L., Li, G., & Seinfeld, J. H. (2020). Unexpected air pollution with marked emission reductions during the COVID-19 outbreak in China. *Science*, *369*(6504), 702–706.

Lee, J.-E., Frankenberg, C., van der Tol, C., Berry, J. A., Guanter, L., Boyce, C. K., et al. (2013). Forest productivity and water stress in Amazonia: Observations from GOSAT chlorophyll fluorescence. *Proceedings of the Royal Society B: Biological Sciences*, *280*(1761), 20130171.

Lee, J., Berry, J. A., van der Tol, C., Yang, X., Guanter, L., Damm, A., et al. (2015). Simulations of chlorophyll fluorescence incorporated into the C ommunity L and M odel version 4. *Global Change Biology*, *21*(9), 3469–3477.

Li, H., Zhou, Y., Xin, W., Wei, Y., Zhang, J., & Guo, L. (2019, December 1). Wheat breeding in northern China: Achievements and technical advances. *Crop Journal*. Crop Science Society of China/ Institute of Crop Sciences.

Li, J. (2009). Production, Breeding and Process of Maize in China. In *Handbook of Maize: Its Biology* (pp. 563–576). Springer New York.

Li, J. (2020). Pollution Trends in China from 2000 to 2017: A Multi-Sensor View from Space. *Remote Sensing*, *12*(2), 208.

Li, K., Jacob, D. J., Liao, H., Shen, L., Zhang, Q., & Bates, K. H. (2019). Anthropogenic drivers of 2013–2017 trends in summer surface ozone in China. *Proceedings of the National Academy of Sciences*, *116*(2), 422–427.

Li, Q., Chen, J., & Moorhead, D. L. (2012). Respiratory carbon losses in a managed oak forest ecosystem. *Forest Ecology and Management*, *279*, 1–10.

Li, S., Wheeler, T., Challinor, A., Lin, E., Ju, H., & Xu, Y. (2010). The observed relationships between wheat and climate in China. *Agricultural and Forest Meteorology*, *150*(11), 1412–1419.

Li, X., & Xiao, J. (2019). A global, 0.05-degree product of solar-induced chlorophyll fluorescence derived from OCO-2, MODIS, and reanalysis data. *Remote Sensing*, *11*(5), 517.

Li, X., Xiao, J., & He, B. (2018). Chlorophyll fluorescence observed by OCO-2 is strongly related to gross primary productivity estimated from flux towers in temperate forests. *Remote Sensing of Environment*, *204*, 659–671.

Li, X., Xiao, J., He, B., Altaf Arain, M., Beringer, J., Desai, A. R., et al. (2018). Solar-induced chlorophyll fluorescence is strongly correlated with terrestrial photosynthesis for a wide variety of biomes: First global analysis based on OCO-2 and flux tower observations. *Global Change Biology*, *24*(9), 3990-4008.

Li, Y., Guan, K., Schnitkey, G. D., DeLucia, E., & Peng, B. (2019). Excessive rainfall leads to maize yield loss of a comparable magnitude to extreme drought in the United States. *Global Change Biology*, *25*(7), 2325–2337.

Li, Z., Lau, W. K. M., Ramanathan, V., Wu, G., Ding, Y., Manoj, M. G., et al. (2016). Aerosol and monsoon climate interactions over Asia. *Reviews of Geophysics*, 54(4), pp.866-929.

Li, Z., Zhang, Q., Li, J., Yang, X., Wu, Y., Zhang, Z., et al. (2020). Solar-induced chlorophyll fluorescence and its link to canopy photosynthesis in maize from continuous ground measurements. *Remote Sensing of Environment*, *236*, 111420.

Lian, X., Piao, S., Li, L. Z. X., Li, Y., Huntingford, C., Ciais, P., et al. (2020). Summer soil drying exacerbated by earlier spring greening of northern vegetation. *Science Advances*, *6*(1), eaax0255.

Lin, X., Rogers, B. M., Sweeney, C., Chevallier, F., Arshinov, M., Dlugokencky, E., et al. (2020). Siberian and temperate ecosystems shape Northern Hemisphere atmospheric CO2 seasonal amplification. *Proceedings of the National Academy of Sciences of the United States of America*, *117*(35), 21079–21087.

Liu, H. Q., & Huete, A. (1995). A feedback based modification of the NDVI to minimize canopy background and atmospheric noise. *IEEE Transactions on Geoscience and Remote Sensing*, *33*(2), 457–465.

Liu, J., Bowman, K. W., Lee, M., Henze, D. K., Bousserez, N., Brix, H., et al. (2014). Carbon monitoring system flux estimation and attribution: impact of ACOS-GOSAT XCO2 sampling on the inference of terrestrial biospheric sources and sinks. *Tellus B: Chemical and Physical Meteorology*, *66*(1), 22486.

Liu, J., Wennberg, P. O., Parazoo, N. C., Yin, Y., & Frankenberg, C. (2020). Observational Constraints on the Response of High-Latitude Northern Forests to Warming. *AGU Advances*, *1*(4), e2020AV000228.

Liu, L., Guan, L., & Liu, X. (2017). Directly estimating diurnal changes in GPP for C3 and C4 crops using far-red sun-induced chlorophyll fluorescence. *Agricultural and Forest Meteorology*, *232*, 1–9.

Liu, L., Liu, X., Chen, J., Du, S., Ma, Y., Qian, X., et al. (2020). Estimating maize GPP using near-infrared radiance of vegetation. *Science of Remote Sensing*, *2*, 100009.

Liu, Y., Wang, J., Yao, L., Chen, X., Cai, Z., Yang, D., et al. (2018). The TanSat mission: preliminary global observations. *Science Bulletin*, *63*(18), 1200–1207. https://doi.org/10.1016/J.SCIB.2018.08.004

Lobell, D. B., Hicke, J. A., Asner, G. P., Field, C. B., Tucker, C. J., & Los, S. O. (2002). Satellite estimates of productivity and light use efficiency in United States agriculture, 1982–98. *Global Change Biology*, *8*(8), 722–735.

Lobell, D. B., & Burney, J. A. (2021). Cleaner air has contributed one-fifth of US maize and soybean yield gains since 1999. *Environmental Research Letters*, *16*(7), 74049.

Lobell, D. B., Thau, D., Seifert, C., Engle, E., & Little, B. (2015). A scalable satellite-based crop yield mapper. *Remote Sensing of Environment*, *164*, 324–333.

Lobell, D. B., & Burke, M. B. (2008). Why are agricultural impacts of climate change so uncertain? the importance of temperature relative to precipitation. *Environmental Research Letters*, *3*(3), 034007.

Lobell, D. B., Burke, M. B., Tebaldi, C., Mastrandrea, M. D., Falcon, W. P., & Naylor, R. L. (2008). Prioritizing climate change adaptation needs for food security in 2030. *Science*, *319*(5863), 607–610. https://doi.org/10.1126/science.1152339

Lobell, D. B., Deines, J. M., & Tommaso, S. Di. (2020). Changes in the drought sensitivity of US maize yields. *Nature Food*, *1*(11), 729–735.

Lobell, D. B., & Field, C. B. (2011). California perennial crops in a changing climate. *Climatic Change*, *109*(SUPPL. 1), 317–333.

Lobell, D. B., & Gourdji, S. M. (2012). The influence of climate change on global crop productivity. *Plant Physiology*, *160*(4), 1686–1697.

Lobell, D. B., Roberts, M. J., Schlenker, W., Braun, N., Little, B. B., Rejesus, R. M., & Hammer, G. L. (2014). Greater sensitivity to drought accompanies maize yield increase in the U.S. Midwest. *Science*, *344*(6183), 516–519.

Lobell, D. B., Schlenker, W., & Costa-Roberts, J. (2011). Climate trends and global crop production since 1980. *Science*, *333*(6042), 616–620.

Lombardozzi, D. L., Bonan, G. B., Levis, S., & Lawrence, D. M. (2018). Changes in Wood Biomass and Crop Yields in Response to Projected CO2, O3, Nitrogen Deposition, and Climate. *Journal of Geophysical Research: Biogeosciences*, *123*(10), 3262–3282.

Lu, C., & Fan, L. (2013). Winter wheat yield potentials and yield gaps in the North China Plain. *Field Crops Research*, *143*, 98–105. https://doi.org/10.1016/j.fcr.2012.09.015

MacBean, N., Maignan, F., Bacour, C., Lewis, P., Peylin, P., Guanter, L., et al. (2018). Strong constraint on modelled global carbon uptake using solar-induced chlorophyll fluorescence data. *Scientific Reports*, *8*(1), 1–12.

Magney, T. S., Bowling, D. R., Logan, B. A., Grossmann, K., Stutz, J., Blanken, P. D., et al. (2019). Mechanistic evidence for tracking the seasonality of photosynthesis with

solar-induced fluorescence. *Proceedings of the National Academy of Sciences*, *116*(24), 11640–11645.

Magney, T. S., Frankenberg, C., Köhler, P., North, G., Davis, T. S., Dold, C., et al. (2019). Disentangling changes in the spectral shape of chlorophyll fluorescence: Implications for remote sensing of photosynthesis. *Journal of Geophysical Research: Biogeosciences*, *124*(6), 1491–1507.

Magney, T. S., Barnes, M. L., & Yang, X. (2020). On the Covariation of Chlorophyll Fluorescence and Photosynthesis Across Scales. *Geophysical Research Letters*, *47*(23), e2020GL091098.

Magney, T. S., Frankenberg, C., Fisher, J. B., Sun, Y., North, G. B., Davis, T. S., et al. (2017). Connecting active to passive fluorescence with photosynthesis: a method for evaluating remote sensing measurements of Chl fluorescence. *New Phytologist*, *215*(4), 1594–1608.

Mallya, G., Zhao, L., Song, X. C., Niyogi, D., & Govindaraju, R. S. (2013). 2012 Midwest Drought in the United States. *Journal of Hydrologic Engineering*, *18*(7), 737–745.

McGrath, J. M., Betzelberger, A. M., Wang, S., Shook, E., Zhu, X. G., Long, S. P., & Ainsworth, E. A. (2015). An analysis of ozone damage to historical maize and soybean yields in the United States. *Proceedings of the National Academy of Sciences of the United States of America*, *112*(46), 14390–14395.

Menemenlis, D., Campin, J.-M., Heimbach, P., Hill, C. N., Lee, T., Nguyen, A. T., et al. (2008). CCO2: High Resolution Global Ocean and Sea Ice Data Synthesis. *Mercator Ocean Quarterly Newsletter*, *31*, 13–21.

Meng, E., Hu, R., Shi, X., & Zhang, S. (2006). *Maize in China: Production Systems, Constraints, and Research Priorities*. CIMMYT. Retrieved from https://agris.fao.org/agris-search/search.do?recordID=QY2016600621

Meng, Q., Chen, X., Lobell, D. B., Cui, Z., Zhang, Y., Yang, H., & Zhang, F. (2016). Growing sensitivity of maize to water scarcity under climate change. *Scientific Reports*, *6*(1), 1–7.

Miao, G., Guan, K., Yang, X., Bernacchi, C. J., Berry, J. A., DeLucia, E. H., et al. (2018). Sun-induced chlorophyll fluorescence, photosynthesis, and light use efficiency of a soybean field from seasonally continuous measurements. *Journal of Geophysical Research: Biogeosciences*, *123*(2), 610–623.

Monteith, J. L. (1972). Solar Radiation and Productivity in Tropical Ecosystems. *The Journal of Applied Ecology*, *9*(3), 747.

Mueller, N. D., Butler, E. E., McKinnon, K. A., Rhines, A., Tingley, M., Holbrook, N. M., & Huybers, P. (2016). Cooling of US Midwest summer temperature extremes from cropland intensification. *Nature Climate Change*, *6*(3), 317–322.

Myers-Smith, I. H., Elmendorf, S. C., Beck, P. S. A., Wilmking, M., Hallinger, M., Blok, D., et al. (2015). Climate sensitivity of shrub growth across the tundra biome. *Nature Climate Change 2015 5:9*, *5*(9), 887–891.

Myers-Smith, I. H., Kerby, J. T., Phoenix, G. K., Bjerke, J. W., Epstein, H. E., Assmann, J. J., et al. (2020). Complexity revealed in the greening of the Arctic. *Nature Climate Change 2020 10:2*, *10*(2), 106–117.

Myers-Smith, I. H., Kerby, J. T., Phoenix, G. K., Bjerke, J. W., Epstein, H. E., Assmann, J. J., et al. (2020). Complexity revealed in the greening of the Arctic. *Nature Climate Change 2020 10:2*, *10*(2), 106–117.

Myneni, R., Knyazikhin, Y., & Park, T. (2015). MOD15A2H MODIS/terra leaf area index. *FPAR 8-Day L4 Global 500 m SIN Grid V006 Data Set*.

Myneni, R. B., Keeling, C. D., Tucker, C. J., Asrar, G., & Nemani, R. R. (1997). Increased plant growth in the northern high latitudes from 1981 to 1991. *Nature 1997 386:6626*, *386*(6626), 698–702.

Oleson, K. (2013). Technical Description of version 4.5 of the Community Land Model (CLM) Report NCAR/TN-503+ STR.

Pallardy, S. G., Gu, L., Wood, J. D., Hosman, K. P., Sun, Y., & hook, L. (2018). Predawn Leaf Water Potential of Oak-Hickory Forest at Missouri Ozark (MOFLUX) Site: 2004-2017.

Parazoo, N. C., Denning, A. S., Kawa, S. R., Pawson, S., & Lokupitiya, R. (2012). Atmospheric Chemistry and Physics CO 2 flux estimation errors associated with moist atmospheric processes. *Atmos. Chem. Phys*, *12*, 6405–6416

Parazoo, N. C., Barnes, E., Worden, J., Harper, A. B., Bowman, K. B., Frankenberg, C., et al. (2015). Influence of ENSO and the NAO on terrestrial carbon uptake in the Texas-northern Mexico region. *Global Biogeochemical Cycles*, *29*(8), 1247–1265.

Parazoo, N. C., Commane, R., Wofsy, S. C., Koven, C. D., Sweeney, C., Lawrence, D. M., et al. (2016). Detecting regional patterns of changing CO2 flux in Alaska. *Proceedings of the National Academy of Sciences of the United States of America*, *113*(28), 7733–7738.

Parent, M. B., & Verbyla, D. (2010). The Browning of Alaska's Boreal Forest. *Remote Sensing 2010, Vol. 2, Pages 2729-2747*, *2*(12), 2729–2747.

Park, T., Chen, C., Macias-Fauria, M., Tømmervik, H., Choi, S., Winkler, A., et al. (2019). Changes in timing of seasonal peak photosynthetic activity in northern ecosystems. *Global Change Biology*, *25*(7), 2382–2395.

Pastorello, G., Trotta, C., Canfora, E., Chu, H., Christianson, D., Cheah, Y. W., et al. (2020). The FLUXNET2015 dataset and the ONEFlux processing pipeline for eddy covariance data. *Scientific Data*, *7*(1), 225.

Peiro, H., Crowell, S., Schuh, A., Baker, D. F., O'Dell, C., Jacobson, A. R., et al. (2022). Four years of global carbon cycle observed from the Orbiting Carbon Observatory 2 (OCO-2) version 9 and in situ data and comparison to OCO-2 version 7. *Atmospheric Chemistry and Physics*, *22*(2), 1097–1130.

Peng, S., Tang, Q., & Zou, Y. (2009). Current status and challenges of rice production in China. *Plant Production Science*, *12*(1), 3–8.

Peng, S., Ciais, P., Chevallier, F., Peylin, P., Cadule, P., Sitch, S., et al. (2015). Benchmarking the seasonal cycle of CO2 fluxes simulated by terrestrial ecosystem models. *Global Biogeochemical Cycles*, *29*(1), 46–64.

Perez-Priego, O., Guan, J., Rossini, M., Fava, F., Wutzler, T., Moreno, G., et al. (2015). Sun-induced chlorophyll fluorescence and photochemical reflectance index improve remote-sensing gross primary production estimates under varying nutrient availability in a typical Mediterranean savanna ecosystem. *Biogeosciences*, *12*(21), 6351–6367.

Peters, W., Jacobson, A. R., Sweeney, C., Andrews, A. E., Conway, T. J., Masarie, K., et al. (2007). An atmospheric perspective on North American carbon dioxide exchange: CarbonTracker. *Proceedings of the National Academy of Sciences*, *104*(48), 18925–18930.

Peters, W., Jacobson, A. R., Sweeney, C., Andrews, A. E., Conway, T. J., Masarie, K., et al. (2007). An atmospheric perspective on North American carbon dioxide exchange: CarbonTracker. *Proceedings of the National Academy of Sciences of the United States of America*, *104*(48), 18925–18930. https://doi.org/10.1073/pnas.0708986104

Piao, S., Liu, Z., Wang, Y., Ciais, P., Yao, Y., Peng, S., et al. (2018). On the causes of trends in the seasonal amplitude of atmospheric CO2. *Global Change Biology*, *24*(2), 608–616.

Ponomarev, E. I., Kharuk, V. I., & Ranson, K. J. (2016). Wildfires Dynamics in Siberian Larch Forests. *Forests 2016, Vol. 7, Page 125*, *7*(6), 125.

Porcar-Castell, A., Tyystjärvi, E., Atherton, J., van der Tol, C., Flexas, J., Pfündel, E. E. E., et al. (2014). Linking chlorophyll a fluorescence to photosynthesis for remote sensing applications: mechanisms and challenges. *Journal of Experimental Botany*, *65*(15), 4065–4095.

Porcar-Castell, A., Tyystjärvi, E., Atherton, J., van der Tol, C., Flexas, J., Pfündel, E. E., et al. (2014). Linking chlorophyll a fluorescence to photosynthesis for remote sensing applications: mechanisms and challenges. *Journal of Experimental Botany*, *65*(15), 4065–4095.

Proctor, J. (2021). Atmospheric opacity has a nonlinear effect on global crop yields. *Nature Food*, *2*(3), 166–173.

Randerson, J. T., Thompson, M. V., Conway, T. J., Fung, I. Y., & Field, C. B. (1997). The contribution of terrestrial sources and sinks to trends in the seasonal cycle of atmospheric carbon dioxide. *Global Biogeochemical Cycles*, *11*(4), 535–560.

Reichstein, M., Falge, E., Baldocchi, D., Papale, D., Aubinet, M., Berbigier, P., et al. (2005). On the separation of net ecosystem exchange into assimilation and ecosystem respiration: Review and improved algorithm. *Global Change Biology*, *11*(9), 1424-1439

Richardson, A. D., Keenan, T. F., Migliavacca, M., Ryu, Y., Sonnentag, O., & Toomey, M. (2013). Climate change, phenology, and phenological control of vegetation feedbacks to the climate system. *Agricultural and Forest Meteorology*, *169*, 156–173.

Rollinson, C. R., Liu, Y., Raiho, A., Moore, D. J. P., McLachlan, J., Bishop, D. A., et al. (2017). Emergent climate and CO2 sensitivities of net primary productivity in ecosystem models do not agree with empirical data in temperate forests of eastern North America. *Global Change Biology*, *23*(7), 2755–2767.

Rosenzweig, C., Tubiello, F. N., Goldberg, R., Mills, E., & Bloomfield, J. (2002). Increased crop damage in the US from excess precipitation under climate change. *Global Environmental Change*, *12*(3), 197–202.

Rossini, M., Nedbal, L., Guanter, L., Ač, A., Alonso, L., Burkart, A., et al. (2015). Red and far red Sun-induced chlorophyll fluorescence as a measure of plant photosynthesis. *Geophysical Research Letters*, *42*(6), 1632–1639.

Running, S. W., Nemani, R. R., Heinsch, F. A., Zhao, M., Reeves, M., & Hashimoto, H. (2004). A continuous satellite-derived measure of global terrestrial primary production. *Bioscience*, *54*(6), 547–560.

Running, S. W., Thornton, P. E., Nemani, R., & Glassy, J. M. (2000). Global Terrestrial Gross and Net Primary Productivity from the Earth Observing System. *Methods in Ecosystem Science*, 44–57.

Ryu, Y., Berry, J. A., & Baldocchi, D. D. (2019). What is global photosynthesis? History, uncertainties and opportunities. *Remote Sensing of Environment*, *223*, 95–114.

Ryu, Y., Jiang, C., Kobayashi, H., & Detto, M. (2018). MODIS-derived global land products of shortwave radiation and diffuse and total photosynthetically active radiation at 5 km resolution from 2000. *Remote Sensing of Environment*, *204*, 812–825.

Schimel, D., Pavlick, R., Fisher, J. B., Asner, G. P., Saatchi, S., Townsend, P., et al. (2015). Observing terrestrial ecosystems and the carbon cycle from space. *Global Change Biology*, *21*(5), 1762–1776.

Schlenker, W., & Roberts, M. J. (2009). Nonlinear temperature effects indicate severe damages to U.S. crop yields under climate change. *Proceedings of the National Academy of Sciences of the United States of America*, *106*(37), 15594–15598.

Schuh, A. E., Jacobson, A. R., Basu, S., Weir, B., Baker, D., Bowman, K., et al. (2019). Quantifying the Impact of Atmospheric Transport Uncertainty on CO2 Surface Flux Estimates. *Global Biogeochemical Cycles*, *33*(4), 484–500.

Seidl, R., Thom, D., Kautz, M., Martin-Benito, D., Peltoniemi, M., Vacchiano, G., et al. (2017). Forest disturbances under climate change. *Nature Climate Change 2017 7:6*, *7*(6), 395–402.

Seinfeld, J., & Pandis, S. (2016). *Atmospheric Chemistry and Physics: From Air Pollution to Climate Change*. John Wiley & Sons.

Shindell, D., Faluvegi, G., Kasibhatla, P., & Van Dingenen, R. (2019). Spatial Patterns of Crop Yield Change by Emitted Pollutant. *Earth's Future*, *7*(2), 101–112.

Shindell, D., Ru, M., Zhang, Y., Seltzer, K., Faluvegi, G., Nazarenko, L., et al. (2021). Temporal and spatial distribution of health, labor, and crop benefits of climate change mitigation in the United States. *Proceedings of the National Academy of Sciences*, *118*(46).

Sippel, S., Forkel, M., Rammig, A., Thonicke, K., Flach, M., Heimann, M., et al. (2017). Contrasting and interacting changes in simulated spring and summer carbon cycle extremes in European ecosystems. *Environmental Research Letters*, *12*(7), 75006.

Smith, W. K., Biederman, J. A., Scott, R. L., Moore, D. J. P., He, M., Kimball, J. S., et al. (2018). Chlorophyll fluorescence better captures seasonal and interannual gross primary productivity dynamics across dryland ecosystems of southwestern North America. *Geophysical Research Letters*, *45*(2), 748–757.

Smith, W. K., Cleveland, C. C., Reed, S. C., & Running, S. W. (2014). Agricultural conversion without external water and nutrient inputs reduces terrestrial vegetation productivity. *Geophysical Research Letters*, *41*(2), 449–455.

Smith, W. K., Reed, S. C., Cleveland, C. C., Ballantyne, A. P., Anderegg, W. R. L., Wieder, W. R., et al. (2016). Large divergence of satellite and Earth system model estimates of global terrestrial CO2 fertilization. *Nature Climate Change*, *6*(3), 306–310.

Sogacheva, L., Rodriguez, E., Kolmonen, P., Virtanen, T. H., Saponaro, G., De Leeuw, G., et al. (2018). Spatial and seasonal variations of aerosols over China from two decades of multi-satellite observations - Part 2: AOD time series for 1995-2017 combined from ATSR ADV and MODIS C6.1 and AOD tendency estimations. *Atmospheric Chemistry and Physics*, *18*(22), 16631–16652.

Song, L., Guanter, L., Guan, K., You, L., Huete, A., Ju, W., & Zhang, Y. (2018). Satellite sun-induced chlorophyll fluorescence detects early response of winter wheat to heat stress in the Indian Indo-Gangetic Plains. *Global Change Biology*, *24*(9), 4023–4037.

Song, L., Guanter, L., Guan, K., You, L., Huete, A., Ju, W., & Zhang, Y. (2018). Satellite sun-induced chlorophyll fluorescence detects early response of winter wheat to heat stress in the Indian Indo-Gangetic Plains. *Global Change Biology*. https://doi.org/10.1111/gcb.14302

Song, Y., Linderholm, H. W., Wang, C., Tian, J., Huo, Z., Gao, P., et al. (2019). The influence of excess precipitation on winter wheat under climate change in China from 1961 to 2017. *Science of the Total Environment*, *690*, 189–196.

Sun, S., Yang, X., Lin, X., Sassenrath, G. F., & Li, K. (2018). Winter Wheat Yield Gaps and Patterns in China. *Agronomy Journal*, *110*(1), 319–330.

Sun, W., Fang, Y., Luo, X., Shiga, Y. P., Zhang, Y., Andrews, A. E., et al. (2021). Midwest US Croplands Determine Model Divergence in North American Carbon Fluxes. *AGU Advances*, *2*(2), e2020AV000310.

Sun, Y., Frankenberg, C., Wood, J. D., Schimel, D. S., Jung, M., Guanter, L., et al. (2017). OCO-2 advances photosynthesis observation from space via solar-induced chlorophyll fluorescence. *Science*, *358*(6360), eaam5747–eaam5747.

Sun, Y., Frankenberg, C., Jung, M., Joiner, J., Guanter, L., Köhler, P., & Magney, T. (2018). Overview of Solar-Induced chlorophyll Fluorescence (SIF) from the Orbiting Carbon Observatory-2: Retrieval, cross-mission comparison, and global monitoring for GPP. *Remote Sensing of Environment*.

Sun, Y., Frankenberg, C., Wood, J. D., Schimel, D. S., Jung, M., Guanter, L., et al. (2017). OCO-2 advances photosynthesis observation from space via solar-induced chlorophyll fluorescence. *Science*, *358*(6360).

Sun, Y., Frankenberg, C., Jung, M., Joiner, J., Guanter, L., Köhler, P., & Magney, T. (2018). Overview of Solar-Induced chlorophyll Fluorescence (SIF) from the Orbiting Carbon Observatory-2: Retrieval, cross-mission comparison, and global monitoring for GPP. *Remote Sensing of Environment*, *209*, 808–823. https://doi.org/10.1016/J.RSE.2018.02.016

Sun, Y., Fu, R., Dickinson, R., Joiner, J., Frankenberg, C., Gu, L., et al. (2015). Drought onset mechanisms revealed by satellite solar-induced chlorophyll fluorescence: Insights from two contrasting extreme events. *Journal of Geophysical Research: Biogeosciences*, *120*(11), 2427–2440.

Swann, A. L. S., Hoffman, F. M., Koven, C. D., & Randerson, J. T. (2016). Plant responses to increasing CO2 reduce estimates of climate impacts on drought severity. *Proceedings of the National Academy of Sciences*, *113*(36), 10019–10024.

Tack, J., Barkley, A., & Nalley, L. L. (2015). Effect of warming temperatures on US wheat yields. *Proceedings of the National Academy of Sciences of the United States of America*, *112*(22), 6931–6936.

Tang, J., Bolstad, P. V., Desai, A. R., Martin, J. G., Cook, B. D., & Carey, E. V. (2008). Ecosystem respiration and its components in an old-growth forest in the Great Lakes region of the United States. *Agricultural and Forest Meteorology*, *148*(2), 171–185.

Tao, M., Chen, L., Su, L., & Tao, J. (2012). Satellite observation of regional haze pollution over the North China Plain. *Journal of Geophysical Research: Atmospheres*, *117*(D12).

Thomas, R. T., Prentice, I. C., Graven, H., Ciais, P., Fisher, J. B., Hayes, D. J., et al. (2016). Increased light-use efficiency in northern terrestrial ecosystems indicated by CO2 and greening observations. *Geophysical Research Letters*, *43*(21), 11,339-11,349.

Thomas, R. T., Prentice, I. C., Graven, H., Ciais, P., Fisher, J. B., Hayes, D. J., et al. (2016). Increased light-use efficiency in northern terrestrial ecosystems indicated by CO2 and greening observations. *Geophysical Research Letters*, *43*(21), 11,339-11,349.

Thoning, K. W., & Tans, P. P. (1989). Atmospheric carbon dioxide at Mauna Loa Observatory. 2. Analysis of the NOAA GMCC data, 1974-1985. *Journal of Geophysical Research*, *94*(D6), 8549–8565. https://doi.org/10.1029/JD094ID06P08549

Tucker, C. J. (1979). Red and photographic infrared linear combinations for monitoring vegetation. *Remote Sensing of Environment*, *8*(2), 127–150.

Turner, A. J., Köhler, P., Magney, T. S., Frankenberg, C., Fung, I., & Cohen, R. C. (2020). A double peak in the seasonality of California's photosynthesis as observed from space. *Biogeosciences*, *17*(2), 405–422.

Turner, D. P., Ritts, W. D., Cohen, W. B., Gower, S. T., Running, S. W., Zhao, M., et al. (2006). Evaluation of MODIS NPP and GPP products across multiple biomes. *Remote Sensing of Environment*, *102*(3–4), 282–292.

Turner, D. P., Ritts, W. D., Cohen, W. B., Gower, S. T., Running, S. W., Zhao, M., et al. (2006). Evaluation of MODIS NPP and GPP products across multiple biomes. *Remote Sensing of Environment*, *102*(3–4), 282–292.

TURNER, D. P., URBANSKI, S., BREMER, D., WOFSY, S. C., MEYERS, T., GOWER, S. T., & GREGORY, M. (2003). A cross-biome comparison of daily light use efficiency for gross primary production. *Global Change Biology*, *9*(3), 383–395.

Ummenhofer, C. C., & Meehl, G. A. (2017). Extreme weather and climate events with ecological relevance: a review. *Philosophical Transactions of the Royal Society B: Biological Sciences*, *372*(1723), 20160135.

Van der Tol, C., Berry, J. A., Campbell, P. K. E., & Rascher, U. (2014). Models of fluorescence and photosynthesis for interpreting measurements of solar-induced chlorophyll fluorescence. *Journal of Geophysical Research: Biogeosciences*, *119*(12), 2312–2327.

van der Tol, C., Verhoef, W., Timmermans, J., Verhoef, A., & Su, Z. (2009). An integrated model of soil-canopy spectral radiances, photosynthesis, fluorescence, temperature and energy balance. *Biogeosciences*, *6*(12), 3109–3129.

Van Der Werf, G. R., Randerson, J. T., Giglio, L., Van Leeuwen, T. T., Chen, Y., Rogers, B. M., et al. (2017). Global fire emissions estimates during 1997-2016. *Earth System Science Data*, *9*(2), 697–720.

Verbyla, D. (2011). Browning boreal forests of western North America. *Environmental Research Letters*, *6*(4), 041003. https://doi.org/10.1088/1748-9326/6/4/041003

Verma, M., Schimel, D., Evans, B., Frankenberg, C., Beringer, J., Drewry, D. T., et al. (2017). Effect of environmental conditions on the relationship between solar-induced fluorescence and gross primary productivity at an OzFlux grassland site. *Journal of Geophysical Research: Biogeosciences*, *122*(3), 716–733.

Verma, M., Schimel, D., Evans, B., Frankenberg, C., Beringer, J., Drewry, D. T., et al. (2017). Effect of environmental conditions on the relationship between solar-induced fluorescence and gross primary productivity at an OzFlux grassland site. *Journal of Geophysical Research: Biogeosciences*, *122*(3), 716–733.

Wang, J. A., Baccini, A., Farina, M., Randerson, J. T., & Friedl, M. A. (2021). Disturbance suppresses the aboveground carbon sink in North American boreal forests. *Nature Climate Change 2021 11:5*, *11*(5), 435–441.

Wang, K., Wang, Y., Wang, X., He, Y., Li, X., Keeling, R. F., et al. (2020). Causes of slowing-down seasonal CO2 amplitude at Mauna Loa. *Global Change Biology*, *26*(8), 4462–4477.

Wang, K., Wang, Y., Wang, X., He, Y., Li, X., Keeling, R. F., et al. (2020). Causes of slowing-down seasonal CO2 amplitude at Mauna Loa. *Global Change Biology*, *26*(8), 4462–4477.

Wang, R., Goll, D., Balkanski, Y., Hauglustaine, D., Boucher, O., Ciais, P., et al. (2017). Global forest carbon uptake due to nitrogen and phosphorus deposition from 1850 to 2100. *Global Change Biology*, *23*(11), 4854–4872.

Wang, X., Manning, W., Feng, Z., & Zhu, Y. (2007). Ground-level ozone in China: Distribution and effects on crop yields. *Environmental Pollution*, *147*(2), 394–400.

Wang, X., Piao, S., Ciais, P., Li, J., Friedlingstein, P., Koven, C., & Chen, A. (2011). Spring temperature change and its implication in the change of vegetation growth in North America from 1982 to 2006. *Proceedings of the National Academy of Sciences*, *108*(4), 1240–1245.

Wang, X., Zhao, C., Müller, C., Wang, C., Ciais, P., Janssens, I., et al. (2020). Emergent constraint on crop yield response to warmer temperature from field experiments. *Nature Sustainability*, *3*(11), 908–916.

Wang, Y., Jiang, J. H., & Su, H. (2015). Atmospheric responses to the redistribution of anthropogenic aerosols. *Journal of Geophysical Research: Atmospheres*, *120*(18), 9625–9641.

Wehr, R., Munger, J. W., McManus, J. B., Nelson, D. D., Zahniser, M. S., Davidson, E. a, et al. (2016). Seasonality of temperate forest photosynthesis and daytime respiration. *Nature*, *534*(7609), 680–683.

Wei, J., Li, Z., Lyapustin, A., Sun, L., Peng, Y., Xue, W., et al. (2021). Reconstructing 1-km-resolution high-quality PM2. 5 data records from 2000 to 2018 in China: spatiotemporal variations and policy implications. *Remote Sensing of Environment*, *252*, 112136.

Welp, L. R., Randerson, J. T., & Liu, H. P. (2007). The sensitivity of carbon fluxes to spring warming and summer drought depends on plant functional type in boreal forest ecosystems. *Agricultural and Forest Meteorology*, *147*(3–4), 172–185.

Wen, J., Köhler, P., Duveiller, G., Parazoo, N. C., Magney, T. S., Hooker, G., et al. (2020). A framework for harmonizing multiple satellite instruments to generate a long-term global high spatial-resolution solar-induced chlorophyll fluorescence (SIF). *Remote Sensing of Environment*, *239*, 111644.

Wen, J., Köhler, P., Duveiller, G., Parazoo, N. C., Magney, T. S., Hooker, G., et al. (2020). A framework for harmonizing multiple satellite instruments to generate a long-term global high spatial-resolution solar-induced chlorophyll fluorescence (SIF). *Remote Sensing of Environment*, *239*, 111644.

Wiik, L., & Ewaldz, T. (2009). Impact of temperature and precipitation on yield and plant diseases of winter wheat in southern Sweden 1983-2007. *Crop Protection*, *28*(11), 952–962.

Winkler, A. J., Myneni, R. B., Hannart, A., Sitch, S., Haverd, V., Lombardozzi, D., et al. (2021). Slowdown of the greening trend in natural vegetation with further rise in atmospheric CO2. *Biogeosciences*, *18*(17), 4985–5010.

Wofsy, S. C. (2011). HIAPER Pole-to-Pole Observations (HIPPO): Fine-grained, global-scale measurements of climatically important atmospheric gases and aerosols. *Philosophical Transactions of the Royal Society A: Mathematical, Physical and Engineering Sciences*, *369*(1943), 2073–2086.

Wohlfahrt, G., & Gu, L. (2015). The many meanings of gross photosynthesis and their implication for photosynthesis research from leaf to globe. *Plant, Cell and Environment*, *38*(12), 2500–2507.

Wolf, S., Keenan, T. F., Fisher, J. B., Baldocchi, D. D., Desai, A. R., Richardson, A. D., et al. (2016). Warm spring reduced carbon cycle impact of the 2012 US summer drought. *Proceedings of the National Academy of Sciences*, *113*(21), 5880–5885.

Wood, J. D., Griffis, T. J., Baker, J. M., Frankenberg, C., Verma, M., & Yuen, K. (2017). Multiscale analyses of solar-induced florescence and gross primary production. *Geophysical Research Letters*, *44*(1), 533–541.

Wood, J. D., Knapp, B. O., Muzika, R.-M., Stambaugh, M. C., & Gu, L. (2018). The importance of drought–pathogen interactions in driving oak mortality events in the Ozark Border Region. *Environmental Research Letters*, *13*(1), 15004.

Wood, J. D., Griffis, T. J., Baker, J. M., Frankenberg, C., Verma, M., & Yuen, K. (2017). Multiscale analyses of solar-induced florescence and gross primary production. *Geophysical Research Letters*, *44*(1), 533–541.

Wu, G., Guan, K., Jiang, C., Peng, B., Kimm, H., Chen, M., et al. (2020). Radiance-based NIRv as a proxy for GPP of corn and soybean. *Environmental Research Letters*, *15*(3), 034009.

Wu, J., Bei, N., Hu, B., Liu, S., Wang, Y., Shen, Z., et al. (2020). Aerosol–photolysis interaction reduces particulate matter during wintertime haze events. *Proceedings of the National Academy of Sciences of the United States of America*, *117*(18), 9755–9761.

Xue, T., Zheng, Y., Tong, D., Zheng, B., Li, X., Zhu, T., & Zhang, Q. (2019). Spatiotemporal continuous estimates of PM2.5 concentrations in China, 2000–2016: A machine learning method with inputs from satellites, chemical transport model, and ground observations. *Environment International*, *123*, 345–357.

Yang, B., Pallardy, S. G., Meyers, T. P., Gu, L. H., Hanson, P. J., Wullschleger, S. D., et al. (2010). Environmental controls on water use efficiency during severe drought in an Ozark Forest in Missouri, USA. *Global Change Biology*, *16*(8), 2252–2271. https://doi.org/10.1111/j.1365-2486.2009.02138.x

Yang, K., Ryu, Y., Dechant, B., Berry, J. A., Hwang, Y., Jiang, C., et al. (2018). Sun-induced chlorophyll fluorescence is more strongly related to absorbed light than to photosynthesis at half-hourly resolution in a rice paddy. *Remote Sensing of Environment*, *216*, 658–673.

Yang, X., Tang, J., Mustard, J. F., Lee, J., Rossini, M., Joiner, J., et al. (2015). Solar-induced chlorophyll fluorescence that correlates with canopy photosynthesis on diurnal and seasonal scales in a temperate deciduous forest. *Geophysical Research Letters*, *42*(8), 2977–2987.

YI, F. jin, FENG, J. ao, WANG, Y. jun, & JIANG, F. (2020). Influence of surface ozone on crop yield of maize in China. *Journal of Integrative Agriculture*, *19*(2), 578–589. https://doi.org/10.1016/S2095-3119(19)62822-4

Yi, F., McCarl, B. A., Zhou, X., & Jiang, F. (2018). Damages of surface ozone: Evidence from agricultural sector in China. *Environmental Research Letters*, *13*(3), 34019. https://doi.org/10.1088/1748-9326/aaa6d9

Yin, Y., Ciais, P., Chevallier, F., Li, W., Bastos, A., Piao, S., et al. (2018). Changes in the Response of the Northern Hemisphere Carbon Uptake to Temperature Over the Last Three Decades. *Geophysical Research Letters*, *45*(9), 4371–4380. https://doi.org/10.1029/2018GL077316

Yoshida, Y., Joiner, J., Tucker, C., Berry, J., Lee, J.-E., Walker, G., et al. (2015). The 2010 Russian drought impact on satellite measurements of solar-induced chlorophyll fluorescence: Insights from modeling and comparisons with parameters derived from satellite reflectances. *Remote Sensing of Environment*, *166*, 163–177.

Yu, K., Keller, C. A., Jacob, D. J., Molod, A. M., Eastham, S. D., & Long, M. S. (2018). Errors and improvements in the use of archived meteorological data for chemical transport modeling: An analysis using GEOS-Chem v11-01 driven by GEOS-5 meteorology. *Geoscientific Model Development*, *11*(1), 305–319. https://doi.org/10.5194/GMD-11-305-2018

Yu, L., Wen, J., Chang, C. Y., Frankenberg, C., & Sun, Y. (2019). High-resolution global contiguous SIF of OCO-2. *Geophysical Research Letters*, *46*(3), 1449–1458.

Yuan, W., Liu, S., Zhou, G., Zhou, G., Tieszen, L. L., Baldocchi, D., et al. (2007). Deriving a light use efficiency model from eddy covariance flux data for predicting daily gross primary production across biomes. *Agricultural and Forest Meteorology*, *143*(3–4), 189–207.

Yuan, W., Piao, S., Qin, D., Dong, W., Xia, J., Lin, H., & Chen, M. (2018). Influence of vegetation growth on the enhanced seasonality of atmospheric CO2. *Global Biogeochemical Cycles*, *32*(1), 32–41.

Yuan, W., Zheng, Y., Piao, S., Ciais, P., Lombardozzi, D., Wang, Y., et al. (2019). Increased atmospheric vapor pressure deficit reduces global vegetation growth. *Science Advances*, *5*(8), eaax1396.

Zeng, N., Mariotti, A., & Wetzel, P. (2005). Terrestrial mechanisms of interannual CO2 variability. *Global Biogeochemical Cycles*, *19*(1), 1–15.

Zeng, N., Zhao, F., Collatz, G. J., Kalnay, E., Salawitch, R. J., West, T. O., & Guanter, L. (2014). Agricultural Green Revolution as a driver of increasing atmospheric CO 2 seasonal amplitude. *Nature*, *515*(7527), 394–397.

Zeng, Y., Badgley, G., Dechant, B., Ryu, Y., Chen, M., & Berry, J. A. (2019). A practical approach for estimating the escape ratio of near-infrared solar-induced chlorophyll fluorescence. *Remote Sensing of Environment*, *232*, 111209.

Zhang, K., Kimball, J. S., Hogg, E. H., Zhao, M., Oechel, W. C., Cassano, J. J., & Running, S. W. (2008). Satellite-based model detection of recent climate-driven changes in northern high-latitude vegetation productivity. *Journal of Geophysical Research: Biogeosciences*, *113*(G3), 3033. https://doi.org/10.1029/2007JG000621

Zhang, Q., Zhang, Y., Li, Z., Li, J., & Zhang, X. (2019). The effects of sun-viewer geometry on sun-induced fluorescence and its relationship with gross primary

production. In *IGARSS 2019-2019 IEEE International Geoscience and Remote Sensing Symposium* (pp. 9048–9051). IEEE.

Zhang, Q., Zheng, Y., Tong, D., Shao, M., Wang, S., Zhang, Y., et al. (2019). Drivers of improved PM2.5 air quality in China from 2013 to 2017. *Proceedings of the National Academy of Sciences of the United States of America*, *116*(49), 24463–24469.

Zhang, T., Yue, X., Unger, N., Feng, Z., Zheng, B., Li, T., et al. (2021). Modeling the joint impacts of ozone and aerosols on crop yields in China: An air pollution policy scenario analysis. *Atmospheric Environment*, *247*, 118216.

Zhang, Y., Joiner, J., Alemohammad, S. H., Zhou, S., & Gentine, P. (2018). A global spatially contiguous solar-induced fluorescence (CSIF) dataset using neural networks. *Biogeosciences*, *15*(19), 5779–5800.

Zhang, Y., Parazoo, N. C., Williams, A. P., Zhou, S., & Gentine, P. (2020). Large and projected strengthening moisture limitation on end-of-season photosynthesis. *Proceedings of the National Academy of Sciences*, *117*(17), 9216–9222.

Zhang, Y., Xiao, X., Jin, C., Dong, J., Zhou, S., Wagle, P., et al. (2016). Consistency between sun-induced chlorophyll fluorescence and gross primary production of vegetation in North America. *Remote Sensing of Environment*, *183*, 154–169.

Zhang, Y., Guanter, L., Berry, J. A., Joiner, J., van der Tol, C., Huete, A., et al. (2014). Estimation of vegetation photosynthetic capacity from space-based measurements of chlorophyll fluorescence for terrestrial biosphere models. *Global Change Biology*, *12*, 3727-3742.

Zhao, B., Zheng, H., Wang, S., Smith, K. R., Lu, X., Aunan, K., et al. (2018). Change in household fuels dominates the decrease in PM2.5 exposure and premature mortality in China in 2005–2015. *Proceedings of the National Academy of Sciences of the United States of America*, *115*(49), 12401–12406.

Zhao, C., Liu, B., Piao, S., Wang, X., Lobell, D. B., Huang, Y., et al. (2017). Temperature increase reduces global yields of major crops in four independent estimates. *Proceedings of the National Academy of Sciences of the United States of America*, *114*(35), 9326–9331.

Zhao, C., Piao, S., Huang, Y., Wang, X., Ciais, P., Huang, M., et al. (2016). Field warming experiments shed light on the wheat yield response to temperature in China. *Nature Communications*, *7*(1), 1–8.

Zhao, F., & Zeng, N. (2014). Continued increase in atmospheric CO 2 seasonal amplitude in the 21st century projected by the CMIP5 Earth system models. *Earth Syst. Dynam*, *5*, 423–439.

Zhao, F., Zeng, N., Asrar, G., Friedlingstein, P., Ito, A., Jain, A., et al. (2016). Role of CO2, climate and land use in regulating the seasonal amplitude increase of carbon fluxes in terrestrial ecosystems: A multimodel analysis. *Biogeosciences*, *13*(17), 5121–5137.

Zhao, J., Kong, X., He, K., Xu, H., & Mu, J. (2020). Assessment of the radiation effect of aerosols on maize production in China. *Science of the Total Environment*, *720*, 137567.

Zhao, M., Heinsch, F. A., Nemani, R. R., & Running, S. W. (2005). Improvements of the MODIS terrestrial gross and net primary production global data set. *Remote Sensing of Environment*, *95*(2), 164–176.

Zhu, Z., Piao, S., Myneni, R. B., Huang, M., Zeng, Z., Canadell, J. G., et al. (2016). Greening of the Earth and its drivers. *Nature Climate Change*, *6*(8), 791–795.

Zuromski, L. M., Bowling, D. R., Köhler, P., Frankenberg, C., Goulden, M. L., Blanken, P. D., & Lin, J. C. (2018). Solar-induced fluorescence detects interannual variation in gross primary production of coniferous forests in the Western United States. *Geophysical Research Letters*, *45*(14), 7184–7193.